Versuchsanstalt für Wasserbau
Hydrologie und Glaziologie
der Eidgenössischen
Technischen Hochschule Zürich

Mitteilungen 223

Unstructured block ramps

Simona Tamagni

Zürich, 2013

Herausgeber: Prof. Dr. Robert Boes

Zitiervorschlag für VAW-Mitteilungen:

Tamagni, S. (2013).
Unstructured block ramps.
Mitteilungen 223, Versuchsanstalt für Wasserbau, Hydrologie und Glaziologie (VAW),
R. M. Boes, Hrsg., ETH Zürich.

Im Eigenverlag der
Versuchsanstalt für Wasserbau,
Hydrologie und Glaziologie
ETH Zürich
CH-8092 Zürich

Tel.: +41 - 44 - 632 4091
Fax: +41 - 44 - 632 1192
e-mail: info@vaw.baug.ethz.ch

Zürich, 2013

ISSN 0374-0056

Preface

In her dissertation thesis project Dr. Simona Tamagni conducted an experimental investigation of so-called unstructured block ramps. As their name suggests, these structures are a special type of block ramps, i.e. hydraulic structures typically with a constant and rather high bed slope, which are more and more applied in river engineering nowadays to replace existing drop structures and sills and to restore longitudinal continuity for the fish fauna and invertebrates. Due to the large number of existing drop structures in Swiss and international rivers and watercourses, this topic deserves to receive scientific attention. In the past, particularly step-pool systems and classical block ramps have been focused on in academia, amongst others in a number of experimental investigations conducted at VAW (e.g. Whittaker and Jäggi 1986, Weichert 2006). Unstructured ramps are advantageous in terms of stability, as they do not fail abruptly, and in terms of fish migration, as their macro-roughness leads to zones of reduced flow velocities that facilitate fish upstream migration.

The overarching objective of this research project was to find new stability criteria of unstructured block ramps following some ramp failure cases in the major 2005 flood event in large parts of Switzerland. This goal included both the determination of an optimum parameter combination such as block size and characteristic bed material diameter (phase A) and the effect of boundary conditions at the upstream and downstream end of unstructured ramps (phase B). Moreover, the understanding of the hydraulic conditions on unstructured ramps, particularly regarding turbulence and flow velocities (phase C), was aimed at to better describe the ecological conditions in terms of migration corridors.

To reach this goal, capturing the relevant processes such as sediment and block erosion, transport and deposition by surface flow, and its interaction with subsurface flow was required. Dr. Tamagni therefore conducted laboratory experiments in a 13.5 m long and 0.60 m wide flume under both steady and quasi-steady conditions using uniform material and sediment mixtures of varying particle size distribution (phases A and B). She further carried out experiments in a 8 m long and 0.4 m wide flume using 2D Laser Doppler Anemometry (LDA) to study turbulence characteristics on unstructured block ramps (phase C), and she took part in two field campaigns led by Eawag fish biologists

to investigate the fish migration capabilities under prototype conditions, one in an Alpine river and the other in a Swiss plateau river.

In phase A of her experiments, Dr. Tamagni systematically analyzed the effects of blocks, ratio between block size D and characteristic grain size d_{90} of the bed material, block placement density, sediment supply (i.e. with and without sediment input by the approach flow), material composition and grain size distribution. From these analyses she deduced a general equation for the calculation of the equilibrium slope of unstructured ramps as function of specific weight, block diameter D and bed material d_{90} as well as block placement density, representing the core result on ramp stability. Furthermore, relationships to compute the uniform flow depth and the mean flow velocities on unstructured block ramps are suggested. As to flow resistance, the experimental data are compared to literature findings, and adaptations of two well-known formulae are suggested to be applied to unstructured block ramps under the parameter range investigated. Regarding energy dissipation, the relative head loss found in the present study is slightly lower than that given by Pagliara and Chiavaccini (2006a) for unstructured ramps, whereas it is pronouncedly lower than that of structured block ramps with cross bars as presented by Oertel and Schlenkhoff (2012).

An analysis of phase B experiments showed that the ramp toe has to be stabilized against erosion to exclude undue bed incision that might trigger ramp or bank failures. These tests further proved that the design criteria developed from steady flow conditions in phase A are “on the safe side” when compared to typical hydrographs of Swiss rivers that served as a basis for the experiments in phase B. However, as local effects like flow concentrations from curvature flow have not been specifically taken into account, a safety margin appears reasonable.

Besides collecting valuable experimental data for numerical flow modeling purposes, phase C showed that at least the maximum velocity criterion for fish upstream migration is satisfied on unstructured block ramps for typical Swiss conditions, indicating a theoretical migratability. Vertical velocity profiles collected by means of LDA for a ramp configuration that proved to be quite stable in phase A can be classified into several zones showing distinct behavior in terms of velocity distribution and turbulence characteristics, namely an sedimentary sublayer, a macro-roughness sublayer and a form-induced sublayer. Large-scale coherent structures do not seem to exist, because the quadrant analysis of relative velocity fluctuations did not result in appreciable correlations.

I wish to express my gratitude to the Swiss Federal Office for the Environment (FOEN) who supported Dr. Tamagni's research financially. The co-reviews of Dr. G.R. Bezzola, FOEN, Prof. Dr. S. Pagliara, University of Pisa, and Dr. V. Weitbrecht, VAW, as well as the contribution of Dr. A. Peter, Eawag, are gratefully acknowledged.

Zurich, December 2013 Prof. Dr. Robert M. Boes

Acknowledgements

This doctoral thesis was written during my employment at the Laboratory of Hydraulics, Hydrology and Glaciology (VAW) at the Swiss Federal Institute of Technology (ETH) Zurich. I would like to thank all who contributed to the present work with particular acknowledgement to

- My supervisor Dr. Volker Weitbrecht, who motivated me to start this doctoral thesis and assisted me with constant scientific and moral support during four years: *Grazie Capo!*
- VAW Director and examiner Prof. Dr. Robert Boes for the support and the detailed review.
- Co-examiner Prof. Dr. Stefano Pagliara of Università di Pisa for the review and the valuable comments during the thesis.
- Co-examiner Dr. Gian Reto Bezzola for his invaluable support: his competence and knowledge both in the research and in the practical field made this thesis more complete and useful for design purposes.
- Dr. A. Peter and his team for their patient support while I tried to get an understanding of fish and ecology, and for their great commitment by the field tests.
- Prof. V. Nikora for his valuable advices about the double averaging method.
- The technical infrastructure team of VAW including workshop, electronics workshop, the photographer and the graphic designers for their excellent work.
- All my colleagues at VAW and friends for their positive inputs and in playing an important role in motivating me.
- My master students for their diligent work and motivating discussions.
- Pierre Yves Mayor from Institut for Geotechnical Engineering (IGT) for his support for the determination of the material permeability.
- Aglaia von Götz for her precise measurements.
- The Bundesamt für Umwelt BAFU for the financial support of the project with number 00.01157.PZ / J234-1541.

- Infine alla mia famiglia, a te Simo e ai miei amici più cari, *grazie di cuore*! Il sostegno che mi avete dato in questi anni ha contato più di qualunque altra cosa.

Zurich, 19th of November 2013 Simona Tamagni

Table of contents

Abstract

Unstructured Block Ramps (UBR) are river engineering structures used to stabilize the river bed against erosion. They represent an alternative to drops and sills offering better ecological conditions particularly in terms of fish migration. The experience with such structures is limited to the past two decades. During the last flood events in Switzerland, many UBR failed, demonstrating that the design was not sufficient. Most design criteria relate to other types of block ramps, in particular to ramps of block carpet type or to structured block ramps.

Physical model tests were conducted at VAW to investigate the ramp stability and the ramp behaviour in case of flood scenarios including the overload case. Different parameter combinations were tested to find an optimal combination in terms of ramp stability. The effects of: (1) ratio between block diameter and characteristic grain size of the sediment material, (2) block placement density, (3) sediment supply and (4) uniformity of the grain size distribution were tested under steady discharge conditions. Furthermore, the overall behaviour was tested by including an erodible downstream reach and by investigating the effect of quasi-steady discharge conditions representing typical flood hydrographs.

A more fundamental part of the study involved 2D Laser Doppler Anemometry (LDA) measurements to determine the hydraulics and the turbulence occurring on heterogeneous rough bed with macro-roughness elements, as for UBR. The local flow conditions were described with local time-averaged quantities, particularly to study the migration possibilities within the UBR. The general flow conditions were characterized with double-averaged quantities, which are decisive for the determination of the flow resistance.

Together with the Swiss Federal Institute of Aquatic Science and Technology (Eawag) field tests were carried out. Fish migration was tested in the field at two different UBR using Passive Integrated Transponders (PIT) tags combined with an antenna to detect the fish passage.

A main result of the present research is a model for the determination of the ramp stability which can be applied for design purposes. The velocity measurements can be used to rate UBR in terms of fish migration and to calibrate numerical models.

Zusammenfassung

Unstrukturierte Blockrampen sind Flussbauwerke, die der Stabilisierung der Flusssohle und dem Schutz gegen Erosion dienen. Sie stellen eine ökologisch vorteilhafte Alternative zu Abstürzen und Schwellen dar, insbesondere bezüglich der Fischwanderung. Die Erfahrung mit solchen Bauwerken ist begrenzt auf die letzten Jahrzehnte. Während der letzten Hochwasserereignisse in der Schweiz versagten mehrere unstrukturierte Blockrampen. Es zeigte sich, dass die Dimensionierung dieser Rampen nicht ausreichend war. Die bestehenden Dimensionierungsgrundlagen beziehen sich besonders auf andere Blockrampentypen, die klassischen oder strukturierten Blockrampen.

An der VAW wurden physikalische Modellversuche durchgeführt, um die Stabilität und das Verhalten von unstrukturierten Blockrampen im Hochwasser- und im Überlastfall zu untersuchen. Unterschiedliche Parameterkombinationen wurden getestet, um eine optimale Kombination hinsichtlich der Rampenstabilität zu finden. Der Einfluss: (1) des Verhältnises zwischen Blockdurchmesser und charakteristischem Korndurchmesser des Sedimentmaterials, (2) der Belegungsdichte der Blöcke, (3) der Geschiebezugabe, und (4) der Form der Kornverteilungskurve wurde für stationäre Abflussbedingungen untersucht. Zudem wurde das Gesamtverhalten der Rampe getestet, indem eine erodierbare Strecke flussabwärts der Rampe installiert und der Einfluss von quasi-stationären Abflussbedingungen untersucht wurde, die typische Hochwasserganglinien repräsentieren.

Ein Teilprojekt beinhaltete detaillierte 2D *Laser Doppler Anemometer* (LDA) Messungen zur Bestimmung der Fliesscharakteristik, die in solch heterogenen rauen Sohlen mit Makrorauheiten auftritt. Die lokalen Strömungsverhältnisse wurden mit lokalen zeitlich-gemittelten Parametern beschrieben, um insbesondere die Wandermöglichkeiten für Fische innerhalb der unstrukturierten Blockrampen zu untersuchen. Die allgemeinen Strömungsverhältnisse wurden durch doppelt-gemittelte (zeitlich und räumlich) Parameter beschrieben, die für die Bestimmung des Fliesswiderstands massgebend sind.

In Zusammenarbeit mit der Eidgenössischen Anstalt für Wasserversorgung, Abwasserreinigung und Gewässerschutz (Eawag) wurden Feldversuche durchgeführt. Die Fischwanderung wurde im Prototyp an zwei unstrukturierten Blockrampen getestet.

Dabei wurden *Passive Integrated Transponder* (PIT) tags (passive Mikrochips) zusammen mit einer Antenne verwendet, um den Fischdurchgang zu detektieren.

Ein Hauptergebnis dieses Forschungsprojektes ist ein Modell zur Bestimmung der Stabilität von unstrukturierten Blockrampen, der für die Dimensionierung verwendet werden kann. Die detaillierten 2D LDA-Geschwindigkeitsmessungen können zudem dazu dienen, die ökologische Effizienz hinsichtlich der Fischwanderung solcher Rampen zu beurteilen oder numerische Modelle zu kalibrieren.

Sommario

Le rampe in pietrame sciolto non strutturato sono opere di ingegneria fluviale che permettono di stabilizzare l'alveo e di proteggerlo da erosione. Rappresentano un'alternativa più ecologica alle opere di caduta in particolare riguardo alla migrazione dei pesci. L'esperienza con il dimensionamento di queste opere è limitata agli ultimi due decenni. Gli ultimi eventi di piena hanno causato la rottura di diverse ramp in pietrame sciolto indicandone il dimensionamento non sufficiente per il carico di piena. La maggior parte dei criteri di dimensionamento si riferisce ad altri tipi di rampe, in particolare a quelle classiche, dove il pietrame ricopre alveo sull'intera larghezza, oppure a quelle in pietrame sciolto ma strutturato.

Delle prove su modello sono state condotte per studiare la stabilità di questo tipo di rampe come pure il loro comportamento in caso di carichi elevati e di sovraccarico. Diversi parametri sono stati testati al fine di ottenere una combinazione ottimale riguardante la stabilità della rampa. L'influenza di: (1) rapporto fra il diametro dei blocchi e la dimensione caratteristica dei grani del materiale di fondo, (2) densità di occupazione dei blocchi, (3) apporto di materiale per il trasporto solido, (4) uniformità della distribuzione granulometrica del materiale di fondo è stata testata in condizioni di deflusso stazionario. Inoltre il comportamento globale della rampa è stato studiato aggiungendo un settore a materiale mobile ed erodibile a valle della rampa e investigando gli effetti di condizioni di deflusso quasi-stazionarie rappresentate da un idrogramma per un tipico evento di piena.

Una parte dello studio è stata dedicata alla ricerca fondamentale, dove delle misurazioni eseguite con la velocimetria laser Doppler in 2D hanno permesso di determinare l'idraulica e la turbolenza che si manifestano su superfici eterogenee e rugose con delle macro rugosità, come nel caso delle rampe in pietrame sciolto non strutturato. Le condizioni di deflusso locali sono state descritte tramite parametri di medie temporali, in modo da poter in particolare studiare le possibilità di migrazione per i pesci all'interno delle rampe in questione. Le condizioni di deflusso generali, invece, vengono caratterizzate tramite parametri di medie doppie (cioè temporali e spaziali), che sono determinanti per definire la resistenza del flusso.

Uno dei maggiori risultati di questa ricerca è il modello per la determinazione della stabilità delle rampe in pietrame sciolto non strutturato, il quale può essere utilizzato

per il dimensionamento di tali opere. Le misurazioni della velocità possono essere utilizzate per valutare tali rampe dal punto di vista della migrazione dei pesci e per calibrare dei modelli numerici.

1 Introduction

1.1 Motivation

Swiss rivers are interrupted by approximately 100'000 drops and sills (about 90%) and artificial structures (about 10%) with an elevation difference larger than 0.5 m (Zeh Weissman *et al.* 2009), precluding the longitudinal connectivity of the watercourses. This situation led to fragmented habitat conditions and to strongly reduced variability as well as reduced occurrence of many species in our rivers (Werth *et al.* 2011, Alp *et al.* 2011). Alternatively to drops and sills, block ramps are more and more used in river restoration projects to stabilize the river bed against erosion due to their better ecological functionality. During the past decades many existing drops have been replaced by block ramps and many more are planned. However, during the last flood events, it turned out that the design of block ramps was not sufficient in any case, as many of them failed (e.g. Bezzola and Hegg 2008).

There are different types of block ramps: on the one hand the block ramps formed by a block carpet, where the entire flume width is covered by blocks, and on the other hand the block ramps formed by different configuration of clusters. The description of each single ramp type is given in Chap. 1.2. Each ramp type establishes different hydraulic conditions and thus needs to be investigated separately. This research project focuses especially on Unstructured Block Ramps (UBR), which are characterized by large isolated roughness elements (blocks) randomly placed on the river bed material (Figure 1.1).

Ecological requirements for river engineering measures are becoming more and more eminent. Particularly with the revised Swiss water protection law (*Gewässerschutzgesetz*) that came into force in January 2011, the exigencies regarding ecology increased: the goal is to remove all man-made obstacles of watercourses within 20 years and to restore the longitudinal connectivity. Therefore, the applicability of block ramps is not only dependent on stability criteria, but also on their ecological behaviour, where structural heterogeneity and flow conditions (particularly water depth, flow velocity and turbulence characteristics) are important. For that reason, research on block ramps has to progress towards two major aims at the same time, namely to develop stability criteria and improved ecological efficiency.

Figure 1.1 Unstructured block ramp at the Landquart River with specific discharge $q \approx 0.28$ m^3/(sm), corresponding approximately to Q_{30} (view against the flow direction).

The need of sustainable river restoration measures and of an uninterrupted longitudinal connectivity of watercourses makes the present research significant especially to the Alpine regions, where UBR find their application. The Laboratory of Hydraulics, Hydrology and Glaciology (VAW) has been investigating with physical models tests different block ramps types for more than 25 years. Whittaker and Jäggi (1986) tested different failure mechanisms of block ramps of "block carpet" type (Chap. 1.2) and provided the corresponding design approaches (Chap. 3.2). The know-how achieved during those years of research on step-pool systems and on block ramps with the large amount of physical experiments led to a workshop held at the VAW in 2006 (VAW 2007). During this workshop experts shared the latest results, in order to outline the state of the art of such structures with focus on ongoing research, existing design guidelines, environmental requirements, and to summarize practical knowledge. The research at the VAW on block ramps and particularly on the unstructured type did not stop with this workshop: the present work represents the results of the investigations of the past years (2009-2013).

1.2 Definition and classification of block ramps

According to the classification given in Figure 1.2 block ramps are divided into two groups. The "*block carpet*" type includes the classic and first developed block ramp designs, involving tightly packed blocks forming a block carpet covering the entire river width. Ramps of block carpet type are subdivided into *interlocked* block ramps characterized by one layer of blocks vertically placed closely together, leading to a compact, hydraulic solid but quasi rigid construction; and *dumped* block ramps where the blocks are dumped in two or more layers, leading to a heavier and more heterogeneous construction. With both types of ramps depending on the existing sediment bed material a filter layer is used to protect the underground material against washout effects (DWA 2009). Experiences with ramps of block carpet type show that these are used up to a bed slope of $S = 10\%$ (Bezzola 2010 and Hunziker, Zarn & Partner 2008). The main difference between these two methods is the needed amount of blocks, causing higher costs for the dumped design. However, dumped block ramps assure a certain flexibility in case of erosion of the river bed (assuming no entrainment of the single blocks). This favourable aspect competes against the better cost-effectiveness of ramps with interlocked blocks. Another difference is that the effective roughness of an interlocked block ramp is lower than of the dumped one, leading to higher flow velocity occurring on such ramps and so to less favourable conditions for fish upstream migration.

Ramps of the "*block cluster*" type are characterized by dispersed configurations of block clusters, leading to more natural conditions due to their distinctive heterogeneity. In case of structured geometrical configuration of the blocks, like e.g. rows or arches generating a step-pool system, they are *structured* block ramps, corresponding to the characteristic morphology of mountain rivers. For low to medium discharge conditions, this sequence of pools with low flow velocity and of little steps offers more suitable hydraulic conditions for the fish migration as in case of a ramp of block carpet type. According to LUBW (2006) the maximal ramp slope for structured block ramps is 6.7%.

In case of *unstructured* block ramps (UBR) the blocks are isolated and randomly placed on the river bed with a certain block placement density λ, which is defined as the ratio between the area covered by blocks and the total ramp area. There is neither contact between the boulders nor a geometrical regular block configuration. The random configuration leads to a strong heterogeneity of the bed: in the resulting flow pattern the

variation of hydraulic conditions is high, offering many possibilities for the fish migration in respect to the different swimming capacities. According to Janisch (2007) the maximal slope of UBR is 3%. With the present work the application range of these ramps is further examined and investigated in detail.

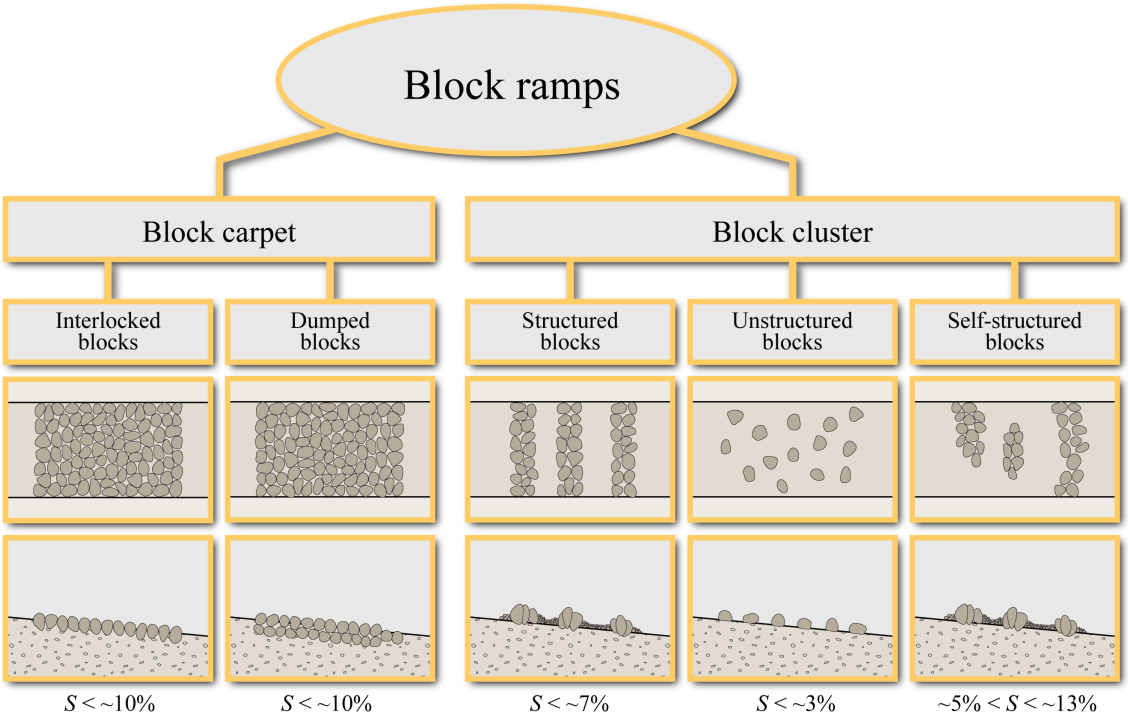

Figure 1.2 Classification of block ramps (Lange 2007, modified)

The fundamental idea by *self-structured* block ramps is to recreate the morphological conditions of steep mountain rivers, characterized by a coarse structured armoured layer, which generates through the erosion process a step-pool system. The steps are given by a block arrangement in rows across the river width. The difference to the structured block ramps is that those rows are not artificially built, but formed through natural hydraulic load occurring on the ramp. In order to achieve suitable conditions for the self-structuring process, typical steep river materials are delivered and the initial ramp slope must be steeper than the final pursued ramp slope. As a result of this the erosion process can occur and build the naturally structured armoured layer. According to Lange (2007) the ramp slope range of self-structured block ramps is between 5% and 13%.

Regarding stability aspects ramps of block carpet type are more suitable in case of high hydraulic load and steep slope due to their higher stability. However, considering

the ecological aspects, they are very homogeneous in flow velocities and bed topography and, therefore, less preferable to the second type of block ramps with distributed block clusters. Additionally, also the failure mechanism in case of overload of unstructured and of self-structured block ramps is more suitable, due to the flexibility of the structure that prevents an abrupt failure. This topic is discussed in detail in Chap. 3.2.3.

Block ramps and in particular *unstructured* block ramps have to achieve different goals, namely:

- To overcome a certain height difference of the river bed in a stable manner
  The block ramp provides a fixed-point affecting the river reach upstream of the ramp. If the ramp slope changes due to erosion, the ramp head is sinking and the fixed-point effect disappears. Adding a buffer area (Chap. 3.2.3) upstream of the ramp head, the fixed-point effect can be maintained also within a certain range of ramp erosion.
- Flexible ramp behaviour
  An abrupt failure or collapse has to be avoided and the ramp should adjust itself to the discharge by a gentle slope flattening or by local block movements.
- Ecological efficiency
  A block ramp has to provide upstream migration possibilities during a certain period and range of discharges for the fish species living in the river (see e.g. Chap. 3.1).

The failure of an unstructured block ramp can be defined in different ways according to the goal considered. The different failure mechanisms are described in detail in Chap. 3.2.3.

1.3 Goals

River engineering measures, like river revitalization or flood protection projects or a combination of both, have to guarantee sufficient hydraulic functionality and adequate ecological standards. The present work aims at improving existing design guidelines by extending their application range while proving the effective ecological functionality of UBR. To achieve this the project has been divided into three physical modelling phases, which mainly focus on different topics and for which two models with different experimental set ups were built; additionally, field tests were carried out with the Swiss Federal Institute of Aquatic Science and Technology (Eawag) and a survey was conducted:

- Phase A – Stability model tests – Flume I
  The stability of UBR and its behaviour for different discharge conditions were investigated, focussing on the determination of an optimal parameter combination in terms of stability and of no abrupt failure. In case of hydraulic overload the ramp should adapt itself by a gentle adjustment of its slope and should not lead to a sudden movement of a number of blocks. Based on the equilibrium slope for each tested discharge the ramp stability was parameterized for design purposes. The tests were conducted under steady flow conditions.

- Phase B – General ramp behaviour model tests – Flume I
  The effect of varying boundary conditions were studied in phase B by linking the block ramp to the up- and downstream river reach. This phase aimed at investigating the general behaviour of UBR in the river system. The tests were conducted under steady as well as quasi-steady conditions to include time dependency and to show the influence of a certain flood event.

- Phase C – Turbulence model tests – Flume II
  Velocity and turbulence characteristics occurring on the ramp were investigated with two dimensional (2D) Laser-Doppler-Anemometry (LDA) measurements with fixed bed topography and optimal parameter combination in terms of stability derived from phase A. The goal was to gain detailed velocity profiles and characterize the turbulence, to better understand the hydraulic conditions of the ramp, but also to describe the ecological conditions, particularly in term of variety of migration corridors. The tests were conducted under steady flow conditions for three different discharges.

- Field tests

  Eawag (group Dr. A. Peter) conducted with our collaboration field tests to prove the effective presence of migration corridors within a prototype UBR.

- UBR survey

  Data about existing UBR in Switzerland were collected consulting the responsible authorities of the 26 Swiss Cantons. The UBRs during the flood event in 2005 were also analysed to gain information about their behaviour in case of overload.

All design-relevant results will be summarized in a design manual that will be written in collaboration with the Swiss Federal Office for the Environment (FOEN).

1.4 Overview

The present work is divided into 8 chapters. Some basic principles of river engineering issues needed for the discussion and the interpretation of the results are presented in Chap. 2. In Chap. 3 a literature review is given with a summary of the current knowledge on block ramps, leading to the identification of the research gaps. The three different experimental setups are described in Chap. 4, followed by the test results in Chap. 5. Chap. 6 contains the description of the procedure of the field tests and their results, whereas in Chap. 7 the results of the UBR survey in Switzerland are presented. Finally, Chap. 8 summarizes the main results and gives an outlook on the further needed research.

2 Fundamentals

The topics and equations introduced in this chapter are limited to the basic principles considered in the present research, deliberately avoiding a comprehensive presentation of each topic. First, the turbulent flows and especially those with macro-roughness elements and low relative submergence are discussed in Chap. 2.1 and 2.2; then the stability and the transport of single grains, of uniform materials as well as of sediment mixtures are presented in Chap. 2.3. The double-averaging method and the data analysis with the quadrant method are exposed in Chap. 2.4 and 2.5, and, finally, essential knowledge about ecology and fish behaviour related to the design of UBR are summarized in Chap. 2.6.

2.1 Flow over turbulent rough beds

River flows are mostly turbulent, namely characterized by Reynolds numbers $\mathrm{R} > 500$ (e.g. Jirka and Lang 2004), where R is defined as the ratio between inertia and viscous forces

$$\mathrm{R} = \frac{U\,L}{\nu}, \tag{2.1}$$

where U = depth-averaged flow velocity, L = characteristic length (for open-channel flows $L = R$ = hydraulic radius), and ν = kinematic viscosity, and by grain Reynolds numbers $\mathrm{R}^* > 70$, where R^* is defined as

$$\mathrm{R}^* = \frac{u_* \, k_S}{\nu}, \tag{2.2}$$

with u_* = shear velocity, and k_s = equivalent sand roughness. The definition of turbulent quantities (as e.g. Reynolds shear stresses or turbulence intensity) as well as the description of turbulent flows is widely presented e.g. in Nezu and Nakagawa (1993).

The 3D flow in a Cartesian coordinate system x, y, z and u, v, w for the velocity components, respectively (right-hand rule: x-axis is parallel to bed with velocity component u, y-axis represents the spanwise direction with v, z-axis is the vertical direction with w), is described by two fundamental equations: the conservation of mass (or continuity equation) and the conservation of momentum (or equation of motion or Navier-Stokes equations). For incompressible fluid, namely for constant fluid density ρ ($\partial\rho/\partial t = 0$), the continuity equation for the instantaneous velocity components u, v, z is

$$\frac{\partial u}{\partial x} + \frac{\partial v}{\partial y} + \frac{\partial w}{\partial z} = 0 \,, \tag{2.3}$$

or, using the Einstein notation (i.e. $u_1 = u$, $u_2 = v$, $u_3 = w$, and $x_1 = x$, $x_2 = y$, $u_3 = z$), $\partial u_i/\partial x_i = 0$. The equation of motion is derived from the second Newton Law, defining the sum of acting forces as the sum of the particle masses multiplied with the acceleration. For fluid particles, the acting forces are the boundary forces (pressure, normal stresses and shear stresses) and the forces due to the gravity (body forces), whereas the particle acceleration du/dt is given by the sum of the local acceleration $\partial u/\partial t$ together with the convective acceleration $u\,\partial u/\partial x + v\,\partial u/\partial y + w\,\partial u/\partial z$. Thus, the equation of motion for instantaneous velocity components u, v, z is written using the Einstein notation as

$$\frac{\partial u_i}{\partial t_i} + u_j \frac{\partial u_i}{\partial x_j} = g_i - \frac{1}{\rho}\frac{\partial p}{\partial x_i} + \frac{\partial}{\partial x_j}\,\nu\,\frac{\partial u_i}{\partial x_j} \,, \tag{2.4}$$

where g = gravity acceleration and p = pressure. In Eq. (2.4) the first term on the left-hand side denotes the local acceleration, the second the convective acceleration, the first on the right-hand side the gravity force, the second the pressure force and the third the viscous shear force. Theoretically, this system of four equations resulting from Eq. (2.3) and Eq. (2.4) (where Eq. (2.4) corresponds to three equations of the three velocity components) is sufficient to obtain a solution for the four unknown parameters u, v, z and p, but only if the kinematic and physical boundary conditions are known. The Navier-Stokes (NS) equations Eq. (2.4) are non-linear second-order partial differential equations, for which a general solution has not yet been found. The solution for laminar flows exists, but is not suitable for river flow applications. The analytical solution for turbulent flows does not exist. For this reason, numerical simulations are often applied to solve the NS equations, whereas the modeling of the turbulence is not trivial and the computing time can be very high.

Since the knowledge of turbulent fluctuations is often not necessary in practical applications and an analytical solution of the NS equations is not possible, time-averaging is often applied. Reynolds proposed in 1894 the time-averaged (or ensemble-averaged) NS equations, introducing the Reynolds decomposition

$$u_i = \overline{u}_i + u_i' \,, \tag{2.5}$$

where u_i = instantaneous velocity components, $\bar{u}_i$ = time-averaged velocity, and u_i' = fluctuations part (Figure 2.1), and averaging rules (for details see e.g. Nikora *et al.* 2007a). The resulting time-averaged continuity equation is

$$\frac{\partial \bar{u}}{\partial x} + \frac{\partial \bar{v}}{\partial y} + \frac{\partial \bar{w}}{\partial z} = 0 \,, \tag{2.6}$$

and the Reynolds time-Averaged Navier-Stokes (RANS) equations are

$$\frac{\partial \bar{u}_i}{\partial x_i} + \bar{u}_j \frac{\partial \bar{u}_i}{\partial x_j} = g_i - \frac{1}{\rho}\frac{\partial \bar{p}}{\partial x_i} + \frac{\partial}{\partial x_j}\, \nu \, \frac{\partial \bar{u}_i}{\partial x_j} - \frac{\partial \overline{u_i' u_j'}}{\partial x_j} \,. \tag{2.7}$$

The RANS equations (Eq. 2.7) contain a new term compared to the NS equations (Eq. 2.4), namely the turbulent force (or Reynolds stress) $-\partial \overline{u_i' u_j'}/\partial x_j$ resulting from the time-averaging of the non-linear term of the convective acceleration $\bar{u}_j \; \partial \bar{u}_i / \partial x_j$.

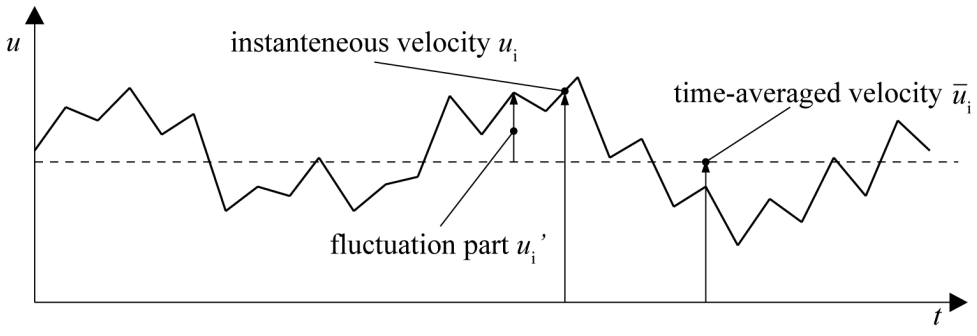

Figure 2.1 Scheme of Reynolds decomposition for velocity component u for an exemplary velocity time series.

For 2D uniform flows, the RANS equations integrated in the vertical direction z result in

$$\rho \; g \; \sin\alpha \; h = \; \rho\nu \; \frac{\partial \bar{u}}{\partial z} - \rho \; \overline{u'w'} \,, \tag{2.8}$$

where α = bed angle against the horizontal and h = flow depth. The term on the left-hand side represents the total bed shear stress τ_0, which balances the laminar (viscous) stress and the turbulent (Reynolds) stress. For river flow applications, the slope is generally not steep, so that $\sin\alpha = \tan\alpha = S$ = river slope, and the turbulent stress usually by far exceeds the laminar stress, allowing the simplification (Schlichting 1960)

$$\tau_0 = \rho \; g \; S \; h = -\rho \; \overline{u'w'} \,. \tag{2.9}$$

The total bed shear stress τ_0 is responsible for the sediment incipient motion and so for the sediment transport. Together with τ_0, the shear velocity $u_{*,\mathrm{I}}$ defined as

$$u_{*,\mathrm{I}} = \sqrt{\tau_0/\rho} = \sqrt{g\,S\,R} \approx \sqrt{g\,S\,h} \tag{2.10}$$

is a direct measure of the flow intensity and its ability to entrain and transport (Garcia 2008). Note that $R \approx h$ for relatively wide channels with $W/h \geq 20$ (Bezzola 2010), where W = channel width.

2.2 Flow resistance

From the mixing length theory suggested by Prandtl (1933) results the universal logarithmic velocity distribution

$$\frac{\bar{u}(z)}{u_*} = \frac{1}{\kappa} \ln z + \text{const.}\,, \tag{2.11}$$

where $\bar{u}(z)$ = time-averaged velocity at level z, u_* = shear velocity (Eq. 2.10), Const. = constant for which a boundary condition is needed, and κ = von Karman's constant (usually $\kappa = 0.41$, e.g. Nezu and Rodi 1986). Eq. (2.11) applies on hydraulic smooth wall conditions ($z/h < 0.2$ near the bed, Nezu and Nakagawa 1993), but it is also commonly used as approximation for most of river flows (Garcia 2008) known as "log law". Nikuradse (1933) proposed the logarithmic law for rough bed conditions as

$$\frac{\bar{u}(z)}{u_*} = \frac{1}{\kappa} \ln \frac{z}{k_s} + B, \tag{2.12}$$

where k_s = equivalent sand roughness and B = constant, which both depend on the boundary condition (e.g. definition of the bed reference level $z = 0$, roughness type) and cannot be valid for every flow conditions. Nikuradse (1933) concluded from his investigations on pipe flows lined with sand that k_s is equivalent to the sand diameter d and that the constant $B = 8.5$, namely

$$\frac{\bar{u}(z)}{u_*} = \frac{1}{\kappa} \ln \frac{z}{k_s} + 8.5 = \frac{1}{\kappa} \ln \frac{30z}{k_s}\,, \tag{2.13}$$

leading to the definition of the bed reference level for hydraulic rough conditions where $\bar{u}(z_0) = 0$ at $z_0 = k_s/30$.

However, the grains covering the river bed are not regular and uniform as for the investigations of Nikuradse (1933): depending on the characteristic grain diameter (often d_{90}) and as may be the case, on the presence of macro-roughness elements, k_s

may be defined differently. Weichert (2006), for instance, presented different definitions of k_s according to different studies. For a flat natural river bed without bed forms, it is often assumed $k_s \approx 2\ d_{90}$ (Bezzola 2010).

By integrating the logarithmic law over the flow depth h, the depth-averaged velocity U (or mean flow velocity) is obtained. In the following, some commonly used approaches derived from the "log law" for the determination of U are presented. For compact channels the hydraulic radius R is generally used, to consider the side-wall effect, whereas for wide channel (e.g. for $W/h > 20$, Bezzola 2010, where W = river width) the flow depth h is used. Thus, integrating Eq. (2.13) for compact channels leads to

$$\frac{U}{u_*} = \frac{1}{\kappa} \ln \frac{R}{k_s} + 6 = \frac{1}{\kappa} \ln \frac{11\,R}{k_s} . \tag{2.14}$$

Eq. (2.14) together with the definition of u_* (Eq. 2.10), leads to the relationship for the determination of the mean velocity

$$U = \frac{1}{\kappa} \ln \frac{11\,R}{k_s} \sqrt{g\ S\ R} \tag{2.15}$$

according to Keulegan (1938), also known as Keulegan's resistance law for rough flow. Hence, from Eq. (2.15) is clear that the flow velocity and so the flow resistance of a full turbulent flow depend on the ratio between hydraulic radius and the equivalent sand roughness, namely the relative submergence R/k_s.

In river engineering applications, the approach according to Chézy is often used, where the Chézy-coefficient c expresses the flow resistance as

$$U = c \sqrt{g\ S\ R} . \tag{2.16}$$

Following from Eqs. (2.15) and (2.16), the Chézy-coefficient c can be written in function of a logarithm

$$c = \frac{U}{u_*} = \frac{1}{\kappa} \ln \frac{11\,R}{k_s} . \tag{2.17}$$

Additionally to the Chézy-approach, in river engineering applications the power law according to Strickler (1923)

$$U = k_{St}\ R^{2/3}\ S^{1/2} \tag{2.18}$$

is widely used, where k_{St} = Strickler-coefficient = $1/n$, expressing the roughness of the river bed, and n = Manning coefficient. Strickler (1923) suggested for k_{St} a relationship with the characteristic grain diameter d_{90}

$$k_{St} = 21.1/\sqrt[6]{d_{90}} \,. \tag{2.19}$$

Another approach is proposed by Aberle (2000), characterizing the roughness of mountain rivers with step-pool systems with the standard deviation of the bed elevations σ_b instead of with k_s or with a characteristic grain size like d_{90}. For the determination of the mean flow velocity for step-pool systems Aberle (2000) suggested the following relationship

$$U = 0.81\ (\sin\alpha)^{0.18} q^{n_A}\ g^{0.5\,(1-n_A)} {\sigma_b}^{0.5\,(1-3n_A)}, \tag{2.20}$$

where $n_A = 0.87\ (\sin\ \alpha)^{0.09}$ and $\sin\alpha$ = bed slope. Eq. (2.20) has a practical and important advantage that the hydraulic parameter R or h does not have to be calculated, but the considered q is directly used. Aberle and Smart (2003) confirmed this approach where σ_b as characterizing roughness gives the best prediction for the flow velocity for the tested slope range between 2% and 10% and suggested for the flow resistance of mountain streams the following equation

$$\frac{U}{u_*} = 3.86\ \ln\frac{h}{\sigma_b} - 1.19 \tag{2.21}$$

The effect of the presence of large roughness on the flow resistance was investigated in different researches, like for instance by Bathurst (1985), who suggested the following relationship for the flow resistance in mountain rivers

$$\frac{U}{u_*} = 5.62 \cdot \log\frac{h}{d_{84}} + 4 \tag{2.22}$$

valid for slopes $0.4\% < S < 4\%$ and for flow without significant sediment transport. Eq. (2.22) was developed by analysing field data from 16 sites in British rivers, where characteristic grain sizes of bed material (d_{50}, d_{84} and σ), discharge Q, slope S, cross-sectional area A, width W, flow depth h, and relative submergence h/d_{84} were measured.

Bezzola (2002) suggested a modification of Eq. (2.13) considering the reduction of the turbulent momentum flux in the roughness layer (Chap. 2.4.3) due to the secondary currents induced by roughness elements for low relative submergence. Bezzola (2002) characterized the roughness with the thickness of the roughness layer z_R and proposed for the flow resistance the relationship

$$\frac{\overline{u}(z)}{u_*} = c_R \cdot \left(2.5 \cdot \ln\left(\frac{z}{z_R}\right) + 8.5\right), \tag{2.23}$$

where $c_R^2 = 1 - z_R/h$ for $h/z_R > 2$, or $c_R^2 = 0.25\, h/z_R$ for $h/z_R \leq 2$, and for natural river beds $z_R \approx 2\, d_{90}$ for $R^* = u_*\, d_{90}/\nu \leq 10^4$ or $z_R \approx d_{90}$ for $R^* = u_*\, d_{90}/\nu > 10^4$ (Bezzola 2010).

Abt *et al.* (1988) experimentally studied the flow resistance of angular shaped riprap in steep channels. The flow resistance was dependent on the slope S and on the relative submergence h/d_{84} for the tested parameter range ($1\% < S < 20\%$, $2.6\text{ cm} < d_m < 15.8\text{ cm}$, $0.41 < h/d_{84} < 7.3$, $0.98 < F < 5.4$).

Maynord (1991) studied the flow resistance of riprap by comparing the results of flume data from different previous studies with the logarithmic and the power-law equation. The data have been collected in experiments with rough turbulent flow, where the bed was stable, and the riprap was made of gravel or crushed stones. For the tested parameter range ($W/h \geq 5$, $h/d_{90} > 2$, $0.5\text{ cm} < d_{90} < 13.4\text{ cm}$, $0.039\% < S < 2\%$), the author recommended for the determination of the flow resistance of riprap for intermediate-scale and small-scale roughness with $h/d_{90} < 30$ the following power-law equation

$$\frac{U}{u_*} = 7.29 \left(\frac{h}{d_{90}}\right)^{0.1664}. \tag{2.24}$$

Additionally to the presence of large roughness elements, also the block placement density λ has a high influence on the flow resistance: boulders produce additional form drag, increasing the flow resistance. The form drag increase results only if boulders are sufficiently distant from each other, so that the energy dissipation of each boulder is maximal and is not reduced by the influence of its neighbours. Different studies were carried out to define the optimal value for the roughness spacing in terms of maximal flow resistance. According to Ferro (1999), a block concentration below 50% assures enough distance between the boulders. Schlichting (1936) found an optimum value of $\lambda_{opt} = 0.4$ for spheres on a fixed bed; O'Loughlin and MacDonald (1964) determined $\lambda_{opt} = 0.26$ for spheres, cubes and sand on a fixed bed; Dittrich and Hamman de Salazar (1993) investigated the relationship between optimal roughness spacing, flow resistance, flow velocity and slope, confirming the results of Schlichting (1936) for glass spheres and of O'Loughlin and MacDonald (1964) for cubes. Based on experiments, Rouse (1965) presented a diagram (Figure 2.2), where the equivalent sand roughness of the blocks k_B normalized with the block diameter D (or cube edge) is

related to the placement density λ for different roughness (cubes or spheres) and different arrangements. Figure 2.2 shows that an optimal placement density λ_{opt} in terms of resistance (expressed as the ratio between the equivalent sand roughness for roughness elements k_B and their diameter D) is between approximately 0.1 and 0.4, depending on the roughness shape and arrangement. Note that λ is generally defined as the ratio between the area covered by the roughness elements and the whole area, but the definition of λ can vary slightly from one study to another.

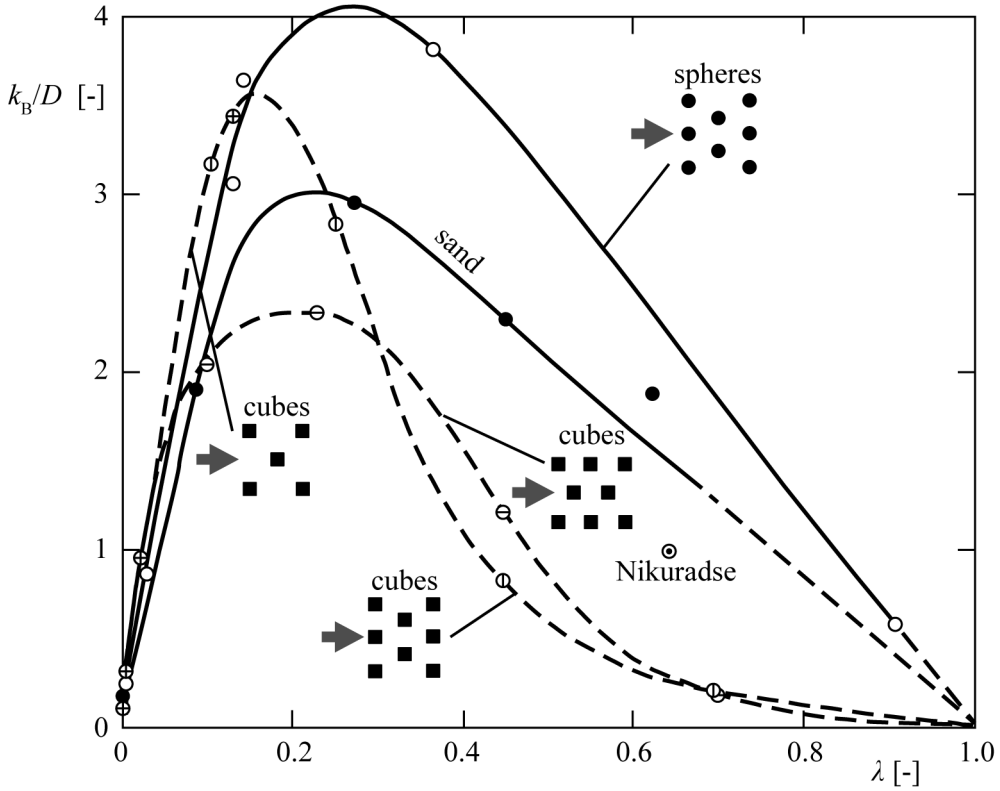

Figure 2.2 Equivalent sand roughness for roughness elements k_B normalized with the roughness diameter or edge D versus roughness placement density λ according to Rouse (1965, modified).

Concerning flow resistance of bed with macro-roughness elements, the model of composite roughness (see e.g. Einstein and Banks 1950, Weichert 2006) suggests another approach. The flow resistance is determined by the superposition of the resistance due to the skin friction of the bed material and to the form resistance (Figure 2.3). Thus, the total bed shear stress τ_0 is subdivided into the shear stress generated by grain friction (i.e. by grains on a plane bed) τ_0' and the shear stress generated by bed irregularities τ_0'' (see e.g. Einstein and Barbarossa 1952), and expressed with the relationship

$$\tau_0 = \tau_0' + \tau_0'' \,. \tag{2.25}$$

Following the definition of τ_0 (Eq. 2.9) the decomposition is applied for the slope S (Figure 2.3)

$$S = S' + S'' \,, \tag{2.26}$$

where the *S'* is the gradient due to the skin friction and *S''* due to the form resistance. Assuming uniform flow conditions with constant mean flow velocity U, applying the Chézy-approach (Eq. 2.16) and the the shear velocity u_* defined in Eq. (2.10), the superposition of the Chézy coefficients *c'* and *c''* (see also Figure 2.3) follows as

$$\rho\, u_*^2 = \rho\, u_*'^{\,2} + \rho\, u_*''^{\,2} \text{ , and so} \tag{2.27}$$

$$\frac{1}{c^2} = \frac{1}{c'^{\,2}} + \frac{1}{c''^{\,2}} \,. \tag{2.28}$$

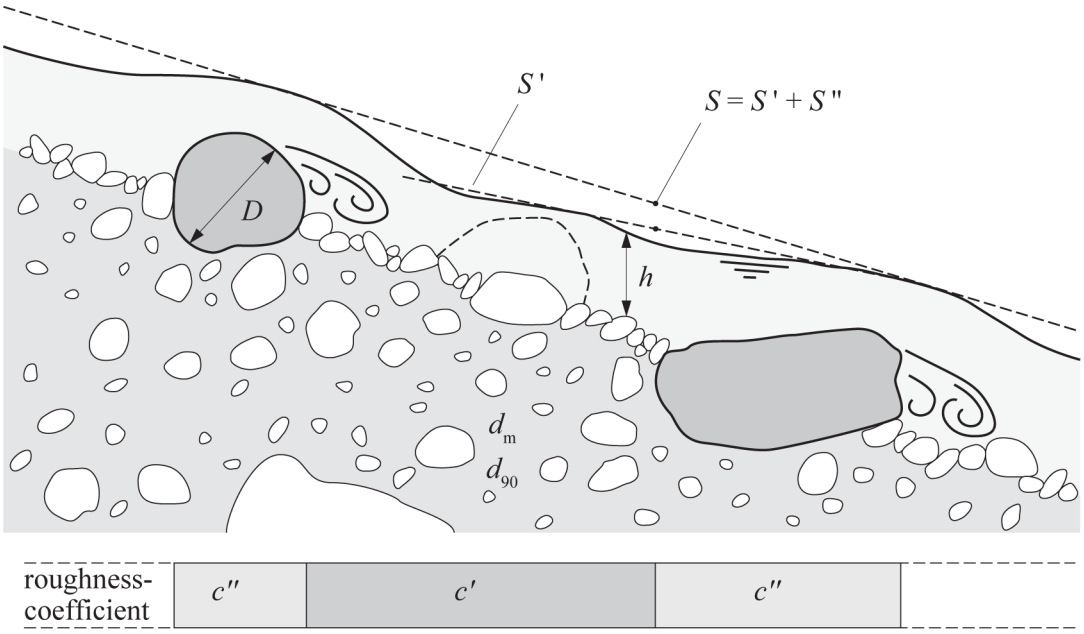

Figure 2.3 Model of composite roughness, where total flow resistance is the sum of resistance due to skin friction (roughness coefficient *c'* and gradient *S'*) and of resistance due to form resistance (*c''* and *S''*) (Bezzola 2010, modified).

Whereas the Chézy coefficient due to the skin friction *c'* can be quantified with the logarithmic law according to Keulegan (1938, Eqs. 2.15 and 2.18), the determination of the Chézy coefficient due to the form resistance *c''* is difficult to generalize. Firstly, the form resistance depends on the relative submergence: increased relative

submergence decreases the influence of bed irregularities, and from a certain relative submergence the form resistance is negligible (e.g. from four times the roughness elements height according to Nikora *et al.* 2001). Then the form resistance depends on the type of bed irregularities: the interaction between flow and e.g. macro-roughness elements differs from the interaction between flow and bed forms. For this reason, an empirical relationship depending on the bed irregularities is often used, leading to the typical uncertainties and limitations connected to empirical equations. Some empirical relationship for *c''* for isolated roughness elements are presented in Chap. 3.2.1

2.3 Incipient motion and sediment transport

The incipient motion of a single grain and generally the sediment transport are fundamental topics in river engineering and therefore, were and still are deeply studied. In this chapter only the approaches and equations used in the present research are introduced stepwise: from the incipient motion of a single grain, over the stability of uniform material, to the stability of sediment mixture.

2.3.1 Incipient motion of a single grain

The forces acting on a non-cohesive single grain (with volume V, projected area of the grain against the flow A_D, base area A_L, and density ρ_s) located on a bed inclined with an angle α against the horizontal are (Figure 2.4)

- G, the force due to the gravity and acting in the vertical,

$$G = V\ \rho_S\ g \tag{2.29}$$

- B, the buoyancy, acting perpendicular to the streamlines and the free surface

$$B = V\ \rho\ g\ \cos\alpha \tag{2.30}$$

- F_D, the hydrodynamic drag force, acting parallel to the river bed

$$F_D = \frac{1}{2}\ U_{ref}^2\ C_D\ A_D \tag{2.31}$$

- F_L, the hydrodynamic lift force, acting perpendicular to the river bed

$$F_L = \frac{1}{2}\ U_{ref}^2\ C_L\ A_L \tag{2.32}$$

G and B act in the centre of mass and do not depend on the discharge, whereas F_D and F_L normally do not act in the centre of mass and depend on the discharge (Figure 2.4). C_D and C_L are the drag and the lift coefficient, respectively: they depend on the dimension, shape and flow around the considered object (in this case the grain) and are experimentally determined (e.g. review in Weichert 2006). U_{ref} is the decisive reference flow velocity acting on the grain particle. With the simplification of a spherical shape for the single grain, V is the volume of a sphere, namely $V = 4/3\ \pi\ (D/2)^3$, where D = equivalent spherical diameter, and A_L correspond to the projected spherical area, namely a circle with diameter D and so $A_L = \pi\ (D/2)^2$, whereas A_D depends on the block protrusion (Chap. 2.3.2).

There are basically two different entrainment mechanisms: rolling and sliding. In the first case, the grain rolls around the pivot point P_p and the limit state for the motion corresponds to the equilibrium of moments around P_p. In the second case, the grain slides along the tangent plane with support point P_p and the limit state for the motion corresponds to the equilibrium of forces in the tangential plane considering the friction force (Bezzola 2010). Both entrainment mechanisms are equally important and both may dominate depending on the grain shape and on the bed configuration (Li and Komar, 1986). The experimental determination of the drag C_D and lift C_L coefficient implicates a limitation, due to their restricted application range, leading to an uncertainty in the determination of the equilibrium of forces and moments.

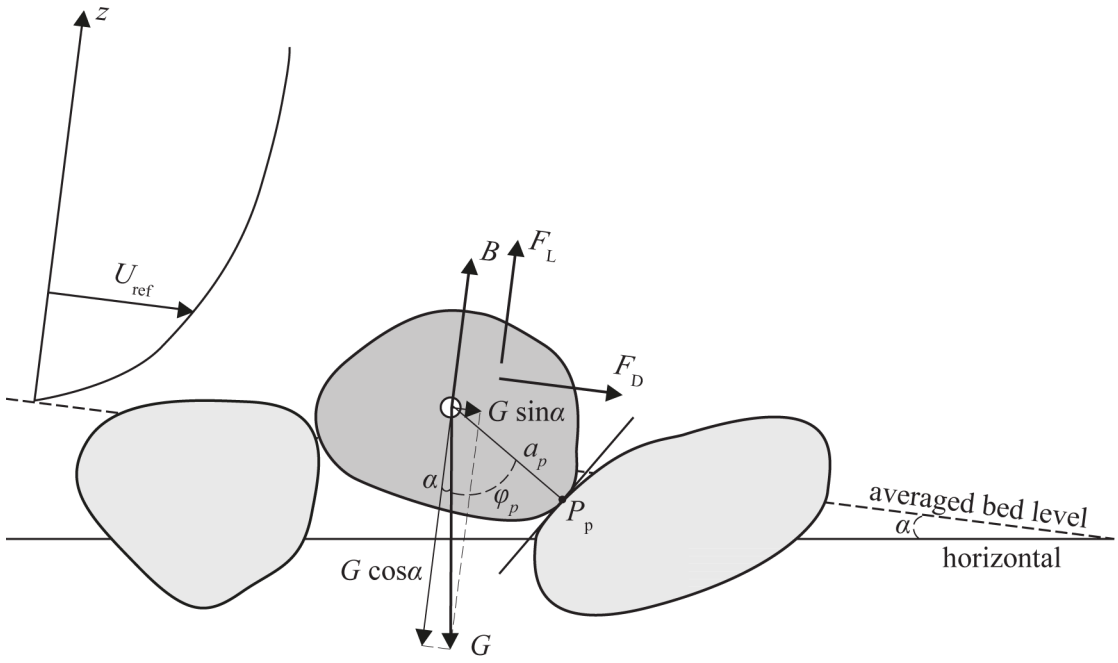

Figure 2.4 Forces acting on a non-cohesive single grain (Bezzola 2010, modified).

2.3.2 Stability of uniform material

The condition for the entrainment in gravel bed is often expressed in terms of dimensionless critical shear stress θ_c defined as

$$\theta_c = \frac{\tau_{0,c}}{g\,(\rho_S - \rho)\,d} \tag{2.33}$$

where $\tau_{0,c}$ = critical bed shear stress at the incipient motion for a grain with diameter d. From his experiments with uniform material at slopes lower than 0.5%, Shields (1936) proposed a relationship between the dimensionless critical shear stress θ_c and the grain Reynolds number R^*. The function $\theta_c = f(R^*)$ is represented in Figure 2.5: for $R^* > 5 \cdot 10^2$ Shields (1936) suggested a constant $\theta_c = 0.06$. After the experiments performed by Shields (1936), many other investigations on incipient motion criteria were conducted (Buffington and Montgomery 1997). The original considerations of Shields (1936) and his diagram remain the most used and accepted approach for the stability of uniform material. Considering the definition of the critical bed shear stress $\tau_{0,c}$

$$\tau_{0,c} = \rho\, g\, R\, S \tag{2.34}$$

and the relationship between bed shear stress τ_0 and shear velocity u_* (Eq. 2.10), θ_c is expressed as

$$\theta_c = \frac{u_*^2}{g\,(s-1)\,d} = \frac{R\,S}{(s-1)\,d} \text{ s} \tag{2.35}$$

where $s = \rho_s/\rho$ = ratio between sediment and water density. Based on Eq. (2.33) or (2.35) and a certain assumed critical shear stress θ_c (for instance $\theta_c = 0.047$, according to Meyer-Peter and Müller 1948), the critical hydraulic conditions for the bed stability can be determined.

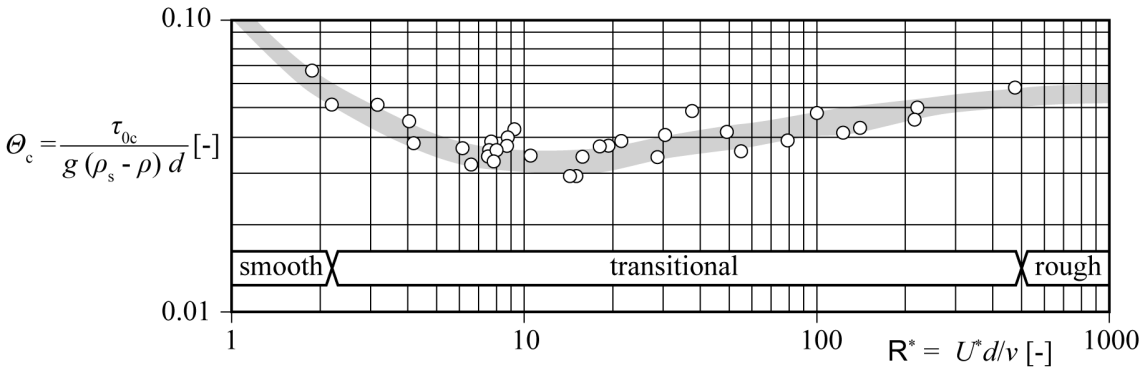

Figure 2.5 Shields diagram for incipient motion of uniform non-cohesive material with additional data resulting from further researches (Marti 2006, modified).

Effects of grain protrusion

The grain protrusion P is defined as the part of the grain diameter exposed to the flow and protruding from the adjacent grains (see scheme in Figure 2.6). According to Fenton and Abbott (1977) P influences the value of the critical shear stress θ_c. Three different series of physical model tests were conducted by them to quantify the effect of P. The first series were performed for grain Reynolds numbers in the transition range, namely for $R^* \approx 30 - 90$; the second for fully turbulent conditions with $R^* \approx 215 - 830$; and finally the third for $R^* \approx 1700 - 3300$ but with fixed maximal relative protrusion of $P/d = 0.82$ in order to determine the dimensionless threshold shear stress θ_{0c}. Figure 2.6 shows the results for fully turbulent conditions (second series of experiments). For a protruding part of approximately 20% ($P/d \approx 0.2$) a critical shear stress of about $\theta_c \approx 0.05$ results, whereas for $P/d \approx 0.4$ θ_c decreases to a value of $\theta_c \approx 0.025$. The extremes are defined by the condition of total embedded grain ($p/d = 0$), leading to $\theta_c \approx 0.1$, and by maximal relative protrusion $P/d = 0.82$, leading to $\theta_c \approx 0.01$ (third series of experiments). That means that a high protrusion has a strong influence on the stability of the single grain, where the critical shear stress can be reduced by up to 90%.

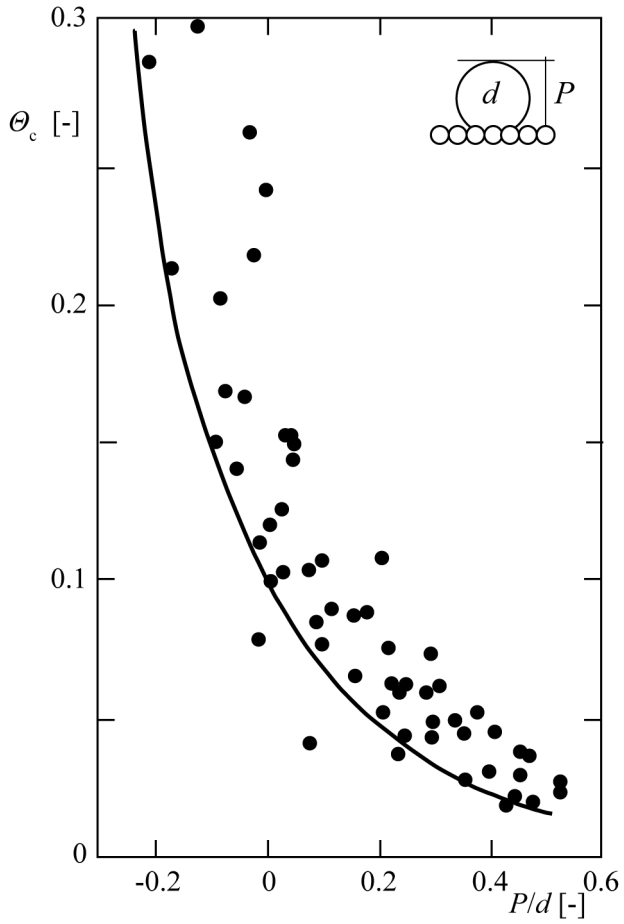

Figure 2.6 Influence of the relative grain protrusion P/d on the dimensionless critical shear stress θ_c according to Fenton and Abbott (1977, adapted).

2.3.3 Stability of sediment mixture and transport equation

For widely graded sediment mixtures (e.g. with standard deviation of grain distribution $\sigma = (d_{84}/d_{16})^{0.5} \geq 1.5$, Little and Mayer 1972), the increase of the discharge up to a certain critical discharge induces the erosion of the finer grain particles only, leading to the formation of an armour layer at the bed surface consisting of coarser grain particles. When the armour layer is formed, it protects the underlying finer bed material (self-stabilization process) up to the critical discharge. for which also the particles of the armour layer are eroded.

Günter (1971) investigated the stabilizing effects of the armour layer for large grain Reynolds number $R^* > 10^3$, suggesting for the dimensionless critical shear stress of the armour layer $\theta_{c,a}$ the relationship

$$\theta_{c,a} = \theta_c \left(\frac{d_{m,a}}{d_m}\right)^{2/3} = \theta_c \left(\frac{d_{90}}{d_m}\right)^{2/3}, \tag{2.36}$$

where $d_{m,a}$ = mean grain size of armour layer and d_m = mean grain size of sediment mixture. From the experiments of Fehr (1987) on coarse sediment mixtures, it is assumed that $d_{m,a} \approx d_{90}$ (Bezzola 2010). There are different studies suggesting a method to determine the grain distribution of the armouring layer based on the grain distribution of the sediment mixture, as e.g. the already mentioned studies of Fehr (1987), Günter (1971) and Gessler (1970). Therefore, knowing d_m and d_{90}, assuming a value for the critical shear stress θ_c and applying Eq. (2.36), the critical hydraulic conditions for the stability of sediment mixtures can be determined.

Meyer-Peter and Müller (1948) performed physical model tests on sediment transport for gravel bed in a rectangular flume for slopes between 0.04% and 2.3% and derived the empirical relationship for the sediment transport

$$q^* = 8(\theta^* - \theta_c)^{3/2}\,, \tag{2.37}$$

where

$$q^* = \frac{q_b}{\sqrt{(s-1)\,g\,d^3}} \tag{2.38}$$

is the dimensionless bed-load transport rate, q_b = volumetric bed-load rate, and where dimensionless shear stress is defined generally as

$$\theta^* = \frac{\tau_0}{g\,(\rho_s-\rho)\,d} \tag{2.39}$$

and specifically applying the Meyer-Peter and Müller equation as

$$\theta^* = \theta\,\left(\frac{k_{St,b}}{k_{St,g}}\right)^{3/2} = \frac{R\,S}{(s-1)\,d}\,\left(\frac{k_{St,b}}{k_{St,g}}\right)^{3/2} = \frac{\tau_0}{g\,(\rho_s-\rho)\,d}\,\left(\frac{k_{St,b}}{k_{St,g}}\right)^{3/2}\,, \tag{2.40}$$

where $k_{St,b}$ = Strickler coefficient due to the bed (grain friction and form drag) and $k_{St,g}$ = Strickler coefficient due to the grain friction. The coefficient $(k_{St,b}/\,k_{St,g})^{3/2}$ considers the additional drag due to the bed forms that reduces the bed shear stress. It is often assumed to be constant at $(k_{St,b}/\,k_{St,g})^{3/2} \approx 0.85$ (Bezzola 2010). Meyer-Peter and Müller (1948) suggested the value $\theta_c = 0.047$ for the critical shear stress and as characteristic grain diameter d the mean diameter d_m of the bed material. The transport equation (Eq. 2.37) was verified during the past decades and the optimal application range resulted for slope $S < 0.5\%$ and gravel bed material, whereas for steeper slopes overestimate the transport capacity (Bezzola 2010). For practical applications, Eq. (2.37) can be rewritten in the extended form

$$q_{\mathrm{b}} = \frac{8\sqrt{g}\,\rho_{\mathrm{s}}}{(s-1)\,d}\left[\left(\frac{k_{\mathrm{St,b}}}{k_{\mathrm{St,g}}}\right)^{3/2} R\,S - 0.047\,(s-1)\,d_{\mathrm{m}}\right]^{3/2} \quad \text{in [kg/(s m)]} \quad (2.41)$$

The sediment transport was and still is a deeply studied river engineering topic, which is not yet determined in a comprehensive way, due to many different parameters playing a decisive role (e.g. open-channel geometry, grain-size distribution, discharge). In the literature many different transport equations are found, like e.g. Yalin (1963), Parker (1979), Smart and Jäggi (1983), Rickenmann (1990), and each of them is limited to a certain application range, due to the limited tested parameters. Since the present research does not focus on sediment transport and the only equation applied is the Meyer-Peter and Müller transport formula (1948), the other transport equations are not further examined.

2.3.4 Special case of sediment transport: bimodal bed material

Raudkivi and Ettema (1982) considered an armouring single layer of uniform particles with size d_1 on a bed of uniform particles with size d_2. The stability of the armour layer was experimentally studied and the two dominant destabilizing processes were defined as follows:

- Embedding: the d_1 particles embed itself into the bed material d_2
- Overpassing: the d_1 particles are entrained and move as bed-load over the bed material d_2

The results of the experiments of Raudkivi and Ettema (1982) are visualized in Figure 2.7, where u_* = shear velocity of the flow, u_{*1} = shear velocity corresponding to the incipient motion of d_1 particles. In the following the most important results of their analysis are listed and shortly described to interpret correctly Figure 2.7.

- The critical condition for entrainment of d_1 particle is

$$\frac{u_*}{u_{*1}} = \frac{u_{*\mathrm{i}}}{u_{*1}} = \sqrt{\frac{\theta_{\mathrm{ci}}}{\theta_{\mathrm{c1}}}}, \quad (2.42)$$

  where θ_{c1} = critical value of dimensionless shear stress for *a bed* made of d_1 particles, which is assumed to be constant at $\theta_{\mathrm{c1}} = 0.056$ (Raudkivi and Ettema 1982), and where

$$\theta_{\mathrm{ci}} = \frac{{u_{*\mathrm{i}}}^2}{g\,(s-1)\,d_1} \tag{2.43}$$

is the dimensionless shear stress for an *individual* particle of size d_1.

- The dimensionless shear stress θ_{ci} depends on the relative block protrusion P/d_1. The function $\theta_{\mathrm{ci}} = \mathrm{f}(P/d)$ was suggested by Fenton and Abbott (1977, Chap. 2.3.2 and Figure 2.6). Their experimental results showed that for low relative protrusion, as e.g. $P/d_1 = 0.08$, the dimensionless shear stress is $\theta_{\mathrm{c}} = 0.10$; for high relative protrusion as e.g. $P/d_1 = 0.82$, $\theta_{\mathrm{c}} = 0.01$. This relationship between P/d_1 and θ_{ci} is given by the horizontal lines in Figure 2.7.

- The minimum particle size that can overpass a stable bed of d_2 under uniform flow condition was proposed by Everts (1973) as

$$d_{1,\mathrm{min}} = 0.087 + 0.236\,d_2 + 0.072\,{d_2}^2 \tag{2.44}$$

  The line corresponding to this criterion is indicated in Figure 2.7 as black bold line and goes up to a value of $d_1/d_2 = 1.0$.

- The maximum particle size $d_{1,\mathrm{max}}$ that can overpass a planar bed of d_2 particles without the flow considerably disturbing the bed of d_2 particles is described by

$$d_{1,\mathrm{max}} = \frac{\theta_{\mathrm{c2}}}{\theta_{\mathrm{ci}}}\,d_2 \tag{2.45}$$

  where θ_{c2} = critical value of dimensionless shear stress for *a bed* of d_2 particles, which is assumed to be constant at $\theta_{\mathrm{c2}} = \theta_{\mathrm{c1}} = 0.056$, and θ_{ci} = dimensionless shear stress acting on d_{i} particle with an upper value of approximately 0.01, leading to

$$\frac{d_{1,\mathrm{max}}}{d_2} \cong 100\,\theta_{\mathrm{c2}} \cong 5.6\,. \tag{2.46}$$

  The point where the vertical line at $d_1/d_2 = 5.6$ crosses the horizontal line at $u_*/u_{*1} = (\theta_{\mathrm{ci}}/\theta_{\mathrm{c1}})^{0.5} = (0.01/0.056)^{0.5} = 0.42$ (Figure 2.7) represents the limiting point for the overpassing condition, due to a combination of the highest relative protrusion set at $P/d_1 = 0.82$ (leading to a minimal $\theta_{\mathrm{ci}} = 0.01$) and of the maximum particle size $d_{1,\mathrm{max}}$ that can overpass the bed of d_2 (Eq. 2.45).

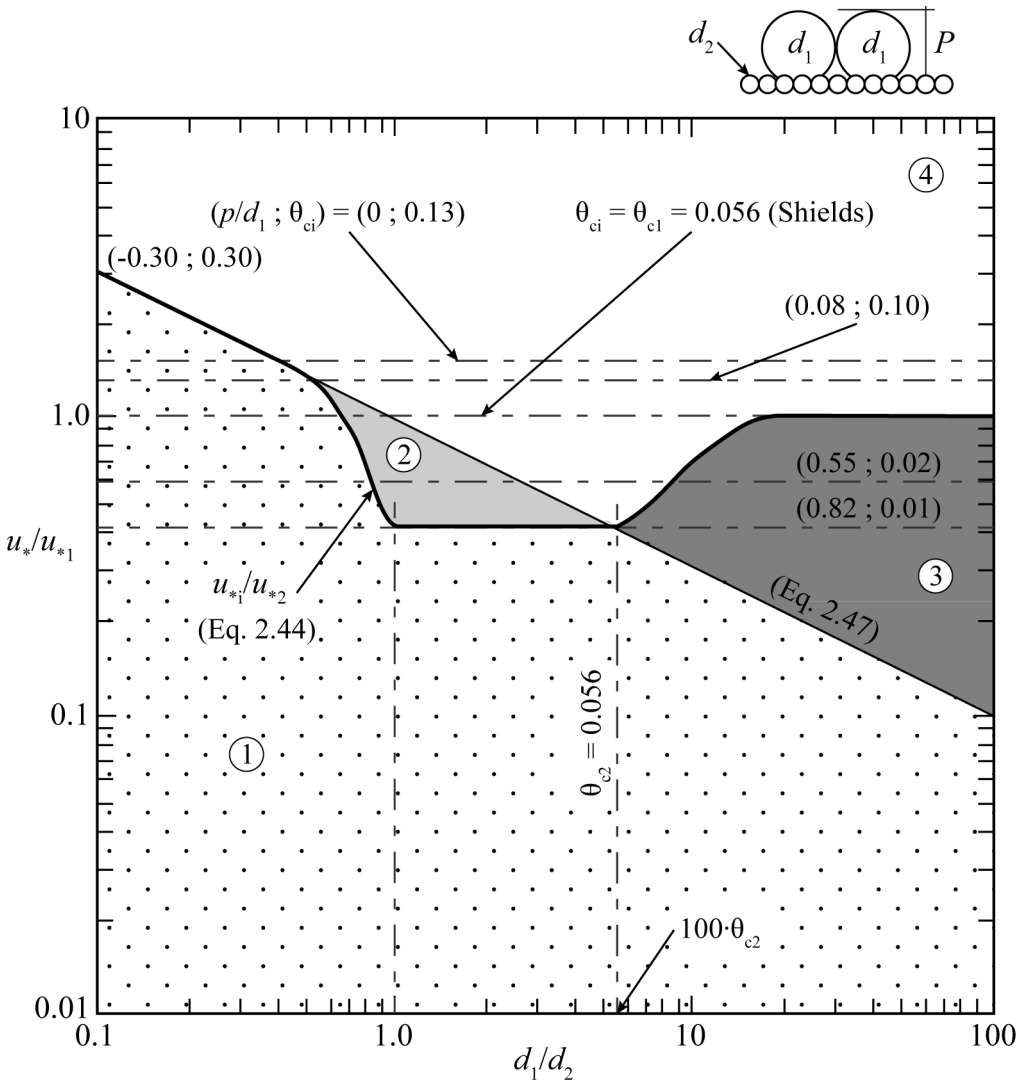

Figure 2.7 Entrainment conditions for a single particle d_1 on a bed of d_2 particles according to Raudkivi and Ettema (1982, adapted).

- The entrainment threshold of d_2 particle from the surface on which d_1 particles rest is reached for $u_* \rightarrow u_{*2}$, namely

$$\frac{u_*}{u_{*1}} = \frac{u_{*2}}{u_{*1}} = \sqrt{\frac{\theta_{c2}}{\theta_{c1}}} = \sqrt{\frac{d_2}{d_1}} = \left(\frac{d_1}{d_2}\right)^{-0.5}. \tag{2.47}$$

  This condition between stable and unstable d_2 particles is plotted in Figure 2.7 with the diagonal line, which reaches the value of approximately $u_*/u_{*1} \approx 3.16$ at $d_1/d_2 = 0.1$ and of exactly $u_*/u_{*1} = 0.1$ at $d_1/d_2 = 100$.

- The black bold line for $d_1/d_2 > 5.6$ limits the area where the embedding of d_1 particles is dominant. The exposed d_1 particles are no longer preferentially entrained from the bed of d_2 because the flow is now capable of entraining d_2 par-

ticles, too (region above the line of Eq. 2.47), leading to the movement of d_2 particles and so of the embedding of d_1 particles, whose relative protrusion P/d_1 decreases continuously. During the experiments it was observed that for a ratio of approximately $d_1/d_2 > 17$, d_1 particles become rapidly embedded and only d_2 particles are entrained. For this reason the line limiting embedding condition reaches its maximum at $d_1/d_2 \approx 17$.

In summary of all these considerations the diagram can be divided into 4 different areas corresponding to the 4 entrainment conditions:

(1) No motion (pointed area): d_1 and d_2 particles are stable ($u_{*1,2} > u_*$)

(2) Overpassing (light grey area): d_2 particles are stable ($u_{*2} > u_* > u_{*1}$)
If $d_1/d_2 > 1.0$: an exposed d_1 particle moves in rolling or sliding mode
If $d_1/d_2 < 1.0$: an exposed d_1 particle moves in bouncing or saltation mode

(3) Embedding (dark grey area): only d_2 particles are entrained ($u_{*1} > u_* > u_{*2}$)

(4) General motion (white area): d_1 and d_2 particles are in motion ($u_* > u_{*1,2}$)

2.4 Double-averaging approach

2.4.1 General

The double-averaged methodology, where the governing flow equations are averaged both in time and in space, was initiated by Wilson and Shaw (1977), who described atmospheric flows within vegetation canopies through a new mathematical model. They observed that canopy effects are more satisfactorily described if the flow is spatially-averaged over a horizontal plane large enough to eliminate the variations due to both interplant spacing and the largest scales of motion contributing to the momentum transport. At the same time, Smith and McLean (1977) introduced this concept in water flows, averaging the velocity profiles measured in the prototype along lines above a wavy surface, namely over dunes in the Columbia River. They suggested the double-averaged approach to determine the skin friction as well as the total boundary shear stress, averaging over one wavelength of the bed form.

The mathematical basis for the new set of equations was given by atmospheric physicists, like e.g. Raupach and Shaw (1982), who studied the averaging procedure for airflows within vegetation canopies and formalized the horizontal averaging operations. They highlighted the importance of describing three-dimensional (3D) processes by reducing the significant parameter in one assembling averaged profile, affirming that "*The horizontal averaging operation is important because it must account for the appearance, within a one-dimensional framework, of various inherently three-dimensional canopy effects: form drag, viscous drag, property emission or absorption, and the generation of wake turbulence at length scales determined by the canopy elements*". They also considered the effects of two different schemes (pure horizontal-averaging at a single instant, and time-averaged followed by horizontal-averaging) on the conservation equations for mean quantities and second moments in a canopy flow, observing that the two schemes produce different results at second order. This aspect was also considered in Nikora *et al.* (2007a), who affirmed that applying spatial-averaging to time-averaged equations seems to be more suitable to describe rough-bed flow hydrodynamics, due to its more clear physical explanation.

Giménez-Curto and Corniero Lera (1996) applied the double-averaging method to describe oscillating turbulent flow over very rough surfaces introducing the effect of the variation of the averaging region under the crest of boundary irregularities. They de-

fined as *boundary disturbances* all the boundary irregularities originating perturbation in the time-averaged flow. In this way they derived spatially-averaged Reynolds equations for steady uniform flow over two-dimensional (2D) roughness with the generalization of a varying fluid area. Based on the equations proposed by Giménez-Curto and Corniero Lera (1996), this concept was further discussed in Nikora *et al.* (2001), where the roughness geometry function ϕ was defined as ratio between area occupied by fluid and total averaging area. The governing equation was redefined considering the variation of ϕ, leading to a general characterization of the spatially-averaged flows for open-channel and rough bed conditions. The determination of ϕ in physical models was studied by Aberle (2007): ϕ was directly measured in the model as well as determined from the corresponding digital elevation model (DEM), which does not account for the porosity of the sediment material. The comparison between the two results showed that the DEM data can be used to accurately estimate ϕ for the region below the roughness crests, although the pore volume is not considered. A correction function for ϕ estimated from DEM data is required only for the region close to the roughness troughs. This statement supports the definition of the roughness geometry function ϕ used herein, where pore volume is zero due to the cement layer fixing the bed material, for the analysis of the results (Chap. 5.4.1).

Different researches contributed to the development of this approach for water flows, like e.g. McLean *et al.* (1999). Velocities profiles were measured with LDA over fixed dune-shaped forms, showing that spatially-averaged velocities at constant elevations above the mean elevation of the bottom yield velocity profiles being highly logarithmic despite the topographic effects. Coleman *et al.* (2007) measured the flow velocities over repeated square-rib roughness and over repeated fixed simulated sand waves and formulated the parameterization of the corresponding form-drag coefficient C_D. Additionally, they highlighted the importance of the double-averaging approach for the description of ecologically significant regions, as the region below roughness crests. There the flow interacts with complex heterogeneous rough-boundary geometries and requires spatial-averaging to eliminate the variation of the time-averaged variables. A similar approach was used e.g. also by Nepf (2012a and 2012b), describing the momentum equations as well as the drag coefficient of canopies with the double-averaging method. The double-averaging method for rough-bed open-channel and overland flows was described in detail and clarified with applications in Nikora *et al.* (2007a and 2007b). This method is applied for the present research.

The flow structure on UBR is highly 3D and strongly heterogeneous in space, making use of the Reynolds time-Averaged Navier-Stokes (RANS, Chap. 2.1) equations not practical, particularly for roughness layer. To account for the spatial variability and heterogeneity of the river bed, the RANS equations are additionally spatially-averaged in planes parallel to the averaged bed level or zero plane (e.g. Nikora *et al.* 2001, 2007a, 2007b, Nepf 2012a). Using the Einstein notation, the double-averaged equation of motion for the region below the representative block crest z_c (see determination of z_c in Chap. 5.4.1) is with u_i = flow velocity component, g_i = gravity acceleration component, ρ = fluid density, p = pressure, and υ = kinematic viscosity

$$\frac{\partial\langle\bar{u}_i\rangle}{\partial t}+\langle\bar{u}_i\rangle\frac{\partial\langle\bar{u}_j\rangle}{\partial x_i}=g_i-\frac{1}{\rho}\frac{\partial\langle\bar{p}\rangle}{\partial x_i}-\frac{1}{\phi}\frac{\partial\phi\langle\overline{u'_\iota u'_j}\rangle}{\partial x_j}-\frac{1}{\phi}\frac{\partial\phi\langle\tilde{u}_i\tilde{u}_j\rangle}{\partial x_j}+\upsilon\frac{\partial^2\langle\bar{u}_i\rangle}{\partial x_j^2}+\upsilon\langle\frac{\partial^2\tilde{u}_i}{\partial x_j^2}\rangle-\frac{1}{\rho}\langle\frac{\partial\tilde{p}}{\partial x_i}\rangle \quad (2.48)$$

Time-averaging is denoted with a straight overbar " $\bar{}$ ", whereas spatially-averaging with an angle bracket " $\langle\ \rangle$ ". The prime " $'$ " denotes the fluctuation term and the tilde " $\sim$ " the spatial disturbance of the time-averaged variables, where $\tilde{u}_i=\bar{u}_i-\langle\bar{u}_i\rangle$, analogue to the Reynolds decomposition $u'_i=u_i-\bar{u}_i$. Compared to RANS momentum equations, the spatially-averaged equations contain additional terms: form-induced stresses $\langle\tilde{u}_\iota\tilde{u}_j\rangle$, form drag $(1/\rho)\langle\partial\tilde{p}/\partial x_i\rangle$ and viscous drag $\upsilon\langle\partial^2\tilde{u}_i/\partial^2x_j^2\rangle$. Moreover, the above mentioned roughness geometry function $\phi(z)$ suggested by Giménez-Curto and Corniero Lera (1996) needs to be introduced to accounting the variation of the averaging area. The viscous fluid stress is assumed to be negligible compared to the spatially-averaged Reynolds shear stresses (as supported by data in Manes *et al.* 2007); this assumption could be verified with the measurements (see Chap. 5.4.3). Assuming steady, uniform, spatially-averaged flow, and mild slope, Eq. (2.48) simplifies for the longitudinal component u for the region above the roughness crests with $z > z_c$ and ϕ = constant = 1 as

$$gS-\frac{\partial\langle\overline{u'w'}\rangle}{\partial z}-\frac{\partial\langle\tilde{u}\tilde{w}\rangle}{\partial z}=0, \quad (2.49)$$

and for the region below the roughness crests with $z < z_c$ and variable roughness geometry function $\phi(z)$ only depending on z as

$$gS-\frac{1}{\rho}\langle\frac{\partial\tilde{p}}{\partial x}\rangle-\frac{1}{\phi}\frac{\partial\phi\langle\overline{u'w'}\rangle}{\partial z}-\frac{1}{\phi}\frac{\partial\phi\langle\tilde{u}\tilde{w}\rangle}{\partial z}+\nu\langle\frac{\partial^2\tilde{u}}{\partial z^2}\rangle=0, \quad (2.50)$$

1 2 3 4 5

where 1 = gravity force (along *x*-direction), 2 = form drag, 3 = turbulent (or Reynolds) stress, 4 = form-induced stress and 5 = viscous drag.

2.4.2 Definition of the averaging area

The averaging area can be defined basically with two different methods: (1) the averaging area follows the Cartesian coordinate system and is located at a fixed height level above the zero-plane (*Cartesian approach*); (2) the averaging area accounts for topographic irregularities and is at constant distance from the local bed elevation (*boundary fitted approach*). In the second case, the averaging area is exactly as irregular as the bed topography, meaning that e.g. for river with dunes, the averaging area is also dune-shaped.

The *Cartesian approach* is based on the Double-Averaged Navier-Stokes (DANS) equations. It is therefore theoretically supported and each double-averaged quantity has a clear hydrodynamic meaning. For this reason, it is used by most application of the double averaging method (e.g. Nikora *et al.* 2001, Nikora *et al.* 2007a and 2007b, Coleman *et al.* 2007, Mignot *et al.* 2009). Regarding the *boundary fitted approach*, the theory about this coordinate system and the interpretation of the double-averaged quantities remains unclear. This approach was applied for instance by Smith and McLean (1977).

Different coordinate system approaches are discussed in Finnigan (2004), where the particularities as well as the advantages/disadvantages of each approach are illustrated. McLean *et al.* (2008) used and compared both approaches for the characterization of the flow over fixed dune shapes. They concluded that the *Cartesian approach* allows the incorporation of the conservation of mass and momentum equations, leading to a clear interpretation of the results. In contrast, the averaging technique applied with the *boundary fitted approach* mixes processes and reduces the applicability of the assumptions.

In the present study, the *Cartesian approach* is applied and the time-averaged variables are spatially-averaged in planes at different heights parallel to the zero-plane (see determination of the zero-plane in Chap. 5.4.1), where the length of the averaging area is at least five times the characteristic roughness length, namely the block protrusion P (Figure 2.8).

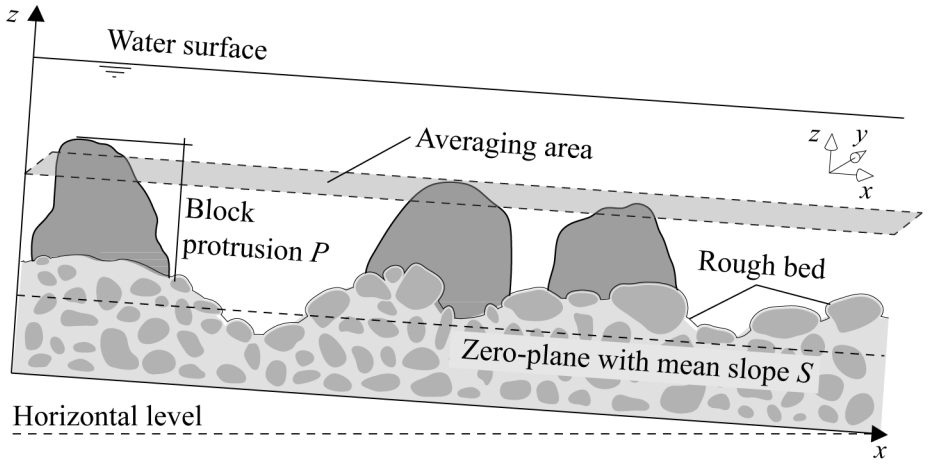

Figure 2.8 Averaging method used for phase C of the present research.

2.4.3 Subdivision of specific flow regions according to Nikora *et al.* (2001)

For rough permeable and impermeable bed Nikora *et al.* (2001) suggested a subdivision into five flow layers (Figure 2.9), where each layer is characterized by different characteristic length scales, stress components and velocity scales:

- *Outer layer*, where viscous effects and form-induced fluxes are negligible and spatially averaged equations are identical to time-averaged equations, exists only for very high relative submergences. Characteristic scales here are the shear velocity $u_* = (\tau_0/\rho)^{0.5}$, the maximum flow velocity U_{max}, the distance from the bed z and the flow depth h. The velocity within this layer is almost constant.
- *Logarithmic layer*, where – as in the outer layer – viscous effects and form-induced fluxes are negligible and spatially averaged equations are identical to time-averaged equations. However, the characteristic scales are here the shear velocity u_*, the distance from the bed z, and characteristic scales of bed topography (e.g. standard deviation of bed elevations, longitudinal and transverse correlation lengths). The velocity distribution follows the logarithmic law.
- *Form-induced sublayer*, the region above the roughness crests, where the flow is influenced by individual roughness elements. Here, the form-induced stresses $\langle \tilde{u}\tilde{w} \rangle$ become important due to flow separation from the roughness elements (Giménez-Curto and Corniero Lera 1996, Eq. 2.49).

- *Interfacial sublayer*, the region between roughness crests and troughs, where the flow is also influenced by individual roughness elements and where, additionally to the form-induced stresses as in the form-induced layer, the form drag plays a role. In this region the roughness geometry function $\phi(z)$ is variable and becomes important (Eq. 2.50): it changes from 0 to 1 for impermeable beds (Figure 2.9 a) and from ϕ_{min} to 1 for permeable beds (Figure 2.9 b).

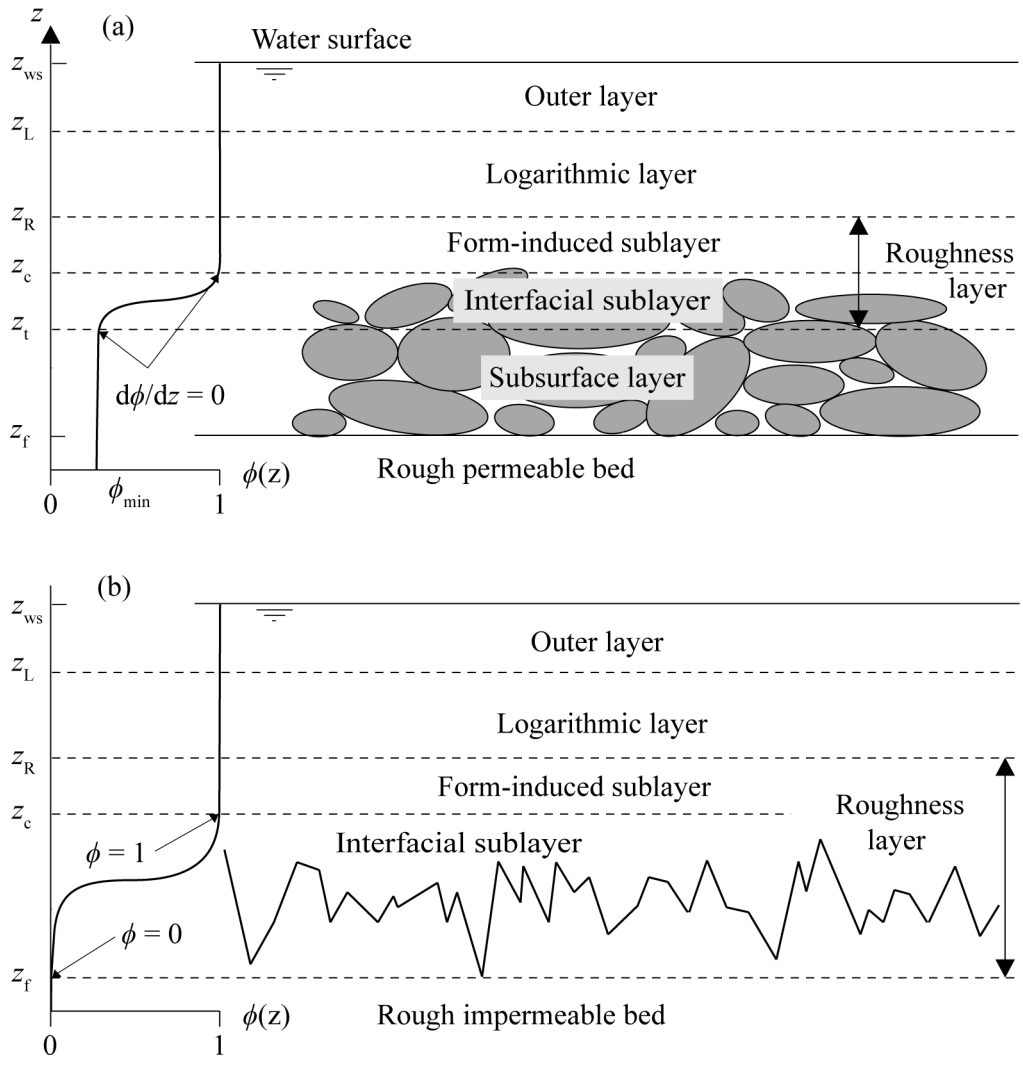

Figure 2.9 Flow subdivision into specific regions with general distribution of the roughness geometry function ϕ. Top: Permeable bed; bottom: Impermeable bed (after: Nikora *et al.* 2001).

- *Roughness layer:* The form-induced sublayer together with the interfacial sublayer is defined as *roughness layer*. The main characteristic scales are the shear velocity u_* and the characteristic lengths of the bed roughness.
- *Subsurface layer*, which exists only for permeable beds. The flow here occupies pores between granular particles and is driven by the gravity force and momentum fluxes from the layer above. The characteristic scales are the shear velocity u_* and the pore characteristic lengths.

Details are found in Nikora *et al.* (2001), where this subdivision into flow regions was presented. The flow is subdivided accordingly also for the present research, where the regions are slightly different to those already illustrated, due to the macro-roughness elements that influence the entire flow column. The considerations and the details are presented in Chap. 5.4.1.

2.5 Quadrant analysis

The conventional quadrant method with the analysis of the fluctuations terms of the velocity (in the present case u' and w') was introduced by Wallace *et al.* (1972), continued by Lu and Willmarth (1973) and Nezu and Nakagawa (1993). They studied the structure of turbulent stresses and defined four different turbulent events described as follows (Figure 2.10):

- *Outward interaction (Quadrant I):* upward motion of high-velocity – faster than the average ($u' > 0$ and $w' > 0$)
- *Ejection (Quadrant II):* upward motion of low-velocity – slower than the average ($u' < 0$ and $w' > 0$)
- *Inward interaction (Quadrant III):* downward motion of low-velocity – slower than the average ($u' < 0$ and $w' < 0$)
- *Sweep (Quadrant IV):* downward motion of high -velocity – faster than the average ($u' > 0$ and $w' < 0$)

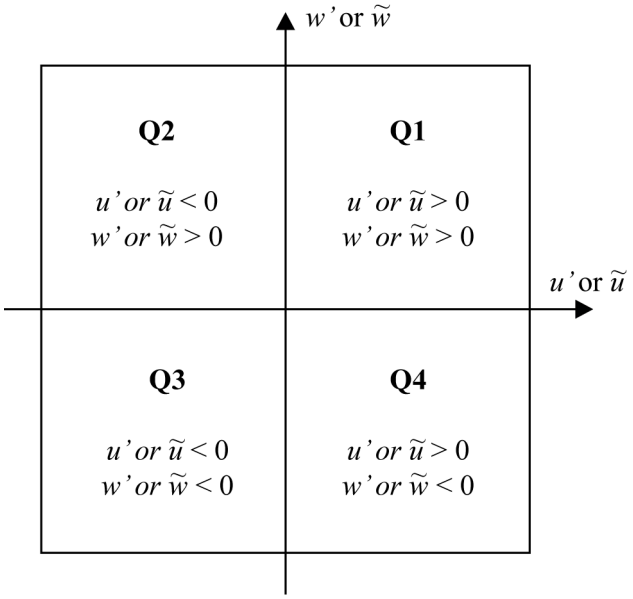

Figure 2.10 Sketch for quadrant decomposition of the velocity fluctuation terms u' and w' of the instantaneous velocity components and for the spatial disturbances $\tilde{u}$ and $\tilde{w}$ of the time-averaged velocity components.

With the quadrant analysis dominant processes occurring at a certain point are identified. Figure 2.11 (a) shows an example of pronounced correlation between *u*' and *w*' in the quadrants Q2 and Q4, indicating dominance of ejections and sweeps events. In contrast, poor correlation between the fluctuation terms is interpreted as an absence of turbulent coherent structures (Nikora *et al.* 2007b, see Figure 2.11 b).

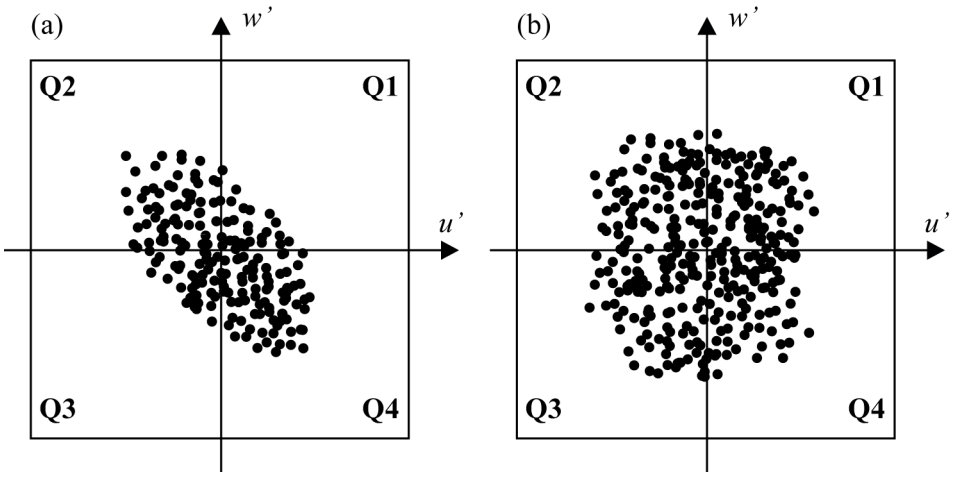

Figure 2.11 Example of quadrant analysis with (a) pronounced correlation between *u*' and *w*' in Q2 and Q4 indicating dominance of ejections and sweeps events; and (b) poor correlation indicating absence of coherent structures.

Quadrant analysis can be applied for river engineering purposes, as shown with the following example. Papanicolaou *et al.* (2001) measured with 3D LDA velocities above three different roughness regimes to provide evidence that roughness affects the structure of turbulence. In other words, an analysis of the turbulent structures was performed on the hypothesis that bursting events (i.e. the cycle of ejections, sweeps, outward and inward interactions) are primarily responsible for the sediment entrainment. The quadrant analysis was therefore used to determine the frequency of each individual event and then to find a correspondence with the mechanisms associated to sediment entrainment.

A similar technique is applied to the spatial disturbances $\tilde{u}$ and $\tilde{w}$ of time-averaged velocity components. In this case, the quadrant analysis improves the understanding of momentum transfer close to a rough-bed produced by the form-induced velocities and their correlation $\langle\tilde{u}\tilde{w}\rangle$ (Nikora *et al.* 2007b). An example of this application is given by Pokrajac *et al.* (2007): velocity measurements with Particle Image Velocimetry (PIV) were conducted over a regular roughness bed (square bars) to improve the knowledge of the near-bed flow structures by combining PIV data with DANS equations. Specifically, the research aimed at developing the application of the quadrant methodology for the analysis of form-induced velocity components and of the structure of the form-induced stresses.

In the first application case (conventional quadrant analysis with *u*' and *w*') a quadrant diagram relates to a particular local point, whereas in the second case (quadrant analysis with $\tilde{u}$ and $\tilde{w}$) it relates to a certain averaging domain parallel to the bed.

2.6 Habitat variability and longitudinal connectivity of rivers

A recent study showed that the Swiss rivers are interrupted by approximately 100'000 human made structures with a level difference larger than 0.5 m (Zeh Weissman *et al.* 2009), representing impassable barriers for fish. Particularly with the introduction of the revised Swiss Federal Act on the Protection of Water (*Gewässerschutzgesetz*) in January 2011, regulating among other things the removal of man-made introduced disturbance within the next 20 years, natural-oriented engineering measures have become more relevant. An important aspect of the rehabilitations measures is the restoration of the longitudinal connectivity, to restore the migration possibilities for fish and improve habitat conditions.

Achieving suitable ecological conditions in water courses is a current pursued goal not only for Swiss rivers, but for many rivers world wide where their natural conditions were compromised by human activities. It is estimated that an average of over 10^9 US$ has been spent annually during the past 20 years in the United States on restoration of streams and rivers (Bernhardt *et al.* 2005). This amount of money shows the significance of restoration aspects and the exigency to achieve a successful project. How are "*suitable ecological conditions*" defined? The answer is complicated due to the complexity of the problem and especially due to the high number of elements (fauna and flora) and parameters playing an important role. Furthermore, the effectiveness of a river restoration project depends on the overall understanding of the decisive ecological processes: without this, the project can easily fail (Roni *et al.* 2008). In particular, the effect of restoration projects which increase habitat diversity on the benthic macroinvertebrates (= macroinvertebrates living in the lowest region of a water body) remain unclear (Jähnig *et al.* 2009).

Due to the complexity of the topic, only a decisive aspect in terms of ecological efficiency of UBR, namely the longitudinal connectivity, is presented herein. Moreover, the effects of the habitat variability are shortly described, as additional possible positive impact on the environment resulting from the construction of UBR.

2.6.1 Migration behaviour and importance of longitudinal connectivity

In the course of evolution fish developed migration behaviour as strategy to reach resources located far away, like e.g. suitable spawning, feeding or wintering habitat

(Northcote 1998). Fish migration and habitat diversification are therefore attitudes developed as strategy to enable an optimal utilization of the resources in terms of feeding, growth and reproduction (DWA 2009). The distances covered vary between few metres and thousands of kilometres: e.g. a common barbel (*Barbus barbus*) can cover about 300 km during its up- and downstream migration, whereas a northern pike (*Esox lucius*) "only" about 25 km (DWA 2010). The migration velocity also varies depending on the fish species between many kilometres per day (e.g. the Atlantic salmon – *Salmo salar* – can reach a maximal velocity of 37 km per day, DWA 2010) and some meters per day (e.g. the bullhead – *Cottus gabio* – about 50 m per week, DWA 2010). The interruption of the longitudinal connectivity can cause quick alterations in fish communities and reduce species richness upstream of the obstacle to less than half of the original species richness (Peter 1998).

According to Myers (1949) and McKeown (1984) migratory fish are classified as follows

- *Diadromous:* fish migrating between sea and fresh water within a life cycle. They are subdivided again into

  Anadromous: Diadromous fish, which spend their lives in the sea, but migrates to fresh water for reproduction;
  Catadromous: Diadromous fish, which spend their lives in fresh water, but migrates to the sea for reproduction;
  Amphidromous: Diadromous fish, which migrate regularly between fresh water and sea, without reproduction purposes.

- *Potamodromous:* fish, living and migrating only within freshwater. It is often related to migrations with reproduction purposes between lakes and rivers, or within a lake or river system.

- *Oceanodromous:* fish, living and migrating only within the sea.

The longitudinal connectivity and so the migration possibilities for the different type of migratory fish are therefore decisive, to assure the possibility to find the habitat needed in a certain life stage (Northcote 1998, Werth *et al.* 2011). The migration possibilities for a certain fish are given, when at least one migration corridor exists, defined as connecting path between down- and upstream of the obstacle, offering suitable hy-

draulic and spatial conditions for the overcoming (DWA 2009). The design of an efficient structure in terms of ecology has to account for the geometrical requirements of the biggest local fish species (and so of a certain minimal necessary flow depth h_{min}) as well as for the limiting swimming capacity of the weaker local fish (and so of a certain maximal acceptable flow velocity U_{crit}, DWA 2009). The more heterogeneous the flow conditions (like e.g. on UBR), the more variety on migration corridors is offered, and therefore, the more possibilities are available for different fish species to overcome the obstacle. The ecological criteria for UBR are presented in Chap. 3.3.

2.6.2 Swimming performance

The swimming velocity and the migration distance depend directly on the muscle force of the fish. The swimming velocity and the fatigue time are specific to a certain fish species and are strongly dependent on the fish body length L_{fish} and on the muscle mass, as well as on environmental factors like water temperature and oxygen content (Adam and Lehmann 2011). Swimming velocities are classified as follows (e.g. Pavlov 1989, Hammer 1995, Pavlov *et al.* 2000, Figure 2.12):

- *Sustained (or cruising) velocity* U_{sust} can be maintained for long period (> 200 minutes), even months, in an aerobic motion and does not exhaust the energy supply.
- *Prolonged velocity* U_{prol} can be maintained between 20 s and 200 minutes and is strongly dependent on the fish species. Depending on the speed, it can lead to exhaustion.
- *Burst velocity* U_{burst} can only be maintained for brief periods, up to approximately 15-20 s (applies to a great number of fish species), it is a high-speed anaerobic motion and leads to exhaustion. This swimming modus occurs only in exceptional conditions, like e.g. to overcome a short obstacle or to escape from an imminent danger.

In the literature different relationships between the swimming velocity and the body length can be found (e.g. Videler 2003, Pavlov 1989, Adam and Lehmann 2011). For instance, according to Jens *et al.* (1997) the sustained velocity is $U_{sust} \approx 2\ L_{fish}/s$, the

prolonged velocity $U_{prol} \approx 5\ L_{fish}$/s and the burst velocity $U_{burst} \approx 10\text{-}12\ L_{fish}$/s for adults Salmonidae, Cypriniformes and Perciformes.

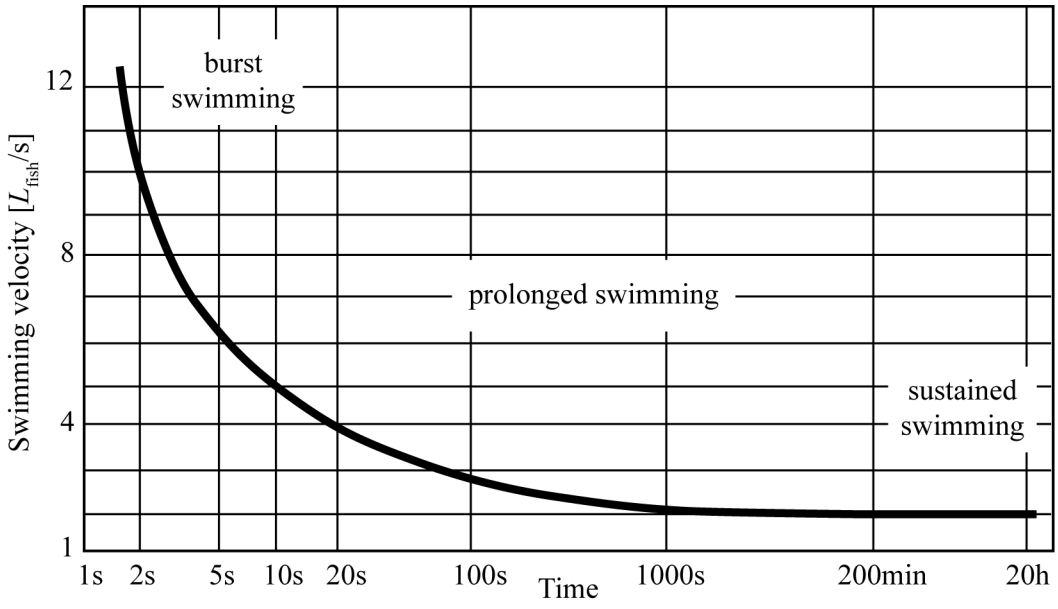

Figure 2.12 Swimming performance according to Pavlov (1989): relationship between fish swimming velocity (expressed in body length per second, i.e. L_{fish}/s) and swimming duration (Adam and Lehmann 2011, adapted).

The critical velocity U_{crit} is defined as the velocity that cannot be exceeded to assure a safely overcoming of obstacles and should be derived from the prolonged velocity (and not from the burst velocity, see DWA 2009) as $U_{crit} \approx U_{prol}\ L_{fish}$ [m/s]. This velocity is decisive for the determination of migration possibilities in the considered river reach or block ramp.

2.6.3 River zonation

Huet (1949) and Müller (1950) divided the water course from the source to the river mouth in regions identified by the key fish species living in it. This classification is important because it is often used in the literature referring the limiting values important for the design of UBR (h_{min} and U_{crit}) to the river zonation. For this reason, the different regions are shortly defined in the following (DWA 2010) and typical fish are listed according to the region of their highest appearance in Swiss rivers (Schager and Peter, 2004)

- The *Trout zone* has in general steep bed slopes (10%-0.45%, depending on the river width) and low water temperatures (5-10°C). The high flow velocities improve the oxygen content and the water is therefore well oxygenated. The river bed is generally made of blocks. Characteristic fish species are the brown trout (*Salmo trutta fario*), the bullhead (*Cottus gobio*), the brook lamprey (*Lampetra planeri*), the stone loach (*Barbatula barbatula*), and the common minnow (*Phoxinus phoxinus*).
- The *Grayling zone* has lower bed slopes than the trout zone (0.75%-0.125%), higher water temperatures (8-14°C), and alternating riffles and pools with currents, however, rather rapid. The water is less oxygenated than in the trout zone, but still satisfactory. River bed material is finer than in the trout zone, often consisting of pebble gravel. The characteristic fish species are those of the trout zone, as well as the grayling (*Thymallus thymallus*), the schneider (*Alburnoides bipunctatus*), the dace (*Leuciscus leuciscus*), the souffia (*Leuciscus souffia*).
- The *Barbel zone* has bed slopes between 0.3% and 0.025% and water temperatures between 12° and 18°C, with alternating rapids and quiet waters. The water is well oxygenated at the surface, but becomes less oxygenated close to the bed. The bed is mostly made of fine gravel. The range of species is wider than in the grayling zone; in general the Cyprinidae dominate like the common barbel (*Barbus barbus*), the gudgeon (*Gobio gobio*), the bleak (*Alburnus alburnus*), the silver bream (*Blicca bjoerkna*) and the common nase (*Chondrostoma nasus*), as well as predatory fish like the eel (*Anguilla anguilla*), the northern pike (*Esox lucius*), and the perch (*Perca fluviatilis*).
- The *Bream zone* has bed slopes between 0.1% and 0% and water temperatures between 16° and 20°C. The oxygen content is often deficient close to the bed, whereas it is sufficient at the surface. The bed is made of sand and silt, and the water is often turbid. In this region the species of the grayling and the barbel zone that like strong currents like the schneider (*Alburnoides bipunctatus*) and the common minnow (*Phoxinus phoxinus*) are missing. Also the barbel (*Barbus barbus*) can only be found locally where the current is relative high. Dominant characteristic species are these with indifferent attitude toward the current, like the bream (*Abramis brama*), the perch (*Perca fluviatilis*), the eel (*Anguilla Anguilla*), and the common roach (*Rutilus rutilus*).

This classification is generally applied for central European water courses; information referring to the subdivision of many fish species into the four zones may be found e.g. in DWA (2010).

2.6.4 Turbulence intensity and fish behaviour

The effects of turbulence on swimming performance of fish were deeply studied, but the results are still unclear and controversial. Firstly, the definition of the turbulence intensity *TI* is not unique: it can be defined as the ratio between the standard deviation of the flow velocity and mean flow velocity (e.g. Odeh *et al.* 2002), as well as the ratio between the standard deviation of the instantaneous velocity and the local time-averaged velocity (Cotel *et al.* 2006). Both definitions represent a measure of the magnitude of velocity fluctuations, but the first refers to time-averaged flow conditions, whereas the second to local flow conditions. In the following some researches are presented to highlight the still existing difficulty to draw clear conclusions on this topic.

In field tests Cotel *et al.* (2006) investigated the effect of turbulence by identifying preferred brown trout (*Salmo trutta*) habitats. They suggested that the locally-defined turbulence intensity is an appropriate indicator. In their experiments brown trout were generally found in areas with low turbulence intensities.

Tritico and Cotel (2010) performed model tests to investigate the effect of turbulent eddies on the stability and on the critical swimming velocity of creek chub (*Semotilus atromaculatus*). The results showed that turbulent eddies, and so their diameter, their vorticity and their orientation, have a significant influence on the swimming performance of this fish species.

Also Lupandin (2005) studied the effect of turbulence on the swimming speed of perch (*Perca fluviatilis*), arguing that the turbulence has an impact on fish behaviour and that the longer the fish body length, the higher turbulence is required to decrease the critical flow velocity. This mechanism is related to the impact of the vortex structure on fish: the vortex affects the fish balance and the torsional moment generated by the hydrodynamic forces favor fish overturn. To stabilize their position, fish spread their pectoral fins increasing their hydraulic resistance and thus decreasing their swimming velocity (see also Pavlov *et al.* 2000).

In contrast Nikora *et al.* (2003) observed that turbulence has no significant effect on the swimming performance of the inanga (*Galaxias maculatus*), because not only the turbulence magnitude (in terms of Reynolds stresses, turbulence intensity and turbulent kinetic energy), but also eddy length scales in relation to the fish dimensions affect their swimming performance. Also Odeh *et al.* (2002) concluded that turbulence has no observable effect on the reaction of rainbow trouts (*Oncorhynchus mykiss*).

Moreover, some authors recognize that the effect of turbulence depends on the eddy size (e.g. Pavlov *et al.* 2000, Webb and Cotel 2011). If the eddy is smaller than the fish body length L_{fish}, it does not affect the fish swimming capacity; if it has a similar size to L_{fish}, it can destabilize the fish (Figure 2.13), whereas if the eddy is much larger than L_{fish}, it can affect its movement but it does not destabilize it.

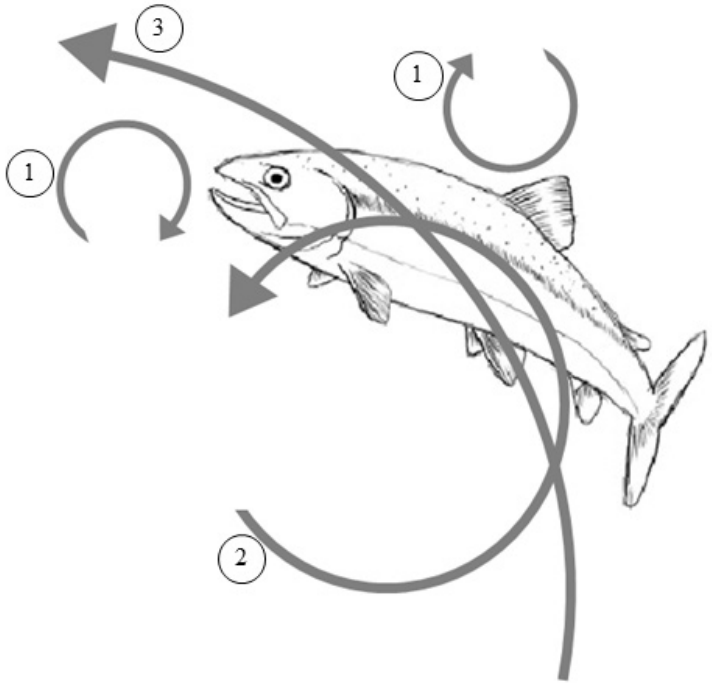

Figure 2.13 Turbulence can destabilize a fish, depending on the eddy size: 1) eddies smaller than L_{fish} do not affect its stability; 2) eddies similar in size to L_{fish} can destabilize it; 3) eddies much larger than L_{fish} may move it, but they do not destabilize it.

In a review paper, Liao (2007) describes the effects of turbulence on fish swimming performance based on different studies. He reassumes the two opposite beliefs: turbulence increases the costs of locomotion on the one hand, whereas fish can reduce their locomotive costs by exploiting turbulence on the other. There are at least two

mechanisms by which fish take advantage of turbulent flow to increase their swimming performance. First, they use regions of reduced velocity behind bluff bodies and rest; and secondly, they capture the energy of discrete vortices and use it to swim, depending on the ratio between the vortex diameter and the fish length. Liao *et al.* (2003) investigated the rainbrow trout (*Oncorhynchus mykiss*) swimming in the Karman street behind different cylinders at two different flow velocities, in the free stream and in the cylinder bow wake. The results showed that rainbow trout voluntarily alter their body kinematics to interact with vortices present in the environment. The fish, aside from choosing to be in the slower flow velocity offered behind the cylinder, are also altering their body kinematic to synchronize it with the shed vortices. Therefore, the authors suggested that fish can capture energy from vortices to maintain station in downstream flow and thus, are able to take advantages of turbulence.

The above review indicates that the effect of turbulence on swimming performance is still unclear. There is no precise relation between turbulence and swimming performance, but there are many other parameters (fish species, eddy size, etc.) which play a decisive role.

2.6.5 Suitable habitat conditions

By extending the ecological effectiveness in terms of migration possibilities for fish also to suitable habitat conditions for macroinvertebrates in general, then – simplifying – the key word could be diversity. That means high variety of flow velocity, of river bed material, of temperature and of oxygen content. The wider the spectrum of the hydraulic, morphological and biological conditions, the higher is the probability to find suitable conditions for different species.

Macroinvertabrates constitute a very important food source for fish. For this reason, aiming at suitable habitat conditions for them is fundamental to achieve the same for fish. Macroinvertebrates are highly sensitive to habitat alteration, disturbance and, presumably, rehabilitation (Roni *et al.* 2008). Unfortunately, the results of many different studies on habitat rehabilitation projects are very variable and the “right recipe” for them remains uncertain.

A functional connectivity, defined as the effective possibility for a certain species to move from one position to another, is of great importance: it determines if a certain species can propagate and find new locations to populate (Alp *et al*. 2011). For the

different life stages of every species (not only fish) the availability and the connection between the different specific habitats is decisive for the preservation of biodiversity.

Liao (2007) concluded that the attempts to increase fish diversity and population density by introducing structures to increase the physical heterogeneity are based on a limited understanding of the interaction between fish and turbulent flows. For this reason, rehabilitation projects often fail.

3 Literature review on block ramps

3.1 Introduction

For a proper design of block ramps, two main design criteria should be fulfilled, namely:

1. *Hydraulic criterion*: The structural integrity of the block ramp has to be ensured up to a certain design discharge. Usually this discharge corresponds to the 100-year flood (HQ_{100} = discharge with a statistical return period of 100 years).
2. *Ecological criterion*: Block ramps have to be ecologically effective in a certain range of discharges, which depends on the discharge regime of the river (DWA 2009). In Switzerland it is often assumed that the ecological efficiency should be guaranteed for 300 days per year, namely between the discharges Q_{30} (= discharge which is statistically not exceeded over 30 days per year) and Q_{330} (= discharge which is statistically not exceeded over 330 days per year).

Both design criteria are important. If a block ramp satisfies the hydraulic criterion and remains stable during HQ_{100}, but is not passable for the fish living in the river during the operation period (Q_{30} – Q_{330}), then the ecological objective is not achieved. The factors supporting the choice of a block ramp (which has more hydraulic limitations than drops and sills) are that it has no abrupt failure in case of overload (see Chap. 3.2.2) and that it fulfills the ecological criteria. Therefore, both the hydraulic and the ecological criteria are important for the design of block ramps.

Nowadays no universally valid approach to characterise flow and ecological conditions is available, especially for UBR, due to the complexity of the flow processes (DWA 2009). Therefore, the design of new block ramps as well as the prediction of their stability and of their ecological effectiveness is still limited. Nevertheless different studies on block ramps were conducted in the past decades and are shortly presented in the following: Chap. 3.2 focuses on the literature review of hydraulic criteria, Chap. 3.3 on ecological criteria, and Chap. 3.4 on the identification of research gaps.

3.2 Hydraulic design criteria for block ramps

Basically the water depth h and the mean flow velocity U constitute the fundamentals for the hydraulic design of block ramps (Figure 3.1). However, both the transversal variation of the block configuration and so of the roughness – especially for block cluster ramp types – across the ramp width and the longitudinal variation leads to highly heterogeneous flow conditions and hence to local strong variation of h and U. A detailed description of the local hydraulics is not possible up to now (DWA 2009). For this reason, the existing approaches require severe simplifications in the modeling, especially for UBR, due to the often violated applicability ranges.

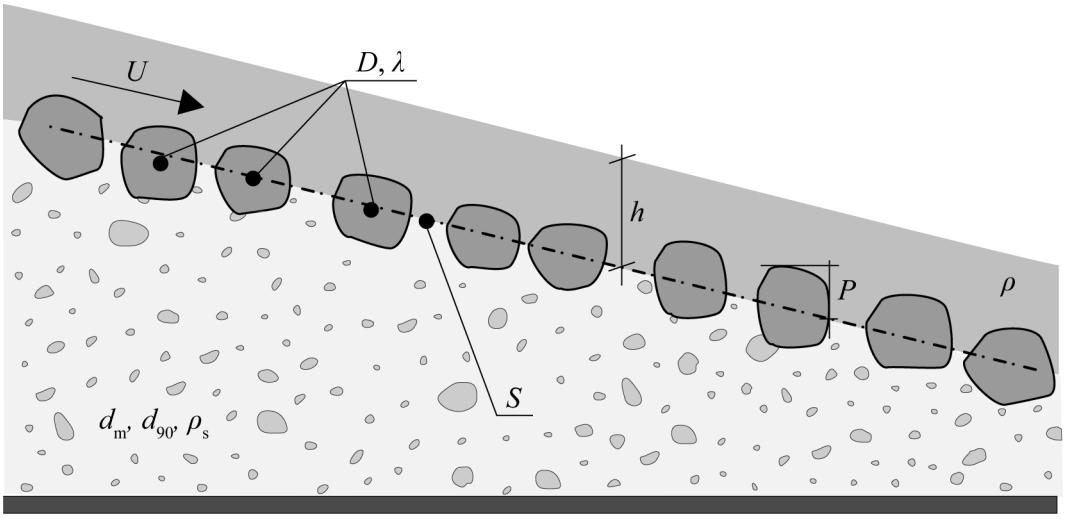

Figure 3.1 Definition sketch of longitudinal section of an UBR including the most important parameters.

3.2.1 Flow resistance

In steep mountain rivers the hydraulic conditions are dominated by the interaction between steep slopes, large roughness elements, coarse bed material and morphological heterogeneities. Aberle and Smart (2003) stated that no standard flow resistance equation for mountain streams can be found in the literature. Most approaches are based on uniform flow conditions and were developed for lowland rivers. In mountain rivers uniform flow conditions are rarely achieved or only for short reaches. Therefore, these approaches have to be applied with caution. Block ramps can be considered similarly: the idea of bed stabilization with big boulders stems from mountain river morphology,

as the block configuration of structured block ramps is similar to the step-pool sequences that can be found in mountain rivers.

The flow resistance is based on the boundary layer theory with the logarithmic law for rough conditions (Chap. 2.2) in the following form

$$\sqrt{\frac{8}{f}} = \frac{U}{u_*} = \frac{1}{\kappa} \ln \frac{h}{k_s} + B, \tag{3.1}$$

where f = Darcy-Weisbach friction factor, U = mean flow velocity, u_* = shear velocity, κ = von Karman constant, k_s = equivalent sand roughness, and B = constant. Different references are found for the determination of κ and of B (i.e. Keulegan 1938, Rouse 1965, Dittrich and Koll 1997, Gaudio *et al.* 2010). Typical values are $\kappa = 0.4$ and $B = 8.5$. Many approaches are based on Eq. (3.1): it is adapted to a certain specific case, often by varying the coefficient $1/\kappa$ and the constant B according to the considered empirical results. Regarding B, there are different approaches for the determination of the flow resistance of a rough bed, depending on the definition of the roughness height or the cross-section geometry: Aberle (2000) and Weichert (2006), amongst others, gave a wide overview on the existing approaches, whose application range is limited to the tested parameters. Following the suggestions of DWA (2009), the flow resistance equations for the different block ramp types are presented hereafter.

Based on a study of Scheuerlein (1968), the flow resistance of *interlocked ramps of block carpet type* can be determined with the following equation, representing an extended version of Eq. (3.1)

$$\sqrt{\frac{8}{f}} = \frac{U}{u_*} = \frac{U}{\sqrt{g\,h\,S}} = 3.93 \ln \left(\frac{1}{\sigma_a (0.425 + 2.025\,\Phi\,S)} \frac{h}{P} \right), \tag{3.2}$$

where $\sigma_a < 1$ = air content parameter, $\Phi = D \cdot N_A^{1/2}$ = packing factor, D = equivalent spherical block diameter, N_A = number of blocks per unit area (m^2), and P = roughness height (or protrusion) here defined as $P = D/3$. The application range of Eq. (3.2) is limited to supercritical aerated uniform flow and to bed slopes $10\% < S < 67\%$. Hassinger (1991) modified Eq. (3.2) for $6.7\% < S < 12.5\%$ reducing the coefficient from 3.93 to 2.46.

For *dumped ramps of block carpet type* DWA (2009) suggested the equation proposed by Rice *et al.* (1998). Using laboratory experiments they determine the roughness and the flow resistance of loose angular riprap on steep slopes. The original relationship

$$\sqrt{\frac{8}{f}} = \frac{U}{u_*} = \frac{U}{\sqrt{g\,h\,S}} = 5.1\ \log\frac{h}{D_{84}} + 6, \tag{3.3a}$$

or the converted equation

$$\sqrt{\frac{8}{f}} = \frac{U}{u_*} = \frac{U}{\sqrt{g\,h\,S}} = 2.21\ \ln\frac{h}{D_{84}} + 6 \tag{3.3b}$$

is valid for 2.8% < S < 33% and median rock diameters ranging from 52 mm to 278 mm.

In different studies the influence of large roughness elements on the flow resistance was investigated (e.g. Baiamonte and Ferro 1997, Ferro 1999), however without quantifying the increase of flow resistance due to the roughness elements. In contrast, Pagliara and Chiavaccini (2006a) determined this influence by testing reinforced block ramps with protruding boulders placed in rows or randomly, which can be defined – according to the presented classification (Chap. 1.2) – as *structured and unstructured block ramps of block cluster type*, respectively. For their study, the blocks were placed and glued on an already fixed layer of bed material (4 mm < d_{84} < 24.7 mm) made of rounded or crushed rocks with an almost uniform granulometric curve (1.05 < σ < 1.26). For this reason, the tested ramps were fixed and reinforced with bigger blocks. With these boundary conditions local block movements or any entrainment or erosion process of the bed material were impossible. The tests performed by Pagliara and Chiavaccini (2006a) are therefore different from the present tests. From the physical experiments the flow resistance for both tested reinforced ramps resulted as

$$\sqrt{\frac{8}{f}} = \frac{U}{u_*} = \frac{U}{\sqrt{g\,h\,S}} = 3.5\ (1+\lambda)^C\ S^{-0.17}\left(\frac{h}{d_{84}}\right)^{0.1}, \tag{3.4}$$

where C = coefficient describing the base material and the block arrangement (see Table 3.1), d_{84} = characteristic grain diameter of the bed material, and λ = block placement density defined as the ratio between the ramp area covered by blocks and the entire ramp area, namely:

$$\lambda = \frac{N\,\pi\,D^2}{4\,W_R\,L_R} \tag{3.5}$$

where N = number of blocks along the entire ramp, D = equivalent spherical block diameter, W_R = ramp width and L_R = ramp length.

Table 3.1 Coefficients C of Eq. (3.4) depending on block material and on block arrangement (Pagliara and Chiavaccini, 2006a).

Bed material	Blocks arrangement	C [-]
rounded	random	-1.6
rounded	rows	-1.8
crushed	random	-2.4
crushed	rows	-3.0

Eq. (3.4) is valid for the tested parameter ranges, namely for ramp slopes $8\% < S < 40\%$, for ratio between blocks and bed material $1.9 < D/d_{50} < 14.5$ (no information about D/d_{90} are given; the bed materials are almost uniform with $1.05 < \sigma < 1.26$), for block placement density $0 < \lambda < 0.3$, for relative submergence levels $0.2 < h/P < 2.6$ (here $P = D/2$), for Reynolds number (Eq. 2.1) $1.5 \cdot 10^4 < \mathsf{R} < 20 \cdot 10^4$ and for Froude number (Eq. 4.2) $0.8 < \mathsf{F} < 2.9$. The flow resistance depends on S, on the block arrangement (blocks in rows are more dissipative than blocks in random disposition) and particularly on λ, while the influence of h/P, of F and of R appears negligible for the tested parameter range.

Oertel and Schlenkhoff (2012) investigated experimentally and numerically the flow regime, the energy dissipation, the friction factor and the drag force of *structured block ramps*. For this type of block ramps they suggest for the friction factor the following relation

$$\sqrt{\frac{8}{f}} = \frac{U}{u_*} = \left(4.4 + \frac{0.09}{S}\right) \log\frac{h}{P} + \left(2.2 - \frac{0.0023}{S}\right) \tag{3.6}$$

Eq. (3.6) is valid for relative submergences $1.5 < h/P < 4$ and for the tested ramp slopes $2\% < S < 10\%$.

The flow resistance for *unstructured block ramps of block cluster type* is also defined by the model of composite roughness (see Chap. 2.2 and Figure 2.3), in which the resistance due to the grain friction of the bed material is added the resistance due to the form drag of macro-roughness elements. Whittaker *et al.* (1988) suggested the application of this model to determine the flow resistance of a river bed with macro-roughness elements. The Chézy coefficients are defined as follows:

$$c' = \frac{U}{\sqrt{g\, R\, S'}} = 2.5\, \ln\frac{12\, R}{k_s} \tag{3.7}$$

for the flow resistance due to the bed material, where k_s is often assumed as k_s = (2.5-3) d_{90} for sediment mixture with exposed grains (Bezzola 2010); and

$$c'' = \frac{U}{\sqrt{g\,R\,S''}} = 2.5\,\ln\frac{12\,R}{k_B} \tag{3.8}$$

for the flow resistance due to the macro-roughness elements, where k_B = equivalent sand roughness for the macro-roughness elements defined according to Whittaker *et al.* (1988) as

$$k_B = N_A\,D^3\,\left(17.8 - 0.47\,\frac{h}{D}\right). \tag{3.9}$$

The resulting Chézy coefficients *c'* and *c''* are then superposed according to Eq. (2.28), leading to the total Chézy coefficient *c*, which is used for the determination of the mean flow velocity (Eq. 2.16). In Eq. (3.9) both the block diameter *D* and the number of block per unit area N_A are considered, and thus indirectly also the block placement density. The application range is limited to 0.1% < *S* <5%, 0.5 < *h*/*D* <4, and $N_A\,D^2 < 0.15$. Note that in this case the block placement density was defined as $N\,D^2$, assuming the block area as a square area with edge length equal to *D*, whereas in the present research as in Eq. (3.5) assuming the block area as a projected spherical area.

Fenzl and Davis (1964) also proposed an empirical relationship for the determination of the Chézy coefficient for the form resistance *c''* depending on the block protrusion *P* (Chap. 2.3.2):

$$c'' = \frac{U}{\sqrt{g\,R\,S''}} = 1.736\,\left(P\sqrt{N_A}\right)^{-1.029}\,(N_A\,h^2)^{0.227}. \tag{3.10}$$

The experiments were carried out with blocks of $D \approx 75$ cm and a constant block protrusion $P \approx 51$ cm by constant slope *S* = 0.5%, for relative submergences 1.25 < *h*/*D* <3.5 and for block placement densities $0.05 < N_A\,D^2 < 0.5$. The applicability range of Eq. (3.10) is limited to these values.

Morris (1959) described a model for isolated roughness flow, where the flow conditions between the isolated blocks differ from these on UBR with a relative close or narrow block configuration. Nevertheless, this model is worth mentioning because it represents a fundamental approach to describe roughness elements in turbulent flow. Applying the model of composite roughness, by superposing the bed shear stresses τ_0' and τ_0'' (see Chap. 2.2 and Eq. 2.25), τ_0'' can be defined as the sum of bed shear stresses generated by each single block as

$$\tau_0'' = N_A F_B \quad , \tag{3.11}$$

where F_B = resistance force of a single block defined as

$$F_B = \frac{1}{2} \rho C_D A_B U^2 \quad , \tag{3.12}$$

where C_D = resistance coefficient and A_B = block flow section and U = cross-sectional averaged velocity. C_D represents a high uncertainty, because it depends on the block shape, on the block placement density, on relative submergence, on the occurring flow conditions (turbulence conditions, influence of the single blocks on the adjacent blocks), and up to now there is no consistent definition for the quantification of C_D (DWA 2009).

3.2.2 Energy dissipation of block ramps

The dissipated energy ΔH on block ramps is determined as the difference between the energy head at the ramp head H_0 and the ramp toe H_1 (Figure 3.2). The energy dissipation is due to the local higher slope and higher bed roughness. The relative energy dissipation $\Delta H/H_0$ of an UBR is determined according to Pagliara and Chiavaccini (2006b) as

$$\frac{\Delta H}{H_0} = \frac{H_0 - H_1}{H_0} = \left[A + (1 - A) e^{(B + C\,S)(h_c/H)}\right] \left(1 + \frac{\lambda}{E + F\,\lambda}\right), \tag{3.13}$$

where $H_0 = H + 1.5 h_c$ = total upstream energy head, $H_1 = h_1 + q^2/(2g h_1^2)$ = energy head at ramp toe, $H = S\,L_R$ = ramp height, $h_c = (q^2/g)^{1/3}$ = critical flow depth, h_1 = flow depth at ramp toe (Figure 3.2), A, B, C = coefficients depending on h_c/d_{50} (A, B, C vary for 3 different ranges of h_c/d_{50}), and E, F = coefficients depending on the arrangement (random or in rows) and on the roughness (rounded or crushed) of the blocks. For random disposition and rounded boulders, assumed for the present research, $E = 0.6$ and $F = 13.3$. Eq. (3.13) is valid for $\lambda < 0.33$, for $0.08 < S < 0.33$, for $1.75 < D/d_{50} < 19$, and for uniform flow conditions.

Oertel and Schlenkhoff. (2012) suggested for structured block ramps with cross-bars the relationship

$$\frac{\Delta H}{H_0} = a_1 + (1 - a_1) e^{(a_2 + a_3\,S)(h_c/H)}, \tag{3.14}$$

where a_1, a_2 and a_3 = coefficients depending on the ramp slope S: $a_1 = 0.17 - 0.0017/S$, $a_2 = -0.7 + 0.0073/S$, $a_3 = -4.9 - 0.26/S$. Eq. (3.14) is valid for the same data range as Eq. (3.6).

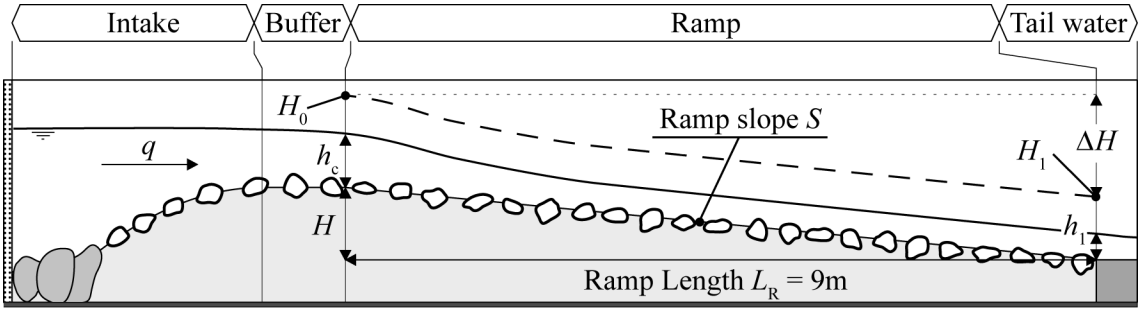

Figure 3.2 Sketch with decisive parameter for the determination of energy dissipation.

3.2.3 Failure mechanisms and stability of block ramps

Failure mechanisms of river engineering structures (Weichert 2007)

Weichert (2007) describes the different failure mechanisms for river engineering structures in general (Figure 3.3). A failure occurs in case of overload, i.e. when the specific discharge q exceeds the design discharge q_d and the critical specific discharge q_{crit}, defined as the discharge causing structure instability. *Case a)* (Figure 3.3, top left) describes a binary failure mechanism without control: for $q < q_{crit}$ the structure remains stable, whereas for $q > q_{crit}$ a damage occurs, which increases in an uncontrolled way. For these structures the design discharge has to be lower than the critical discharge, namely $q_d < q_{crit}$, to account for design uncertainties and assure a certain buffer. *Case b)* (Figure 3.3, top right) represents the same failure mechanism as in case a), but with controlled damage processes: in case of overload the damage is confined to a certain limit and therefore predictable. *Case c)* (Figure 3.3, bottom left) corresponds to a gradual failure mechanism: a discharge $q > q_d$ does not lead to an abrupt structural failure (binary mechanisms, as for a) and b)) but to a gradual one. There is no control on the failure and, therefore, no limit to the maximal damage, which cannot be predicted. The design discharge corresponds to the critical discharge, namely $q_d = q_{crit}$. *Case d)* (Figure 3.3, bottom right) differs from case c) only in the controlled damage process, which is confined and predictable.

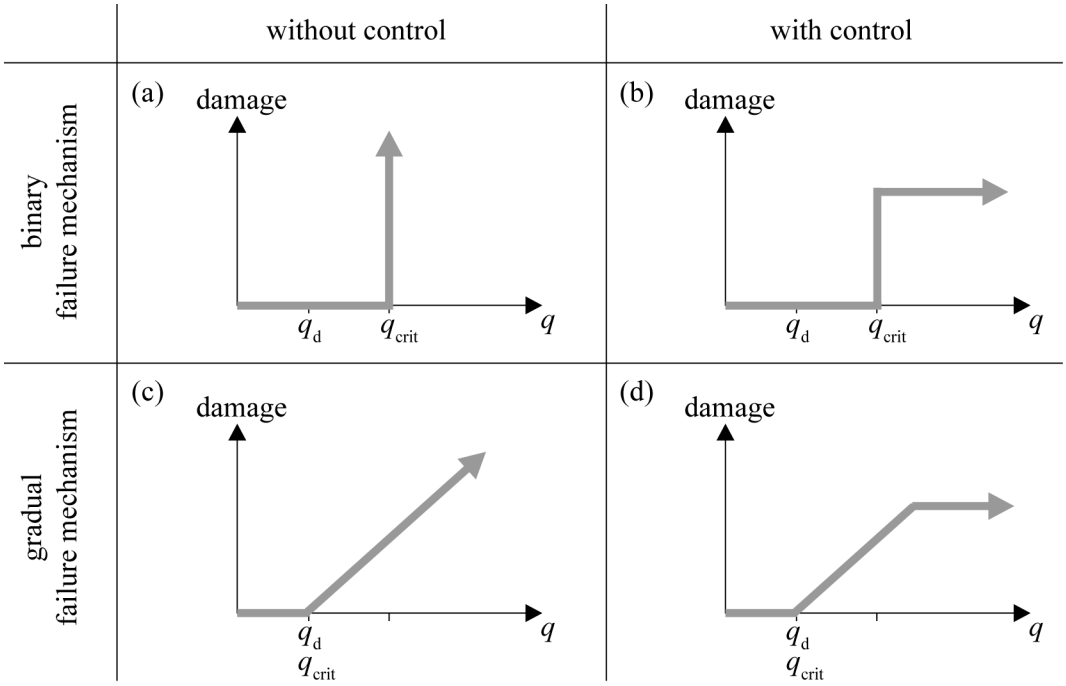

Figure 3.3 Failure mechanisms for river engineering measures (Weichert 2007, adapted) depending on failure type (gradual or binary) and on the control of the damage.

Implication of the model of Weichert (2007) for block ramps

The failure mechanism classification suggested by Weichert (2007) can be applied to the different block ramp types. Ramps of block carpet type and structured ramps of block cluster type show binary failure mechanism in case of overload: These ramps are rigid structures having relatively high stability, but if one point along the ramp fails, it causes generally the general ramp failure. In contrast, assuming a ramp configuration that excludes dominant overpassing or dominant embedding conditions (see Chap. 2.3.4), UBR and self-structured ramps adjust themselves to the higher discharge through an erosion and thus to a decreased slope, without leading to an abrupt failure. For this reason, UBR and self-structured block ramps show a gradual failure mechanism, representing an advantage compared to the other block ramp types and to drops and sills.

Often block ramps are built attached to existing weirs or drops. In this case a certain guarantee regarding the maintenance of a certain bed level exists. Assuming a stable structure (weir or drop) placed upstream of the ramp, in case of ramp collapse the damage is controlled and limited to the ramp, but the fixed level of the weir or drop remains. Another possibility to limit the damage is to introduce a buffer area upstream

of the ramp (see Chap. 4.2.4). It leaves the ramp additional space to flatten without failing, as well as block provision if some blocks are transported. If the damage process is controlled and reaches a certain maximum damage (e.g. with a drop structure upstream of the ramp), then the ramp shows a failure mechanism of type *b)* or *d)* (Figure 3.3).

Existing approaches describing the failure mechanisms and the stability of block ramps

Whittaker and Jäggi (1986) defined three different failure mechanisms for *interlocked and dumped ramps* of block carpet type: (1) destabilization of single blocks, (2) entrainment and washout of bed material below the blocks, and (3) scour and failure of ramp toe. In all three cases the failure may lead to a binary process (Figure 3.3). From each failure mechanism a corresponding stability criterion results for ramps of block carpet type, which are presented in the following.

- *Destabilization of single blocks* corresponds to a particular case of incipient motion of bed material and can be considered as the dominant overpassing process described by Raudkivi and Ettema (1982) for bimodal material (Chap. 2.3.4). Combining the Shields approach (1936, Chap. 2.3.2) with the Strickler power law (1923, Chap. 2.2), and assuming uniform and steady flow conditions, negligible wall effects and no backwater effects on the ramp, the following empirical relationship for the maximum critical specific discharge q_{crit} results from the experiments

$$q_{crit} = \frac{0.257}{S^{7/6}} \sqrt{g\,(s-1)\,D_{65}^3}\,. \tag{3.15}$$

- *Entrainment and washout of bed material* corresponds to the dominant embedding process described by Raudkivi and Ettema (1982) for bimodal material (Chap. 2.3.4). From the experiments the following empirical relationship for the maximum critical specific discharge q_{crit} results

$$q_{crit} = 14.47 \sqrt{g} \left(\frac{s-1}{\rho_s}\right)^{2.35} \left(\frac{d_{65}}{D}\right)^2 \frac{\beta^{2.35}}{D^{0.85}\,S^{1.9}}\,, \tag{3.16}$$

where β = necessary block placement density expressed in block mass per unit area [t/m^2], and D = equivalent spherical block diameter defined as

$$D = 1.06\,D_{65} \tag{3.17}$$

or as

$$D = \sqrt[3]{\frac{6M_B}{\rho_S \pi}}, \tag{3.18}$$

where M_B = block mass.

- *Scour and failure of ramp toe:* if the scour at the ramp toe reaches a certain depth which endangers the stability of the ramp toe, it leads to increased erosion at the ramp toe having effects on the whole ramp length and so affecting the ramp stability. For this reason the scour depth at the ramp toe has to be predicted, to design, if necessary, the measures against scour. According to Whittaker and Jäggi (1986) the scour depth h_S at the ramp end (referred from the mean bed level) is estimated with the modified Tschopp-Bisaz empirical equation (1972)

$$h_{TW} + h_S = 0.85 \sqrt{q\ U_E} - 7.125\ d_{90}\ , \tag{3.19}$$

where h_{TW} = tail water depth (downstream of the ramp, where uniform flow conditions occurs) and U_E = flow velocity at ramp toe, which can be determined for relative submergences $0.3 \leq h/D \leq 7$ with the relationship

$$U_E = 1.32\ \frac{(g\ S)^{0.2}\ q^{0.6}}{D^{0.4}}\ . \tag{3.20}$$

DWA (2009) suggests the following equation according to Hartung and Scheuerlein (1970) for the stability of *interlocked ramps of block carpet type*

$$U_{crit} = 1.2 \sqrt{2\ g\ (s-1)\ cos\ \alpha\ D}, \tag{3.21}$$

where U_{crit} = critical flow velocity, α = ramp inclination angle (in degree) and, if the blocks are simplified as sphere, D is defined according to Eq. (3.17) or (3.18). DWA (2009) suggests as stability criterion for *dumped ramps of block carpet type* with $S > 5\%$ the empirical relationships (Eqs. (3.13) and (3.14)) according to Whittaker and Jäggi (1986). Further researches, like e.g. Palt and Dittrich (2002), suggested modifications of Eq. (3.15), mostly in the power coefficient of the ramp slope S and in the value of the numerical coefficient, while maintaining the structure of the equation.

According to Aberle (2000) the stability of *structured block ramps of block cluster type* is determined with

$$q_{crit} = 0.062\ S^{-1.11} \sqrt{g\ (s-1)\ D^3}, \tag{3.22}$$

which has the same structure as Eq. (3.15) but lower numerical coefficient and slightly lower power coefficient of the ramp slope S. Vogel (2003), Weichert (2006), and Wei-

chert *et al.* (2009) also suggested modifications of Eq. (3.15) determining the stability of structured block ramps.

Pagliara and Chiavaccini (2007) investigated the failure mechanisms of base and reinforced block ramps, namely of ramps of block carpet type with or without protruding boulders placed in rows, arcs or random configuration (see also Pagliara and Chiavaccini 2006a, and Chap. 3.2.1) for ramp slopes 8.3% < S < 25%. The ramp failure was defined through three different steps of the failure evolution: (1) *initial movement* of the base material, in which the base material (here: rocks) begins to vibrate and some isolated blocks are entrained; (2) *local failure*, in which one or more blocks leave their position simultaneously, producing a defined circular or semicircular scour hole; (3) *global failure*, in which different local failures happen, leading to large area unprotected by blocks. The local failure was considered here as the critical condition, because it causes a change in the original ramp geometry. In a similar way, defining four different phases of failure of *dumped ramps of block carpet type*, Pagliara and Palermo (2011) proposed a new approach to estimate critical discharge for each failure phase by using the critical stone Froude number.

Combining the experimental results with the relationship for the flow resistance of reinforced block ramps (Pagliara and Chiavaccini 2006a, Chap. 3.2.1) and with the definition of the densimetric Froude number, the following relationship was obtained for the critical densimetric Froude number F_{dc} for block arrangement in rows and randomly placed

$$\mathsf{F}_{dc} = 1.98\,(1+\lambda)^{a_1}\,S^{0.18}\,(h/D_{84})^{0.36}\,, \tag{3.23}$$

where a_1 is the coefficient describing the block arrangement: a_1 = -2.2 for rows, a_1 = -2.6 or -2.8 for the two different reinforced arc types, a_1 = -2.6 for arc, and a_1 = -2.0 for random disposition. The local ramp failure is expressed with F_{dc} (Eq. 3.23) to depend on the ramp slope, the relative submergence and on the block placement density. For design purpose, Eq. (3.23) was transformed in an expression to explicitly estimate the critical or failure discharge q_{crit}

$$q_{crit} = 1.8\;S^{(-0.52+b_1)}\,{D_{50}}^{1.5}\,(1+\lambda)^{b_2}\,, \tag{3.24}$$

where b_1 and b_2 are coefficients that depend on the block arrangement: b_1 = -0.2 and b_2 = 1.7 for rows, b_1 = -0.17 or -0.3 and b_2 = 1.2 or 0.4 for the tow different reinforced

arc types, b_1 = -0.17 and b_2 = 1.2 for arc, and b_1 = -0.27 and b_2 = 0.8 for random disposition.

Another approach for the determination of the stability of *unstructured block ramps of block cluster type* is represented by the equilibrium condition of all forces exerted on a block (Eq. 3.12). The details of this method and the description of all the forces considered is found in Janisch *et al.* (2007) and in DWA (2009). The approach presented by Janisch *et al.* (2007) combines the superposition of the Chézy-coefficients (Eq. 2.28) and of the shear stresses (Eq. 2.25) together with the equilibrium condition of all forces on a block with the definition of the resistance coefficient C_D according to Flammer *et al.* (1970).

On the basis of the above mentioned equations and further suggestions from literature, the required block diameter D and the required block placement density λ are determined for the considered block ramp type and design conditions. Note that all the above mentioned approaches do not take into account the stabilizing or destabilizing effect of sediment transport.

Failure mechanisms of UBR

The definition of failure mechanism for UBR with finer bed material (and not with a layer of rocks, like in the investigations of Pagliara and Chiavaccini 2006a and 2007) is not unique and distinct. It depends on the system considered and on the goals defined for the UBR (Chap. 1.2). On the one hand there is the ramp as structure, which has to sastisfy the hydraulic and the ecological criteria (Chap. 3.1), and on the other hand there is the river reach where the ramp is built in, comprehending the ramp, as well as the upstream and downstream sections. Considering exclusively the ramp, the following failure mechanisms can occur (Figure 3.4):

- Ramp flattening (Figure 3.4 a, see also embedding process described by Raudkivi and Ettema 1982, Chap. 2.3.4)
  The blocks remain stable but the finer bed material is eroded, leading to a slope decrease and to a ramp flattening. Assuming stable conditions downstream of the UBR, the erosion process corresponds to a rotation around the ramp toe.

- Block loss (Figure 3.4 b, see also overpassing process described by Raudkivi and Ettema 1982, Chap. 2.3.4)
  When the blocks are entrained and transported downstream of the UBR, the block placement density decreases. The remaining blocks cannot exercise the

same flow resistance as before, exposing the finer bed material to a higher load. This leads to an erosion of the bed material and to a flattening of the ramp (see above); often in this case the process occurs very fast, causing an abrupt failure, which is herein referred as collapse.

- Absence of migration corridors (Figure 3.4 c).
  If the bed configuration (blocks + finer bed material) do not provide suitable flow conditions in terms of migration possibilities for the target fish within a certain range of discharges, the UBR does not satisfy the ecological criterion (Chap. 3.1).

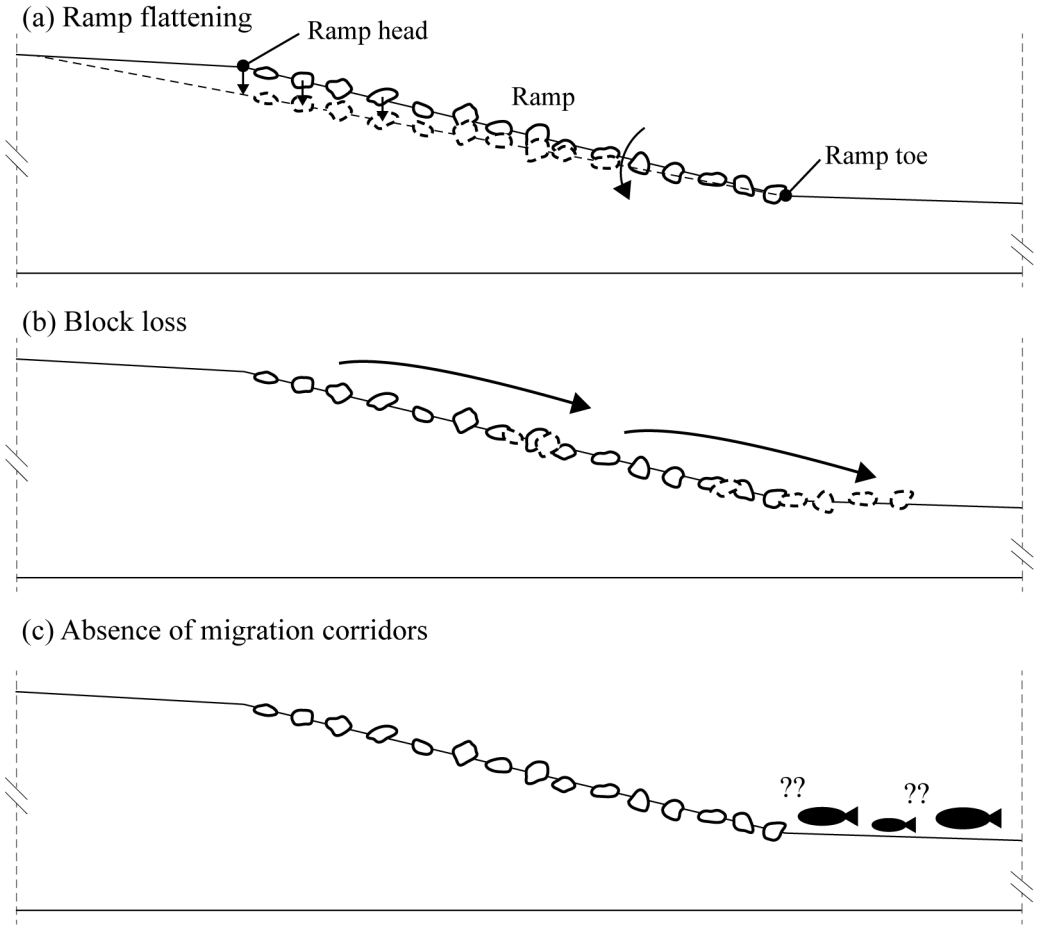

Figure 3.4 Failure mechanisms for UBR considering exclusively the ramp structure.

Considering the river system where the ramp is built, the following failure mechanism can occur:

- Decrease of the ramp head or ramp toe elevation (Figure 3.5)

  A variation of the ramp head elevation affects the upstream reach of the UBR, leading to the loss of the fixed-point effect and to a variation of the bed elevation upstream of the ramp. A variation of the ramp toe elevation directly affects the ramp slope, leading to the variation of the ramp head elevation and so of the already mentioned effect. In both cases the longitudinal section of the river reach changes, leading to potential problems for other existant structures attached at the UBR, as e.g. drops or sills or bank protection structures.

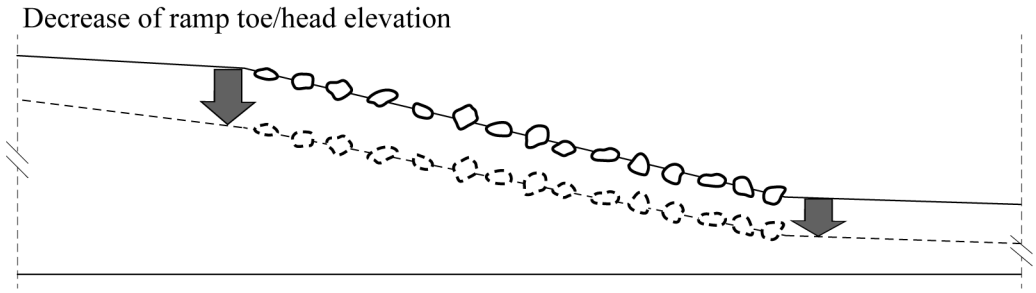

Figure 3.5 Failure mechanism for UBR considering the river system up- and downstream of the ramp.

There are different mechanisms leading to the failure of the ramp. The definition of failure depends on the definition of the goals which have to be achieved by the UBR. Therefore, the failure mechanisms and also the countermeasures depend on these goals.

3.3 Ecological design criteria for block ramps

The ecological functionality of a block ramp is mainly determined by the availability of suitable hydraulic conditions, which allow fish living in the considered water course to migrate up- and downstream (Chap. 2.6.1). Nature-oriented heterogeneous structures covering the complete river width, and particularly structured and unstructured ramps of block cluster type, have many relevant benefits: (1) they provide a multitude of adequate migration corridors; (2) the migration corridors can be easily found compared with fish facilities, where the bypass entrance (often at one river shore) has to be found first; (3) they guarantee heterogeneous bed structures leading to areas with low flow velocities, and (4) they can provide different habitat conditions (Chap. 2.6.3).

As mentioned in Chap. 3.1, block ramps do not have to be ecologically effective for all flow condition (Gebler 2007, Hunziker, Zarn und Partner 2008, DWA 2009, DWA 2010), but only in between a certain range of discharges, depending on the discharge regime (DWA 2009). The efficient period in terms of ecologiy can be defined as operation period. In Switzerland there is no defined prescription and it is often assumed that the operation period corresponds to 300 days per years, i.e. between Q_{30} and Q_{330} (Chap. 3.1). In general, ecological efficiency of fish passage facilities means that they have to be found and to be passable for fish during the operation period (DWA 2009). In the case of block ramps, they can always be found, because they cover the entire river width, and so only the second requirement (ramp passable) is considered.

3.3.1 Maximum flow velocity and minimum water depth

The two main parameters determining the adequacy of the hydraulic conditions for a migration corridor, namely the maximum acceptable flow velocity U_{crit} (limiting fish: weakest one) and the minimum required water depth h_{min} (limiting fish: biggest one), are presented for some selected fish species hereafter.

Table 3.2 shows some characteristic velocities (U_{burst} = burst velocity, U_{sust} = sustained velocity, U_{crit}, see Chap. 2.6.2) for different fish species derived from the body length L_{fish}. To obtain suitable ecological conditions, migration corridors with flow velocities $U < U_{crit}$ of the target fish have to be guaranteed on the block ramp.

Table 3.2 Swimming velocities U_{burst} = coefficient × L_{fish}, U_{sust} = coefficient × L_{fish}, and U_{crit} (Chap. 2.6.2) for different fish species depending on the body length L_{fish} (DWA 2005 adapted).

Fish species	L_{fish} [m]	U_{burst}/L_{fish} [1/s]	U_{sust}/L_{fish} [1/s]	U_{crit} [m/s]	Source
Atlantic salmon *Salmo salar*	0.15		4.7	0.70	Beamish 1978
	0.20		5.0	1.00	Beamish 1978
	0.47		2.8	1.33	Pavlov 1989
	0.75	5.7		1.93	Denil 1937
	0.85	7.1		2.70	Denil 1937
Blue bream (zope) *Ballerus ballerus*	0.03		10.7	0.32	Pavlov 1989
	0.04		9.8	0.39	Pavlov 1989
	0.05		9.2	0.46	Pavlov 1989
	0.06		8.3	0.50	Pavlov 1989
Brown trout *Salmo trutta fario*	0.13	10.5		0.62	Blaxter and Dickson 1959
	0.20	10.0	4.0	0.80	Geitner and Drewes 1990
	0.34		2.7	0.92	Jens *et al.* 1997
	0.35	10.0	2.9	1.00	Geitner and Drewes 1990
	0.37	8.2		1.37	Blaxter and Dickson 1959
Bullhead *Cottus gobio*	0.02		9.5	0.19	Pavlov 1989
	0.03		9.0	0.27	Pavlov 1989
	0.04		8.5	0.34	Pavlov 1989
Burbot *Lota lota*	0.12		3.0	0.36	Beamish 1978
	0.62		0.7	0.41	Beamish 1978
Common bleak *Alburnus alburnus*	0.02		17.0	0.34	Pavlov 1989
	0.03		17.3	0.52	Pavlov 1989
	0.03		16.3	0.52	Pavlov 1989
Common bream *Abramis brama*	0.22	4.2		0.42	Jens *et al.* 1997
	0.30	4.3	3.3	1.00	Geitner and Drewes 1990
	0.50	4.2	3.0	1.50	Geitner and Drewes 1990
Common carp *Cyprinus carpio*	0.35	6.7		1.06	Beamish 1978
Common roach *Rutilus rutilus*	0.03		12.0	0.36	Pavlov 1989
	0.04		11.0	0.44	Pavlov 1989
	0.15	5.1		0.35	Geitner and Drewes 1990
	0.22	3.8		0.37	Jens *et al.* 1997
	0.30	5.1		0.69	Geitner and Drewes 1990

Fish species	L_{fish} [m]	U_{burst}/ L_{fish} [1/s]	U_{sust}/ L_{fish} [1/s]	U_{crit} [m/s]	Source
Common dace *Leuciscus leuciscus*	0.10	12.0	5.0	0.50	Bainbridge 1958
	0.10	11.0	4.6	0.46	Bainbridge 1960
	0.10	11.5	5.3	0.55	Bainbridge 1958
	0.15	11.0	4.3	0.62	Bainbridge 1958
	0.15	11.8	5.3	0.80	Bainbridge 1958
	0.17	12.0	4.8	0.80	Bainbridge 1958
	0.18	9.3		0.77	Gray 1953
	0.20	11.3	4.0	0.80	Bainbridge 1958
	0.21	11.2	4.2	0.90	Bainbridge 1958
	0.21	11.2	4.5	0.96	Bainbridge 1960
Crucian carp *Carassius carassius*	0.02		13.0	0.26	Pavlov 1989
	0.03		14.0	0.42	Pavlov 1989
	0.04		12.0	0.48	Pavlov 1989
Eel *Anguilla anguilla*	0.07		8.6	0.60	Sörensen 1951
	0.10		7.0	0.70	Sörensen 1951
	0.16		2.9	0.47	Jens *et al.* 1997
	0.40		2.1	0.83	Jens *et al.* 1997
	0.60	1.9		0.51	Blaxter and Dickson 1959
Gudgeon *Gobio gobio*	0.12		4.7	0.55	Stahlberg und Peckmann 1986
Moderlieschen *Leucaspius delineatus*	0.03		12.0	0.36	Pavlov 1989
	0.04		13.8	0.55	Pavlov 1989
	0.05		7.6	0.39	Stahlberg und Peckmann 1986
Northern pike *Esox lucius*	0.12		1.6	0.19	Beamish 1978
	0.62		0.8	0.47	Beamish 1978
Perch *Perca*	0.05		9.3	0.42	Pavlov 1989
	0.05		8.8	0.44	Pavlov 1989
	0.06		8.0	0.48	Pavlov 1989
	0.22	5.5		0.55	Beamish 1978

Fish species	L_{fish} [m]	U_{burst}/ L_{fish} [1/s]	U_{sust}/ L_{fish} [1/s]	U_{crit} [m/s]	Source
Sea lamprey *Petromyzon marinus*	0.15		1.1	0.17	Beamish 1978
	0.39		1.1	0.41	Beamish 1978
Spined loach *Cobitis taenia*	0.04		7.3	0.29	Pavlov 1989
	0.05		6.8	0.34	Pavlov 1989
	0.06		6.2	0.37	Pavlov 1989
	0.07		5.9	0.41	Pavlov 1989
Stickleback *Gasterosteidae*	0.05		7.4	0.36	Stahlberg und Peckmann 1986
Stone loach *Barbatula barbatula*	0.02		9.6	0.22	Pavlov 1989
	0.03		9.7	0.29	Pavlov 1989
	0.04		9.3	0.37	Pavlov 1989
	0.10		5.9	0.61	Stahlberg und Peckmann 1986
Tench *Tinca tinca*	0.02		8.3	0.19	Pavlov 1989
	0.03		8.3	0.25	Pavlov 1989
	0.04		7.8	0.31	Pavlov 1989
	0.05		7.2	0.36	Pavlov 1989
	0.06		6.7	0.40	Pavlov 1989
	0.26	5.4		0.62	Beamish 1978

Often the limiting values for U_{crit} are presented not in dependence of a specific fish species, but of a specific zone (Chap. 2.6.3). An example is given in Table 3.3, where U_{crit} depends on the zone and on the length of the migration corridor.

Table 3.3 Maximum acceptable flow velocities U_{crit} for migration corridors within UBR depending on the river zone (DWA 2010, adapted).

Migration corridor length	Trout zone	Grayling zone	Barbel zone	Bream zone
< 5 m	2.0 m/s	1.9 m/s	1.7 m/s	1.6 m/s
5 m – 10 m	1.8 m/s	1.8 m/s	1.6 m/s	1.5 m/s
> 10 m	1.6 m/s	1.5 m/s	1.4 m/s	1.3 m/s

Table 3.4 Geometric dimensions for UBR depending on $L_{fish,max}$, and $H_{fish,max}$ = maximal body length and height, respectively, with $h_{MC,min}$ = minimum flow depth in the migration corridor, $d_{b,x}$ $d_{b,y}$ = clearance between blocks in flow and in spanwise direction, respectively, (DWA 2009, adapted).*) Alpine rivers; **) other rivers

Fish species	$L_{fish,max}$ [cm]	$H_{fish,max}$ [cm]	$h_{MC,min}$ [cm]	$d_{b,x}$ [cm]	$d_{b,y}$ [cm]
Allis shad *Alosa alosa*	70	21	53	140	93
Atlantic salmon *Salmo salar*	110	22	44	220	147
Asp *Aspius aspius*	80	18	45	160	107
Barbel *Barbus barbus*	90	15	38	180	120
Brown trout *Salmo trutta fario*	*)60	12	24	120	80
	**)70	14	28	140	93
Lake resident brown trout *Salmo trutta lacustris*	90	18	36	180	120
Burbot *Lota lota*	60	10	24	120	80
Common bream *Abramis brama*	75	23	58	150	100
Common nase *Chondrostoma nasus*	50	12	29	100	67
Common roach *Rutilus rutilus*	40	11	28	80	53
Chub *Squalius cephalus*	60	14	35	120	80
European sea sturgeon *Acipenser sturio*	400	60	120	600	400
Grayling *Thymallus thymallus*	50	10	30	100	67
Northern pike *Esox lucius*	120	14	34	240	160
Sea trout *Salmo trutta trutta*	90	18	36	180	120
Twait shad *Alosa fallax*	50	15	38	100	67
Wels catfish *Silurus glanis*	200	40	100	400	267
Zander *Sander lucioperca*	100	15	38	200	133

As mentioned above, additionally to U_{crit}, also the minimum required water depth h_{min} is decisive for a successful upstream migration. Table 3.4 shows the minimum required water depth $h_{MC,min}$, as well as the minimum clearance needed between the blocks in the flow direction $d_{b,x}$ and in the spanwise direction $d_{b,y}$, respectively, for selected fish species. The limiting values are determined by approximating relationships depending on the fish body length $L_{fish,max}$ and height $H_{fish,max}$. DWA (2009) suggests the following relationships for the three parameters

- Minimum h_{MC}: for big sea sturgeon and Salmonidae $h_{MC,min} = 2.0\ H_{fish,max}$
  for grayling $h_{MC,min} = 3.0\ H_{fish,max}$
  for all other species $h_{MC,min} = 2.5\ H_{fish,max}$
- Clearance $d_{b,x}$: for big sea sturgeon $d_{b,x} = 1.5\ L_{fish,max}$
  for all other species $d_{b,x} = 2.0\ L_{fish,max}$
- Clearance $d_{b,y}$: for big sea sturgeon $d_{b,y} = 1.0\ L_{fish,max}$
  for all other species $d_{b,y} = 1.33\ L_{fish,max}$

Similar relationships are also given for ramps of block carpet type as well as for structured ramps of block cluster type (see tables in DWA 2009). Note that this method is not suitable for fish species with high ability to bend their body, like e.g. eels and sea lamprey.

Note further that generally the limiting values U_{crit} and $h_{MC,min}$ suggested in Table 3.2, Table 3.3 and Table 3.4 are representative for a certain fish species or zone, but they do not always account for the variability present within the considered fish species (e.g. juvenile or adult fish). For this reason, a successful migration cannot generally be assured for each single fish even if the limiting values are respected.

3.3.2 Dissipated specific power density

The power density dissipated along a river engineering structure (e.g. fish passage facilities or block ramp) induces turbulence along it and can disturb or impede the upstream migration of fish. The specific power density P_D [W/m^3] for a structured block ramp with a step-pool system is defined as (DWA 2010)

$$P_D = \rho\ g\ Q\ \Delta h/V\ , \tag{3.25}$$

where Δh = drop height between the pools and V = volume of the pool, or for other ramp types without regular structures (like UBR) as (DWA 2010)

$$P_D = \rho \, g \, U \, S \, . \tag{3.26}$$

This specific power density can be interpreted as turbulence of the flow and when it exceeds a certain value, the fish cannot swim through this kind of barrier. The bigger is the specific power density, the higher can be the destabilizing effect on the fish and the energy demand of the fish to swim against the flow. DWA (2010) gives some limiting value for P_D depending on the river zone and on the type of fish passage facility (Table 3.5). These values can be adapted to block ramps, assuming the value for fish passages with pools to be valid for structured block ramps with step-pool systems, and these for fish passages with protruding boulders valid for UBR. In this consideration, the specific power density has to be determined for both limiting discharges of the operation period, namely for Q_{30} and for Q_{330}.

Table 3.5 Maximum acceptable specific power density for structured and unstructured ramps depending on the river zone (adapted from DWA 2010).

River zone	Specific power density P_D	
	Structured ramps with step-pool systems	Unstructured ramps
Trout zone	225 W/m^3	275 W/m^3
Grayling zone	200 W/m^3	250 W/m^3
Barbel zone	150 W/m^3	200 W/m^3
Bream zone	125 W/m^3	175 W/m^3

For structured block ramps with step-pool systems DWA (2010) suggests a maximum specific power density P_D per drop between 225 W/m^3 for trout zone and 125 W/m^3 for bream zone. UBR are more effective in terms of energy dissipation and the maximal P_D can be 1-1.5 times higher than in case of steps-pools systems. For the other block ramp types DWA (2010) gives no indication about P_D.

3.3.3 Block ramps as habitat for macroinvertebrates

Especially ramps of block cluster type, where protruding blocks cover a certain river reach, can provide suitable conditions for oviposition (= deposition of eggs) for certain

stream insects. For instance, adult mayflies genus *Baetis* alight on protruding rocks, crawl under water and deposit an egg mass under the rock (Peckarsky *et al.* 2000). The investigations of Peckarsky *et al.* (2000) show that the distribution of mayfly eggs was determined by the availability of protruding blocks. Therefore, protruding blocks give a better chance to find suitable locations to alight and so to surely reach the oviposition site under water.

As additional example, the oviposition of caddisfly, which deposits egg masses on the undersides of boulders, may be mentioned. Often stream beds in urban areas are dominated by fine substrate (e.g. sand and silt) and large cobbles, whereas protruding blocks or wood are often missing, leading to poor availability of suitable oviposition sites and therefore to a limitation for caddisflies and other aquatic insects (Blakely *et al.* 2006). The investigations of Blakely *et al.* (2006) also showed that by adding large boulders in such streams, more egg masses were observed. The same was found in the experiments of Alp *et al.* (2011), where bricks were put on the river bed to test the dependence of the mass eggs with the presence of protruding objects.

Note that a suitable oviposition site is not the only aspect leading to a successful or unsuccessful river restoration project, but many other parameters (e.g. flow conditions, occurring water depths, composition of the substrate, etc.) play a decisive role. The effect of increased and simplified possibility for the oviposition of certain species can be considered as a positive aspect of UBR with protruding boulders in addition to their stabilizing function, as well as their heterogeneity offering various migration possibilities.

But here again, the effect of the introduction of boulders on the environment is unclear and controversial. Roni *et al.* (2008) wrote in their review on stream habitat rehabilitation techniques that boulder clusters appear to be ineffective for fish rehabilitation. In contrast, Van Zyll de Jong *et al.* (1997) investigated three different types of habitat improvement structures (boulder clusters, V-dams and half-log covers) and their correlation with fish density of Atlantic salmon (*Salmo salar*). The results showed that boulder clusters are the most effective structure increasing fish densities. Furthermore, the addition of boulders created higher habitat complexity, increasing the variability in depth, substrate and current velocity, leading to additional positive effects.

3.3.4 Investigations on the ecological efficiency of block ramps

In the literature, many different studies on the ecological efficiency of certain type of structures can be found. For instance, Studer and Schleiss (2009) investigated the flow velocities occurring on different ramp types (interlocked ramps of block carpet type and structured ramps of block cluster type) for ramp slopes of 6% and 10%. The experimental results were compared with the limiting value for the trout zone, assuming $U_{crit} = 2$ m/s and $h_{MC,min} = 0.2$ m. The results showed that interlocked block ramps can rarely satisfy the criteria for fish migration regarding trouts, due to the high velocities occurring on steep ramps (6% or 10%). On the contrary, structured block ramps are much more efficient; although optimum conditions for migration are only achieved for $S < 6\%$ and for $q < 1.0 - 1.5$ m^2/s. In contrast to these pure hydraulic experiments, Weibel and Peter (2013) investigated the effectiveness of different block ramp types in field tests. Translocation experiments based on mark-recapture and on use of Passive Integrated Transponders (PIT tags, see Chap. 6.2) were conducted in eight different existing ramps (of block carpet type, structured and UBR) in seven different Swiss rivers with slopes ranging from 3.6% to 13.4%. The results showed that upstream passage efficiency depends on fish species, size classes and block ramp type. Additionally, the experiments revealed that a block ramp with $S > 5\%$ is ineffective for the small-sized cyprinid species and is passable only for large-sized brown trout (*Salmo trutta fario*). Furthermore, structured block ramps with their step-pool systems offer advantages by providing resting pools. However, for low discharge conditions they present vertical drops, hindering the migration of species with low leaping potential like bullhead (*Cottus gobio*) if higher than 0.15 m.

The above mentioned two studies are examples of the difficulties existing to obtain general considerations about the ecological functionality of block ramps: either the experiments are conducted by hydraulic engineers, where the hydraulic conditions are measured in detail and analysed, or they are conducted by biologist or ecologist, where the fish behaviour is investigated but limited to the fish species living in the considered water courses. To link two different languages, standards and requirements is not trivial, but it is nowadays becoming more and more important and pursued to improve the success of river rehabilitation projects.

3.4 Summary and identified research gaps

The existing empirical approaches for the determination of the flow resistance and of the stability of the different block ramp types were presented in Chap. 3.2. The decisive ecological criteria for the upstream migration (maximum flow velocity, minimum required water depth, and maximum power density) are introduced in Chap. 3.3 and, where available, the limiting value for the different fish species was listed.

Due to the complex flow processes occurring on block ramps, there is no universal approach describing these flow conditions (DWA 2009). For this reason, each approach describing the flow resistance or the stability of a block ramp has an empirical nature and is, therefore, limited to the application ranges derived from the tested parameters. Particularly for UBR, the existing approach for the flow resistance according to Pagliara and Chiavaccini (2006a) was developed for different conditions: the ramps investigated had protruding boulders placed on a layer of blocks and not of natural sediment material as considered in the present research. The bed material (protruding blocks and base layer of blocks) was fixed during the experiments. Furthermore, it was shown that some existing approaches under- or overestimate the ramp stability, as e.g. described in Janish *et al.* (2007) regarding the approach of Whittaker *et al.* (1988).

The aim of this research is to extend the application range of these existing approaches for the hydraulic design criteria of UBR by investigating ramps with similar conditions as in the prototype, e.g. using natural blocks and testing the ramps without fixing the bed material. Furthermore, the flow is investigated with LDA measurements of high spatial and temporal resolution, to describe the local flow variability and the turbulence as well as to generally characterize the flow with double-averaged quantities. The investigation on the local flow conditions allows assessing the ecological effectiveness of UBR. However, the limited knowledge on the critical values regarding suitable migration conditions for a certain fish limits the comparison between the occurring hydraulics (experimental results) and the fish swimming performance (literature data), but will still provide additional data for this comparison.

To reduce the limited availability of theoretical and field data on the swimming performance depending on the hydraulics (flow velocity and turbulence intensity) and to test the effective migration paths on UBR, Eawag conducted with our collaboration field tests.

4 Experimental setup

4.1 Introduction

The laboratory experiments are divided into three different phases (A, B, and C) and were conducted in two different hydraulic models, flume I and flume II. In the stability model tests (phase A, flume I) the ramp behaviour by increasing load was investigated aiming at determining an optimal parameter combination in terms of ramp stability and design criteria. The general ramp behavoiur tests (phase B, flume I) studied the effect of varying the boundary conditions downstream of the ramp, to examine the general behaviour of UBR in the river system. In the turbulence model tests (phase C, flume II) the local flow velocities and turbulence were measured with 2D LDA, to characterize the hydraulic and ecological conditions of UBR. For all three sets of tests the experimental setup represented a longitudinal slice, taken from the middle part of a river within an UBR (2D tests). Smooth side walls guaranteed a minimum effect of the side boundaries. Compared to typical prototype conditions in the Swiss Alps, the geometrical model scale varies between 20 and 30.

In the past decade VAW investigated different projects related to UBR, by modelling, testing and optimizing UBR. Due to the experience acquired, no preliminary tests were necessary to develop a convenient model setup. In this chapter both flumes with the corresponding instrumentation, the material used as well as the experimental procedure and the test program are described in details.

4.2 Phase A – Stability tests

The main objective of phase A was to test different parameter combinations, to determine the influence of each parameter and the optimal combination in terms of hydraulic stability and design criteria. The erosion process of the ramp was studied by increasing the discharge up to the failure of the ramp, namely either up to a dominant transport of the blocks with an important decrease of the block placement density or up to complete ramp erosion up to total flattening of the ramp ($S \approx 0$). In this way, not only the most stable configuration within the tested range was determined, but also the failure mechanisms could be observed and described. Furthermore, paramount hydraulic parameters

like flow velocity or water depth were measured, to compare them with suitable ecological conditions and to analyse hydraulic conditions.

4.2.1 Model flume I

The phase A tests were conducted in a rectangular tilting flume, 13.50 m long, 0.60 m wide and 0.60 m deep (Figure 4.1). Its sidewalls were made of glass and PVC, to assure smooth conditions and minimize the wall effect on the hydraulic conditions. The intake was 1.5 m long and a flow straightener assured an undisturbed flow and thus uniform water depth in lateral direction. At the downstream flume end the bed level was fixed with a PVC plate, so that erosion on the ramp led to a rotation of the bed around this point (Chap. 4.2.4). Hence, the lower boundary condition was known and constant, avoiding an additional parameter variation. A uniform flow depth at the outflow section was almost achieved with an adjustable needle weir to regulate it. The transported sediment was caught in a submerged (with constant water level) filtering basket at the outflow section.

4.2.2 Instrumentation

The flume was equipped with two pumps, delivering a maximum discharge of $Q_{max,1} = 20$ l/s and $Q_{max,2} = 100$ l/s, respectively, which was measured by a magnetic-inductive flow meter (MID, Figure 4.1). A sediment feeder was placed above the flume intake, delivering the designed sediment supply more than 3 meters upstream of the ramp head. Its minimum delivering rate was 25 g/s and its maximum 1200 g/s. At the end of the flume, three weighing cells were installed at the filtering basket to weigh the transported sediment.

The water level was continuously measured with four pairs of ultrasonic sensors positioned respectively at 1 m, 4 m and 7 m downstream of the ramp head, as well as just before the needle weir above the fixed PVC plate. The bulk flow velocity was measured with the salt dilution method (Lee 1998, Weichert 2006). Salty water was injected instantaneously over the entire flume width, approximately 1 m upstream of the ramp head. The water conductivity was measured at three cross-sections with three pairs of electrodes consisting of metal bands attached to the sidewalls. The bulk flow velocity was determined by calculating the time-lag between two summation curves of two different cross-sections (Chap. 4.2.7).

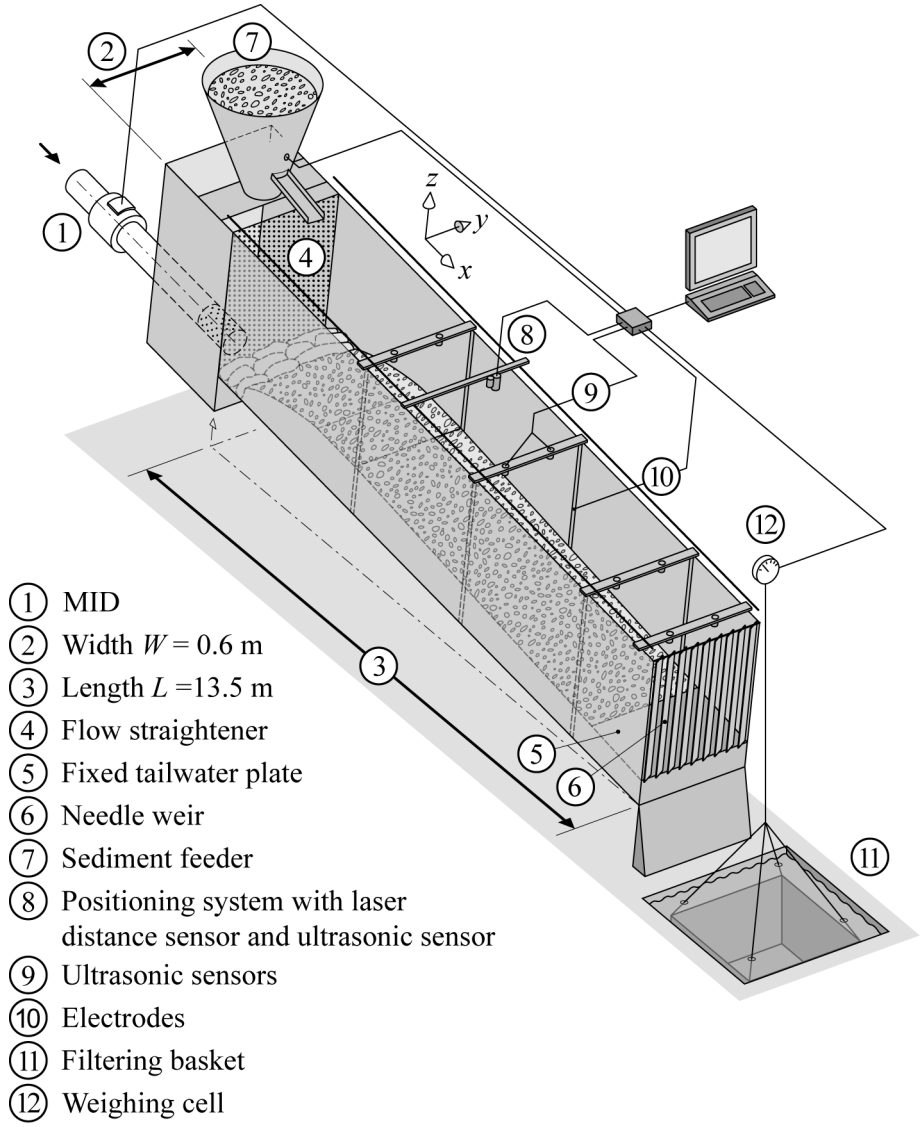

Figure 4.1 Flume and instrumentation used for the stability tests (phase A) as well as slightly modified for the general ramp behaviour tests (phase B, Chap. 4.3)

In order to determine the local flow conditions, a point gauge was used to measure the flow depth in some selected points or cross-sections, as well as to validate the measurements of the ultrasonic sensors; likewise, a mini-propeller was used to measure the local flow velocity. The bed topography was scanned with a laser distance sensor, installed together with an additional ultrasonic sensor on a positioning system, which was automatically moved and controlled by a computer in the x-direction (flow direction) and in the y-direction (spanwise direction).

The experiments were continuously observed with a fixed camera placed below the laboratory ceiling. During each run, photos were taken almost every 20 minutes so that each boulder movement and macro bed modifications were documented.

4.2.3 Block and bed material

Requena (2008) defined two sediment mixtures typical of Swiss rivers. In her study nine different Swiss river reaches were selected and subdivided into two different groups, depending on the average bed slope S: flat reaches with slope $0.2\% < S < 0.8\%$ (Emme, Moesa und Thur River) and steep reaches with $1\% < S < 1.5\%$ (Rhone, Landquart, Kleine Emme, Engelberger Aa, Muota and Tresa River). Each group is represented by an "averaged" sediment mixture, derived from the grain-size distribution curves of the considered reaches and downscaled with a geometrical scale factor between 20 and 75. From these two resulting sediment materials, two different sediment mixtures were derived (fine mixture FM and coarse mixture CM) and reproduced for the present research. The grain-size distribution curves of FM and CM are illustrated in Figure 4.2 and their characteristic parameters are listed in Table 4.1. Due to their high value of the standard deviation of the grain-size distribution $\sigma = (d_{84}/d_{16})^{0.5} = 2.7$ and 3.3, respectively, they are considered as wide distributions and according to Little and Mayer (1972) as potential armouring bed materials. The mixtures were prepared with natural non-cohesive sand or gravel material (Figure 4.3), with a density of $\rho_s \approx 2650$ kg/m^3 and with a minimum grain size of $d_{min} = 0.25$ mm, to avoid cohesive effects (Chap. 4.5).

Additionally, two uniform materials (Figure 4.3) were used to investigate the effect of the standard deviation σ of the bed material on the ramp stability. Due to the armouring characteristics of the two sediment mixtures FM and CM, the sediment entrainment is dependent on the armoured layer and, therefore, on the d_{90} of the bed material. For this reason, the uniform materials used are directly related to the d_{90} of the corresponding mixtures in order to reproduce the same stability of the armoured layer as well as the same sediment entrainment threshold. Thus a ratio between d_{90} of the mixtures and d_m of the corresponding uniform material $d_{90,M}/d_{m,UM} \approx 1$ was pursued. The characteristic parameters of the two investigated uniform materials are also shown in Table 4.1. The characteristic grain sizes were determined with granulometric analysis made with square-hole sieves for FM, UM-FM and CM, and with line sampling analysis for UM-CM. Note that the characteristic grain sizes determined with line sampling analysis were converted into equivalent grain sizes determined with granulometric analysis wit square-hole sieves, in order to compare the data.

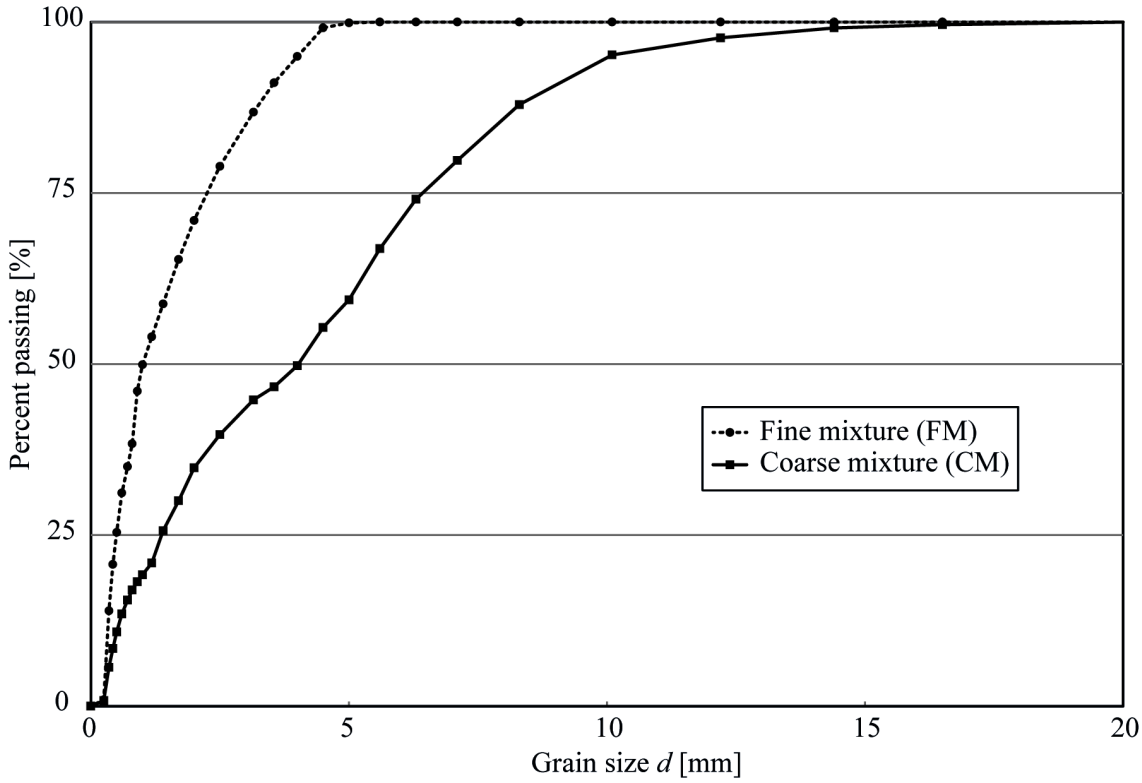

Figure 4.2 Grain-size distribution curves of the fine and the coarse mixture used for the present research. The grain size d refers to model dimensions.

Table 4.1 Characteristic parameters of the sediment materials used. *) determined with line sampling analysis

Sediment material	d_m [mm]	d_{10} [mm]	d_{16} [mm]	d_{60} [mm]	d_{84} [mm]	d_{90} [mm]	σ [-]	$d_{90,M}/d_{m,UM}$ [-]
Fine mixture (FM)	1.5	0.3	0.4	1.5	2.9	3.5	2.7	1.13
Uniform fine material (UM – FM)	3.1	2.6	2.7	3.2	3.3	3.5	1.1	
Coarse mixture (CM)	4.3	0.5	0.7	5.0	7.7	8.8	3.3	1.04
Uniform coarse material (UM – CM) *)	8.5	6.7	6.9	8.4	9.5	9.8	1.2	

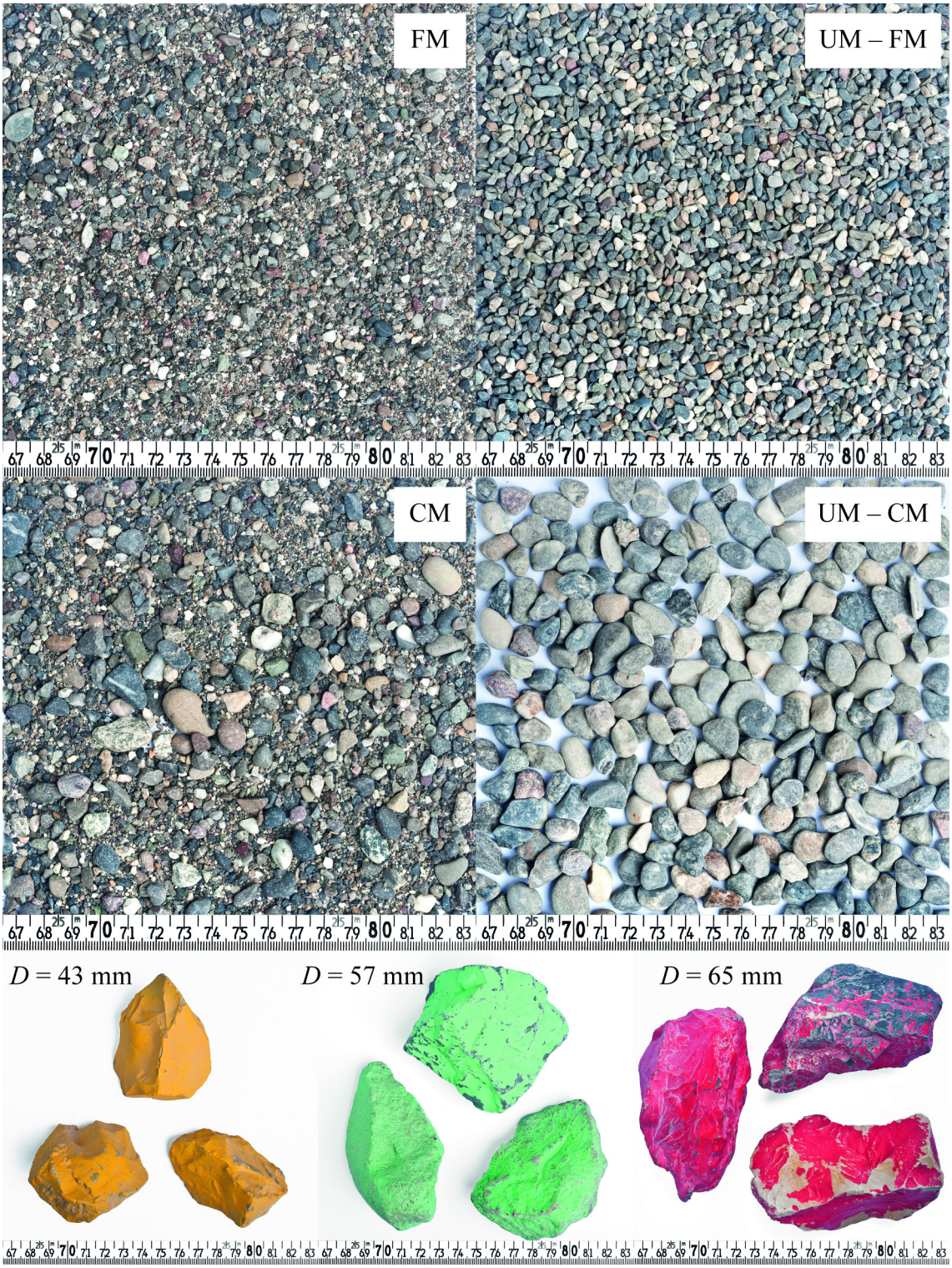

Figure 4.3 Material used for the physical experiments. Top: fine mixture (FM) and corresponding uniform fine material (UM – FM); middle: coarse mixture (CM) and corresponding uniform coarse material (UM – CM); bottom: three different blocks with corresponding equivalent spherical block diameter D.

The characteristic grain size of the blocks corresponds to the equivalent spherical block diameter D, defined as the diameter of a sphere of equivalent volume as the considered block. The blocks were angular natural limestones (Figure 4.3), which were ideally approximated as ellipsoid and characterized through the three semi-axes (a- and b-axis: minor and major semi-axis of the plane ellipse, respectively; c-axis: semi-axis in the vertical direction), where conventionally the longest axis (b-axis) was placed parallel to the bed. For each block type approximately 70 – 100 samples were measured (the three semi-axes), their mass M weighted and their volume V determined with the water displacement method. In this way, the average density of 2640 to 2670 kg/m^3 was determined and the equivalent spherical block diameter D was derived from the average volume V (Table 4.2).

A UBR is also characterized by the block placement density λ, which is defined as the ration between the ramp area covered by blocks and the entire ramp area (see Eq. 3.5). Two different block placement densities were investigated, namely $\lambda = 0.15$ and 0.25.

Table 4.2 Characteristic parameters of the blocks used. The mean values are averaged from 70 – 100 samples; σ_D = standard deviation of the equivalent spherical block diameter D.

D [mm]	σ_D [mm]	a-axis [mm]	b-axis [mm]	c-axis [mm]	M [kg]	V [m^3]
43	2.0	52	68	32	0.115	$0.431 \cdot 10^{-4}$
57	1.4	61	86	44	0.246	$0.919 \cdot 10^{-4}$
65	3.1	67	101	48	0.376	$1.420 \cdot 10^{-4}$

4.2.4 Permeability coefficient

The permeability coefficient k_f of the sediment material used was theoretically calculated according to the equations of Beyer (1964) and Hazen (1892), respectively, as well as measured with two permeability tests, one with the uniform coarse material UM – CM and another with the coarse mixture CM. The goal of the permeability tests and of the determination of the permeability coefficient k_f was to estimate the discharge distribution between surface flow and the flow within the bed material. UM – CM represents the material with the highest porosity. Therefore, UM – CM corresponds to the most

critical case in terms of high groundwater flow and for that reason its permeability was experimentally determined. The block ramp was built in the same way as in phase A (Chap. 4.2.5), apart from the placement of the blocks. The ramp without blocks had an initial slope of S_R = 5% and a length of 9 m, whereas the buffer area was 1 m long and had a slope of S = 1% like the flume (Figure 4.4).

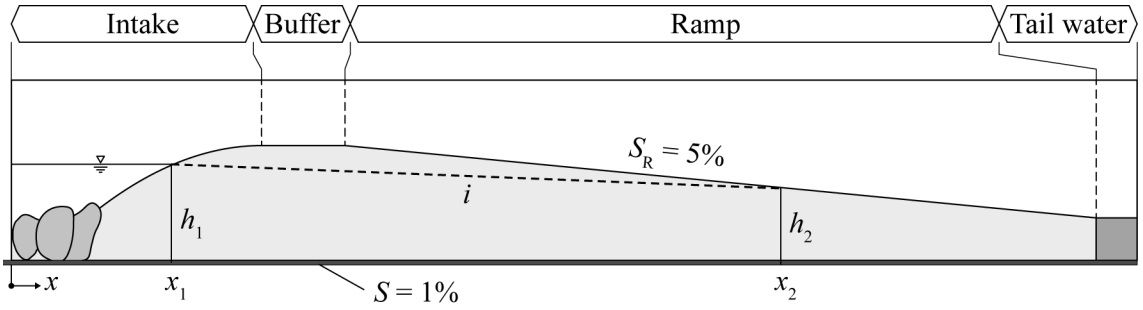

Figure 4.4 Sketch of the experiment to determine the permeability coefficient k_f of the sediment material with i = hydraulic gradient.

At the beginning of the experiment the intake basin was filled up to a level below the top level of the ramp with a very low discharge. The ground water level (dashed line in Figure 4.4) that develops in the sediment body of the ramp was easy to detect by eye. Then the discharge was varied up to a certain Q for which the water level at the intake section remained constant. At that flow condition the ground water level reached the river bed at the cross-section located at x_2 (Figure 4.4), where water above the sediment body was visible. The point at x_2 was defined by eye and was considered as critical cross-section with critical area A_{CS}. The ground water flow capacity of the bed material reached its limit at that section; therefore, the critical section was used to determine the permeability of the material with the following steps:

a) Hydraulic gradient i: $i = (h_1 - h_2)/ (x_2 - x_1)+S$

b) Area of the critical cross-section A_{CS}: $A_{CS} = h_2 \cdot W$

where W = flume width = 0.6 m

c) Ground water flow velocity u_f: $u_f = Q / A_{CS}$

where Q = 1.3 l/s

d) Permeability coefficient k_f: $k_f = u_f / i$

Since the definition of the points x_1 and x_2 was made by eye, a sensitivity analysis was carried out to quantify the influence of the possible personal error (see below)

Calculation of the permeability coefficient k_f

To estimate the permeability of the tested sediment materials, two empirical equations were applied, namely the Hazen equation (1892) and the Beyer equation (1964). Both equations depend on the characteristic grain diameter d_{10} and contain empirical coefficients. The two equations are defined as

- Empirical Hazen equation (1892) $k_f = 0.0166 \cdot d_{10}^2$

  where k_f = permeability coefficient [m/s] and d_{10} = characteristic grain diameter [mm]; valid for sand.

- Empirical Beyer equation (1964) $k_f = C \cdot d_{10}^2$

  where C = empirical coefficient (see Figure 4.5, with $U_{coeff} = d_{60}/d_{10}$ = uniformity coefficient, assuming the curve "mittl. natürl. Lagerung" = mean natural packing); valid for both sand and gravel and 0.06 mm < d_{10} < 0.6 mm.

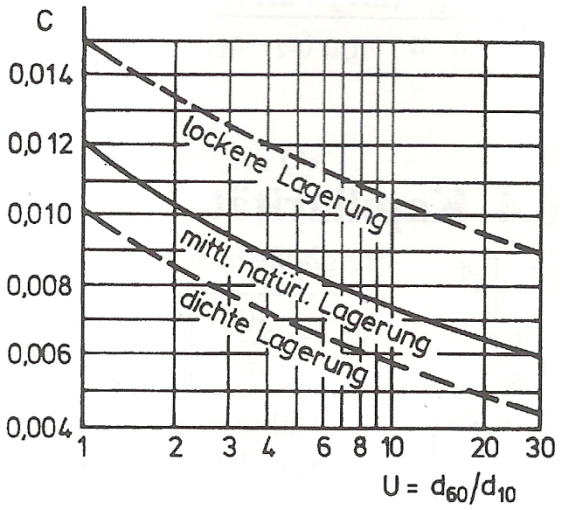

Figure 4.5 Diagram for the determination of the coefficient C of the Beyer equation taken from Schneider (2004), where *"lockere Lagerung"* = loose packing, *"mittl. natürl. Lagerung"* = mean natural packing, and *"dichte Lagerung"* = compact packing.

The values of the permeability coefficient determined with the Hazen equation are much larger than those determined with the Beyer equation (Table 4.3). The application

range of the two equations is violated in both cases of the two uniform materials, because their d_{10} are larger than the typical grain size of sand. In order to understand which equation is more suitable for the considered sediment materials, we compare these results with the measured permeability in the following.

Table 4.3 Calculated and measured permeability of the sediment materials (Table 4.1). Values in italic: boundary conditions of equation used are not satisfied.

Sediment material	U_{coeff} [-]	C [-]	k_f Hazen [m/s]	k_f Hazen [cm/s]	k_f Beyer [m/s]	k_f Beyer [cm/s]	k_f measured [cm/s]
FM	5.0	0.0085	0.0015	0.15	0.0008	0.08	Experimentally not determined
UM – FM	*1.23*	*0.0118*	*0.1122*	*11.22*	*0.0798*	*7.98*	
CM	10	0.0075	0.0042	0.42	0.0019	0.19	0.18
UM – CM	*1.25*	*0.0117*	*0.7452*	*74.52*	*0.5252*	*52.52*	41.9

Results of the permeability coefficient tests

The permeability tests were conducted for the uniform coarse material UM – CM and for the coarse mixture CM (why not for UM – FM and FM: see below). The steps presented in Chap. 4.2.4 are applied below for the permeability test for UM – CM (see also first line in Table 4.4):

a) Hydraulic gradient i: $\Delta h = h_1 - h_2 = 33.2 - 26.7 = 6.5$ cm

$L = x_2 - x_1 = 8.90 - 1.95 = 6.95$ m

$i = \Delta h / L + S_{Flume} = 0.01935$

b) Area of critical cross-section A_{CS}: $A_{CS} = h_2 \cdot W_R = (26.7/100)$ m $\cdot$ 0.6 m =

$= 0.1602$ m^2

c) Ground water flow velocity u_f: $u_f = Q/A_{CS} =$

$= (1.3/1000)$ m^3/s / 0.1602 m^2 =

$= 0.00812$ m/s $= 0.812$ cm/s

d) Permeability coefficient k_f: $k_f = u_f / i = 0.812$ cm/s / 0.01935 =

$= 41.9$ cm/s

Following the same procedure, the permeability coefficient for the coarse mixture CM was determined and resulted in $k_f = 0.184$ cm/s. Comparing the tests results with the values determined with the two empirical equations (Table 4.3), the Beyer equation (1964) gave a better estimation of k_f. For UM – CM, where the application range was violated, the Beyer equation overestimated the value of k_f. In contrast, for CM the Beyer equation resulted in nearly the same value of k_f.

As mentioned above, UM – CM represents the material with the highest porosity, corresponding to the most critical case in terms of high groundwater flow. Assuming $k_f = 41.9$ cm/s and a cross-section in the middle of the ramp body, the groundwater flow Q_{GW} can be estimated to 20% of the total discharge Q for $Q = 8$ l/s, to 10% for $Q = 16$ l/s, and to 6% for $Q = 24$ l/s. For higher discharges, Q_{GW} is therefore negligible. Applying the same considerations for CM with $k_f = 0.184$ cm/s, the groundwater flow Q_{GW} corresponds in the worst case to less than 0.4% of the total discharge Q. For this reason and due to the lower permeability coefficients for FM and UM – FM, the groundwater flow Q_{GW} was considered negligible for all experiments, aside from experiment A15 (Chap. 4.2.6) where UM – CM was used.

Sensitivity analysis

To estimate the uncertainties – especially due to the definition of the ground water level and so of the critical cross-section from visual observation – a sensitivity analysis is performed. Table 4.4 shows the results for the uniform coarse material UM – CM. The most sensitive terms are the two ground water levels h_1 und h_2, as they strongly influence the hydraulic gradient i and so k_f. The permeability coefficient varies up to 4% for an inaccuracy in the measurement of h_1 und h_2 bigger than 0.5 cm. Whereas the measurement of h_1 is quite distinct, the determination of h_2 is more uncertain. In case of an error between 0.5 cm and 1 cm as to h_2, the permeability coefficient changes with a difference between - 3% and + 4%. On the contrary, an inaccuracy in the position of x_1 and x_2 up to 10 cm, which is quite a conservative assumption, leads to a k_f difference of only ± 0.7%. It is assumed that the measurement of h_1 and x_1 was performed with an accuracy of ± 0.1 cm and of ± 5 cm, respectively, and that the measurement of h_2 and x_2 have an accuracy of ± 1.0 cm and of ± 10.0 cm respectively. The maximum error is therefore assumed to be less than ± 6%. This holds for the permeability tests with UM-CM material with high porosity. The error for the other less permeable materials would be higher. However, in view of the above-mentioned discussion, this error is irrelevant.

Table 4.4 Sensitivity analysis for measured parameters of the permeability tests for UM – CM. First column: varied parameter in the analysis. Only one parameter was varied, each line corresponds to a different parameter combination. Δk_f = difference between k_f resulting from the measurement and k_f resulting from a varied parameter in the sensitivity analysis. Underlined value: measured k_f. Grey blocks: assumed possible errors and corresponding Δk_f. VP = varied parameter, M = measured parameters.

VP	h_1 [cm]	h_2 [cm]	x_1 [m]	x_2 [m]	L [m]	i [-]	A_{CS} [m^2]	v_f [cm/s]	k_f [cm/s]	Δk_f [cm/s]	Δk_f [%]
M	33.2	26.7	1.95	8.90	6.95	0.01935	0.1602	0.812	41.93		
h_1	32.2	26.7	1.95	8.90	6.95	0.01791	0.1602	0.812	45.30	3.37	8.0
	32.7	26.7	1.95	8.90	6.95	0.01863	0.1602	0.812	43.55	1.62	3.9
	33.1	26.7	1.95	8.90	6.95	0.01921	0.1602	0.812	42.25	0.31	0.7
	34.2	26.7	1.95	8.90	6.95	0.02079	0.1602	0.812	39.03	-2.90	-6.9
	33.7	26.7	1.95	8.90	6.95	0.02007	0.1602	0.812	40.43	-1.50	-3.6
	33.3	26.7	1.95	8.90	6.95	0.01950	0.1602	0.812	41.62	-0.31	-0.7
h_2	33.2	25.7	1.95	8.90	6.95	0.02079	0.1542	0.843	40.55	-1.38	-3.3
	33.2	26.2	1.95	8.90	6.95	0.02007	0.1572	0.827	41.20	-0.73	-1.7
	33.2	26.6	1.95	8.90	6.95	0.01950	0.1596	0.815	41.78	-0.15	-0.4
	33.2	27.7	1.95	8.90	6.95	0.01791	0.1662	0.782	43.66	1.73	4.1
	33..2	27.2	1.95	8.90	6.95	0.01863	0.1632	0.797	42.75	0.82	2.0
	33.2	26.8	1.95	8.90	6.95	0.01921	0.1608	0.809	42.09	0.16	0.4
x_1	33.2	26.7	1.85	8.90	7.05	0.01922	0.1602	0.812	42.22	0.29	0.7
	33.2	26.7	1.90	8.90	7.00	0.01929	0.1602	0.812	42.08	0.15	0.3
	33.2	26.7	1.94	8.90	6.96	0.01934	0.1602	0.812	41.96	0.03	0.1
	33.2	26.7	2.05	8.90	6.85	0.01949	0.1602	0.812	41.64	-0.29	-0.7
	33..2	26.7	2.00	8.90	6.90	0.01942	0.1602	0.812	41.79	-0.15	-0.3
	33.2	26.7	1.96	8.90	6.94	0.01937	0.1602	0.812	41.90	-0.03	-0.1
x_2	33.2	26.7	1.95	8.80	6.85	0.01949	0.1602	0.812	41.64	-0.29	-0.7
	33.2	26.7	1.95	8.85	6.90	0.01942	0.1602	0.812	41.79	-0.15	-0.3
	33.2	26.7	1.95	8.89	6.94	0.01937	0.1602	0.812	41.90	-0.03	-0.1
	33.2	26.7	1.95	9.00	7.05	0.01922	0.1602	0.812	42.22	0.29	0.7
	33..2	26.7	1.95	8.95	7.00	0.01929	0.1602	0.812	42.08	0.15	0.3
	33.2	26.7	1.95	8.91	6.96	0.01934	0.1602	0.812	41.96	0.03	0.1

4.2.5 Experimental procedure

The experimental procedure described below was applied to each experiment of phase A. To every experiment (A1, A2, A3… see Table 4.5) corresponds a certain parameter combination and each experiment is subdivided into 6 – 12 single runs. Each run represents a certain specific discharge q ranging from 3.3 to 140 l/(sm), which is kept constant during each run (steady condition). The block ramp was built over the entire flume width and over a length of $L_R = 9$ m, except for one experiment (A4, see Table 4.5) where $L_R = 2.4$ m. The ramp was built with movable bed material with initial slope $S_0 = 5\%$, and then covered with blocks of a certain equivalent spherical diameter D and a certain block placement density λ (Figure 4.6). For each combination D and λ a 1 m long pattern was used, to reproduce always the same random configuration by same D and λ. Afterwards some unconsolidated material (the same used for bed material) was dispersed over the blocks so that the final block protrusion P was $P \approx 0.5\ D$.

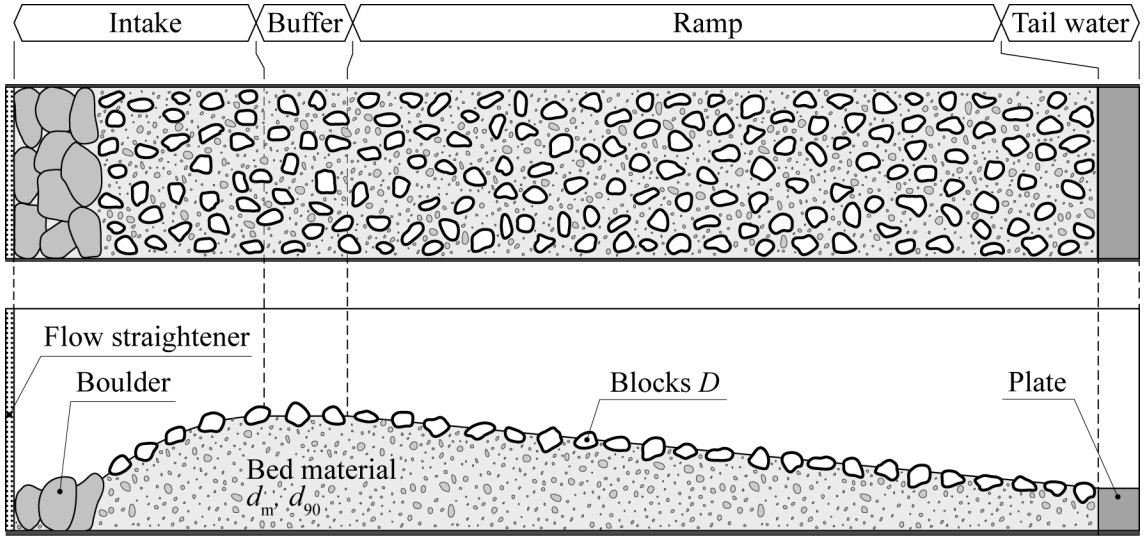

Figure 4.6 Plan view (top) and side view (bottom) of UBR built for stability tests with ca. 2 m long intake section, 1 m long buffer area, 9 m long ramp, and fixed tail water plate at the flume end.

Upstream of the ramp, a buffer area was arranged with a length of 1 m, a slope of 1% (= flume slope) and covered with the same blocks and the same block placement density as along the ramp (Figure 4.6). The basic idea of the buffer area was to provide a stabilization of the upper part of the ramp, even if the ramp slopes became smaller due to erosion. Through the slope decrease, the ramp length increases and thanks to the

buffer area, the upstream section of the ramp disposes of blocks and of their stabilizing function. Therefore, an abrupt failure of the ramp due to increased erosion at the ramp head can be avoided or at least delayed to a higher discharge. The very upstream part (intake, Figure 4.6) was approximately 2 m long and at the bottom of it some boulders with $D \approx 250$ mm were placed on the flume bed. This configuration of the inlet part assured undisturbed flow condition at the beginning of the ramp and guaranteed smooth flow transition between intake and ramp.

Table 4.5 Investigated parameter combinations of each experiment of phase A. The initial ramp slope S_0 was set to 5% for all the experiments, as well as the ramp length L_R to 9 m, except for A4 (*) where L_R = 2.4 m (model dimensions).

Experiment	D	Sediment	d_{90}	D/d_{90}	λ	q	Number of runs	Q_s
	[mm]	[-]	[mm]	[-]	[-]	[l/(sm)]		[g/s]
A1	43	FM	3.5	12.3	0.15	3.3 – 60	6	0
A1rep	43	FM	3.5	12.3	0.15	3.3 – 60	6	0
A2	-	FM	3.5	-	0	3.3 – 60	6	0
A3	43	UM-FM	3.5	12.3	0.15	3.3 – 60	6	0
A4*	43	FM	3.5	12.3	0.15	3.3 – 60	6	0
A5	43	FM	3.5	12.3	0.25	3.3 – 60	6	0
A6	65	FM	3.5	18.6	0.15	3.3 – 40	5	0
A7	65	FM	3.5	18.6	0.25	3.3 – 60	6	0
A8	43	CM	8.8	4.9	0.15	3.3 – 27	4	0
A9	43	CM	8.8	4.9	0.25	3.3 – 40	5	0
A10	65	CM	8.8	7.4	0.15	3.3 – 140	12	0
A11	65	CM	8.8	7.4	0.15	3.3 – 140	9	10 – 363
A12	57	CM	8.8	6.5	0.15	3.3 – 140	11	0
A13	65	CM	8.8	7.4	0.25	3.3 – 140	11	0
A14	65	CM	8.8	7.4	0.25	3.3 – 140	8	10 – 363
A15	65	UM-CM	9.8	6.6	0.15	3.3 – 140	10	0

Before the start of the experiment the ramp topography was scanned with the laser distance meter with the measuring grids 10×2 cm^2 and 1×1 cm^2 (Chap. 4.2.7). The first run with the lowest specific discharge (generally q = 3.3 or 6.7 l/(sm)) was then started. The discharge was kept constant during each run until an equilibrium ramp slope was

achieved (see definition of equilibrium below). The bulk velocity with the salt dilution method, the local velocities with the mini-propeller and the local water levels with the point gauge were measured after equilibrium conditions had been reached. Afterwards the run was stopped by decreasing the discharge slowly in order to avoid alteration of the resulting bed topography. Then the bed topography was scanned again with the same spatial resolution as before. The next run started with a higher constant specific discharge, which was reached by increasing very slowly the discharge to avoid alteration of the bed topography (see above). The discharge was increased stepwise until the ramp was either almost completely horizontal (bed material completely eroded) or until most of the blocks had been transported downstream of it to the sediment basket, leading to a significant reduction of the block placement density λ. One of these two conditions corresponded to the end of the experiment.

Definition of equilibrium

The definition of the equilibrium condition plays a central role in the stability tests. The basic consideration is that the ramp reaches its equilibrium condition when the sediment input and the sediment output are equivalent. For *experiments without sediment supply* this condition is ideally given when no more sediment is eroded and then transported along the ramp and, therefore, when the weight of the filtering basket at the flume end remains constant. In practice it could take weeks until the equilibrium condition is reached and for this reason, a reasonable compromise between realistic experiment duration and suitable equilibrium conditions is found. During the first experiments the stop criterion for the case without sediment supply was investigated by letting the runs continue after a first assumed equilibrium criterion as well as by analysing the resulting ramp slope and weight increase of the filtering basket after each additional time step. The following stop criterion was defined: the ramp reached its equilibrium condition when the average increase of the weighed sediment was less than 1.26 kg per hour (on average 0.35 g/s) for at least consecutive three hours, corresponding to a slope change of less than 0.01% every ten hours.

For the *experiments with sediment supply* another stop criterion was applied. The filtering basket was filled with sediments within a few hours, precluding the possibility to have an uninterrupted measurement and a suitable statistic over the run duration. For this reason, a second stop criterion was defined. The equilibrium condition was given when the mean water levels measured with the ultrasonic sensors at all four cross-

sections (see Figure 4.1) did not vary more than 1% compared to the mean values from the three last consecutive hours.

The time needed to reach equilibrium conditions t_{eq} varied approximately between 3 and 100 hours. Table 4.6 shows the results from four different experiments. The total experimental time cannot be compared directly, because not all experiments had the same number of runs with constant q. The experiments with uniform material (see e.g. A15, Table 4.6) needed longer to reach equilibrium conditions compared to these with sediment mixtures. The run with high specific discharges $q > 80$ l/(sm) for experiments with sediment supply (see e.g. A11, Table 4.6) were particularly short compared to those without sediment supply. Presumably, the sediment rate supplied was sufficiently high to avoid additional ramp erosion, fastly leading to the equilibrium condition. Note that the equilibrium criteria were different for experiments with and without sediment supply, as described above.

Table 4.6 Time needed to reach equilibrium t_{eq} for four different experiments: A1, A10, A15 = without sediment supply, A11 = with sediment supply, A15 = with uniform material (see Table 4.5 for details of the parameter combinations). The values refer to model dimensions.

	A1	A10	A11	A15
q [l/(sm)]	t_{eq} [hours]	t_{eq} [hours]	t_{eq} [hours]	t_{eq} [hours]
3.3	7	-	-	-
6.7	23	5	5	-
13.3	16	9	10	3
26.7	13	27	37	3
40.0	14	30	22	34
50.0	-	51	-	47
60.0	8	19	22	46
70.0	-	61	-	19
80.0	-	30	29	48
100.0	-	8	14	75
120.0	-	42	11	65
140.0	-	45	7	95
Tot.	81	327	157	435

4.2.6 Test program

Table 4.5 gives an overview of all conducted experiments of phase A with the corresponding most important parameters. The experiments are chronologically listed and named: to every new experiment corresponds the variation of just one parameter. All experiments were carried out under steady conditions (Chap. 4.2.4) and without sediment supply, except for A11 and A14. For these two experiments, the sediment supply corresponded to the transport capacity upstream of the ramp calculated with the formula of Meyer-Peter and Müller (1948) with an assumed bed slope of 1%, representing a typical mean slope for an alpine Swiss river. The sediment supply was not varied within each single run and corresponded always to the 100% theoretical transport capacity according to Meyer-Peter and Müller (1948). The goal was to determine the general effect of transported sediment on the ramp stability and not to study in detail the different sediment supply rates.

The fundamental idea was to investigate the entire erosion process of the ramp for different parameter combinations. For this reason, the initial ramp slope S_0 was set on purpose to be quite steep for UBR, namely $S_0 = 5\%$ for all experiments. Previous tests at VAW showed that the effect of S_0 on the final equilibrium slope S_e is negligible. In the following, each experiment is shortly described by highlighting the parameter varied:

- A1: First and reference experiment, where the ratio between blocks and sediment material was chosen at $D/d_{90} = 12.3$, so that according to Raudkivi and Ettema (1982) neither dominant transport of the blocks over the finer material, nor block embedding in the finer material should occur (Chap. 2.3.4).
- A1rep: Exactly the same ramp as A1 (same parameter combination and same runs), to test the repeatability of the model tests.
- A2: Ramp without blocks consisting of the same sediment material as A1, to quantify the stabilizing effect of the blocks.
- A3: Ramp with uniform material (UM-FM) corresponding to the mixture used in A1 (FM) with same D and λ as A1, to quantify the effect of grain size distribution
- A4: Shorter ramp with $L_R = 2.4$ m instead of $L_R = 9$ m and same D and λ as A1, to test the effect of L_R, particularly on the developing bed morphology by low specific discharges.

- A5: Effect of block placement density for $D/d_{90} = 12.3$, by increasing the value from $\lambda = 0.15$ to $\lambda = 0.25$.
- A6: Effect of different D/d_{90}, by increasing the ratio up to $D/d_{90} = 18.6$, where theoretically the block embedding in the finer material is the dominant process (Raudkivi and Ettema, 1982, Chap. 2.3.4).
- A7: Effect of block placement density for $D/d_{90} = 18.6$, same parameter combination like A6 but with $\lambda = 0.25$.
- A8: Effect of ratio D/d_{90}, by decreasing the ratio down to $D/d_{90} = 4.9$, where theoretically the block transport over the fine material is the dominant process (Raudkivi and Ettema, 1982, Chap. 2.3.4).
- A9: Effect of block placement density for $D/d_{90} = 4.9$, same parameter combination like A8 but with $\lambda = 0.25$.
- A10: Search of an optimal ratio D/d_{90} in terms of stability between the two possible dominant processes, by testing the ratio $D/d_{90} = 7.4$ with $\lambda = 0.15$.
- A11: Effect of the sediment supply by otherwise same parameter combination like A10.
- A12: Search of a better ratio D/d_{90} in terms of stability, by testing the ratio $D/d_{90} = 6.5$ with $\lambda = 0.15$.
- A13: Effect of block placement density for $D/d_{90} = 7.4$, same parameter combination like A10 but with $\lambda = 0.25$.
- A14: Effect of sediment supply by otherwise same parameter combination like A13.
- A15: Effect of uniform material UM-CM by same D and λ like in A10.

Often the investigated parameter combination was directly derived from the results of the previous experiments. For this reason, the detailed motivation of the selection of the parameter combinations is described in the results section (Chap. 5.2).

4.2.7 Data analysis

Bed levels – Ramp slope S and mean block protrusion P

Bed level measurements were performed with a laser distance sensor (Chap. 4.2.2) with two different spatial resolutions (Figure 4.7): (1) measuring grid 10×2 cm^2 = a cross-section measured every 10 cm in the *x*-direction and a measurement point every 2 cm in the *y*-direction over the entire ramp length; (2) measuring grid 1×1 cm^2 = a measurement point every 1 cm in *x*- and in *y*-direction along a section of 1 m in the middle of the ramp. The bed level measurements were carried out after each run in phase A as well as in phase B.

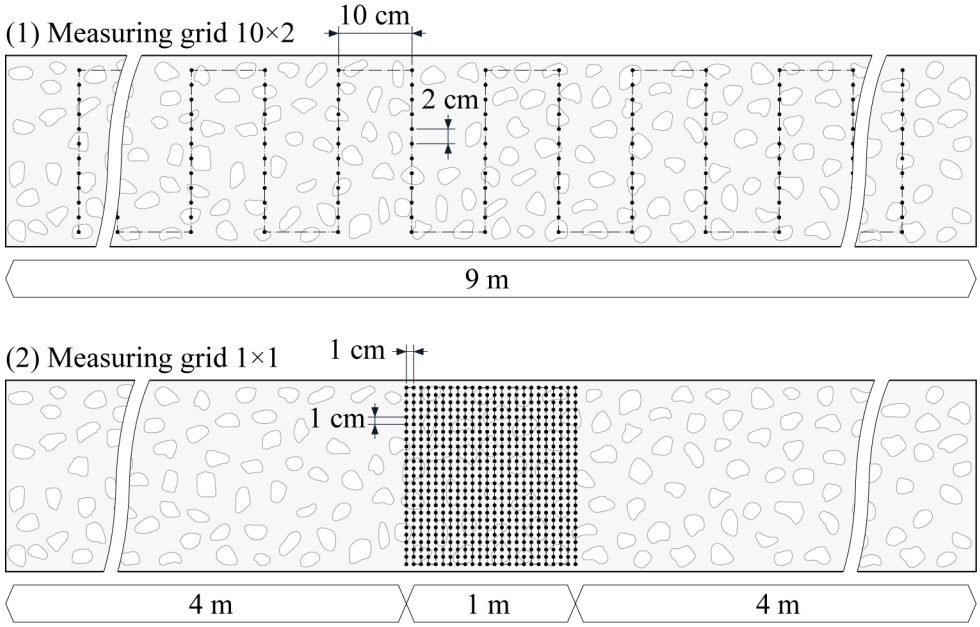

Figure 4.7 Measuring grids used for the topography measurements with the laser distance sensor (1) measuring grid 10×2 cm^2; (2) measuring grid 1×1 cm^2.

The ramp slope *S* and the equilibrium ramp slope S_e (Chap. 4.2.5), respectively, were determined by averaging the bed levels of each cross-section measured with spatial resolution 10×2 and then by fitting the mean bed levels over the ramp length. Therefore, the ramp areas covered by blocks as well as the areas without blocks were considered together as bed topography, leading to an average ramp slope *S*.

The block protrusion *P* (Chap. 5.2.7) was derived from the bed level measurements with spatial resolution 1×1. The blocks within the measured area were detected,

so that the corresponding block crest heights could be analysed separately for each single block. The block protrusion P was defined as the difference between the block crest and the mean bed level of sediment. The average of the block protrusion of each block that was detected in one measurement resulted in the mean block protrusion P.

Salt dilution method (Chap. 4.2.2) – Bulk flow velocity u_b

The bulk flow velocity (subscript b) u_b was determined by analysing the water conductivity data (Figure 4.8 top) with cumulative time series of three repeated measurements (Figure 4.8 bottom). The time intervals between two cumulative curves at 30% ($\Delta t_{30\%,1\text{-}2}$ and $\Delta t_{30\%,2\text{-}3}$), at 50% ($\Delta t_{50\%,1\text{-}2}$ and $\Delta t_{50\%,2\text{-}3}$) and at 70% ($\Delta t_{70\%,1\text{-}2}$ and $\Delta t_{70\%,2\text{-}3}$) were divided by the distance between two electrodes ($\Delta x_{1\text{-}2} = \Delta x_{2\text{-}3} = 3$ m), leading to three bulk velocities

$$u_{\mathrm{b,sum,i\%}} = \mathrm{mean}\left(\frac{\Delta t_{\mathrm{i\%},1-2}}{\Delta x_{1-2}}, \frac{\Delta t_{\mathrm{i\%},2-3}}{\Delta x_{1-2}}\right), \tag{4.1}$$

with $i = 30\%$, 50% and 70%. These three threshold values were analysed and determined during this research and some master thesis (see e.g. Tamagni 2006, Rüedlinger 2012). The average of $u_{\mathrm{b,sum,30\%}}$, $u_{\mathrm{b,sum,50\%}}$ and $u_{\mathrm{b,sum,70\%}}$ leads to u_{b}.

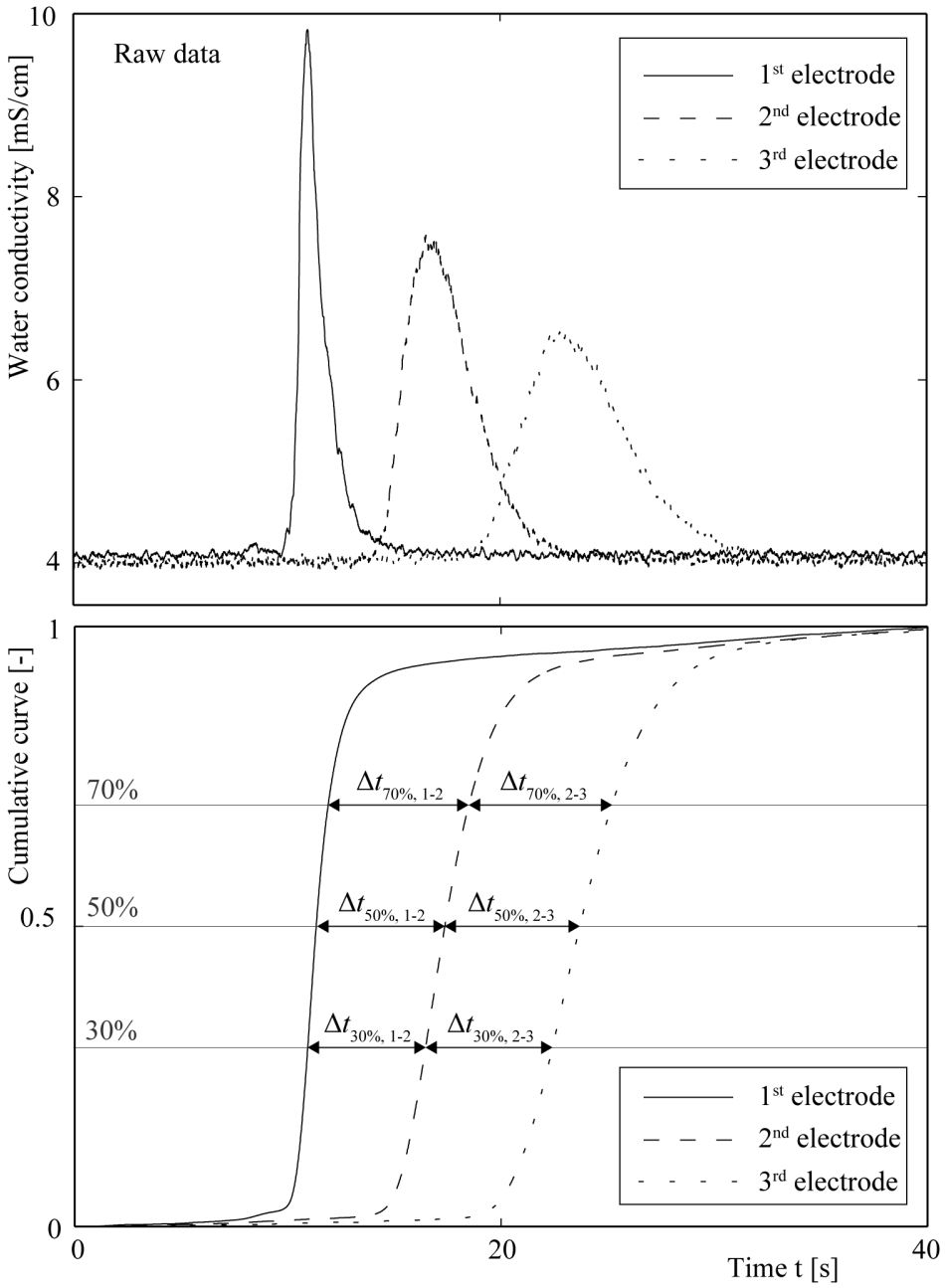

Figure 4.8 Example of a measurement and analysis of the salt dilution method data. Top: raw data; bottom: resulting cumulative curve.

4.3 Phase B – General ramp behaviour tests

The goal of the tests in phase B was to investigate the general ramp behaviour within the river system, by extending the considered river reach to a ramp with a erodible tail water reach. To test the ramp also in case of erosion at ramp toe, the fix point at the flume end was lowered. The tests were carried out under steady and unsteady flow conditions, so that the effect of a hydrograph, representing a characteristic high flood event ($\approx HQ_{100}$) of Swiss Rivers, and of the duration of a certain discharge could be investigated.

4.3.1 Model flume I, instrumentation and material

The model flume as well as the instrumentation used in this phase was the same as in phase A (Chap. 4.2.1 and 4.2.2). The sediment material and the blocks used were selected between the combinations already investigated in phase A (Chap. 4.2.3). However, compared to the model flume in phase A, the tail water level at the flume end was modeled with five 2 cm thick steel plates, so that it could be lowered by removing one or more of these plates, inducing increased erosion and simulating erosion of the river bed downstream of the ramp.

4.3.2 Experiment procedure

For each experiment of phase B, the UBR was modeled over a length of $L_R = 7$ m instead of $L_R = 9$ m as in phase A, introducing a 2 m long erodible tail water reach at the same level as the tail water plates (Figure 4.9). The ramp had an initial slope of $S_0 = 5\%$, whereas the buffer area upstream of the ramp and the erodible tail water reach downstream of it had a slope of 1% as the flume. The blocks were placed in the same way as in phase A (Chap. 4.2.4). The inlet section was also exactly the same used as in phase A.

For the experiment with *steady flow conditions* (B1, see Table 4.7), the experimental procedure as well as the measurements taken (topography with the laser distance sensor, bulk velocity with the salt dilution method, local flow velocities and the local water levels with the mini-propeller and the point gauge, respectively) was the same as in phase A.

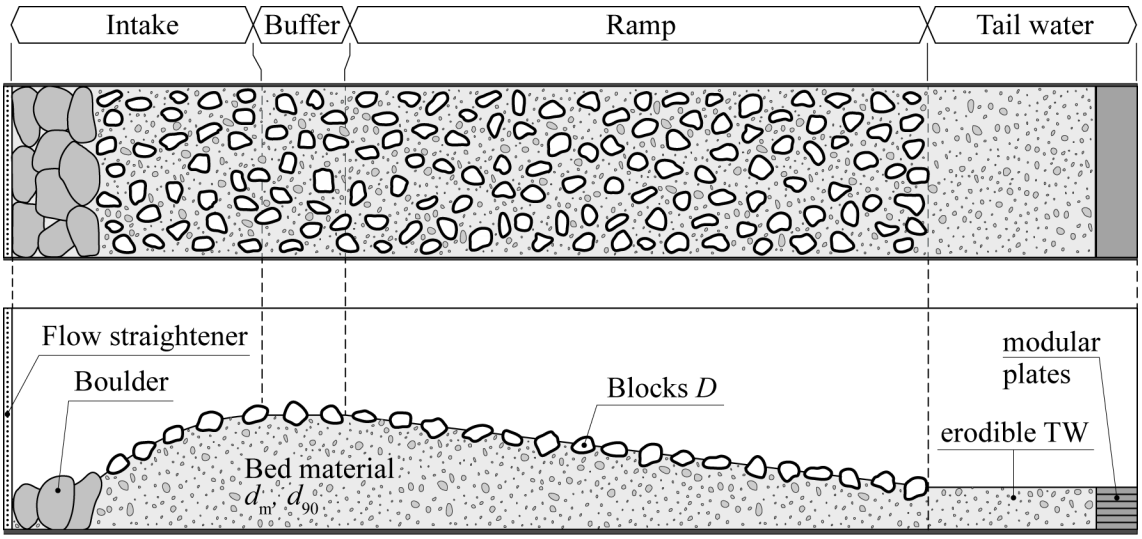

Figure 4.9 Plan view (top) and side view (bottom) of UBR for the general ramp behaviour tests. A 2 m long erodible tail water reach was introduced downstream of a 7 m long ramp. Tail water level was lowered by removing one or more modular plates.

For the experiments with *quasi-steady flow conditions* (B2 – B5, s. Table 4.7), after a preliminary constant discharge step at q = 13.3 l/(sm) performed to provide more natural and already loaded bed topography, the discharge was regulated according to the selected hydrograph described in details below. At certain points the discharge was interrupted in order to scan the bed topography and thus to define the slope reached at that time. Before stopping the discharge, the bulk flow velocity was determined with the salt dilution method, as well as local flow velocities were measured with the mini-propeller and local water levels with the point gauge.

Definition of the considered hydrograph

The effect of quasi-steady flow conditions and of the duration of a certain discharge step was investigated exclusively with one hydrograph, covering a good range of Swiss river conditions. Different hydrographs of recent flood events of the same Swiss rivers considered for the selection of representative sediment mixtures (Chap. 4.2.3) were evaluated. In particular the flood events in 1999 and in 2005 which concerned a long area of Switzerland were analyzed. The peaks of these floods often reached or even exceeded HQ_{100}, as in the case of the Engelberger Aa River, the Thur River, the Kleine Emme River or the Muota River. The time to peak varied between 19 and 48 hours in these events.

From these considerations a simplified triangular shaped hydrograph with equal rising and falling limb gradient was assumed (Figure 4.10). The peak was set to q = 140 l/(sm), corresponding to the maximum investigated specific discharge in phase A under steady conditions and to a discharge in the prototype between HQ_{30} and EHQ (= extreme flood event), depending on the geometrical scale factor. The duration between the lowest discharge of the hydrograph set at q = 20 l/(sm) and the peak was fixed at 7.2 hours, which corresponded to 36 hours in the prototype with an assumed geometrical scale factor of 25. Hence, the duration of the entire hydrograph was 14.4 hours. To measure bulk flow velocities, local flow velocities and local water levels at certain steady flow conditions, the hydrograph was discretized in regular discharge steps of 24 minutes each (Figure 4.10).

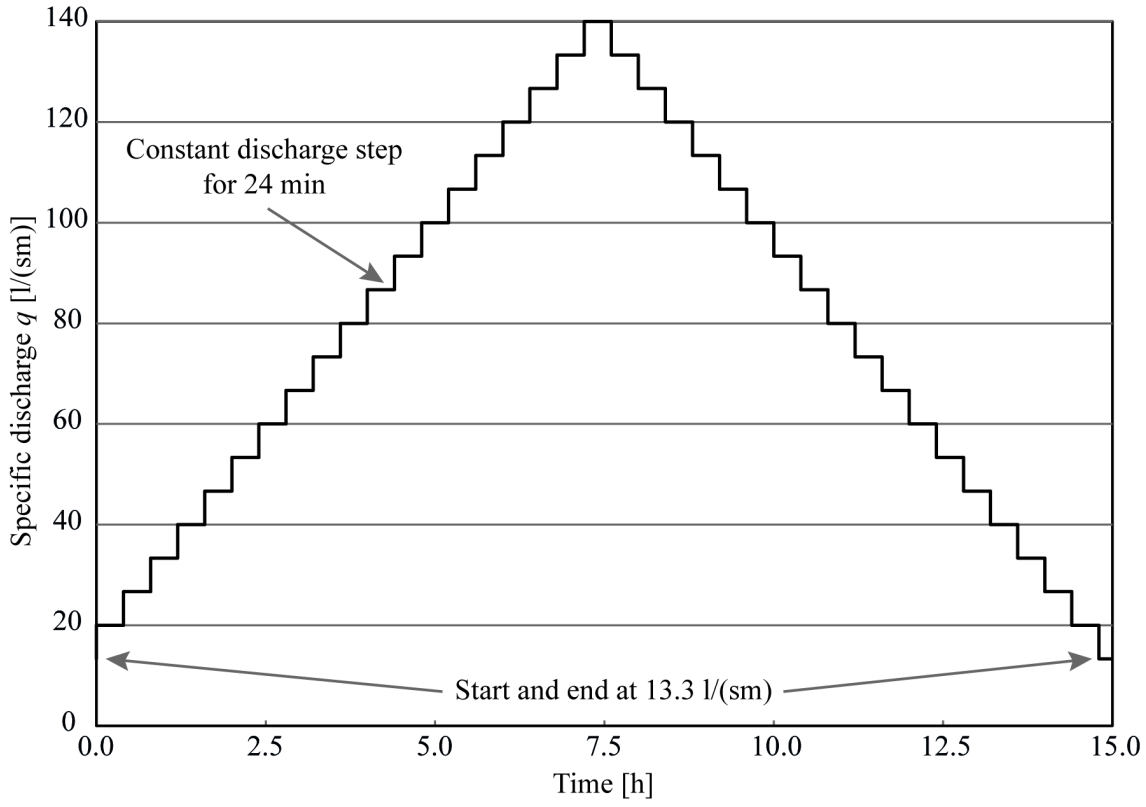

Figure 4.10 Hydrograph for the experiments with quasi-steady flow conditions of phase B (model dimensions) representing floods roughly between HQ_{30} and EHQ.

4.3.3 Test program

All the experiments carried out in phase B and their most important characteristics are summarized in Table 4.7. Only two parameter combinations (D/d_{90} and λ) were tested, namely the most stable in terms of ratio D/d_{90} but less expensive in terms of low λ (experiments B1 – B3 with $D/d_{90} = 7.4$ and $\lambda = 0.15$), and the one with a less stable configuration in terms of D/d_{90} but with higher λ (experiments B4 – B5 with $D/d_{90} = 12.3$ and $\lambda = 0.25$). All these experiments were performed *without sediment supply*.

In the following each experiment is shortly characterized (Figure 4.11)

- B1: Effect of the 2 m long erodible tail water reach on the ramp stability by testing the same parameter combination as in experiment A10 (Table 4.5) under the same steady flow conditions and fixed tail water plate.
- B2: Effect of quasi-steady flow conditions (hydrograph) on ramp stability by testing the same ramp as in experiment B1. Both the rising and the falling limbs of the hydrograph were tested.
- B3: Effect of increased erosion downstream of the ramp by lowering the tail water level by a maximum of 10 cm. Only the rising limb of the hydrograph was tested (see Chap. 5.3).
- B4: Effect of quasi-steady flow conditions on ramp stability by parameter combinations as in experiment A5 ($D/d_{90} = 12.3$ and $\lambda = 0.25$, Table 4.5). Only the rising limb of the hydrograph was tested.
- B5: Influence of an increased erosion downstream of the ramp by lowering the tail water level by a maximum of 10 cm. Same parameter combinations ($D/d_{90} = 12.3$ and $\lambda = 0.25$) like in B4. Only the rising limb of the hydrograph was tested.

The increased erosion was induced as follows:

- 1st plate (2 cm) removed after discharge step $q = 53.3$ l/(sm)
- 2nd plate (2 cm) removed after discharge step $q = 73.3$ l/(sm)
- 3rd plate (2 cm) removed after discharge step $q = 93.3$ l/(sm)
- 2 more plates (4 cm) removed after discharge step $q = 133.3$ l/(sm)

The induced erosion was specifically introduced for high discharges, to test the ramp under particularly unfavourable conditions. Lowering the TW reach caused by the removal of the plates was in the range of 2 cm – 10 cm (see above), corresponding to the maximal erosion rates measured after the flood event in Switzerland in 2005 (Bezzola and Hegg 2008). The choice to remove one or two plates was given by the experimental setup: five plates were available and their removal was distributed over the highest discharge steps.

Table 4.7 Parameter combinations of experiments of phase B (model dimensions) with S_0 = 5% and L_R = 7 m.

Experiment	D	Sediment*)	D/d_{90}	λ	Flow condition	Increased TW erosion
	[mm]	[-]	[-]	[%]		
B1	65	CM	7.4	0.15	steady	no
B2	65	CM	7.4	0.15	quasi-steady	no
B3	65	CM	7.4	0.15	quasi-steady	yes
B4	43	FM	12.3	0.25	quasi-steady	no
B5	43	FM	12.3	0.25	quasi-steady	yes

*) Characteristic grain sizes of the two sediment mixture FM and CM are found in Table 4.1.

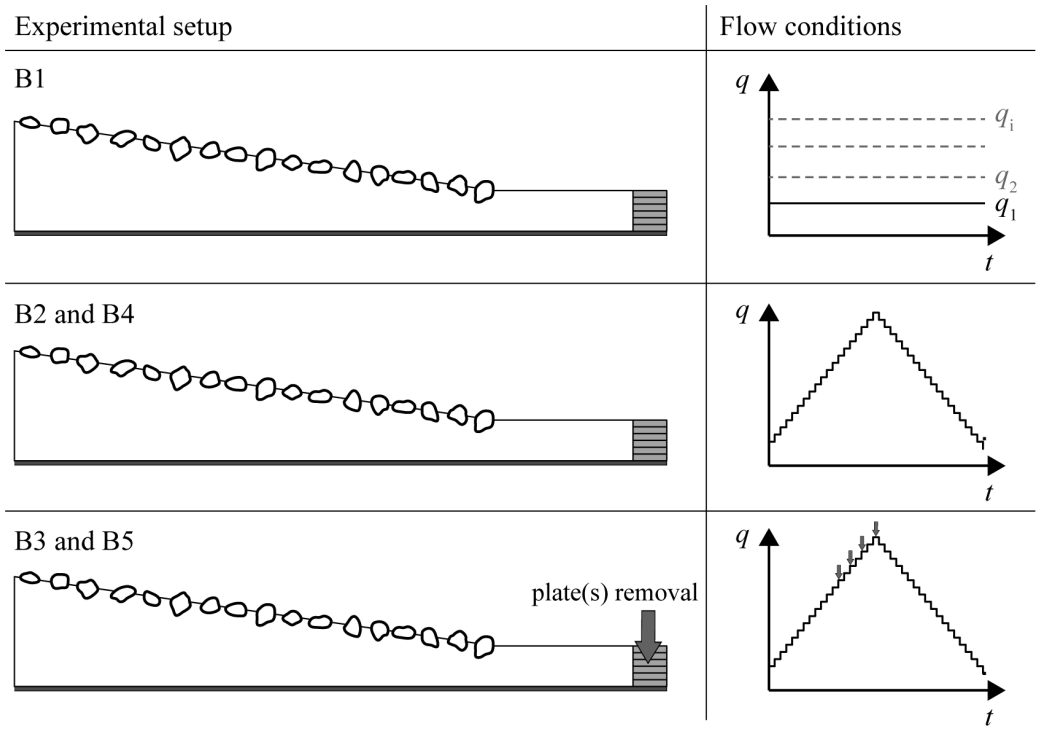

Figure 4.11 Schematic representation of the different boundary conditions for the experiments of phase B.

4.4 Phase C – Turbulence tests

The main objective of phase C was to describe with 2D Laser Doppler Anemometry LDA velocity measurements the hydraulic conditions in strong heterogeneous bed topography with macro-roughness elements. Thanks to the gained velocity, shear stress and turbulence intensity profiles, the general flow conditions and the variety of migration corridors can be described.

4.4.1 Model flume II

The phase C tests were conducted in a rectangular tilting flume 8 m long, 0.40 m wide and 0.70 m high, with both sidewalls made of glass. The intake was approximately 0.7 m long and a flow straightener assured undisturbed flow conditions and thus uniform water depth in lateral direction. At the flume end a 0.50 m long horizontal fixed plate and an adjustable needle weir (see model flume I, Chap. 4.2.1) controlled the flow depth to assure almost uniform conditions at the outflow section. Uniform flow conditions along the ramp were checked by measuring the water level with the point gauge in 54 points along the entire ramp (3 points in each cross-section). The maximum difference between the water surface and bed slopes averaged over the entire ramp length was 0.2%. Therefore, general uniform flow conditions are assumed, whereas the flow is locally strongly non-uniform. The undulating surface waves (Figure 4.12) above the blocks illustrate the latter.

4.4.2 Laser Doppler Anemometry (LDA) system

Laser Doppler Anemometry (LDA) is a point measurement technique of very high accuracy in terms of mean and turbulent flow properties (Durst *et al.* 1981, Ruck 1987). It determines velocities with the help of the Doppler-Effect that is evoked by the light refraction of small particles travelling through a measurement volume within the crossing point of two laser beams. LDA represents an optical non-intrusive measurement technique. In the present case LDA measurements have been performed without adding any seeding particles, due to the sufficient presence of fine particle. LDA measurements are used in the present research to determine the turbulence characteristics of UBR and to add information about the hydraulic conditions occurring on UBR obtained with the stability experiments in phase A.

To measure both the *u* and *w* velocity component (Figure 4.12 and Figure 4.13) a 2D LDA System (Dantec Dynamics©, FlowLite) with two diode lasers (green and green-yellow with a wave length of 532 and 561 nm, respectively) and 2×200 mW power, placed at the flume side on a 3D positioning system, was used (Figure 4.12). The sensor head uses backscatter technique, resulting with a diameter of 60 mm in a focal length of 400 mm. The sensor was connected to the beam-separator with a 20 m long fibre cable. For the present configuration the system led to a temporal resolution between 100 and 1000 Hz; the size of the measurement volume was 4×10^{-2} mm^3. The accuracy of the system given by the producer is in the order of 2% (absolute error) and 0.002% (relative error, see Chap. 4.6). With the help of an automatic 3D positioning system on which the LDA probe was installed, different vertical profiles have been measured. All the measurements were taken from the flume side through the glass sidewall. Only the *u* and the *w* velocity components were measured: the measurement of the spanwise component *v* was not possible, due to the highly undulating flow, which precluded a measurement from above through the water surface, neither with the help of a little glass boat or plate, like e.g. in the work of Detert *et al.* (2010).

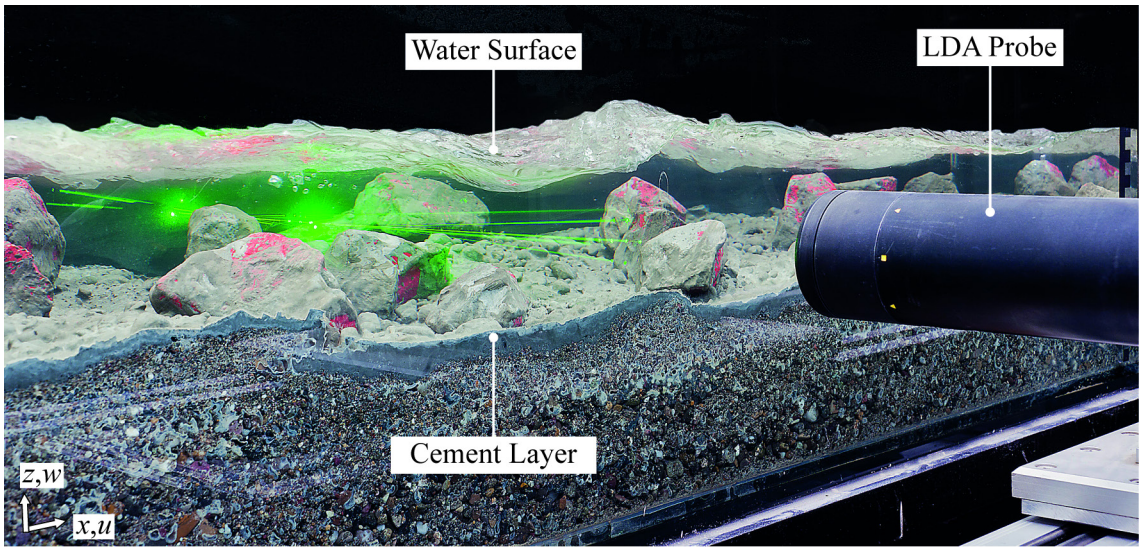

Figure 4.12 Photo of experimental setup, showing 2D LDA probe installed at the flume side to measure *u* and *w* components of the flow velocity and tested UBR with fixed bed material and blocks.

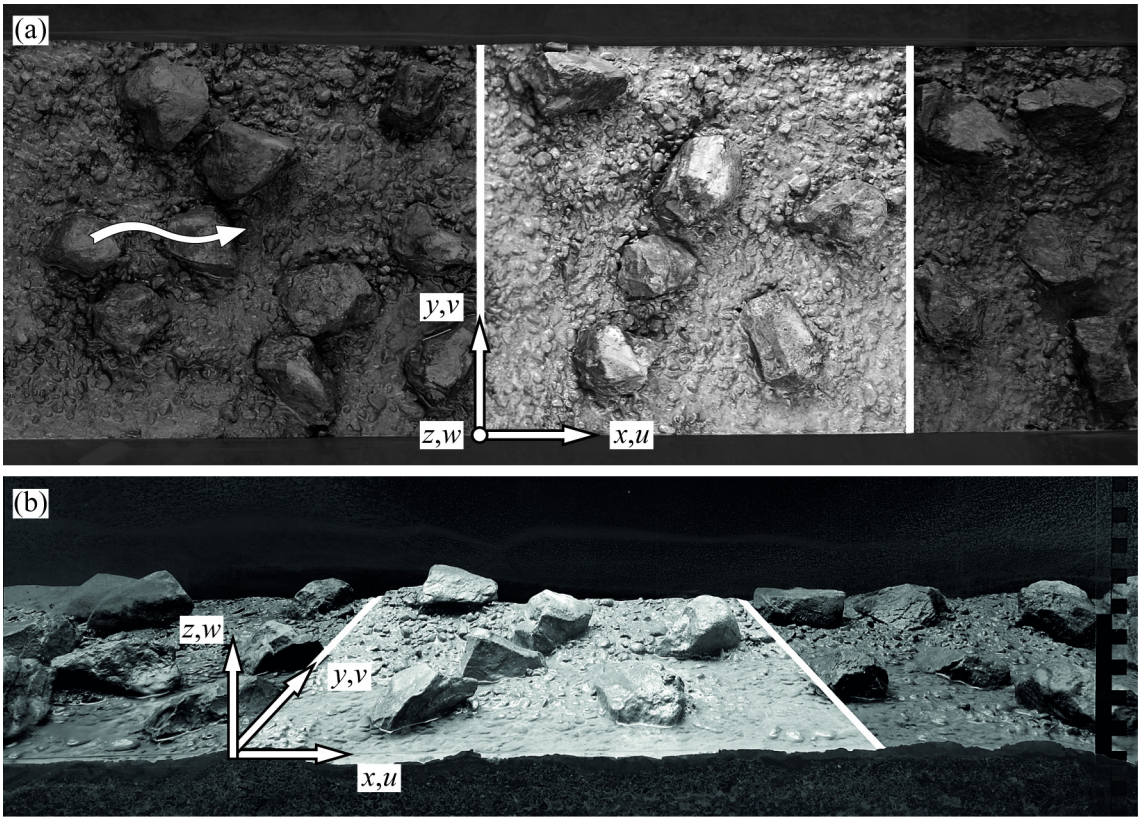

Figure 4.13 (a) Plan view of UBR with fixed bed topography. White lines indicate 0.42 m long measurement area; (b) side view.

Measurements were performed with a spatial resolution of 10 mm in *x*-, 7 mm in *y*- and 5 mm in *z*-direction (Figure 4.13). The measurements were limited to the water volume reached with the laser that is not in the shadow of any obstacle. Regions behind the blocks or close to the bed behind bed forms or close to the water surface in the shadow of a surface wave could not be reached. Due to the viewing angle of the lower laser beam the minimum distance between the bed and the measurement point depends on *y*, lying between 1 mm and 15 mm (the same holds for measurements close to the water surface). However, the effectively measured area included regions up- and downstream of a block as well as regions between blocks, leading to a representative description of the different flow phenomena. At each measurement point a maximum number of 20'000 velocity samples or a maximum sampling time of 100 s was recorded. The sampling time was evaluated with preliminary tests, showing that 100 s are sufficient to obtain constant moving average for turbulence intensity values over the entire measurement volume. The velocity components *u* and *w* were measured simultaneously using the coincidence mode, in which the two bursts (raw velocity signal) in the *x*- and *z*-direction overlap. Due to the heterogeneous geometry of the entire measurement area,

each measured cross-section at a certain location x returned different numbers of measured grid points in the y- and z-direction (Table 4.8), leading to a measurement duration of roughly 850 hours for all three discharges. After an interruption of the measurement the discharge could be reproduced with an accuracy of ±0.1 l/s. The data sufficiency at each height z where double-averaging was applied was controlled by analyzing the statistical moments of 2nd to 4th order. If the statistical moments converge, data sufficiency is given, if not, they are statistically not significant and are shown in brackets (see Figures in Chap. 5.4.3). Regarding the double-averaged properties of the vertical velocity component w, the convergence of the higher order moments was not fully sufficient, suggesting that the measurement window should have been larger.

4.4.3 Other instrumentations

The flume was equipped with a pump to deliver a maximum discharge of Q_{max} = 70 l/s, measured by a magnetic-inductive flow meter (MID). The discharge was regulated with a manual valve. Flow velocities and local water levels were measured locally along the ramp with a mini-propeller and a point gauge, respectively. Bulk flow velocities u_b were determined with the salt dilution method (Chap. 4.2.2) at three cross-sections with three pairs of electrodes consisting of metal bands attached to the sidewalls. The bed topography was scanned with a laser distance sensor, installed on a positioning system, manually manoeuvrable in the x- and in the y-directions.

4.4.4 Experimental setup

To keep the number of parameters small, only one combination of λ and D/d_{90} was tested for three relative submergences h_m/P. This configuration comprised the most stable ratio D/d_{90} = 7.4 (blocks with equivalent spherical diameter D = 65 mm and coarse mixture CM, see Chap. 4.2.3) derived from phase A and the lower block placement density λ = 0.15 (Experiment A10, see Table 4.5), and allowed to investigate a stable configuration that was both convenient and cost effective. To achieve natural morphological conditions a 4 m long ramp with an initial slope of S_0 = 4% was built with a movable bed. The buffer area and the inlet area were similar as in phase A (Chap. 4.2.4 and Figure 4.6), i.e. 1 m and approximately 2 m long, respectively.

Then the ramp was loaded with a constant specific discharge q = 26.7 l/(sm) until stable bed conditions were achieved. This discharge corresponds roughly to a 1 to 10

years flood event for typical Swiss Rivers with a relative submergence $h_m/P = 1.23$. The mean block protrusion P resulted as mean exposed block height of 74%, i.e. $P = 0.74 \cdot D \approx 48$ mm. The resulting equilibrium bottom slope was $S_e = 2.86\%$ with a cross-sectional-averaged bulk flow velocity of approximately $u_b \cong 0.5$ m/s. Next, the resulting bed topography was fixed with a thin cement layer (Figure 4.12) and measured with the laser distance sensor with a measuring grid of 1×1 cm^2 in the x-y-plane along the entire ramp of 4 m in length and 0.4 m in width. In general UBR have a permeable bed. These experiments were conducted with a fixed bed and therefore under impermeable bed conditions to compare the velocity measurements for a certain discharge at equal flow conditions. With movable bed, the geometrical boundaries would continuously change. Not only the sediment material could be eroded or change locally the morphology of the river bed, but also the blocks could locally move, making it impossible to directly compare the data. The present bed material features a typical grain size distribution with a hydraulic conductivity experimentally determined to 0.18 cm/s (Chap. 4.2.4). Without the cement layer, the discharge through the subsurface layer was negligible (0.4% of the total discharge). The bulk flow velocity u_b and the mean flow depth h_m were measured before and after fixing the bed material. The values of h_m compared well to the estimates from the equation of continuity using u_b from the salt dilution method: the differences between the values were between 1% and 6%. The differences in u_b determined with the salt dilution method and h_m determined with the point gauge before and after fixing the bed were below the measuring accuracy. No LDA measurements were carried out before fixing the bed material; therefore, local changes of the turbulence conditions very close to the bed could not be identified. The bed roughness was locally changed with the cement layer, e.g. by filling some pores between the grains of the sediment material. However, the present research aims at describing the macro flow conditions within the water body and does not focus on the very near-bed region. These macro flow conditions are especially affected by the blocks and the occurring bed forms. For this reason the effect of adding the cement layer was considered as negligible herein.

4.4.5 Test program

The measurements were performed under steady flow conditions for $q_1 = 6.8$ l/(sm), $q_2 = 13.8$ l/(sm) and $q_3 = 40.0$ l/(sm), representing typical Swiss Rivers conditions with

a discharge roughly between Q_{30} and HQ_{10}. These three discharges correspond to the three relative submergences of $h_{m,1}/P = 0.63$, $h_{m,2}/P = 0.88$ and $h_{m,3}/P = 1.46$, where $h_{m,1}$, $h_{m,2}$ and $h_{m,3}$ are the mean flow depths along the ramp. The three different relative submergences represent: (1) $h_m < P$: emerging blocks, (2) $h_m \approx P$: blocks barely submerged, and (3) $h_m > P$: blocks fully submerged. Table 4.8 summarizes all tested parameters and corresponding boundary conditions.

Table 4.8 Tested parameters in phase C and resulting measured data in model dimensions. $D = 65$ mm, $\lambda = 0.15$, $d_{90} = 8.8$ mm and $d_m = 4.3$ mm (CM), and $S_e = 2.86\%$ remained constant for each test. Bulk shear velocity is $u_{*,b,i} = (g\, h_{m,i}\, S)^{0.5}$. Froude and Reynolds numbers are determined using $u_{b,i}$ and $h_{m,i}$ as $\mathsf{F} = u_{b,i}/(g\, h_{m,i})^{0.5}$ and $\mathsf{R} = u_{b,i}\, h_{m,i}/\nu$, respectively, with $\nu = 10^{-6}$ m^2/s.

Exp.	q	h_m/P	h_m	u_b	$u_{*,b}$	F	R	No. of measured points
	[l/(sm)]	[-]	[m]	[m/s]	[m/s]	[-]	[-]	
C1	6.8	0.63	0.030	0.24	0.092	0.44	$0.7 \cdot 10^4$	6164
C2	13.8	0.88	0.042	0.34	0.109	0.53	$1.4 \cdot 10^4$	10174
C3	40.0	1.46	0.070	0.61	0.140	0.74	$4.3 \cdot 10^4$	15949

4.5 Model similarity and scale effects

The physical scaling method is used to achieve similar flow conditions and transport behaviour in the physical model and the prototype. Geometric, kinematic and dynamic similarity criteria have to be fulfilled for the model similarity (see e.g. Heller 2011). The geometric similarity requires similarity in all sizes: model lengths, areas and volumes are geometrically downscaled in relation to the prototype. The geometrical scale factor Ω is generally defined as the ratio between the characteristic length in the prototype L_P and the characteristic length in the model L_M, namely

$$\Omega = L_P / L_M \ . \tag{4.2}$$

Hence, lengths are scaled with Ω, areas with Ω^2 and volumes with Ω^3, respectively. The kinematic similarity requires constant ratio for motion process, namely constant ratio of time, velocity, acceleration and discharge (Table 4.9). Finally, the dynamic similarity requires constant force ratio, where the relevant forces in fluid dynamics are e.g. gravitational force, inertial force, pressure force and viscous force (Heller 2011).

Depending on the governing forces in the considered process, a certain law of similitude based on a dimensionless ratio of forces defines the scaling factors to reproduce prototype dimensions in model dimensions and the other way around. In open-channel flows the Froude similarity is often applied, where the Froude number F is the ratio between the inertial and the gravity force

$$\mathsf{F} = U / \sqrt{g\, L} \ . \tag{4.3}$$

where U = characteristic velocity and L = characteristic length (normally the water depth h). Applying the Froude similarity, the other force ratios (e.g. inertial force/viscous force = Reynolds number R, or inertial force/surface tension force = Weber number W) cannot be identical in the prototype and in model and may therefore result in non-negligible scale effects (Heller 2011). In general, if the model is scaled (i.e. $\Omega \neq 1$), model tests always involve scale effects. For this reason, the decisive question is whether scale effects can be neglected (Heller 2011): this cannot be directly derived from the scale factor Ω, because it is not the only parameter affecting scale effects. In order to determine these scale effects, scale family tests (not carried out in the present research) can be carried out.

Table 4.9 Scale factors Ω according to the Froude similarity for some selected quantities.

Quantity	Scale factor
Length	Ω
Area	Ω^2
Volume	Ω^3
Time	$\Omega^{1/2}$
Velocity	$\Omega^{1/2}$
Discharge	$\Omega^{5/2}$

Applying the Froude scaling method, only geometrical and kinematic similarity are therefore achieved. In case of rough bed and so of UBR, the effects of R (defined as $\mathsf{R} = 4hU/\nu$) and so of the viscosity on the flow resistance are negligible for $\mathsf{R} > 10^4$ (Pagliara and Chiavaccini 2006a, Ferro 1999, Lawrence 1997). All the performed tests satisfy this condition and, therefore, the dynamic similarity is not decisive.

To downscale the sediment material, scale effects due to cohesion are avoided for grain sizes $d > 0.22$ mm (Zarn 1992): for this reason, the sediments used for the model tests do not have grain fraction finer than 0.25 mm (Chap. 4.2.3). The scaling of the transported sediment is not geometrical, because the incipient motion expressed through the critical shear stress θ_c is dependent on the grain size diameter d, but also on the grain Reynolds number R^* (Shields 1936). The Shields diagram (Figure 2.5) shows that θ_c is constant for $\mathsf{R}^* > 500$, which is normally given in prototype conditions but often not in models. For this reason, a geometrically scaled grain in the model is entrained at smaller discharge compared to the correspondent entraining discharge in the prototype. Zarn (1992) suggested a method for the scaling of sediment mixtures, which considers the above mentioned effects, leading to coarser mixtures compared to simply geometrically scaled mixtures.

To determine the geometrical scale factor Ω the river bed material (d_m, d_{90} and σ) and the block diameter D are used. On the one hand, the existing sediment mixture of the considered river is compared to the two tested sediment mixtures, resulting in a scale factor Ω by comparing d_{90}. On the other hand, the upscaling of the equivalent spherical block diameter D with the scale factor Ω resulting from the sediment mixture, gives the applicability of the test results to the considered river. The blocks in the proto-

type should not exceed a certain diameter and a certain weight, respectively. Otherwise the transport and the placement of the blocks become very expensive.

4.6 Accuracy and repeatability

Each measurement device and geometrical part of the experimental setup has a certain measurement or construction limitation, giving each measurement a certain inaccuracy or systematic error. The *systematic error* is reproducible (= it is always the same), because it is caused by the test setup and procedure itself. By improving the test procedure, systematic errors can be reduced or corrected after the measurements (e.g. by calibration). In the following, the systematic error of each measurement device and geometrical parts are listed.

Systematic errors of phase A and B (model flume I)

- Width and length of flume ±3.0 mm
- Flume slope ±0.1‰
- Small pump ±1 l/s
- Large pump ±3 l/s
- Magnetic-inductive flow meter ±0.6%
- Point gauge ±0.1 mm
- Mini-propeller ± ca. 8%
- Ultrasonic sensors < ±1%
- Laser distance sensor ±1 mm
- Positioning system ±1 mm
- Temperature variations (ultrasonic sensors) < ±2%
- Tension measurements (for water conductivity measurements) ±1%

Systematic errors of phase C (model flume II)

- Width and length of flume ±2.0 mm
- Flume slope ±0.1‰
- Magnetic-inductive flow meter ±0.6%

- Valve ±0.1 l/s
- Point gauge ±0.5 mm
- Mini-propeller ± ca. 8%
- Tension measurements (for water conductivity measurements) ±1%
- 2D LDA system
  absolute error max ±2%
  relative error ±0.002%

Systematic errors in general

- Temperature variation by ±2°C affects fluid proprieties
  (e.g. viscosity or surface tension) inappreciable
- Atmospheric pressure variation inappreciable
- Personal errors inappreciable

Additionally to the systematic errors, also *random errors* caused by undeterminable fluctuation of the measured object, of the instrumentation, of the environment or by the observation (Martin and Pohl 2009) may occur during each measurement. Random errors are not reproducible and cannot be reduced or avoided improving the test procedure. They are usually assumed to be normally distributed.

The *error* f_i of a physically measured value x_i is defined as the difference between the mean average of the sample $\bar{x}$

$$\bar{x} = \frac{1}{n}\sum_{i=1}^{n} x_i \ , \tag{4.4}$$

where n = number of samples measured, x_i = single measured value (sample), and the single sample x_i, namely

$$f_i = \bar{x} - x_i \ . \tag{4.5}$$

The *relative error*, defined as

$$e_i = f_i/\bar{x} \ , \tag{4.6}$$

quantifies the effect of a certain error on the expected value. To evaluate the quality of a measurement method, the standard deviation σ_i

$$\sigma_i = \sqrt{\frac{\sum f_i^2}{n-1}} = \sqrt{\frac{\sum_{i=1}^{n}(\bar{x}-x_i)^2}{n-1}}, \tag{4.7}$$

is used to quantify the mean error of a data series, so that the standard error

$$\bar{\sigma} = \sqrt{\frac{\sum f_i^2}{n(n-1)}} = \frac{\sigma_i}{\sqrt{n}}, \tag{4.8}$$

is determined and the data series is expressed as $x = \bar{x} \pm \bar{\sigma}$.

For the present research, two decisive quantities are not directly measured, but derived from measurement data: (1) ramp slope S, derived from the topography data measured with the laser distance sensor; (2) bulk flow velocity u_b, derived with the salt dilution method from the measurement of the changes in the water conductivity. The exact methods for the determination of S and u_b are described in Chap. 4.2.7.

The determination of the ramp slope S is affected by the inaccuracy of the positioning system as well as by the mesh grid used, which has to be representative for the heterogeneous bed topography. The effects of these inaccuracies were investigated by repeating 20 times exactly the same measurement with the mesh grid used during the experiments (measuring grid 10×2 cm^2, Chap. 4.2.7), as well as by varying the mesh grid in 10 slightly different ways (displacement of 1, 2, 3, 4, 5 cm in the x- direction and 1 cm in the y- direction). From the 20 identical measurements a mean slope $\bar{S} = 0.0162$ and a standard deviation $\sigma_S = \pm 0.00002$ resulted, leading to $S = 0.0162 \pm 0.00002 = 1.62\% \pm 0.002\%$. The topography data measured with 10 slightly different meauring grid resulted in a mean slope $\bar{S} = 0.0160$ and a standard deviation $\sigma_S = \pm 0.00012$, leading to $S = 0.0160 \pm 0.00012 = 1.6\% \pm 0.012\%$. Considering both inaccuracies, the value of the calculated ramp slope S is afflicted with an error of less than 1%.

The determination of the bulk flow velocity u_b is associated with the inaccuracy of the tension measurements, as well as with the procedure of the salt dilution method, which was manually performed and, therefore, not exactly identical at each run. For this reason, this method was repeated 20 times for a single parameter combination for $q = 24$ l/s, resulting in a mean bulk velocity $\bar{u}_b = 0.505$ m/s and a standard deviation $\sigma_S = \pm 0.00744$ m/s ≈ 0.01 m/s, leading to $u_b \approx 0.51$ m/s ±0.01 m/s.

Test Repeatability

The test repeatability was investigated by repeating exactly the same experiment with identical boundary conditions, equal experimental procedure and performing the same runs with constant discharge. The reference experiment A1 with $D/d_{90} = 12.3$ and $\lambda = 0.15$ was repeated (experiment A1rep, Chap. 4.2.6). The criterion for the equilibrium condition was applied for each run of both experiments according to Chap. 4.2.4.

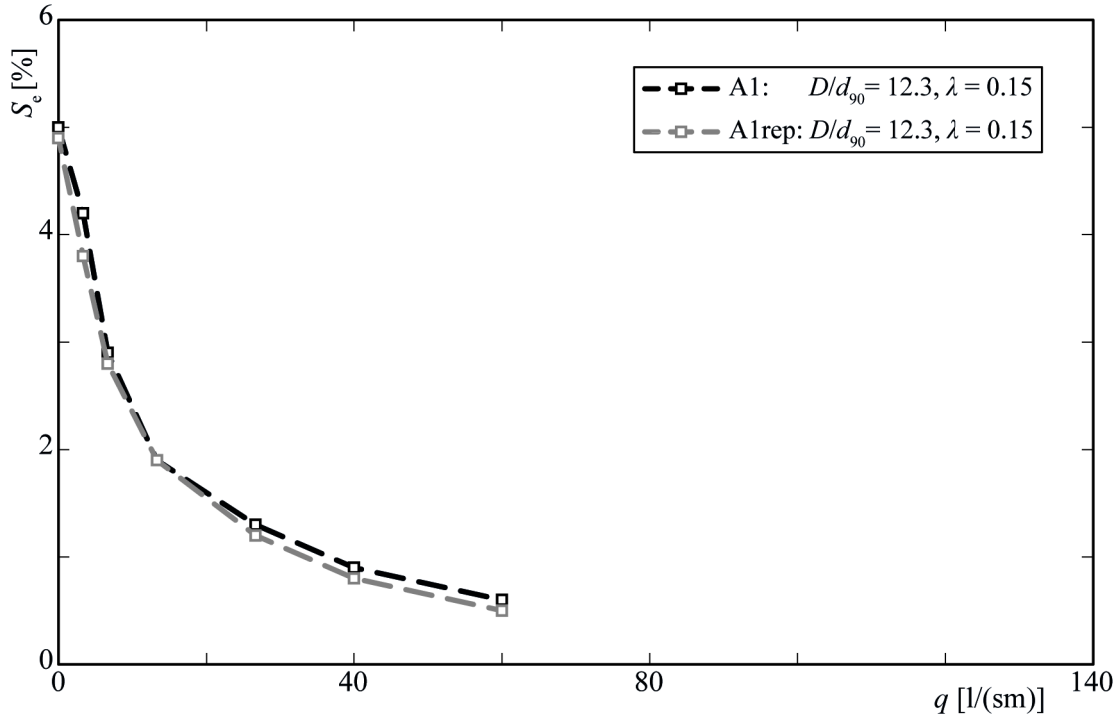

Figure 4.14 Stability diagram with equilibrium slope S_e in function of the specific discharge q for the repeatability test A1 and A1rep with $D/d_{90} = 12.3$ and $\lambda = 0.15$.

Figure 4.14 shows the stability diagram (Chap. 5.2.1) resulting from A1 and A1rep: each point in the curve corresponds to one run with constant discharge q carried out until equilibrium conditions were reached. The equilibrium slope S_e was determined by averaging the bed levels measured in each cross-section and then fitting them along the whole ramp (see Chap. 4.2.7). The resulting equilibrium slopes differ approximately between 0% and 12% and the measured bulk velocities between 3% and 8%. The trend of the two stability curves is the same and the differences between the two experiments can be considered satisfactorily small. Due to the employment of natural blocks that implies a certain dimension range, it is impossible to have exactly the same block configuration. The natural erosion process of the sediment material depends on the local

conditions and can differ from one experiment to another, also at the same boundary conditions. For these reasons, the difference between the two identical experiments of approximately 10% can be accepted and the experiments can be considered as repeatable.

5 Results

5.1 Overview

The results of the physical model tests are presented in this chapter subdivided into the three phases A, B, and C (Chaps. 5.2, 5.3 and 5.4). Chap. 5.2 illustrates the results of the stability tests of phase A, focussing on the effect of each single parameter and on the determination of an optimal parameter combination (D/d_{90} and λ) in terms of hydraulic stability. An approach for the determination of the flow resistance of UBR is presented. The results of the general behaviour tests of phase B are presented in Chap. 5.3, where the effect of an erodible tail water reach, of quasi-steady flow conditions and of increased erosion downstream of the ramp are the focus of the analysis. In Chap. 5.4 the results of the turbulence tests of phase C are analysed both from a hydromechanical and from an ecological point of view. A subdivision into characteristic flow layers is suggested and the different representative heights are defined. Local quantities such as time-averaged velocities or turbulence intensities, as well as flow characteristics are analysed. This allows considerations about the theoretical migration possibilities for a target fish and about the ecological effectiveness of UBR. Furthermore, the double-averaging approach is applied to describe the general flow conditions along the ramp and to determine the bed shear stress.

5.2 Stability tests – Phase A

5.2.1 Stability diagram

The decisive parameter in terms of ramp stability is the resulting equilibrium slope S_e for a certain specific discharge q corresponding to a certain experimental run. The stability diagram (e.g. Figure 5.1) represents this relationship graphically. The duration of each run varied between various hours (3-8 h) and various days (up to 4-5 days) until equilibrium conditions were reached. Note that compared to prototype conditions the duration of a single run especially in case of flood discharges was much higher than typical prototype conditions. Presumably a flood event does not take as long as one of the single runs tested. Therefore, the equilibrium slope S_e reached during the experiments is assumed to be the lower limit and the conservative assumption for the ramp

slope at a certain discharge. The equilibrium slope S_e is directly related to the specific discharge q so that the effect of the considered parameter can be easily understood. A parameterisation is carried out in Chap. 5.2.7 in terms of flow resistance and the generalization of the results. Figure 5.1 shows the stability diagram for the reference test A1 with a ratio between equivalent spherical block diameter and the characteristic grain size of the sediment $D/d_{90} = 12.3$ and a block placement density $\lambda = 0.15$ (Chap. 4.2.6). With a specific discharge of $q \approx 14$ l/(sm) (corresponding to $\approx 1.2 - 2.2$ m^2/s in the prototype depending on the scale) the ramp flattened to a slope $S_e < 2\%$, whereas for $q = 40$ l/(sm) ($\approx 3.6 - 6.6$ m^2/s) to $S_e < 1\%$. This means that a ramp build with this parameter combination would flatten below 1% already for discharges in the magnitude of HQ_1 or HQ_2. A ramp should maintain its stabilizing function also for higher discharges, like HQ_{100}. Therefore, for the design of a UBR, the limited stability resulting from this parameter combination might be traded off against block size and ramp costs.

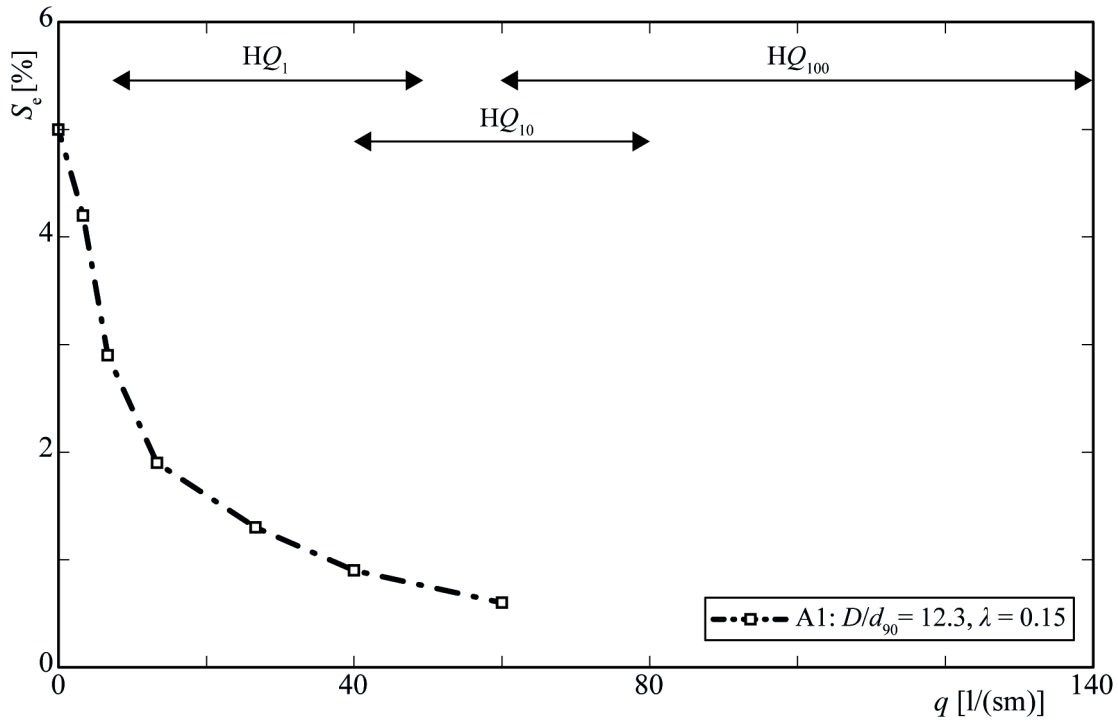

Figure 5.1 Stability diagram with equilibrium slope S_e versus specific discharge q for reference experiment A1 (model dimensions). HQ_i are determined for geometrical model scale $\Omega = 25$ for various Swiss rivers.

Together with the flattening of the ramp, by increasing the discharge the block patterns and the bed topography also changed. Figure 5.2 shows the top view of UBR

A1 after the achievement of equilibrium conditions for different specific discharges. For q = 3 l/(sm) only few local block movements can be observed, whereas for q = 7 l/(sm) the local changes are more distinct. With increasing discharge more blocks moved locally, forming some structures as e.g. rows or arches. The hypothesis is that the ramp tries to adjust itself to the higher discharge not only by flattening but also by rearranging the blocks in a more stable pattern. During other experiments, the blocks moved not only locally, but were transported along the ramp leading to ramp failure (see Chap. 5.2.3). The block movement depends on the ratio D/d_{90}.

In the following chapters the influence of each single investigated parameter on the ramp stability is discussed with the help of stability diagrams. The following notation is applied for each stability diagram: Different line types (dotted, dashed, etc.) denote different D/d_{90}; square symbols (□) denote $\lambda = 0.15$ and circles (○) $\lambda = 0.25$; empty symbols denote experiments without sediment supply and filled symbols with sediment supply; black lines denote experiments with sediment mixtures and grey lines with uniform material.

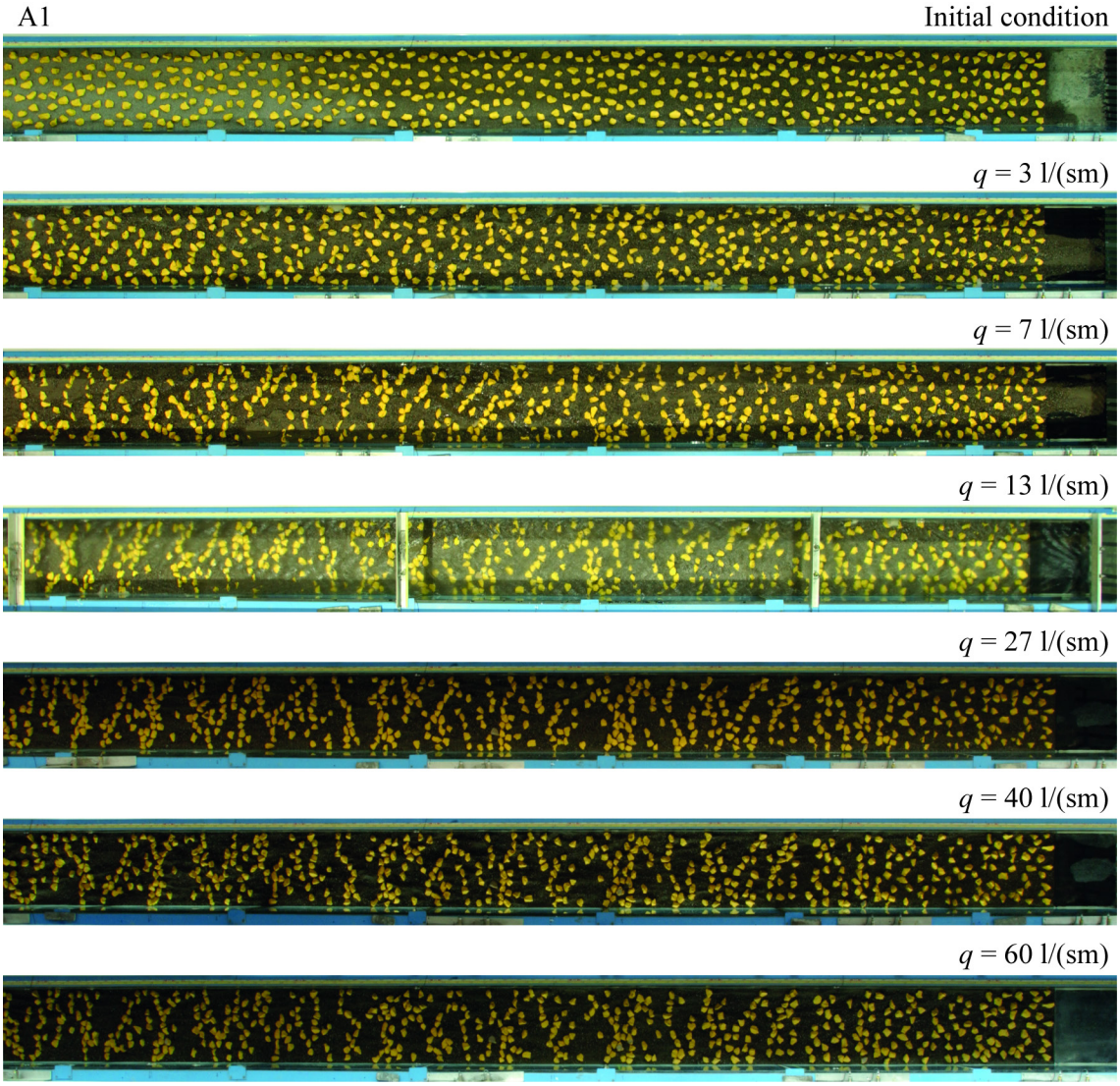

Figure 5.2 Top view of the block ramp of experiment A1 with $D/d_{90} = 12.3$ and $\lambda = 0.15$ at equilibrium conditions for different specific discharges. With increasing discharge, the blocks moved locally and some row-like patterns formed.

5.2.2 Effect of blocks

In order to quantify the stabilizing effect of the blocks the experiment A2 was carried out without blocks but with the same sediment (fine mixture FM) as for A1. Figure 5.3 shows the resulting stability diagram for A1 and A2, together with the stability curves according to Günter (1971, see Eq. 2.36) for two different assumed dimensionless critical shear stresses, namely for $\theta_c = 0.047$ (Meyer-Peter and Müller 1948) and for $\theta_c = 0.03$ (high grain protrusion, Chap. 2.3.2) combined with the approach for the determination of the flow resistance according to Chézy (Eq. 2.16).

The stability curve A2 is between the two stability curves according to Günter (1971), reflecting the expectations and confirming the reliability of the test procedure. For $q < 20$ l/(sm) the ramp with blocks (A1) is two times steeper than without blocks (A2). For $q > 20$ l/(sm) the stabilizing effect decreases with increasing relative submergence h/P. For $q > 40$ l/(sm) the results of A2 differ from those according to Günter (1971), which represent a theoretical stability behaviour never reaching $S_e = 0\%$. The experimental setup of the present research is not adapted for ramps or river beds with very low flow resistance and very low bed slope (as in this case without blocks). The inflow conditions should have been handled with more care for these cases with $q > 40$ l/(sm).

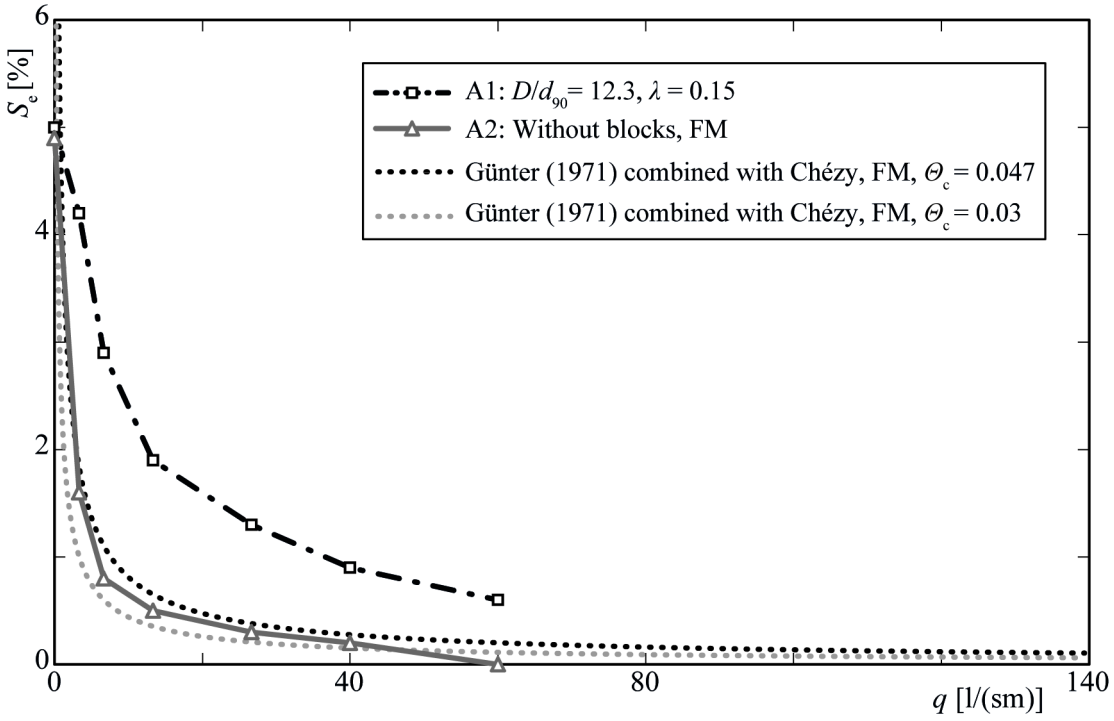

Figure 5.3 Ramp stability of A1 (with blocks) and A2 (without blocks) compared to stability curves according to Eq. (2.36) (Günter, 1971) combined with Eq. (2.16) (flow resistance according to Chézy) for FM and for $\theta_c = 0.047$ and $\theta_c = 0.03$, respectively. Values in this and in the following diagrams refer to model dimensions.

Figure 5.4 compares the stability curve A10 with the results with coarse material (CM) and higher stability than A1, and the correspondent stability curves according to Günter (1971). At a given q, the ramp with blocks (A10) is up to 4 times steeper than a

ramp built only with sediment material. Also in this case, the stabilizing effect of the blocks decreases with increasing q.

Figure 5.3 and Figure 5.4 show that for low relative submergences h/P, where the blocks protrude ($h < P$) or are just overflown ($h \approx P$), the form drag plays a decisive role together with the grain friction for the determination of the flow resistance of UBR (Chap. 3.2.1). Each single roughness element (block) induces energy dissipation due to flow separation occurring around and downstream of it, resulting in a higher flow resistance compared to the bed without blocks, where only the grain friction of the sediment material plays a role. Increasing q and h/P, respectively, the flow separation occurring at each block decreases in relation to the overall energy dissipation, leading to lower energy dissipation. The relative roughness of the bed is lower and the form drag is less pronounced compared with the case of low h/P, meaning that the river bed is smoother, and the resulting flow resistance is lower (Chap. 5.2.7). The processes remain similar for high h/P compared to low h/P, but the effect of the blocks on the overall behaviour decreases.

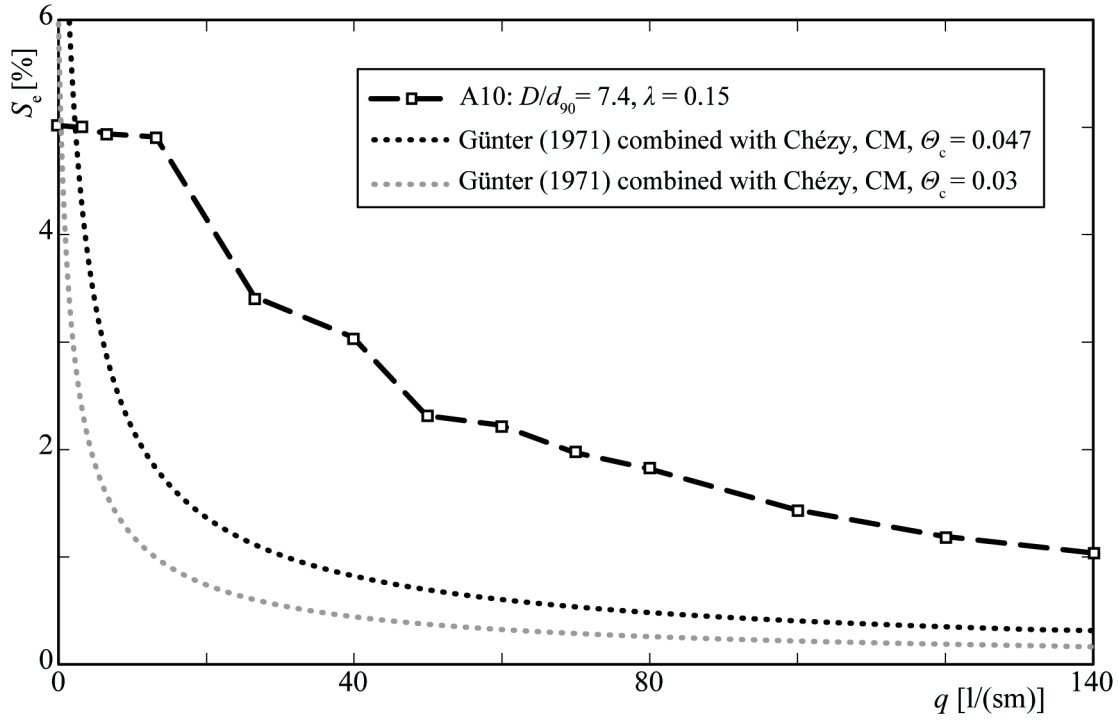

Figure 5.4 Ramp stability of A10 compared to theoretical stability curves according to Eq. (2.36) (Günter, 1971) for CM and for $\theta_c = 0.047$ and $\theta_c = 0.03$, respectively

5.2.3 Effect of ratio between block diameter *D* and characteristic grain size *d*

According to Raudkivi and Ettema (1982) the ratio between the block diameter and characteristic sediment diameter D/d is decisive for the transport processes of bimodal material (Chap. 2.3.4). The four entrainment conditions are applied and adapted to UBR, considering the ramp as a simplified bimodal material with big particles D (in Chap. 2.3.4 defined as d_1) placed with a certain constant relative protrusion P on a uniform finer bed material d (in Chap. 2.3.4 defined as d_2). The application range of Figure 2.7 is reduced to $D/d > 1.0$ – because for block ramps D is always bigger than d – and to $u_*/u_{*D} > 0.1$, where d could become unstable. Figure 5.5 shows the diagram adapted from Raudkivi and Ettema (1982) to UBR. The dominant overpassing of the blocks over the finer bed material or the dominant embedding of the blocks in the finer bed material are defined as *failure mechanisms* for UBR, considering UBR as bimodal material. According to Figure 5.5, UBR should be therefore designed so that the ratio between blocks and sediment material is in the transition area, namely $6 < D/d < 17$. For sediment mixtures a characteristic grain diameter has to be selected to determine D/d_c. For typical Alpine conditions where the river bed material is a mixture with generally $\sigma = (d_{84}/d_{16})^{0.5} \geq 1.5$ and so potentially armouring (Little and Mayer 1972), the decisive characteristic grain size in terms of stability is d_{90} of the sediment material. Janisch *et al.* (2007) showed on the basis of experimental results that the choice of d_{90} as decisive parameter is suitable. The experiments were carried out varying D/d_{90} between these limits to find the optimal value in terms of ramp stability.

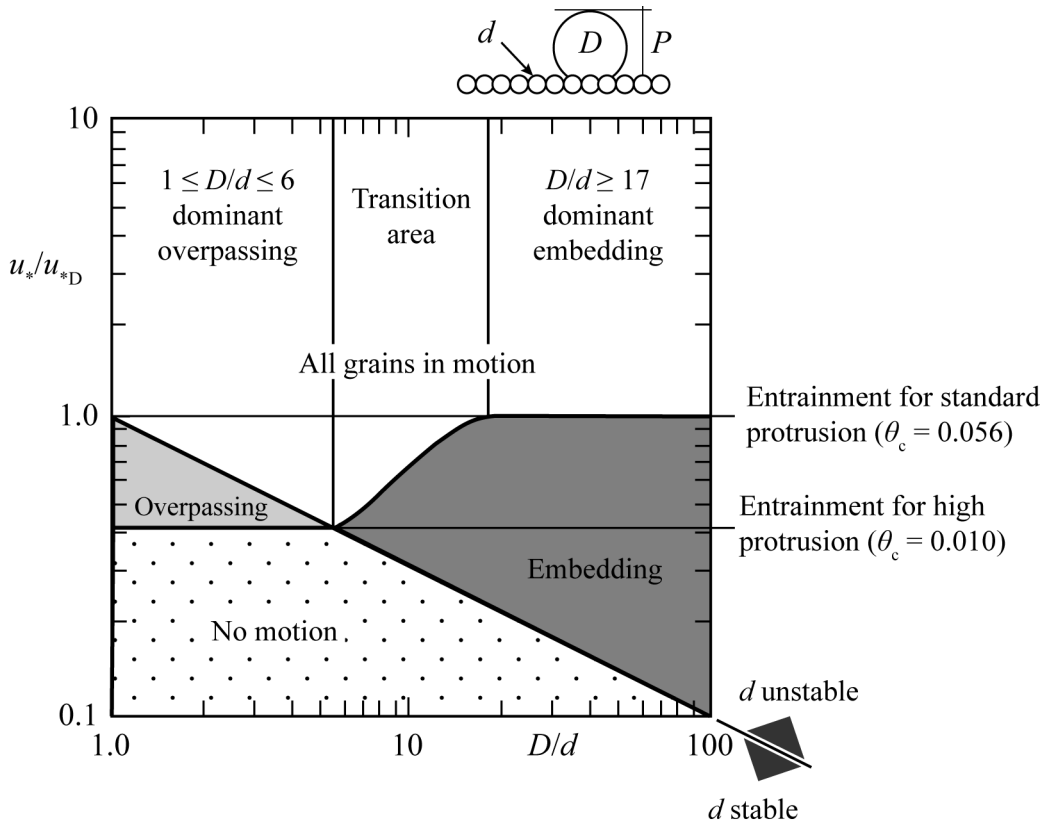

Figure 5.5 Dominant processes for bimodal materials derived from the entrainment conditions according to Raudkivi and Ettema (1982) (adapted from Bezzola, 2010).

Figure 5.6 shows the results of the experiments A1, A6, A8, A10 and A12, where D/d_{90} was varied between 4.9 and 18.6 with a constant $\lambda = 0.15$. The ramp of A6 with $D/d_{90} = 18.6$ is the least stable UBR tested, confirming the theory of Raudkivi and Ettema (1982). Through the embedding process of the blocks in the finer sediment material, the block protrusion P decreased with the increase of q, leading to a decrease of the relative bed roughness and also of the flow resistance. The changes in the bed topography and in the block pattern are shown in Figure 5.7. As for A1 (Figure 5.2), by increasing the discharge some blocks locally moved, forming some block clusters in particular for $q > 13$ l/(sm). The irregularities of the bed formed by the sediment material are also visible in Figure 5.7.

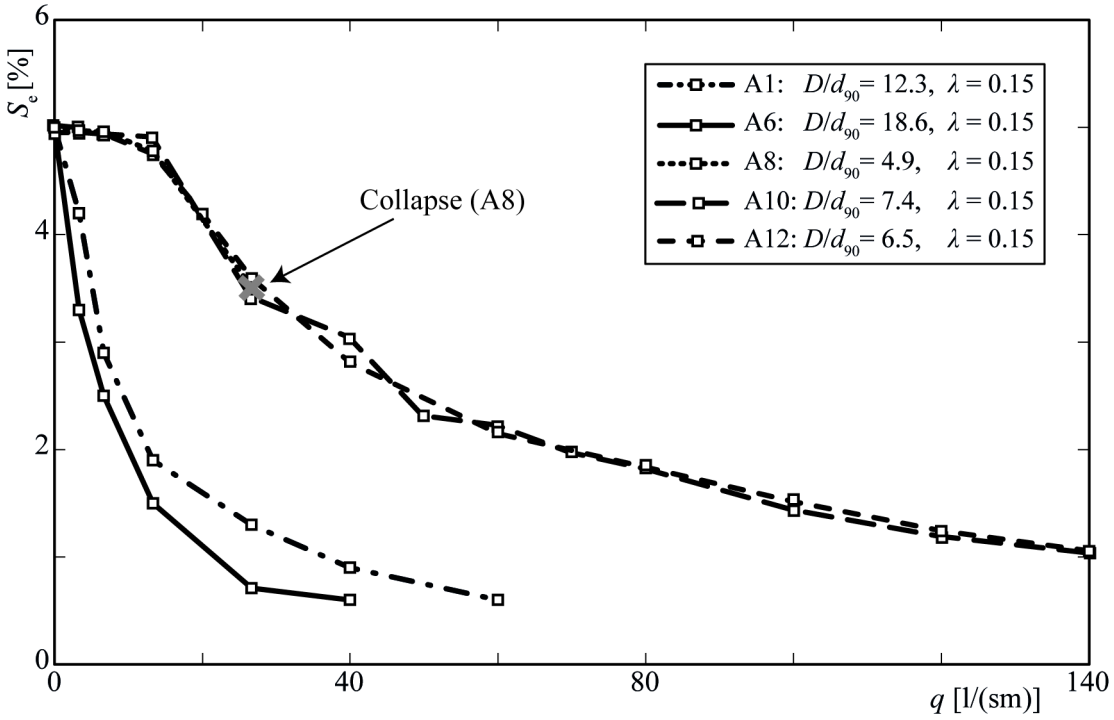

Figure 5.6 Stability diagram for five different experiments (A1, A6, A8, A10 and A12) with different D/d_{90} (different line types) but same $\lambda = 0.15$ (□).

Experiment A8 with $D/d_{90} = 4.9$ also confirmed the theory of Raudkivi and Ettema (1982): up to a certain specific discharge the ramp remained stable. By increasing q the blocks suddenly started to move and they were transported along the ramp. This sudden reduction of λ led to reduced flow resistance and to a sudden failure of the ramp. This sudden failure is here defined as collapse and represented with a cross in Figure 5.6 and in the following stability diagrams. The transition from stable to unstable conditions happened rapidly during a short period, precluding the adjusting process to the higher discharge with a lower slope. In this case, the failure mechanism was similar to the one of classical block ramps, where the failure of local blocks immediately leads to the failure of the complete structure (see Chap. 3.2.2). Figure 5.8 illustrates the development of the bed pattern during A8 with the discharge increase. Up to $q = 13$ l/(sm) very few local blocks movements are recognizable, whereas for $q = 27$ l/(sm) the bed pattern changed completely. Many blocks were transported downstream of the ramp leading to local increased erosion of the sediment material and to the ramp failure (Figure 5.6).

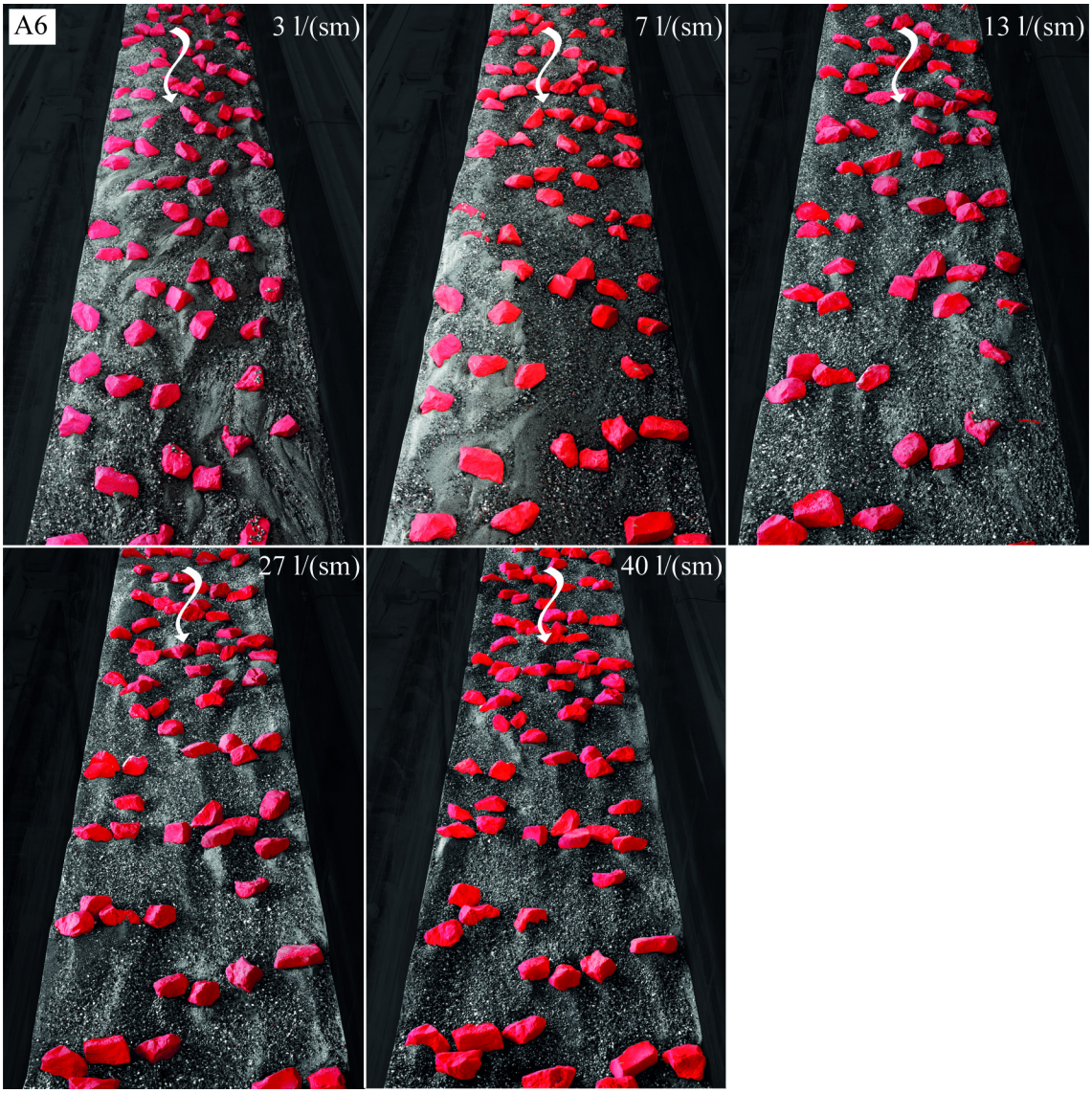

Figure 5.7 Bed pattern in the middle part of the ramp after achievement of equilibrium conditions for different specific discharges during A6 with $D/d_{90} = 18.6$ and $\lambda = 0.15$.

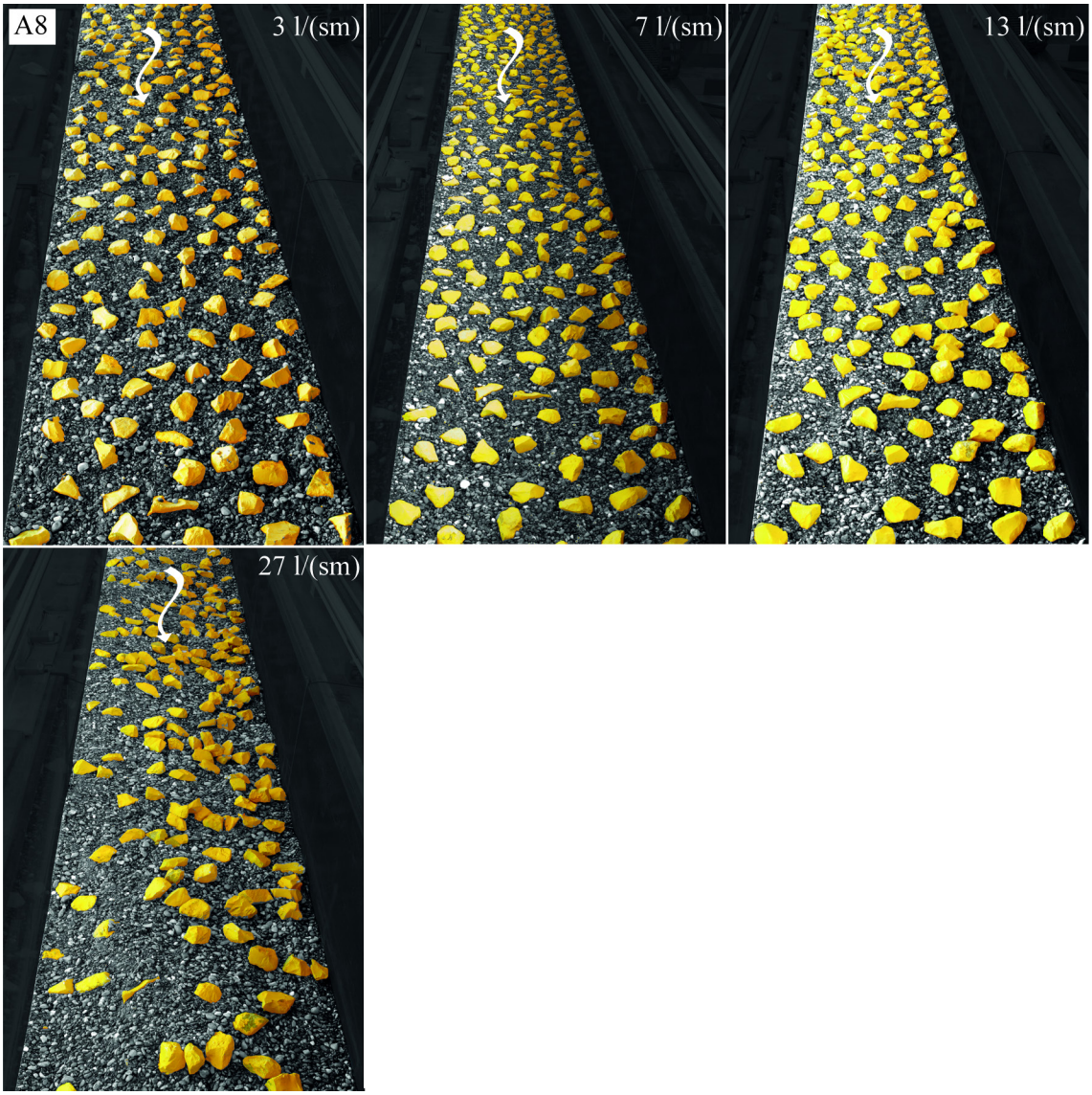

Figure 5.8 Bed pattern in the middle part of the ramp after achievement of equilibrium conditions for different specific discharges during A8 with $D/d_{90} = 4.9$ and $\lambda = 0.15$.

More stable behaviour was reached with $D/d_{90} = 7.4$ (A10): the ramp remained stable also for high discharges ($q = 140$ l/(sm)) corresponding to HQ_{100} or even higher floods in a typical Swiss river, and it did not flatten below 1%. In this case, neither dominant block embedding, nor dominant block overpassing was observed. Figure 5.9 shows the bed pattern during A10 for different discharges. Up to $q = 13$ l/(sm) no significant change was observed; only topography given by the sediment material changed locally leading to bed irregularities. For $q > 13$ l/(sm) the blocks moved locally and grouped in some irregular clusters.

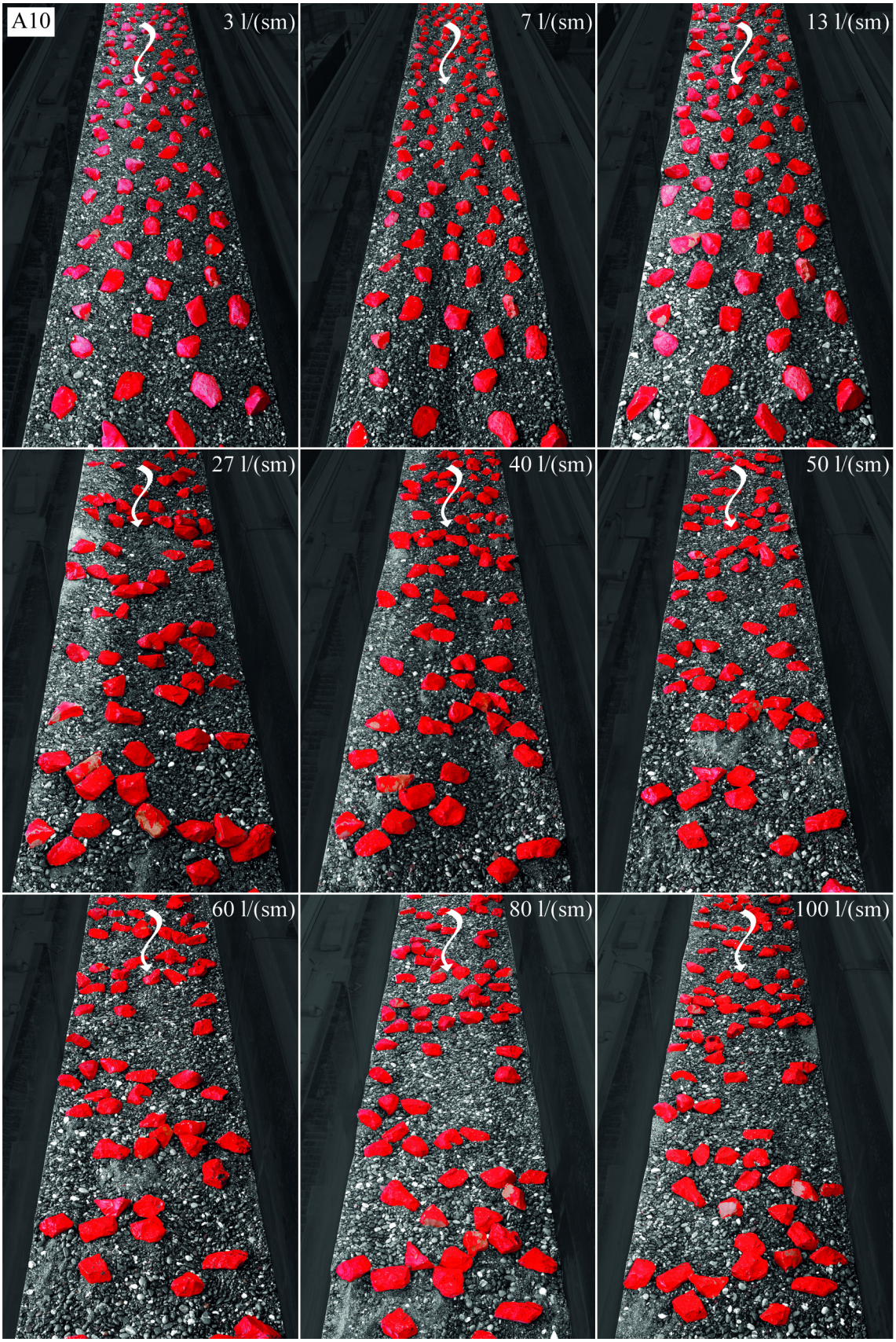

Figure 5.9 Bed pattern in the middle part of the ramp after achievement of equilibrium conditions for different specific discharges during A10 with $D/d_{90} = 7.4$ and $\lambda = 0.15$.

By varying slightly D/d_{90} to 6.5 (A12, Figure 5.6), no significant differences in terms of ramp stability were observed: the stability curves of A10 with $D/d_{90} = 7.4$ and of A12 with $D/d_{90} = 6.5$ show similar erosion process with increasing specific discharge. Therefore, the best ratio D/d_{90} in terms of ramp stability and no abrupt failure mechanism lies in the range of $6.5 \leq D/d_{90} \leq 7.4$. Similar ramp behaviour for $D/d_{90} = 6.5$ and 7.4 confirms the validity of the results: there is no sharp limit between stable and unstable ramp. A gradual and slow erosion process by increasing q was reached within this range of D/d_{90}, so that the uncertainty related to a certain characteristic grain size of the sediment material or block diameter in model as well as in prototype conditions become less important. Note that this applies exclusively for the optimal ratio $6.5 \leq D/d_{90} \leq 7.4$: within this range, the ratio D/d_{90} can vary without affecting the ramp stability significantly. Outside this range, a small change of D/d_{90} can lead to undesired consequences, as e.g. for $D/d_{90} = 4.9$, to an abrupt ramp failure. Therefore, the choice of D/d_{90} is decisive in the design process for the ramp stability and its behaviour during the erosion process.

Similar ramp behaviour was observed by experiments with higher block placement density λ. Figure 5.10 show the results of A5, A7, A9 and A13, where D/d_{90} was varied between 4.9 and 18.6 for constant $\lambda = 0.25$. A dominant embedding process was observed for A7 with $D/d_{90} = 18.6$, similar to A6, leading to a ramp failure already for discharges of $q \approx$ 40-50 l/(sm), corresponding to $HQ_1 - HQ_{10}$. A dominant overpassing process took place during A9, where the ramp behaviour was similar to A8 with a sudden collapse. The ratio $D/d_{90} = 7.4$ led to the most stable ramp, confirming the results with lower $\lambda = 0.15$ (Figure 5.6). $D/d_{90} = 6.5$ was not investigated in combination with $\lambda = 0.25$, assuming similar behaviour as for $D/d_{90} = 7.4$ (Figure 5.6).

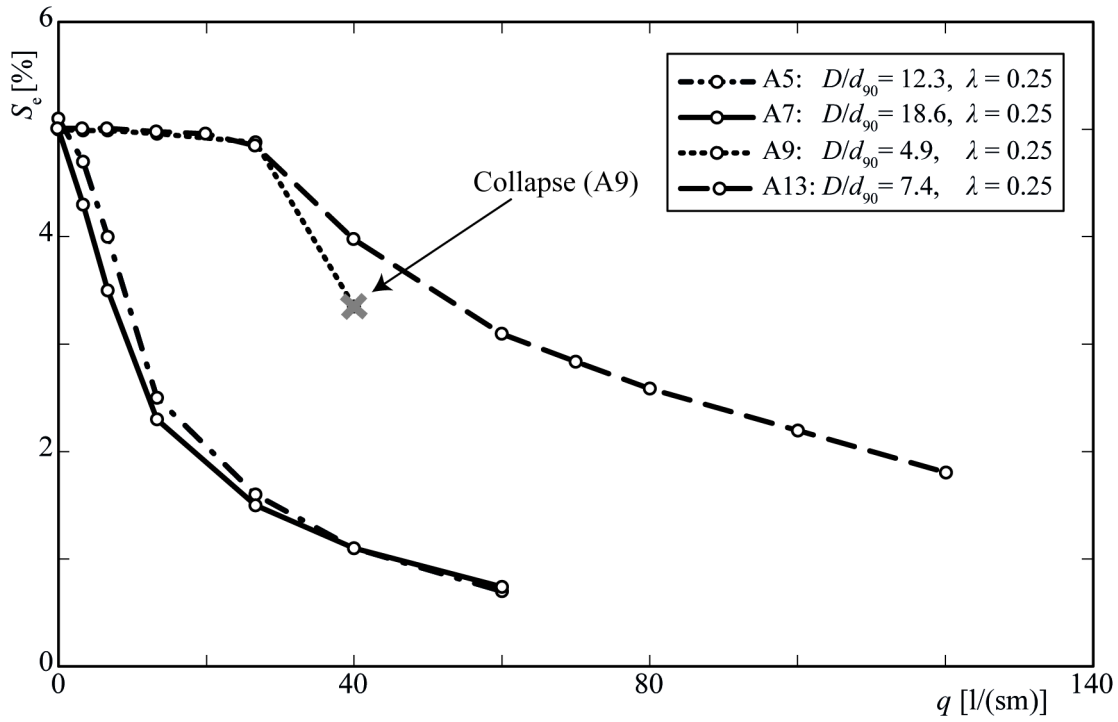

Figure 5.10 Stability diagram for four different experiments (A5, A7, A9 and A13) with different D/d_{90} (different line types) and $\lambda = 0.25$ (○).

The results of A8 and A9 are presented together in Figure 5.11. The ramps with $D/d_{90} = 4.9$ were the only ones that led to a significant block loss. This abrupt failure mechanism (see Chap. 3.2.3) is here defined as collapse. When the ramp collapsed, the test was interrupted and the discharge was not further increased. Figure 5.11 shows the erosion process (grey lines), which is assumed to be realistic for the further ramp flattening for higher discharges. After the block loss, leading to reduced λ, further increase of the discharge would lead to very low equilibrium slopes corresponding to this new λ, still representing $D/d_{90} = 4.9$. The limit situation would be a total block loss, leading to $\lambda = 0$. In this case the erosion process after the ramp collapse would reach and afterwards follow the stability curves determined according to Günter (1971, see Figure 5.3 and Figure 5.4). Block losses lead to reduced flow resistance and to reduced bed protection against erosion. The ramp flattening gets faster and faster, indicated by the grey lines in Fig. 5.4.

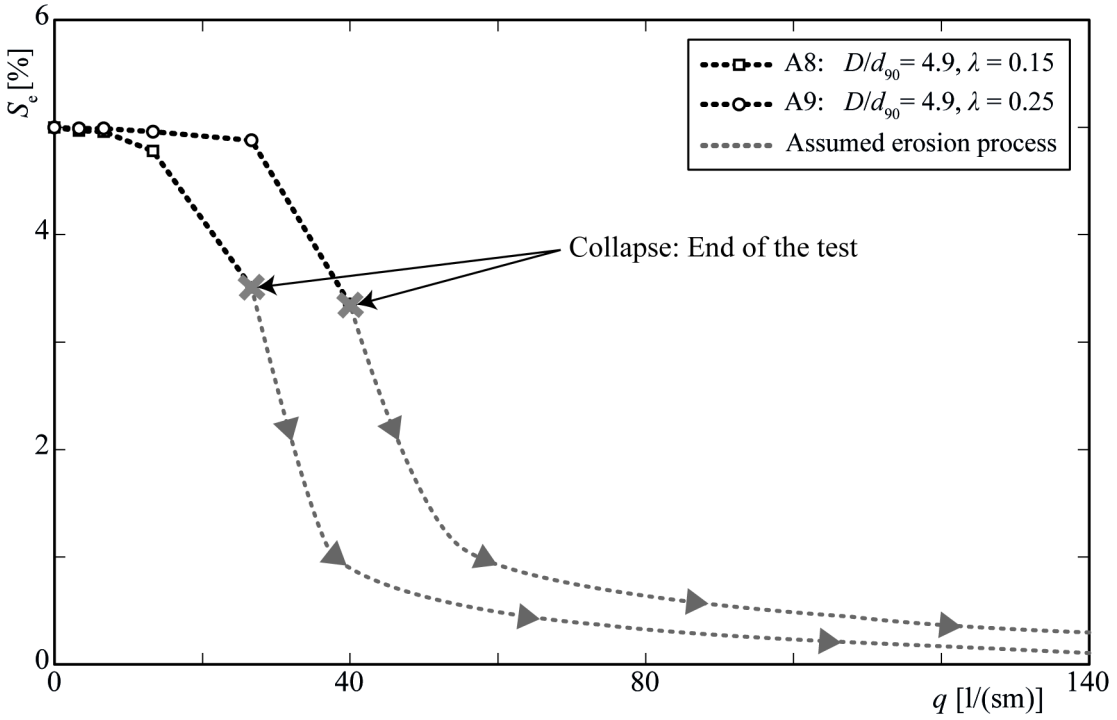

Figure 5.11 Stability diagram for the two tests which led to a ramp collapse (A8 and A9). In grey the assumed further erosion process for discharges higher than these tested is indicated (no measurements, but schematic representation).

Both Figure 5.6 and Figure 5.10 suggest two processes in terms of ramp behaviour: one for D/d_{90} = 12.3 and 18.6 and one for D/d_{90} = 4.9, 6.5 and 7.4. If there is a regular transition from one process to the other or if there is a clear separation between the two processes by varying D/d_{90} between 7.4 and 12.3, it cannot be answered without testing additional D/d_{90}. The parameterisation suggested later in Chap. 5.2.7 with Eqs. (5.2) and (5.3) does not consider the two different trends separately. The effect of D/d_{90} is considered in the definition of a dimensionless specific discharge q_d^* (Eq. 5.1).

5.2.4 Effect of block placement density λ

According to Rouse (1965, see Chap. 2.2 and Figure 2.2) an optimal placement density in terms of flow resistance is between 10% and 40%, depending on the roughness shape and arrangement. The present research aims at finding an optimal parameter combination in terms of ramp stability but also in terms of project feasibility (e.g. cost effectiveness). For this reason, the maximal block placement density investigated here was λ = 0.25.

Figure 5.12 shows the comparison between stability of ramps with $\lambda = 0.15$ and $\lambda = 0.25$ for different D/d_{90}. In the case of $D/d_{90} = 12.3$ (A1 and A5) the higher block placement density λ led to an equilibrium slope S_e approximately 20% higher compared to $\lambda = 0.15$. For $q < 10$ l/(sm) the equilibrium slope with $\lambda = 0.25$ was 40% steeper than with $\lambda = 0.15$. Figure 5.13 compares the bed pattern of A1 and A5: the block rearrangement for A5 is less recognizable, due to the high block placement density and to less free area available for block displacements. However, in general also during the experiments with $\lambda = 0.25$ the blocks moved locally. The influence of λ was higher in the case of $D/d_{90} = 18.6$ (A6 and A7) compared to $D/d_{90} = 12.3$, where the ramp with $\lambda = 0.25$ was almost 1.5 to 2 times steeper than the ramp with $\lambda = 0.15$ for $10 \text{ l/(sm)} \leq q \leq 40 \text{ l/(sm)}$. In the case of $D/d_{90} = 4.9$ (A8 and A9), where both ramps remained stable up to a certain discharge and then collapsed, the higher λ "delayed" the collapse to a higher discharge without impeding it. For $q < 20$ l/(sm) λ did not influence significantly the ramp stability. Also in the case of the most stable ratio $D/d_{90} = 7.4$ (A10 and A13), λ did not influence significantly the ramp stability for $q < 20$ l/(sm), while the slope increased by approximately 30%-50% for $q > 30$ l/(sm) with increasing λ from 0.15 to 0.25.

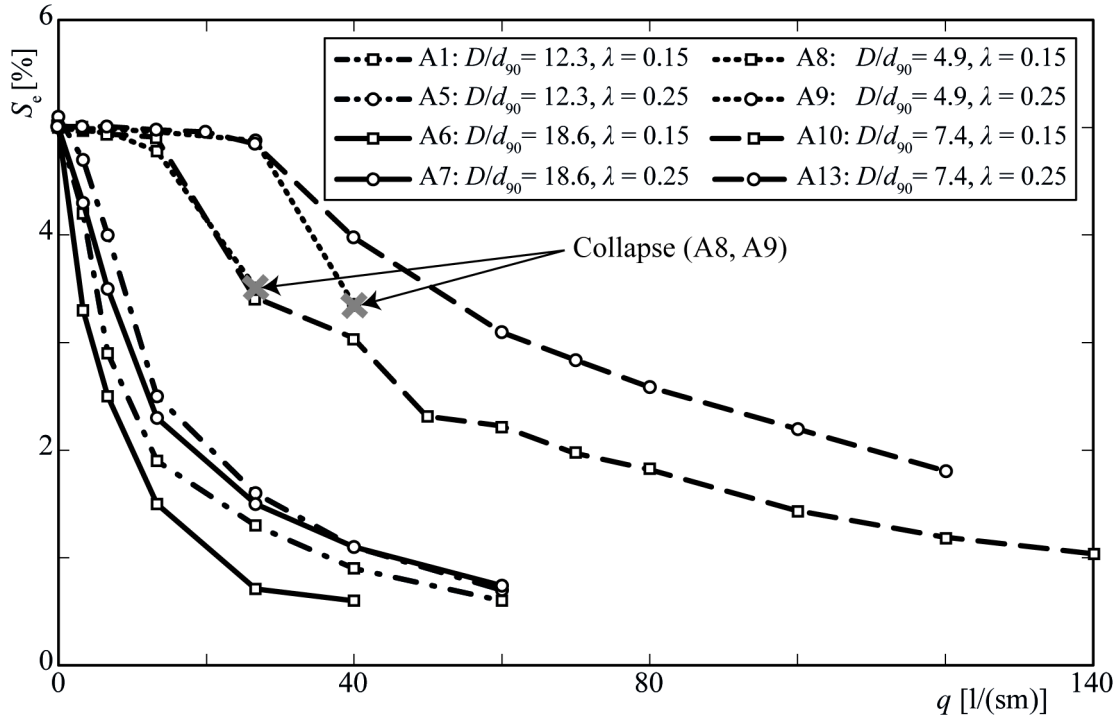

Figure 5.12 Resulting equilibrium slopes for $\lambda = 0.15$ (□) and $\lambda = 0.25$ (○) for different D/d_{90} (different line types).

With these experiments the effect of λ was shown. It is now possible to better evaluate the optimal parameter combination during the design process, balancing the pursued ramp stability and the ramp costs (higher λ, higher costs). It was not investigated, however, which block placement density λ corresponds to an optimum. Rouse (1965) suggested for spheres an optimal block placement density in terms of flow resistance of $\lambda_{opt} \approx 0.26$ (Figure 2.2). For lower λ the maximum relative roughness and the maximum form drag, respectively, are not achieved. For higher λ, the roughness elements are too close to each other: the area affected by one single block is "disturbed" by the presence of the next block and the flow separation cannot develop completely, leading to reduced energy dissipation compared to lower λ. For λ_{opt} each single block contributes with its maximum form drag to the flow resistance. An interesting analogy can be found e.g. in Brumley and Jirka (1987), suggesting that a grid in a tank produces the highest turbulence when its degree of obstruction is about 0.36.

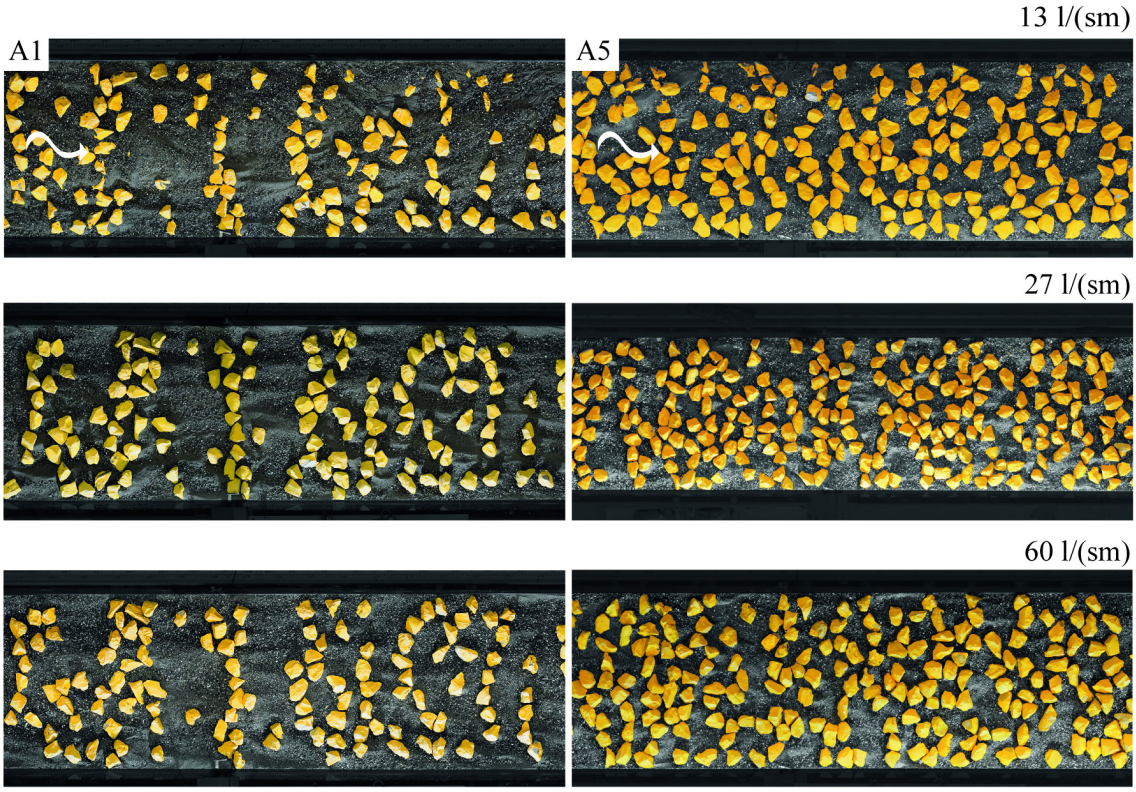

Figure 5.13 Bed pattern in the middle part of the ramp after achievement of equilibrium conditions for different specific discharges during A1 with $\lambda = 0.15$ and A5 with $\lambda = 0.25$ (both experiments with $D/d_{90} = 12.3$).

5.2.5 Effect of sediment supply

As described in Chap. 4.2.6, the aim of the experiments with sediment supply was to determine a general influence of transported sediment on the ramp stability. A theoretical transport capacity according to Meyer-Peter and Müller (1948) for an assumed bed slope of 1% upstream of the ramp was tested. The resulting supply rate was e.g. 45 g/s for q = 40 l/(sm), 236 g/s for q = 100 l/(sm) and 360 g/s for q = 140 l/(sm). Considering the time t_{eq} needed to reach equilibrium conditions of these three runs (see Chap. 4.2.5 and Table 4.6), a total sediment mass of 3.6 t, 11.9 t and 9.1 t, respectively, was supplied. The transported sediment filled the filtering basket at the flume end (Figure 4.1) within 0.5 to 2 hours, forcing an interruption of the run to empty the basket and leading to very high experimental durations. Therefore, the effect of the sediment supply was only tested on the ramp with optimal parameter combination in terms of stability, namely for D/d_{90} = 7.4 with λ = 0.15 (A11) and λ = 0.25 (A14), respectively.

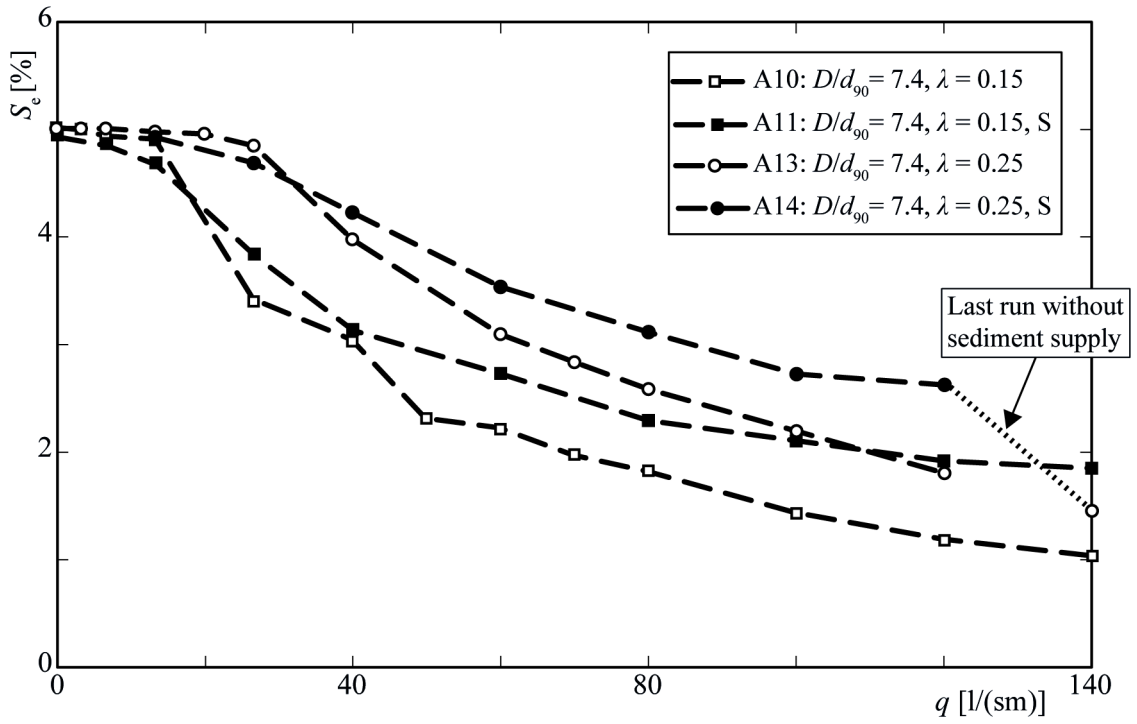

Figure 5.14 Stability curves for experiments without (empty symbols) and with (filled symbols) sediment supply (S) of ramps with D/d_{90} = 7.4 and λ = 0.15 (□) and λ = 0.25 (○).

The sediment supply had a stabilizing effect on the block ramps tested (Figure 5.14). The equilibrium slopes S_e of A11 and A14 resulted for $q > 40$ l/(sm) about 15% to 75% steeper than in the case without sediment supply (A10 and A13). Due to the resulting higher stability of the experiments with sediment supply, those without sediment supply are considered as critical load cases and as representative for the design.

The stabilizing effect of the sediment supply cannot be generalized for other sediment supply rates (not investigated), but it can be assumed to be generally valid. The sediment transported on the ramp fills the local scour holes that are generated when the discharge conditions do not reach the transport capacity and erosion occurs. They are generally located downstream of the blocks. Due to the scour holes filled by the transported sediment, the blocks are "packed" more thightly within the sediment layer, leading in general to a higher stability.

Figure 5.15 compares the bed pattern development during A10 without and A11 with sediment supply. The block rearrangement was stronger when the slope decrease was high, namely for 27 l/(sm) < q < 80 l/(sm) for A11 (see Figure 5.14). It can be observed how the blocks are generally packed more thightly within the sediment layer in the pictures of A11 than for A10, in particular for $q > 40$ l/(sm). Figure 5.16 illustrates the bed patterns of A11 and of A14 after the run with highest specific discharge $q = 140$ l/(sm). The packing effect of the sediment supply is distinct in both cases.

Last run without sediment supply

The last run at $q = 140$ l/(sm) of A14 was carried out without sediment supply. Two considerations can be drawn from its results: 1) the influence of the sediment supply is quite distinct, especially for high discharges. When the transported sediment rate is low (e.g. during the rising limb of a flood when the armour layer is still stable), the erosion trend increases. 2) It is supposed that the equilibrium slope S_e does not significantly depend on initial conditions and on initial ramp slope, respectively. The resulting S_e of A14 for $q = 140$ l/(sm) corresponds to the trend of the stability curve resulting from A13 without sediment supply. This aspect supports the reliability of the results of single runs, due to their independency on the previous run as long the ramp is in an erosive trend. Previous experiments conducted on UBR at VAW investigated this independency on initial conditions. The results showed that ramps built with the same parameter configuration but with different initial slopes (3%, 5% and 7%) have the same behaviour

after the first runs with low load (e.g. Tamagni 2006). The ramp is affected by initial conditions exclusively for low specific discharges, where in particular its morphological and local conditions change, but not the slope. In contrast, the resulting equilibrium slope after a run with high load, where the local conditions become more homogeneous and the slope strongly varies between one run and the next one, is not affected by initial conditions.

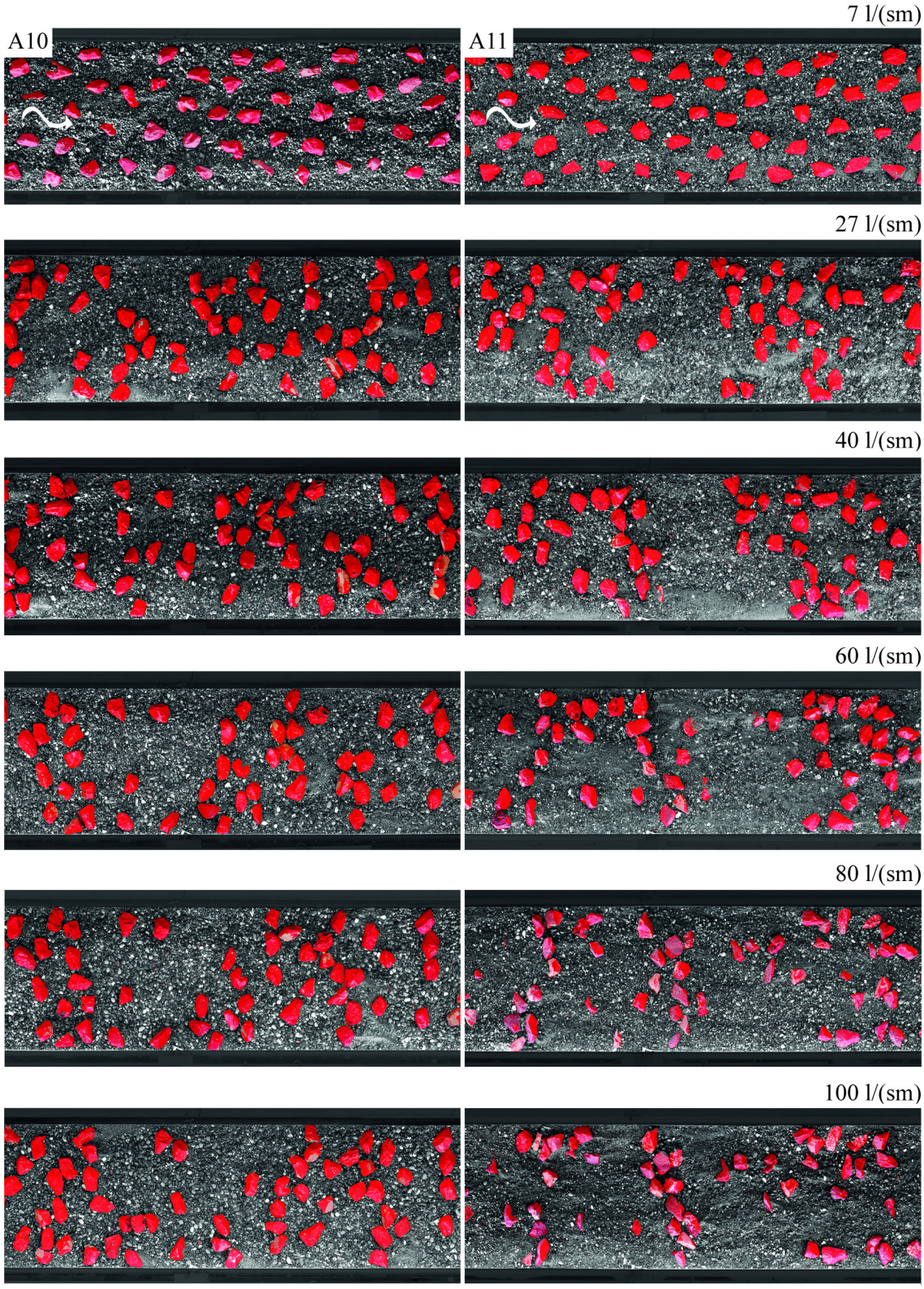

Figure 5.15 Bed pattern in the middle part of the ramp after achievement of equilibrium conditions for different specific discharges during A10 without sediment supply and A11 with sediment supply (both experiments with $D/d_{90} = 7.4$ and $\lambda = 0.15$).

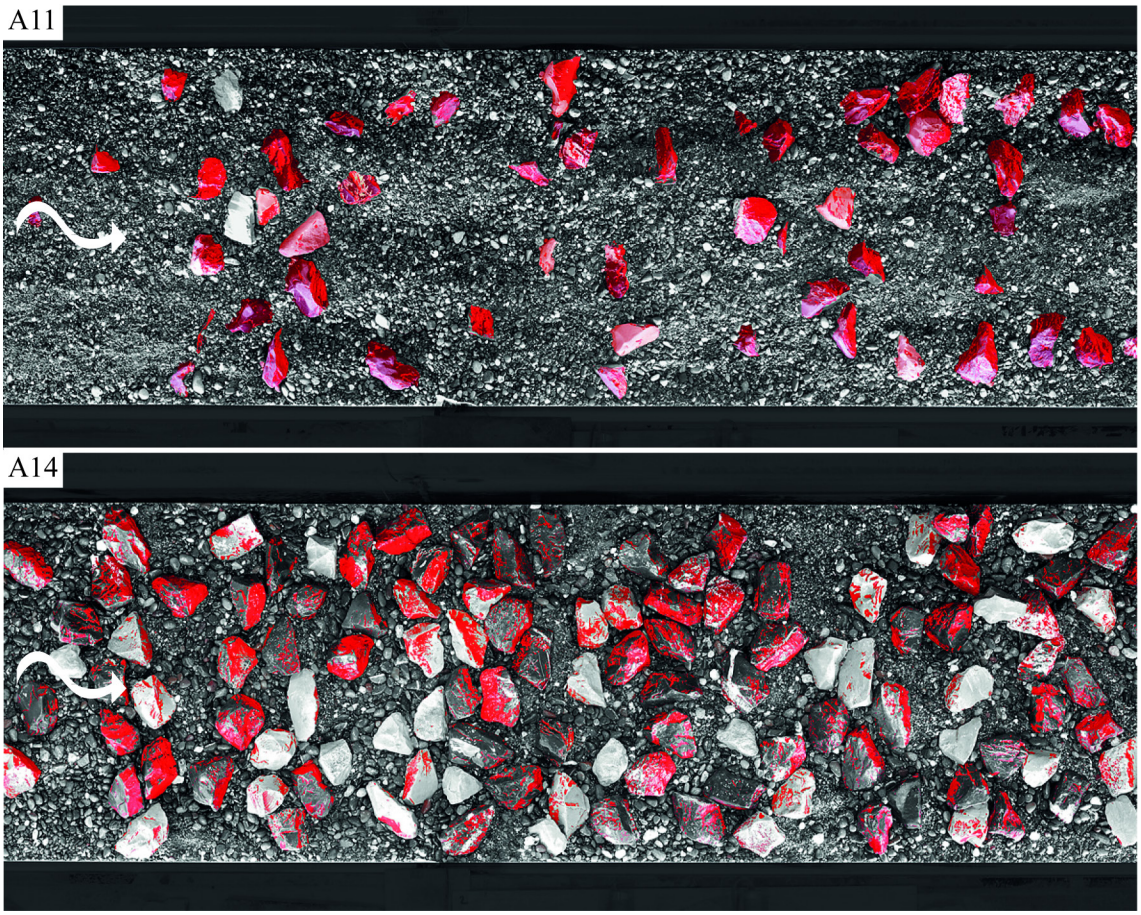

Figure 5.16 Bed pattern in the middle part of the ramp after achievement of equilibrium conditions for q = 140 l/(sm) during A11 with λ = 0.15 and A14 with λ = 0.25 (both experiments with D/d_{90} = 7.4 and sediment supply).

5.2.6 Effect of material composition and grain size distribution

Two uniform materials were used to investigate the effect of the standard deviation σ of the bed material on the ramp stability (Table 4.1). This effect is particularly important for model purposes: a certain sediment mixture is often modelled as uniform material to simplify the investigation and especially to reduce operational efforts. Therefore, it is important to understand which differences exist by modelling the sediment material in the two ways, namely as a mixture or as a representative uniform material. For the present research, the mean grain size of the uniform material d_m nearly corresponds to the d_{90} of the sediment mixture, in order to reproduce the erosion resistance of the armour layer of the mixture (Chap. 4.2.3).The difference in the behaviour of a ramp built with sediment mixture (FM or CM in A1 and A10) and with uniform material (UM-FM or UM-CM in A3 and A15) is illustrated in Figure 5.17.

For $D/d_{90} = 12.3$ the ramp built with uniform material UM-FM (A3) led to 10% to 30% higher equilibrium slope S_e compared to the ramp with the fine mixture FM (A1). The finer grain fractions of FM, which are entrained during low discharges already, are missing in the uniform material UM-FM. The erosion process started at higher discharges, leading to higher equilibrium slopes for the same discharge conditions.

Also for $D/d_{90} = 6.6$ the ramp with uniform material UM-CM (A15) led to more stable conditions than on the ramp with the coarse mixture CM (A10). In this case S_e was 40% to 70% steeper for $q > 20$ l/(sm). The stabilizing effect of UM-CM is the same as already described for the case of UM-FM. The grain size distribution of CM is wider compared to FM ($\sigma_{CM} = 3.3$ and $\sigma_{FM} = 2.7$, Table 4.1) leading to a bigger difference in the ramp behaviour between CM (A10) and UM-CM (A15) than between FM (A1) and UM-FM (A3). Note that this bigger difference in the ramp behaviour could also derive from the different ratios D/d_{90}: A1 and A3 had same ratio $D/d_{90} = 12.3$, whereas A10 and A15 had different ratio, $D/d_{90} = 7.4$ and 6.6, respectively. It is not possible to quantify which aspect (uniform material or different ratio D/d_{90}) plays a more decisive role in terms of ramp stability. However, based on similar results for $6.5 \leq D/d_{90} \leq 7.4$ as for A10 and A12 (see Figure 5.6), the effect of the grain size distribution is supposed to be more relevant here.

Figure 5.18 illustrates the bed patterns for the experiments A1 and A10 with sediment mixture (left) and those for A3 and A15 with uniform material (right). The local bed irregularities were stronger for the experiments with the sediment mixtures. The sediment bars formed during A3 (Figure 5.18 top right) was not a characteristic only of A3, but similar sediment bars were also found during A1 and A1rep for low specific discharges.

It can therefore be concluded that the modelling of a block ramp with uniform material nearly corresponding to d_{90} of the sediment mixture overestimates the ramp stability. It is assumed that modelling a UBR with uniform material corresponding to d_m of the sediment mixture underestimates the ramp stability but better describes the sediment transport rate. The stability is underestimated because the grains of uniform material are entrained during lower specific discharges than the grains of the sediment mixture, containing also coarser grains than d_m that are entrained only during higher discharges. Which grain size of a sediment mixture should be selected for the corresponding uniform material depends on the main research question (sediment entrainment, river bed

stability, sediment transport rate, morphology) and on the characteristics of the grain size distribution: the wider the grain size distribution, the more difficult it is to reproduce the sediment transport processes with uniform material.

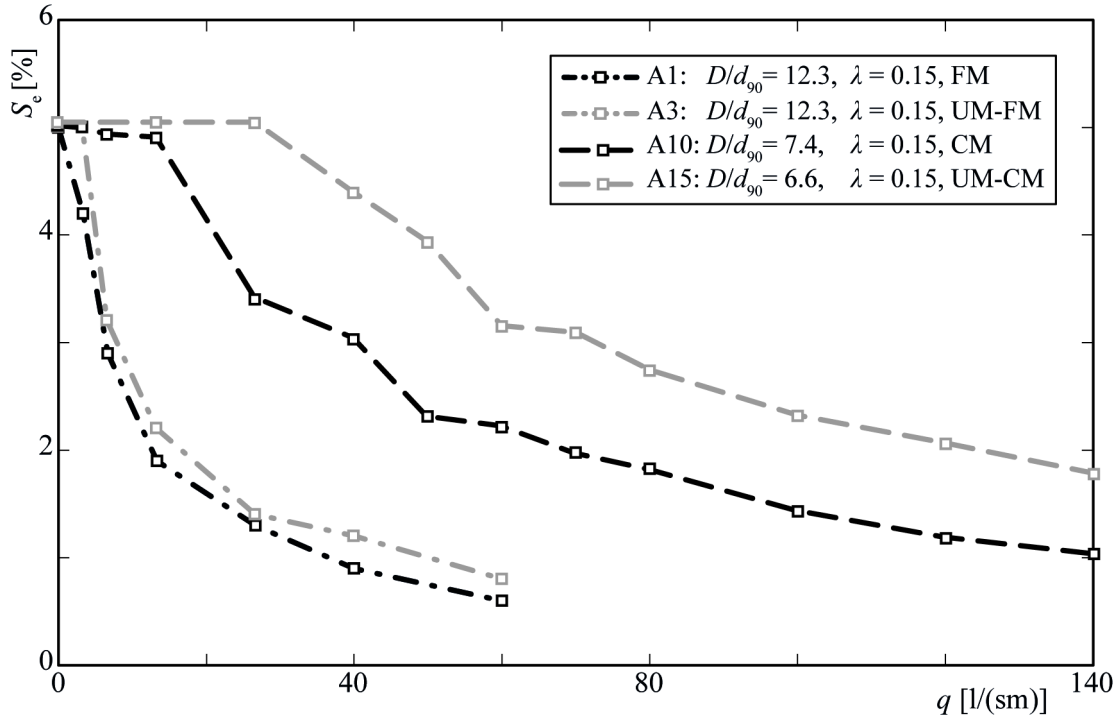

Figure 5.17 Stability of ramps with sediment mixture (FM or CM, black lines) and ramp with correspondent uniform material (UM-FM and CM-FM, grey lines).

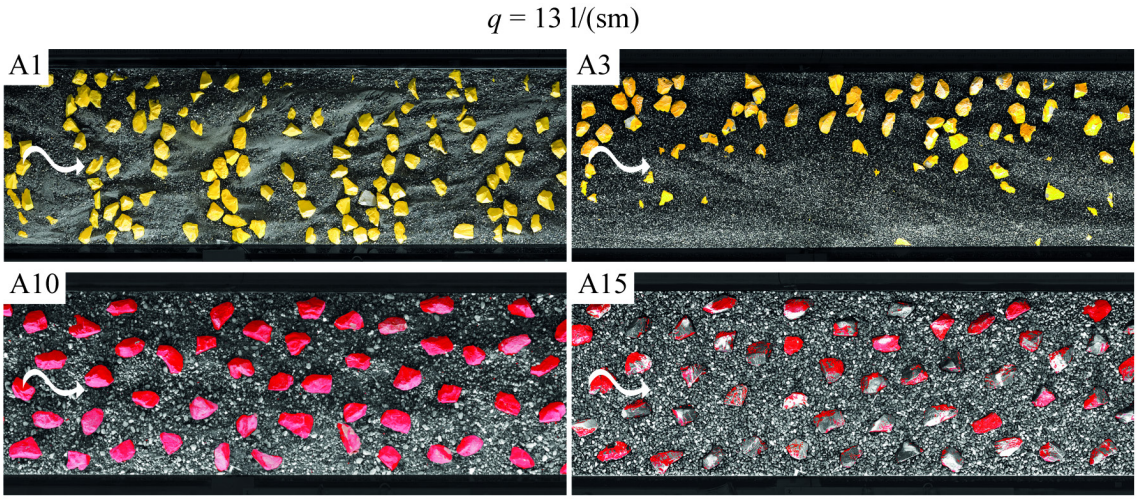

Figure 5.18 Bed pattern in the middle part of the ramp after achievement of equilibrium conditions for q = 13 l/(sm) during A1 with FM, A3 with UM-FM, A10 with CM and A15 with UM-CM (all experiments with λ = 0.15).

5.2.7 Ramp stability

In this chapter a model for the determination of the ramp stability is presented. The model consists of a parameterisation, allowing to generalize the experimental results and to apply them to other data sets. The relative block protrusion P/D with P = block protrusion or exposed block height (Figure 2.8) and D = block diameter describes the roughness of the bed and is decisive for the determination of the ramp stability and the flow resistance. Large values of P/D are not suitable in terms of block stability, because strongly exposed blocks have a low entrainment threshold and critical shear stress (see Chap. 2.3), respectively. A too low P/D is not suitable in terms of flow resistance, because the protruding block area is small and does not produce the maximum form drag and flow resistance. An optimum value of P/D needs to be found. In our case P/D is changing during the ramp flattening.

As described in Chap. 4.2.7, P/D was derived from the measurements with the laser distance sensor with the measuring grid 1×1 cm^2. Figure 5.19 shows the mean relative block protrusion of each run and of each experiment. Considering only the results for $q > 13$ l/(sm) to eliminate the effect of the initial conditions, the mean relative block protrusions measured were mostly in the range between 0.7 and 0.9. For practical and design purposes it is suggested to assume a relative block protrusion $P/D = 0.7$, corresponding to a conservative value in terms of flow resistance.

P/D was also determined separately depending on e.g. D/d_{90} or λ. No particular influence of any parameter was identified. An exception is represented by the experiments with sediment supply (A11 and A14 with filled symbols in Figure 5.19) that indicated lower $P/D \approx 0.5 - 0.7$, because of the transported but also deposited sediment along the ramp. Lower P/D should lead to lower ramp stability because the form drag resulting from the protruding blocks is lower than for higher P/D. But in the case of experiment with sediment supply, the ramp stability was higher than for experiments without sediment supply (Chap. 5.2.5) even with lower P/D. Presumably the "filling and packing effect" of the transported sediment on the block ramp (Chap. 5.2.5) had a higher effect on the ramp stability than the lower resistance given by the blocks with lower P/D. Note that the effect of the block shape on the flow resistance was not investigated and the natural blocks used were simplified as spheres with equivalent diameters D (see standard deviations of D in Table 4.2).

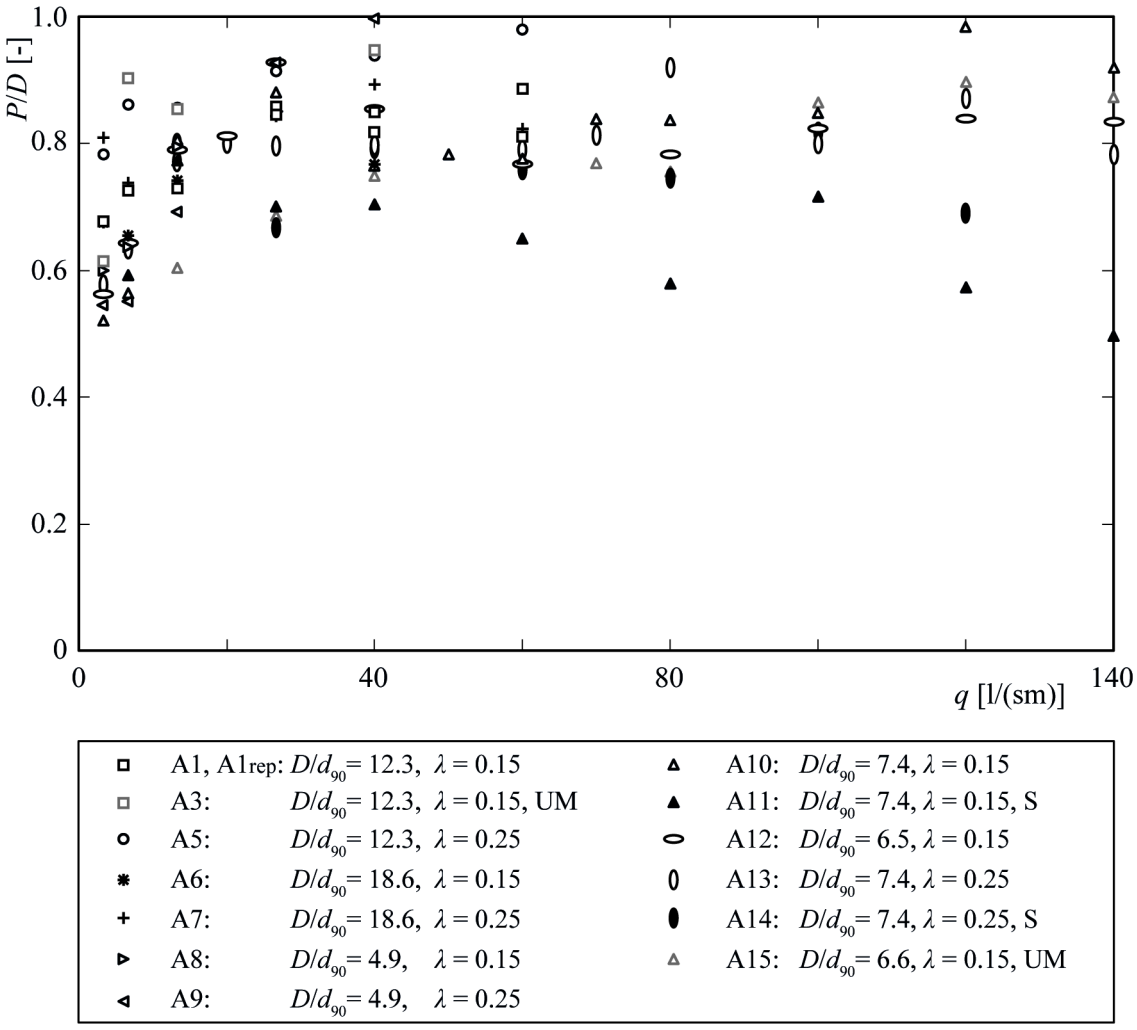

Figure 5.19 Relative block protrusion P/D versus specific discharge q of all conducted experiments.

The experiments of phase A under steady conditions represent the minimum possible slope in function of a certain specific discharge ($S_e = f(q)$) for the considered ramp due to the long test duration and the harsh criterion to reach equilibrium conditions, which are rarely reached under prototype conditions. Therefore, the resulting stability curves $S_e = f(q)$ represent a conservative assumption for the ramp design, covering a certain range of uncertainties associated with natural irregular block shape and diameter and natural variability in the bed material.

To parameterize the equilibrium slope S_e the following parameters were considered: specific discharge q, equivalent spherical block diameter D, the ratio between block diameter and characteristic grain size D/d_{90}, block placement density λ, the gravity acceleration g and the ratio between sediment and water density $s = \rho_s/\rho = 2.65$, so that $S_e = f(q, D, D/d_{90}, \lambda, g, s)$. In order to find a suitable function describing S_e, the

effect of these parameters was analyzed and introduced stepwise as follows. Figure 5.20 (a) illustrates the stability diagram for all the experiments conducted under steady conditions during phase A (Chaps. 5.2.1 –5.2.6). The effect of D, g, and s was introduced by normalizing the specific discharge with these parameters, resulting in q / (g (s-1) D^3)$^{0.5}$. It was derived applying the dimensional analysis with the Buckingham Π Theorem (e.g. Martin and Pohl 2009) and assuming the three considered parameters decisive for the ramp stability, in particular D as characterizing diameter of the bed. Figure 5.20 (b) shows the relationship between S_e and the newly defined dimensionless specific discharge. No trend is clearly recognisable, although the data scatter is smaller than for Figure 5.20 (a).

In a second step the effect of λ was included by multiplying the above defined dimensionless specific discharge with λ with a suitable power coefficient, in order to bring together the experiments with same D/d_{90} but different λ. Figure 5.21 (a) illustrates S_e as function of this new parameter. Compared to Figure 5.20 (b) the results of experiments with same D/d_{90} but different λ (A1 and A5, A6 and A7, A8 and A9, A10 and A13) now follow a similar trend.

Finally the effect of D/d_{90} was included: the block diameter and the characteristic grain size of the sediment material were considered together due to their influence on the failure mechanisms and transport processes occurring on UBR (Raudkivi and Ettema 1982 and Chap. 2.3.4). The best power coefficient was determined in order to merge the data on a curve with least scatter possible. Figure 5.21 (b) shows the relationship between S_e and the dimensionless specific discharge including also D/d_{90} as

$$q_d{}^* = \frac{q}{\sqrt{g(s-1)D^3}}\,\lambda^{-1}\left(\frac{D}{d_{90}}\right)^2. \qquad (5.1)$$

The dimensionless specific discharge $q_d{}^*$ represents the parameterisation of the equilibrium slope S_e resulting from the experimental results and can be considered as design parameter for UBR.

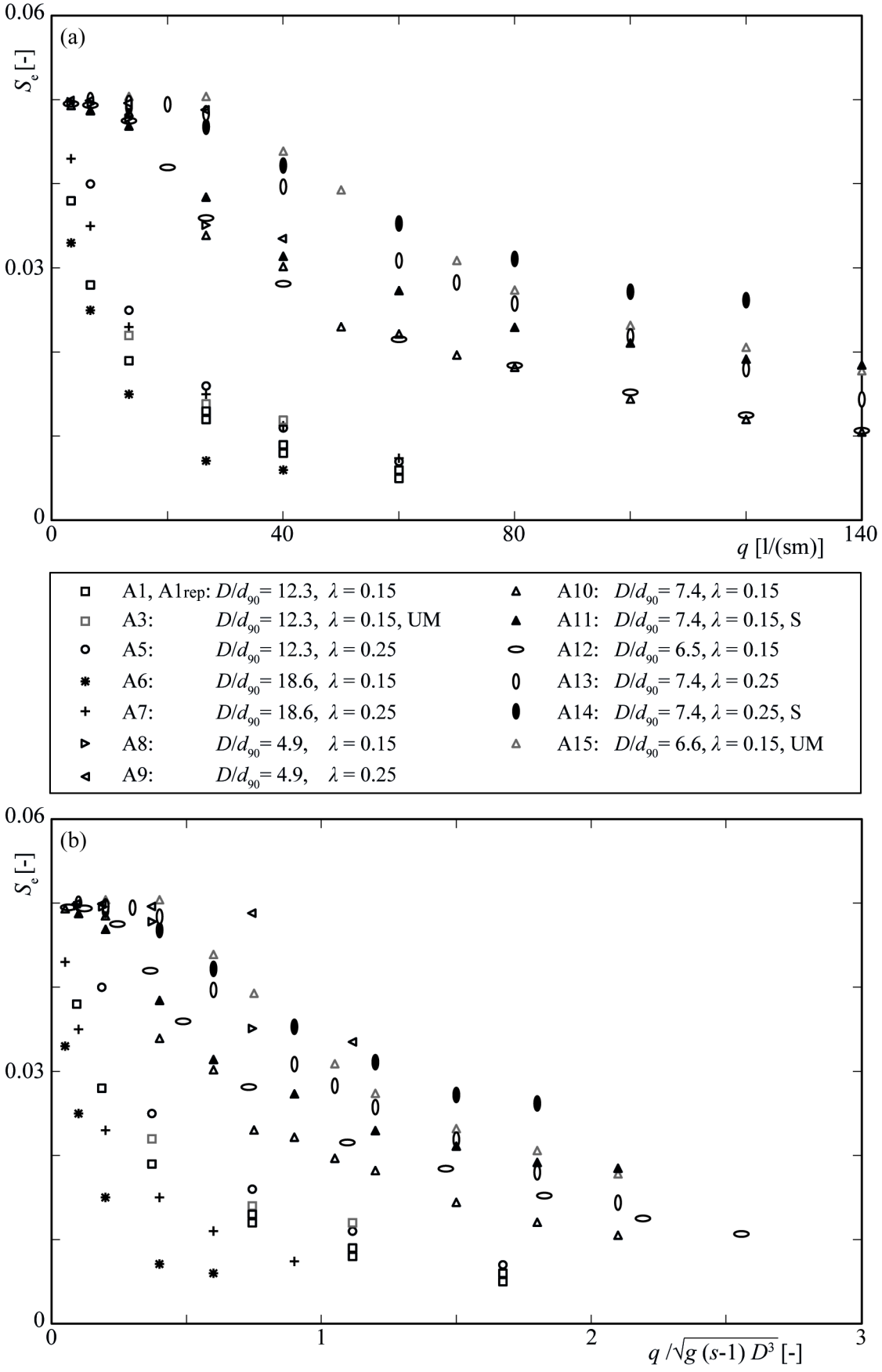

Figure 5.20 Equilibrium slope S_e versus (a) specific discharge q, and (b) dimensionless specific discharge q / (g (s-1) D^3)$^{0.5}$ for all experiments of phase A.

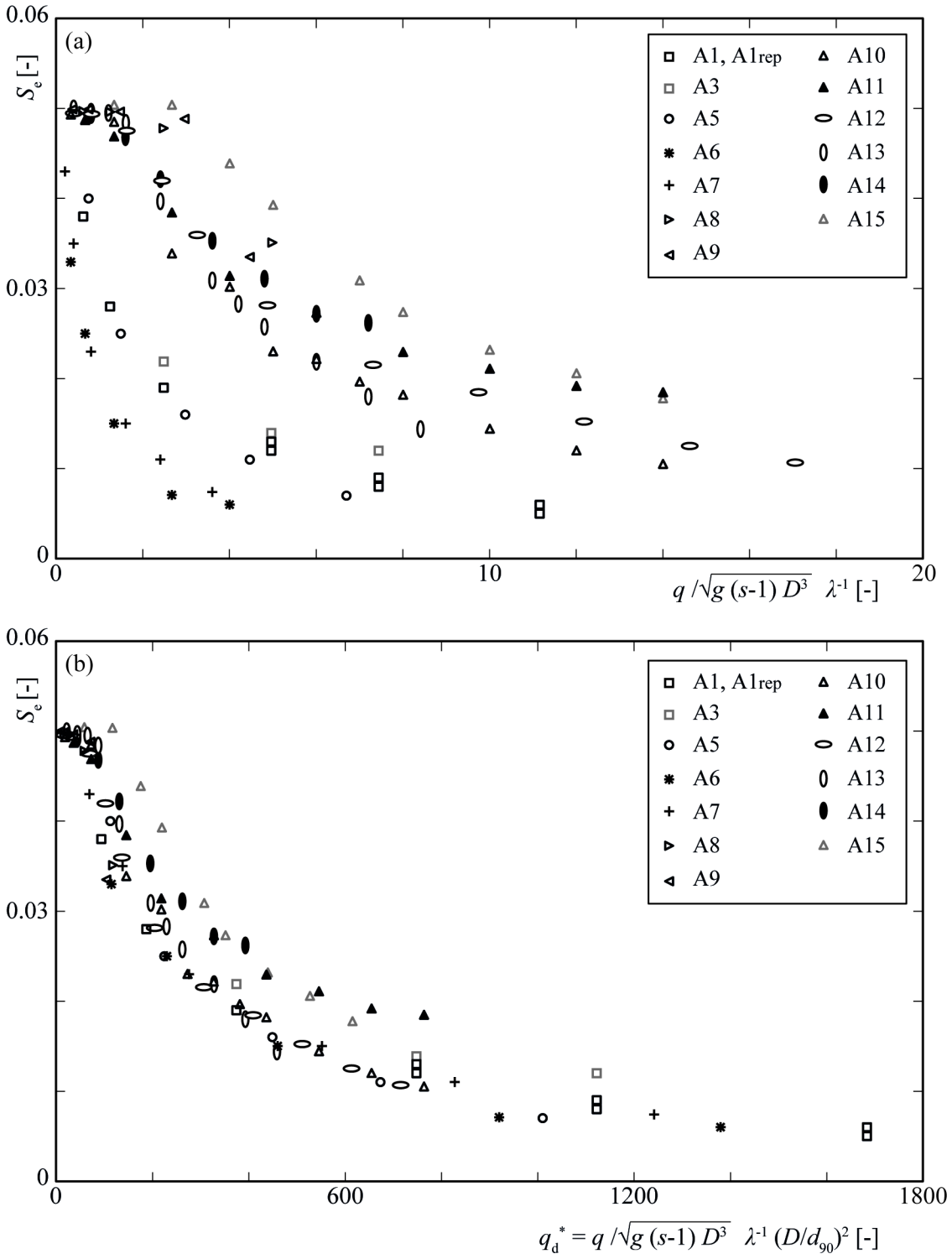

Figure 5.21 Equilibrium slope S_e versus (a) dimensionless specific discharge accounting for block placement density, and (b) dimensionless specific discharge taking into account the ratio D/d_{90} for all experiments of phase A.

All data in Figure 5.21 (b) follow a similar trend. The results of the experiments with sediment supply (A11 and A14) as well as those with uniform material (A15) also

follow a similar trend, but lie above the other data due to their more stable behaviour (see Chaps. 5.2.5 and 5.2.6). The data of A3 follow the trend but due to the uniformity of the bed material were not considered in the data fit. In order to find a conservative fit for design purposes (see above), A3, A11, A14 and A15 were not considered in the following data fit. Figure 5.22 shows S_e versus q_d^* for all experiments. The black line represents the data fit for all experiments considered describing the determined points with R^2 = coefficient of determination = 0.97:

$$S_e = \frac{11}{q_d^* + 200} \qquad \text{for } q_d^* < 1700. \tag{5.2}$$

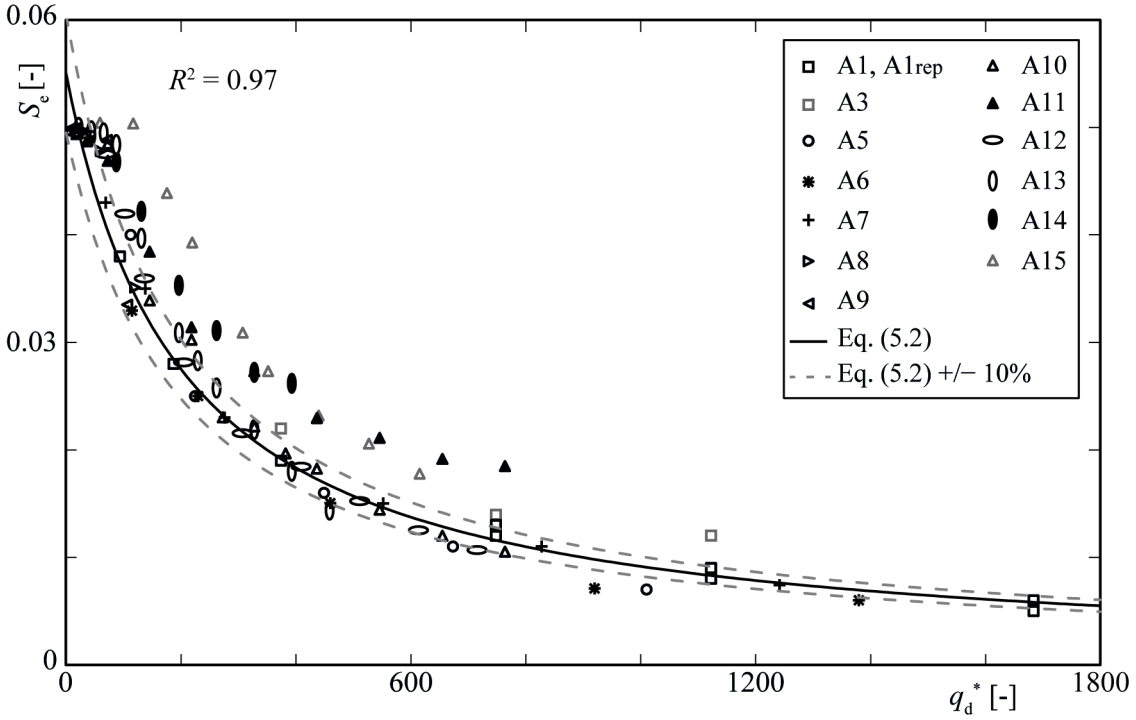

Figure 5.22 Ramp stability in terms of equilibrium slope S_e for all conducted experiments versus dimensionless specific discharge q_d^*. Black line: Eq. (5.2); dotted grey lines: variation range of +/− 10% with respect to Eq. (5.2). Particularly stable experiments (A3, A11, A14 and A15) were not considered in Eq. (5.2)

The grey dotted lines illustrate the lower and upper limit of the variation range +/− 10% of Eq. (5.2). Almost all data fit in between this variation range, except those representing the more stable configurations of experiments A3, A11, A14 and A15 (see above) with a 10% to 30% higher S_e. In case of pronounced sediment transport, the

equilibrium slope S_e can be assumed to be at least 10% higher than determined with Eq. (5.2).

Eq. (5.2) is valid for the tested application range, namely for $4.9 < D/d_{90} < 18.6$, $0.15 < \lambda < 0.25$, $S_0 < 5\%$, and $0 < q_d^* < 1700$. The application of Eq. (5.2) up to $q_d^* = 1700$ is arguable, due to the resulting $S_e < 1\%$. Usually UBR require a higher S_e, but the data fit is shown also for these low slopes to illustrate the trend derived from the results. Note that for Eq. (5.2) only two placement densities $\lambda = 0.15$ and $\lambda = 0.25$ were investigated.

5.2.8 Flow depth and mean flow velocity on UBR

To parameterize the resulting mean flow depth h_m, the data were analysed in a similar way as for S_e, accounting for the relative submergence h_m/D. The mean flow depth h_m is related to the block diameter D and not to the block protrusion P, because during the design of a UBR, when this parameterization can be applied, only D is known. The flow depth was measured continuously during all the experiments with 3 pairs of ultrasonic sensors at three different cross sections along the ramp (see Figure 4.1). The measured h_i were strongly affected both from the local bed levels (e.g. block below the ultrasonic sensor) and from the surface waves occurring for $h/P \approx 1$. Therefore, the 6 different measured flow depths h_i varied significantly from each other (Figure 5.23 a). Therefore, the mean flow depth h_m was derived from the bulk velocity u_b determined with the salt dilution method and applying continuity. The effective flow cross-sectional area A_{eff} was determined as $A_{eff} = Q/u_b$, from which the effective flow depth h_{eff} was easily derived with $h_{eff} = A_{eff}/W_R$ (Figure 5.23 b). According to the considered parameter combination D, P and λ, a theoretical total volume occupied by the blocks along the ramp was determined, from which the theoretical mean area per cross-section A_B and so the theoretical mean depth occupied by the block h_{th} was derived as $h_{th} = \Sigma A_B/W_R$. The mean water depth h_m resulted from the sum of the effective flow depth h_{eff} and the theoretical flow depth occupied by blocks h_{th} as $h_m = h_{eff} + h_{th}$ (Figure 5.23 b). For design purpose it is important to determine the water level for a certain discharge. Considering exclusively h_{eff} (derived from the continuity equation) would underestimate this water level, whereas h_m, which also considers the presence of the blocks, represents a better approximation for the first design steps. Therefore, for the following considerations h_m was assumed as representative mean flow depth.

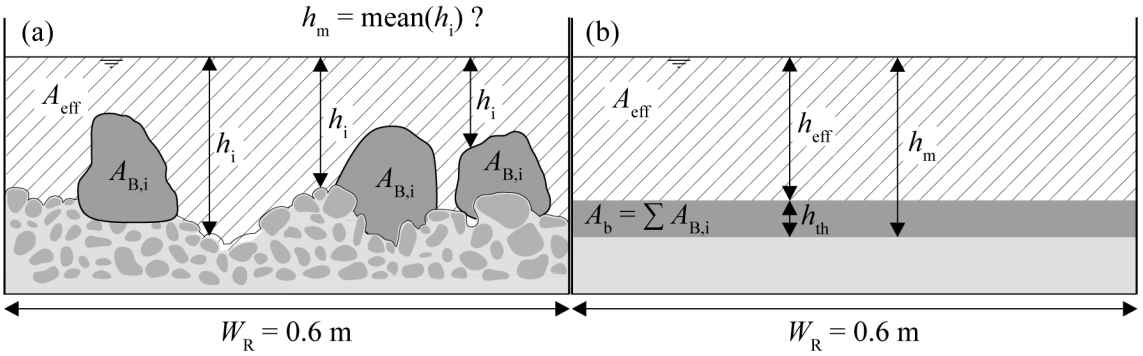

Figure 5.23 (a) Cross-section of the UBR with indicated flow depths h_i, effective flow cross-sectional area A_{eff} and area occupied by a block $A_{B,i}$, and (b) sketch for the determination of the mean flow depth h_m as sum of effective flow depth h_{eff} and theoretical mean depth occupied by block h_{th}.

In a similar way as presented above for the parameterization of S_e, a dimensionless specific discharge q_d^{**} was defined considering the decisive parameters D/d_{90} and λ as

$$q_d{}^{**} = \frac{q}{\sqrt{g(s-1)D^3}}\ \lambda^{-0.2}\left(\frac{D}{d_{90}}\right)^{0.5}. \qquad (5.3)$$

Figure 5.24 shows h_m/D versus q_d^{**} for all conducted experiments. The black line represents the power data fit describing the determined points with $R^2 = 0.98$:

$$h_m/D = 0.69\ q_d{}^{**0.64} \qquad \text{for } q_d^{**} < 10. \qquad (5.4)$$

Eq. (5.4) was determined without considering the data of experiments A3, A11, A14 and A15, as above for Eq. (5.2). The grey dotted lines illustrate the lower and upper limit of the variation range +/− 10% of Eq. (5.4). Data of experiments with sediment supply (A11 and A14) lie mostly below the lower grey line, indicating lower h_m/D and thus lower flow resistance. For $q_d^{**} < 2$ some data deviate from Eq. (5.4) up to 20%, particularly data with $D/d_{90} = 4.9$ and 12.3.

Eqs. (5.2) and (5.4) can be used for design purposes: given a specific design discharge q and assuming a parameter configuration for the ramp bed (D/d_{90} and λ), the corresponding equilibrium slope S_e can be determined with Eq. (5.2). If S_e does not correspond to the required slope, a new parameter combination has to be assumed and the process repeated until suitable conditions are achieved. The mean flow depth h_m can be determined with Eq. (5.4) and the bulk flow velocity is calculated as $u_b = q/h_{eff} = q/(h_m - h_{th})$. Note that h_m represents normal flow conditions by equilibrium

slope: Eq. (5.4) cannot be used to estimate the flow depth under non-equilibrium conditions. It is valid for the tested application range, namely for $4.9 < D/d_{90} < 18.6$, $0.15 < \lambda < 0.25$, $S_0 < 5\%$, and $0 < q_d^{**} < 10$.

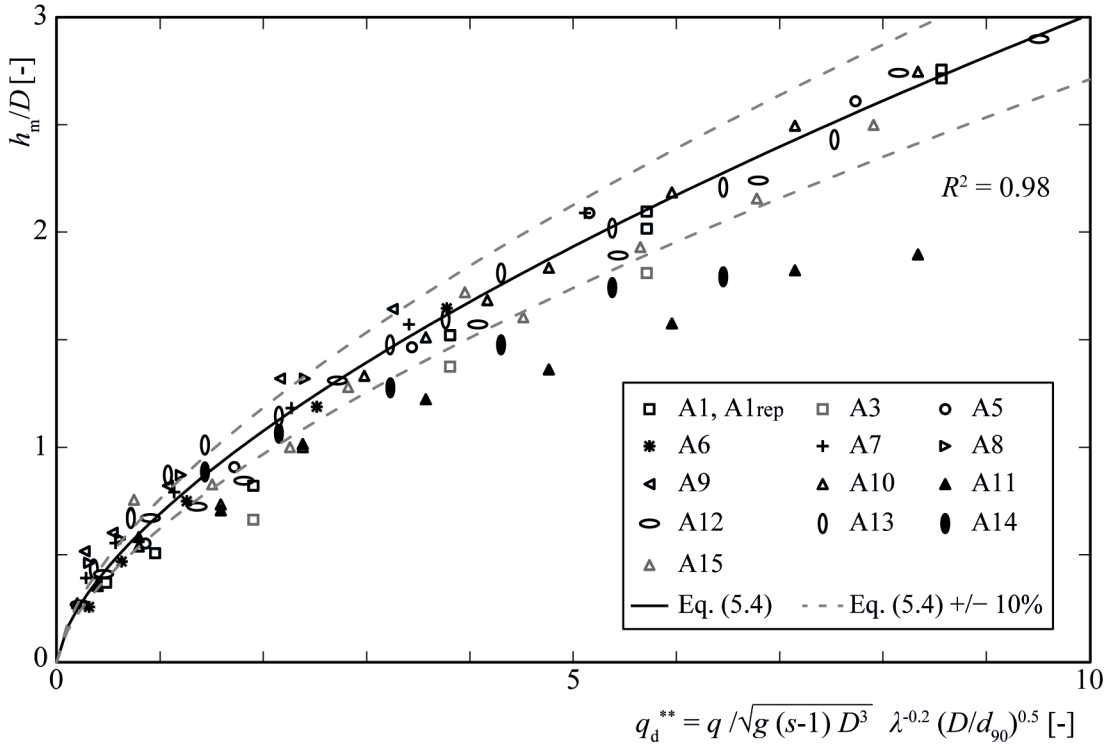

Figure 5.24 Relative submergence h_m/D versus dimensionless specific discharge q_d^{**} for all conducted experiments. Black line: Eq. (5.4); dotted grey lines: variation range of +/− 10%.

The relationship suggested by Pagliara and Chiavaccini (2006a) for the flow resistance presented in Chap. 3.2.1 with Eq. (3.4) is used herein in comparison with the experimental results. Figure 5.25 shows the comparison between measured bulk velocities u_b and bulk velocities determined by solving Eq. (3.4) according to Pagliara and Chiavaccini (2006a) for U as

$$U = u_b = \sqrt{g\,h\,S_e}\;3.5\;(1+\lambda)^{-2.4}\;S_e{}^{-0.17}\left(\frac{h}{d_{84}}\right)^{0.1}. \qquad (5.5)$$

Eq. (5.5) generally overestimates u_b due to the relative submergence defined in relation to d_{84} of the bed material and not considering the protruding blocks. Where the effect of the protruding blocks decreases the bulk velocities according to Eq. (5.5) fit rather well

with the measured velocities. Therefore, Eq. (5.5) could be also used for the estimation of bulk velocities for high discharges such typically the design discharges.

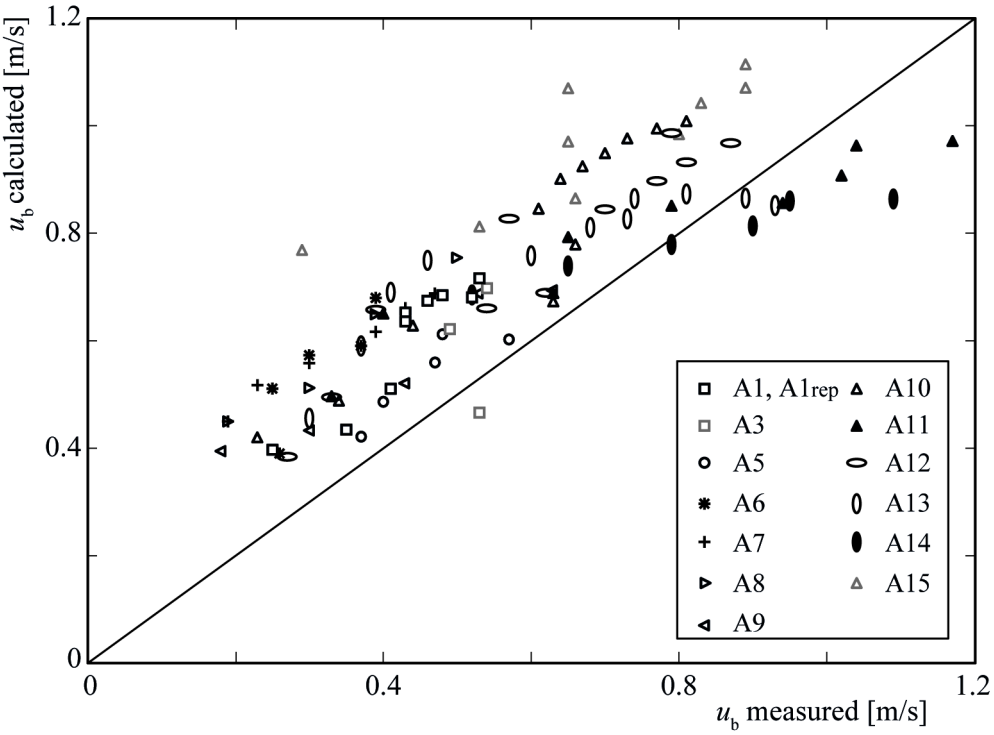

Figure 5.25 Comparison between measured u_b and u_b calculated with Eq. (5.5) according to Pagliara and Chiavaccini (2006a).

5.2.9 Flow resistance

In this chapter the resulting flow resistance is compared with equation Eq. (2.22) suggested by Aberle and Smart (2003) and with Eq. (3.4) by Pagliara and Chiavaccini (2006a) for the flow resistance of mountain rivers and of UBR, respectively. These equations were used to fit the results by the coefficients, without changing the structure of the equation. The data of the experiments with uniform material (A3 and A15) and with sediment supply (A11 and A14) were not considered (s. Chap. 5.2.7) as well as those representing less stable configurations (A6, A7, A8 and A9). Only the data resulting from experiments A1, A1rep, A5, A10, A12 and A13 are analysed, representing the conservative and more suitable (e.g. no ramp collapse) configurations for design purposes. Figure 5.26 (a) compares the flow resistance expressed as the ratio between bulk flow velocity u_b and bulk shear velocity $u_{*,b}$, defined as $u_{*,b} = (g\, h_m\, S)^{0.5}$, resulting from the experiments ($u_b/u_{*,b}$ measured) and determined with Eq. (2.22) from Aberle and Smart (2003, $u_b/u_{*,b}$ calculated). As for the block protrusion P (Chap. 5.2.7), the standard deviation of the bed elevations σ_b (blocks included) was derived with the laser distance sensor with the measuring grid 1×1 cm^2. With $u_b/u_{*,b} < 5$ Eq. (2.22) underestimates the flow resistance, wheras for $u_b/u_{*,b} > 5$ it is overestimated. The value u_b increases more than $u_{*,b}$ for high discharges, leading to higher ratios $u_b/u_{*,b}$ for higher discharges. That means that Eq. (2.22) overestimates the flow resistance for high discharges, which are decisive for the ramp stability and for the ramp design. For this reason, Eq. (2.22) is not suitable for design purposes and was therefore adapted as follows

$$\frac{U}{u_*} = \frac{u_b}{u_{*,b}} = 2.5\ \ln\frac{h}{\sigma_b} + 0.4\ , \tag{5.6}$$

better fitting the experimental results (Figure 5.26 b). However, a certain data scatter is still present.

In a similar way, in Figure 5.27 (a) the flow resistance resulting from the experimental data is compared with the flow resistance determined with Eq. (3.4) according to Pagliara and Chiavaccini (2006a) for UBR. As described in Chap. 5.2.8, the relationship suggested by Pagliara and Chiavaccini (2006a) generally overestimates u_b and the flow resistance, due to the relative submergence defined in relation to the characteristic grain size of the bed material d_{84} and not considering the protruding blocks. In order to consider the effect of the protruding blocks, d_{84} was replaced by P in Eq. (3.4)

$$\frac{U}{u_*} = \frac{u_\mathrm{b}}{u_{*,\mathrm{b}}} = 1.9\,(1+\lambda)^{-0.5}\,S^{-0.21}\left(\frac{h}{P}\right)^{0.29}, \tag{5.7}$$

to better fit the experimental results (Figure 5.27 b). Due to the better fit with the experimental results and to the similarity between UBR investigated by Pagliara and Chiavaccini (2006a) and those in the present research, Eq. (5.7) is suggested for the determination of the flow resistance of UBR with natural movable bed material and protruding blocks.

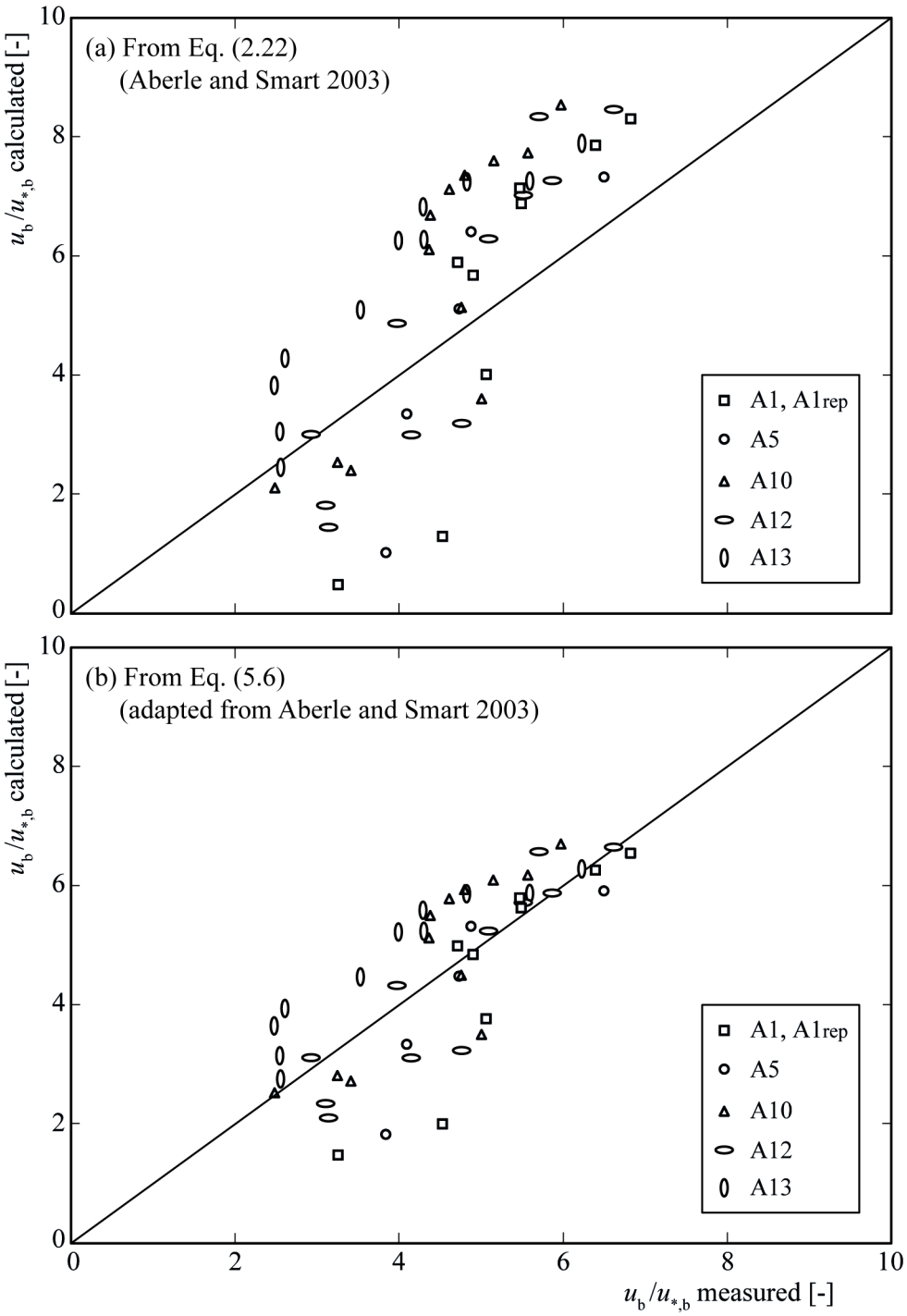

Figure 5.26 Comparison between measured $u_b/u_{*,b}$ and $u_b/u_{*,b}$ calculated with (a) Eq. (2.22) according to Aberle and Smart (2003), and (b) Eq. (5.6) adapted from Eq. (2.22).

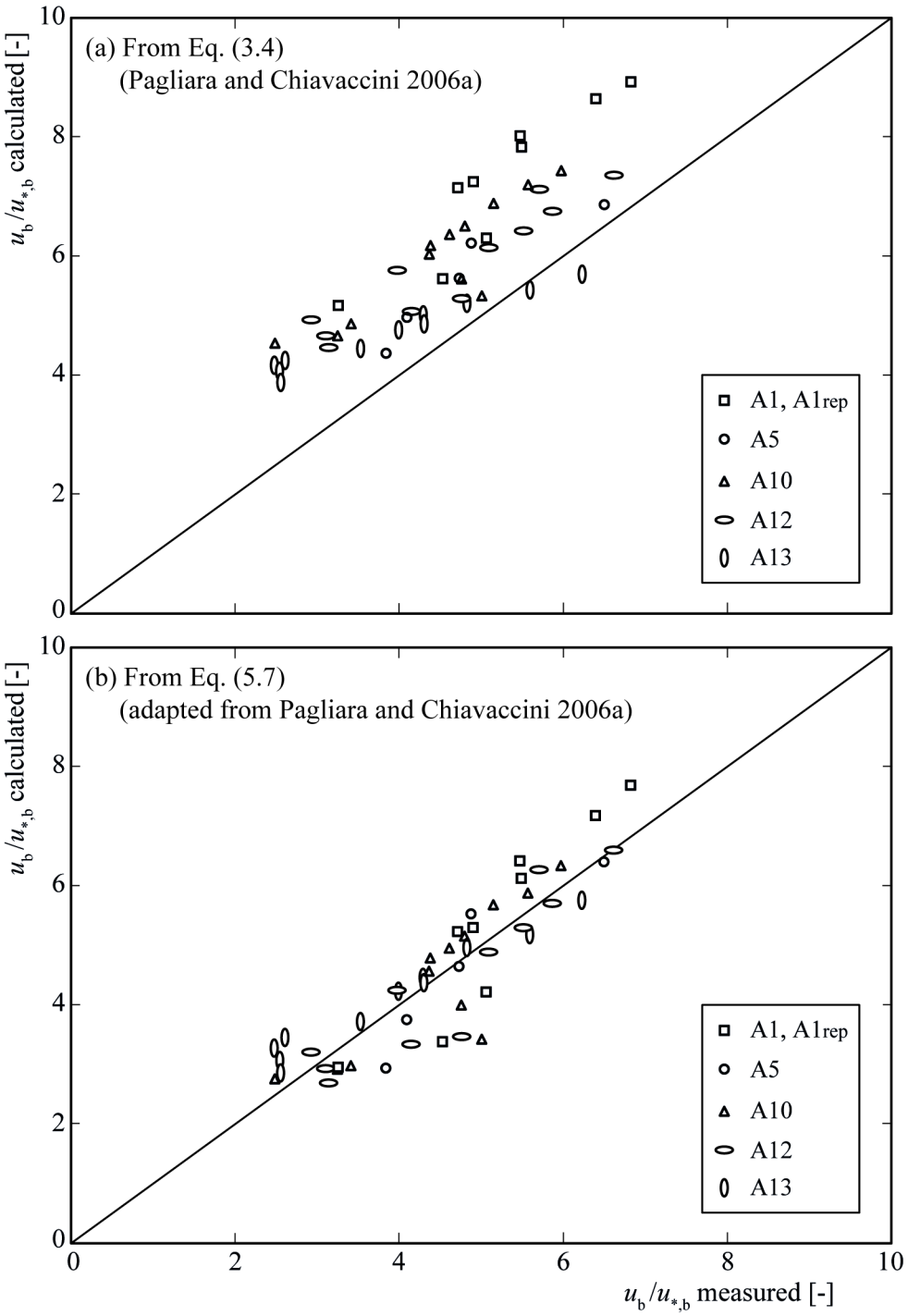

Figure 5.27 Comparison between measured $u_b/u_{*,b}$ and $u_b/u_{*,b}$ calculated with (a) Eq. (3.4) according to Pagliara and Chiavaccini (2006a), and (b) Eq. (5.7) where the paremeter d_{84} is replaced by the protrusion of the blocks P.

5.2.10 Energy dissipation and dissipated specific power density

The energy dissipation was determined from the experimental data as $\Delta H/H_0 = (H_0 - H_1)/H_0$ with $H_0 = H + 1.5h_c$ = total upstream energy head, $H_1 = h_1 + q^2/(2gh_1^2)$ = energy head at ramp toe, $H = S\,L_R$ = ramp height, $h_c = (q^2/g)^{1/3}$ = critical flow depth, and $h_1 = h_m$ assuming uniform flow as described in Chap. 3.2.2 (Figure 3.2). Figure 5.28 shows the relative energy dissipation $\Delta H/H_0$ determined from the experimental data (black dots) compared to $\Delta H/H_0$ determined according to Eqs. (3.13) from Pagliara and Chiavaccini (2006b) (grey squares) and (3.14) from Oertel and Schlenkhoff (2012) (grey triangles), respectively. Generally Eq. (3.13) overestimates $\Delta H/H_0$ compared to the experimental results, presumably due to steeper tested ramp slopes ($0.08 < S < 0.33$) by Pagliara and Chiavaccini (2006b). Also Eq. (3.14) overestimates $\Delta H/H_0$, suggesting that the structured block ramps with crossbars investigated by Oertel and Schlenkhoff (2012) dissipate more energy compared to UBR.

The relative energy dissipation $\Delta H/H_0$ resulting from the experiments can be described maintaining a similar form as in Eqs. (3.13) and (3.14) with $R^2 = 0.98$ as

$$\frac{\Delta H}{H_0} = 0.94\, e^{-0.37\,(D/d_{90})^{0.5}(h_c/H)} \qquad \text{for } h_c/H\,(D/d_{90})^{0.5} < 6. \tag{5.8}$$

Assuming $h_1 = h_m$ determined from the bulk flow velocity u_b as presented above, the results are similar and the variation from Eq. (5.8) is slightly reduced. The effect of the block placement density λ is included in the value of H, which depends on S_e and so also on λ.

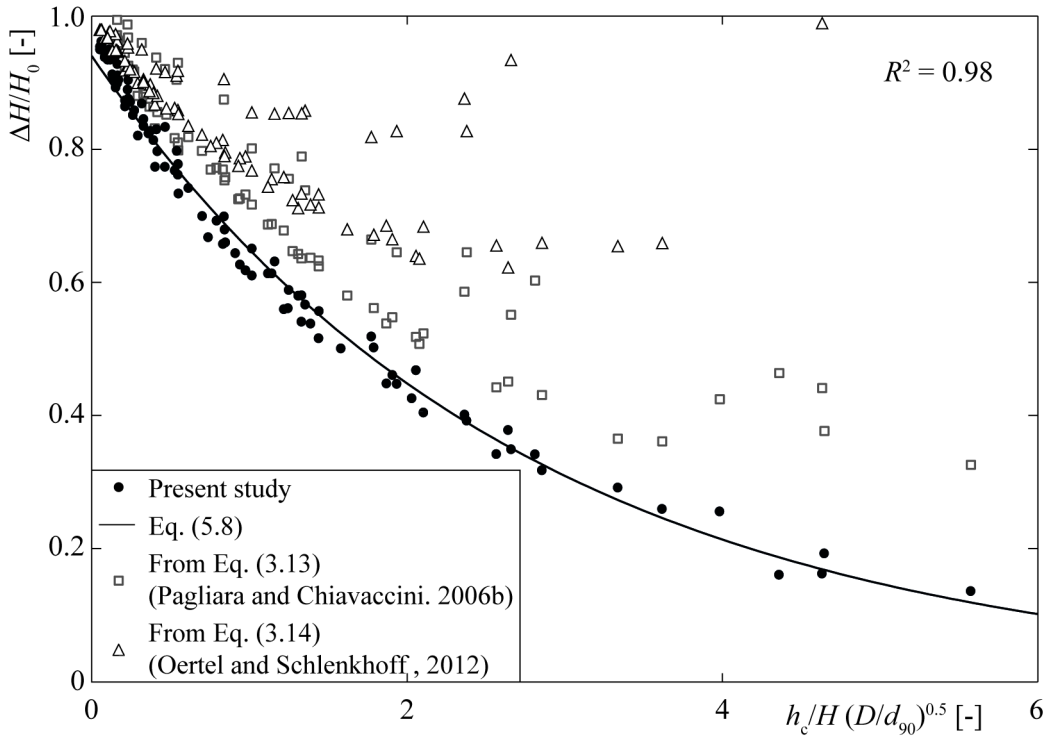

Figure 5.28 Relative energy dissipation $\Delta H/H_0$ versus $h_c/H\,(D/d_{90})^{0.5}$ determined for the experimental data as $\Delta H/H_0 = (H_0\text{-}H_1)/H_0$, according to Pagliara and Chiavaccini (2006b, Eq. 3.13) for UBR, and to Oertel and Schlenkhoff (2012, Eq. 3.14) for structured block ramps. The curve fit related to the present experiment is described by Eq. 5.8.

The quantification of the specific power density P_D dissipated along a UBR (Chap. 3.3.2) is important in terms of fish migration possibilities. The idea herein is to rate some exemplary UBRs in terms of tolerable P_D for the operation period (from Q_{30} to Q_{330}), where the ramp has to be passable for fish. An example is given for four ramps with the same parameter combination as in experiment A10 (upscaled to prototype conditions assuming Froude similarity and a geometrical scale factor $\Omega = 25$) but with different slopes. P_D was determined with Eq. (3.26) (Chap. 3.3.2), where the flow depth h was calculated from the adapted equation derived from Pagliara and Chiavaccini (2006a, Eq. 5.7) with $u_{*,b} = (g\,h\,S)^{0.5}$ and with $u_b = Q/(h\,W) = q/h$ according to the continuity equation. The resulting P_D is illustrated in Figure 5.29 as function of the specific discharge q (prototype dimensions), which represents roughly the range of typical HQ_1 of Swiss rivers (see Table 5.1). P_D increases with increasing q, similarly as the increase of the flow depth h with increasing q.

According to Table 3.5, P_D on UBR should not exceed a value varying from 175 W/m^3 to 275 W/m^3 during the operation period, depending on the river zone. Figure 5.29 gives an idea for which specific discharge the resulting specific power density results too high compared to the limiting values suggested in Table 3.5. Note that these data were not investigated for very low discharge conditions (as during the operation period), because this phase of experiments focussed on ramp stability and so on high discharge conditions and that the values of P_D presented herein were determined with an approach (Eq. 5.7) suggested for equilibrium conditions.

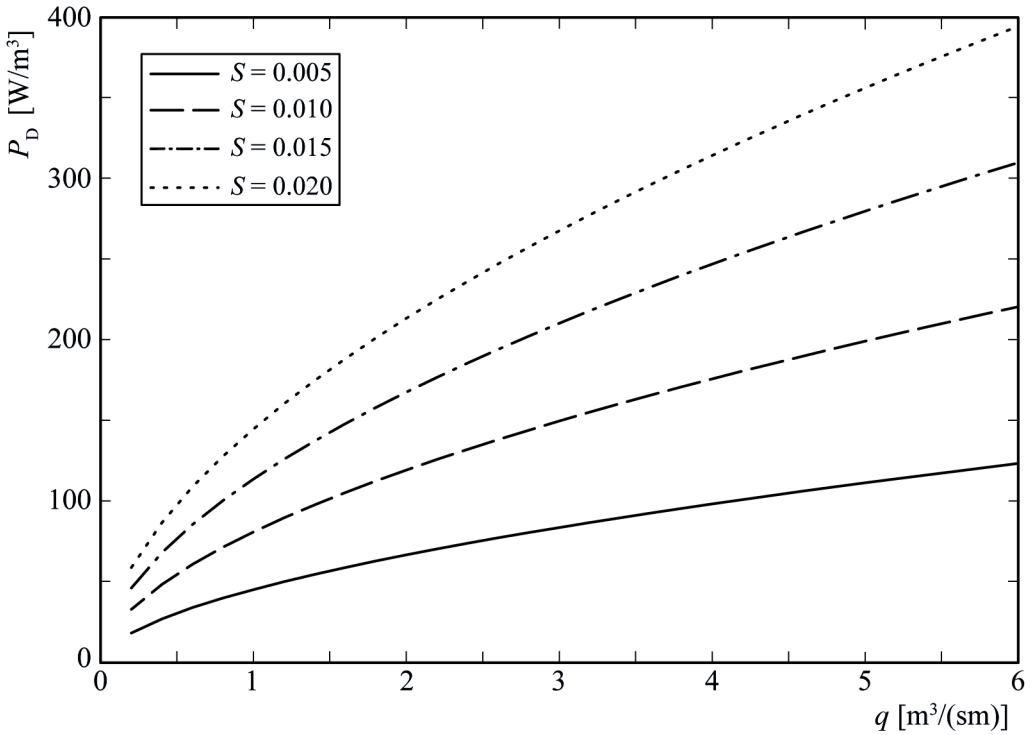

Figure 5.29 Dissipated specific power density P_D determined for different ramp slopes S versus specific discharge q for a ramp built with the parameter combination of experiment A10 upscaled to prototype conditions assuming Froude similarity and a geometrical scale factor $\Omega = 25$.

5.3 General ramp behaviour – Phase B

5.3.1 Effect of erodible tail water reach

The general ramp behaviour within the river system was investigated in phase B by extending the considered river reach to a ramp with an erodible tail water reach (Figure 4.9). The ramp was tested allowing erosion at the ramp toe under steady and quasi-steady flow conditions, so that the effect of a hydrograph (Figure 4.10), representing a characteristic high flood event ($\approx HQ_{100}$) of Swiss Rivers, and of the duration of the discharge were determined (Chap. 4.3). The goal of this phase is to investigate the effect of a erodible tail water (TW) and of quasi-steady discharge condition on ramp stability for one example with the selected hydrograph. For this reason, it is not possible to generalize the results for other different quasi-steady or unsteady flow conditions. However, these results allow a better comprehension of the processes occurring under different conditions from phase A. The boundary conditions of these experiments are summarized in Table 4.7 and represented in Figure 4.11.

The effect of an erodible TW simulating an erodible river reach downstream of the block ramp is shown in Figure 5.30, where the stability curves for experiments A10 and B1 with the same parameter combination (D and λ) are compared. The ramp of A10 was 9 m long and without TW as in every ramp tested in phase A (Figure 4.6), whereas that of B1 was 7 m long and with 2 m long erodible TW (Figure 4.9). Up to $q = 50$ l/(sm) the equilibrium slope S_e is nearly equal, whereas for $q > 60$ l/(sm) the ramp of B1 resulted in a reduced S_e, i.e. S_e of B1 was approximately 20% flatter than S_e of A10. The general ramp behaviour was similar for A10 and B1.

The longitudinal profiles of the 2 m long erodible TW after different discharge steps are shown in Figure 5.31. For $q = 13$ l/(sm) the sediment eroded on the ramp between the blocks was deposited on the TW reach (Figure 5.31) due its lower slope (1%) compared to the ramp slope. For $q = 27$ l/(sm) this deposition was eroded and the bed elevation at TW was similar to the initial elevation. For $q \geq 60$ l/(sm) the longitudinal profiles indicate direct erosion at TW. Firstly, the ramp toe lowered but the ramp head remained at the initial position, leading to higher ramp slope. Then, when the ramp head also lowered, the ramp slope decreased and the entire ramp lowered. The erosion downstream of the ramp toe affected the ramp stability and increased the erosion process along the ramp, leading to a slope decrease.

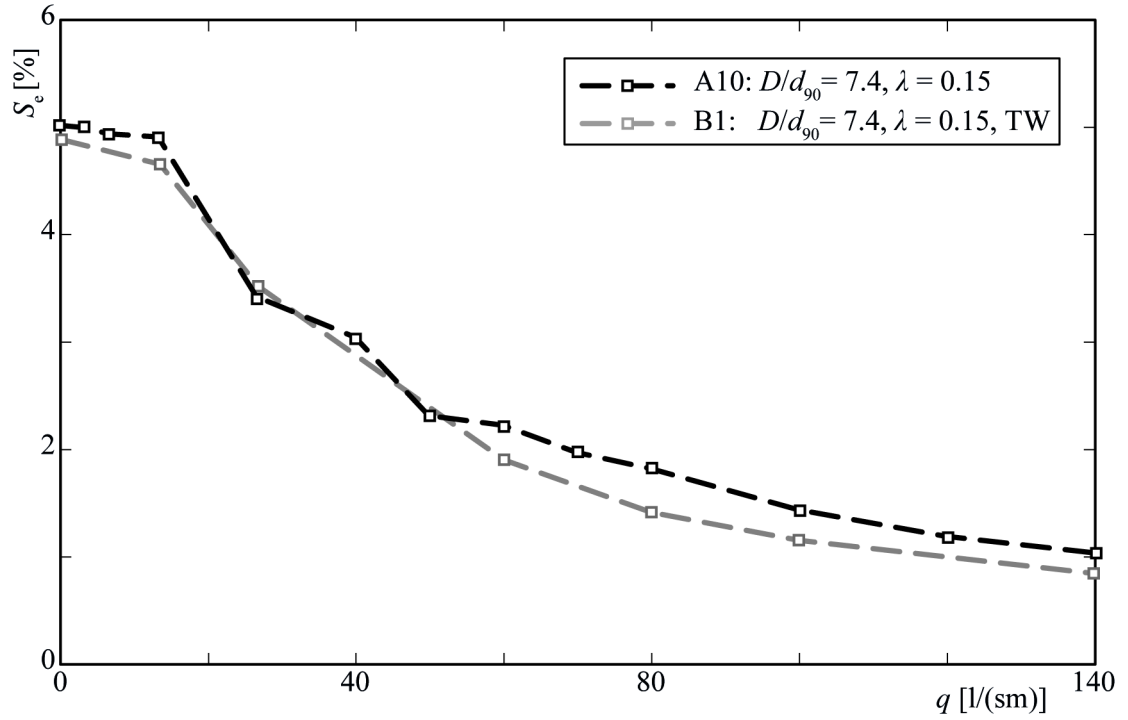

Figure 5.30 Stability diagram of A10 without (black) and B1 with erodible tail water (TW, grey), respectively. Both experiments were conducted with $D/d_{90} = 7.4$ and $\lambda = 0.15$.

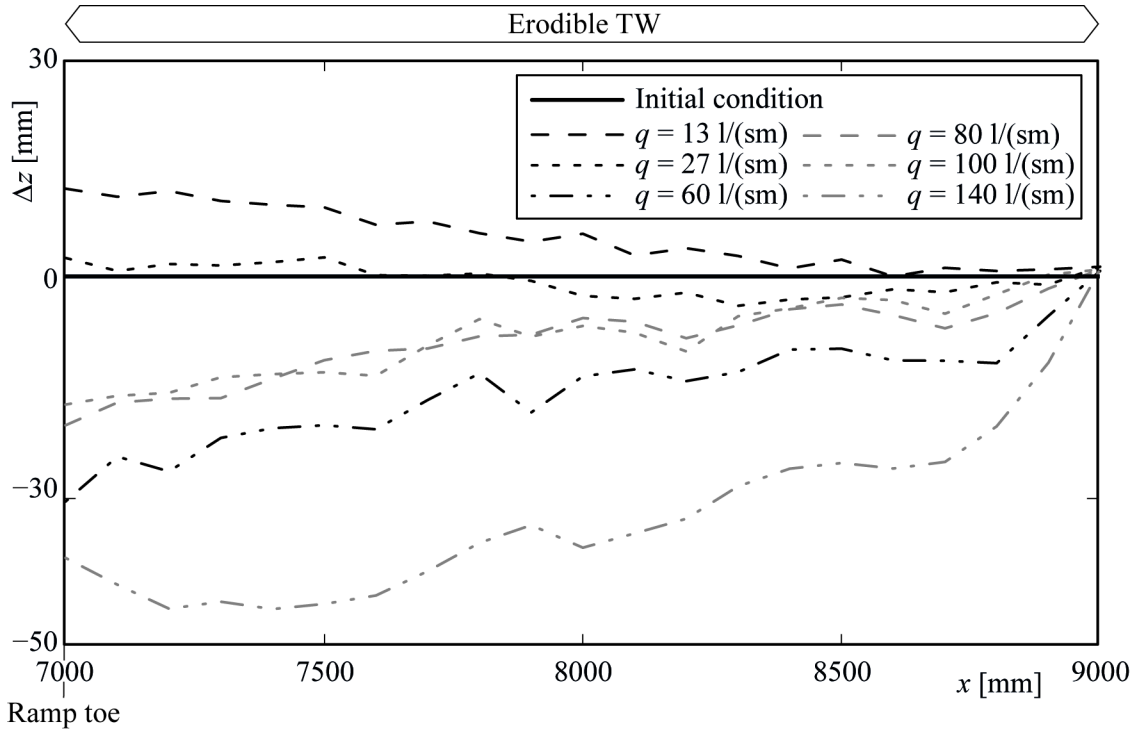

Figure 5.31 Longitudinal profiles downstream of ramp toe for q = 13, 27, 60, 80, 100 and 140 l/(sm) of B1 ($D/d_{90} = 7.4$, $\lambda = 0.15$) with erodible tail water (TW) under steady conditions. The zero elevation refers to the initial condition.

The lowering of the ramp head and of the ramp toe and the loss of the fixed-point function of the UBR can negatively affect other existing structures. For instance, if the ramp is built downstream of a drop or sill, lowering the ramp head would lead to an elevation difference that can disturb or preclude the fish migration. If a bank protection exists, the lowering of the ramp would damage the transition point between ramp and bank protection and could also affect the stability of the latter.

To prevent strong erosion at TW, the river reach downstream of the ramp has to be stabilized against increased erosion or scour (Whittaker and Jäggi 1986, Bezzola 2010). For instance, blocks can be placed directly on the sediment in a similar way as along the ramp (Figure 5.32 a), so that a stable transition zone between the stabilized bed (ramp) and the unprotected bed (river) is introduced. Alternatively, blocks can be placed below the river bed in the sediment body (Figure 5.32 b), so that in case of washout of the upper sediment layer they can prevent severe bed degradation.

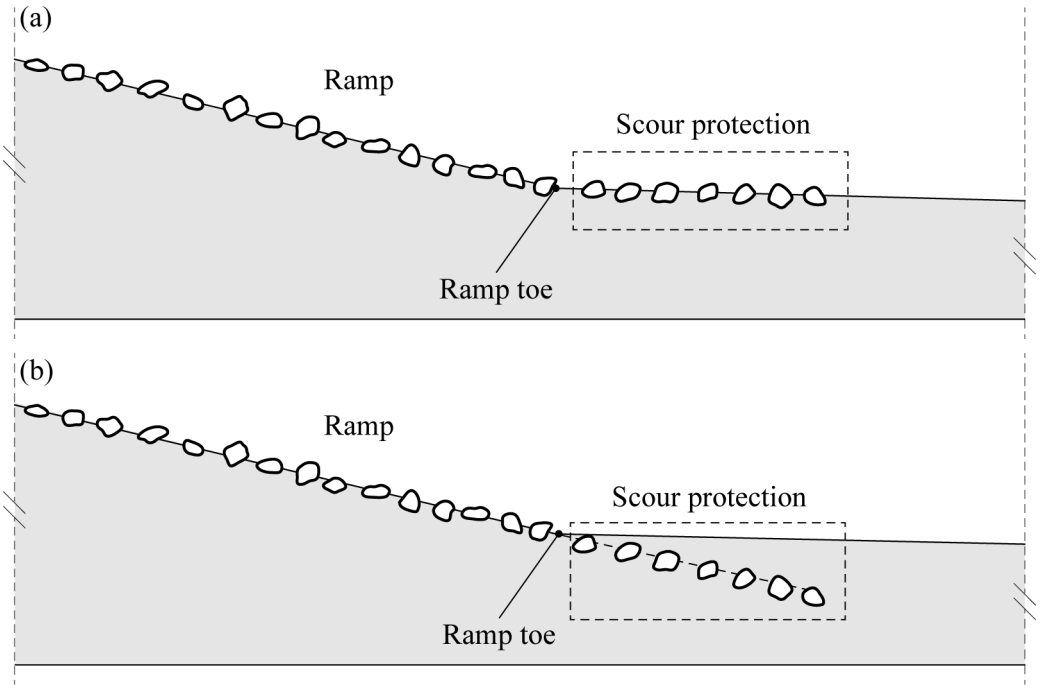

Figure 5.32 Examples of scour protection measures: (a) blocks are placed directly on the sediment downstream of the ramp; (b) blocks are placed below the river bed.

5.3.2 Steady and quasi-steady flow conditions

For the experiments under quasi-steady conditions the discharge was regulated according to the hydrograph presented in Chap. 4.3.2 (Figure 4.10), roughly representing a

characteristic flood event (≈ HQ_{100}) of Swiss Rivers. The hydrograph was simplified with a triangular shape with identical rising and falling limbs. The time step under quasi-steady conditions was 24 minutes long (model time), whereas during the experiments under steady conditions it varied between 3 and 100 hours until equilibrium conditions were reached.

The effect of the duration of discharge steps on the ramp stability is shown in Figure 5.33. The ramp flattening under quasi-steady conditions (B2) is less pronounced than under steady conditions (A10). The resulting ramp slope of B2 was approximately 20% steeper as for A10 (q > 20 l/(sm)). Although the durations of the discharge steps strongly differed, the difference in the resulting ramp slope was not that pronounced. This suggests that the erosion process occurs generally immediately after the increase of the discharge. Afterwards, the slope decrease reduces (see also Figure 5.34).

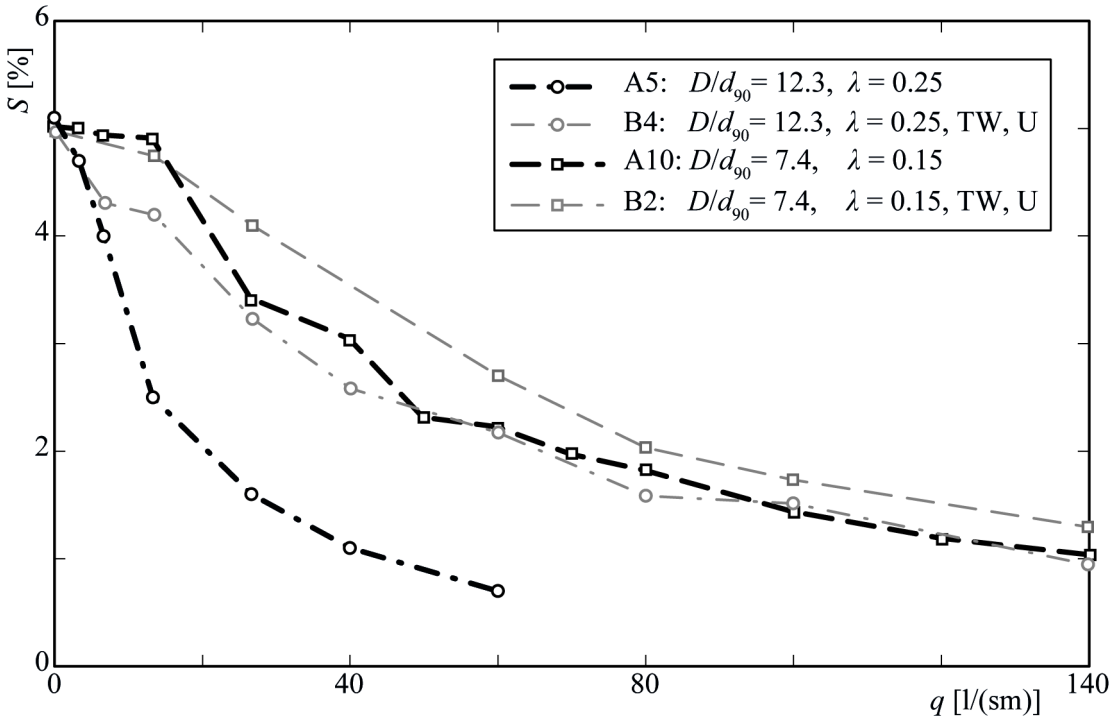

Figure 5.33 Stability diagram of A5 and A10 under steady conditions and B2 and B4 under quasi-steady conditions (U) and with erodible tail water (TW).

In contrast, the duration of discharge steps strongly affects the stability of ramps with less stable parameter combination (D/d_{90} = 12.3 and λ = 0.25). The erosion process of B4 under quasi-steady conditions is much less intense than of A5 under steady conditions. For q > 10 l/(sm) the difference between the two resulting $S(q)$ curves is more

than 70%. For larger discharges the ramp behaviour of B4 is similar to that of A10, resulting in a ramp slope $S > 1\%$ also for $q > 140$ l/(sm). This suggests that the duration of a certain discharge is decisive for the stability of a ramp with $D/d_{90} = 12.3$. Since only one hydrograph was tested and so the duration of discharge step was not varied, a general quantification of this effect on the ramp stability is not possible.

The effect of the duration of a discharge step on the ramp slope is shown in Figure 5.34. The change in the slope S/S_0 with S_0 = initial ramp slope during the discharge step $q = 27$ l/(sm) is illustrated for two experiments under steady conditions (A5 and A10) and for two experiments under quasi-steady conditions with same equal parameter combination (B2 and B4). The transported sediment (catched in the filtering basket at the flume end, see Figure 4.1, and measured during the entire experiment duration) was converted into volume and assuming a triangular longitudinal ramp section converted into a ramp slope S. The resulting change in the slope S/S_0 for B2 and B4 is similar to that for A5 and A10 during the same discharge duration. The highest slope decrease happens during the first 500-1000 minutes, corresponding to 2500-5000 minutes (approximately 42-84 hours) in the prototype assuming a geometrical scale factor of 25. In general, high discharges do not remain constant for so long. The quasi-steady tests show that the stability diagrams resulting from the tests under steady conditions (phase A) characterize the absolute lower stability limit for the tested ramp (Figure 5.34), representing a conservative assumption for the design. A conservative assumption is required, due to the uncertainties associated with the prototype conditions, e.g. the estimated flood discharge, the variations of the block shape, weight and position, or the irregularities of the existing river bed. However, to avoid overdesigned D or λ leading to high costs, the effect of different discharge duration should be further investigated.

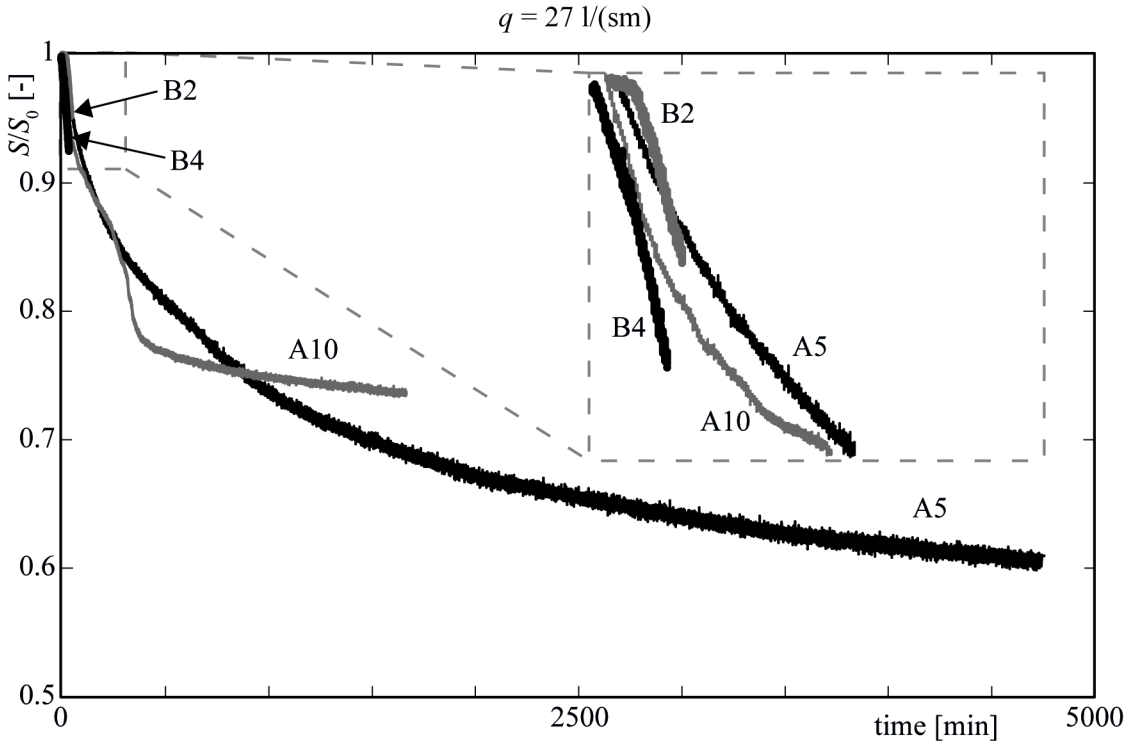

Figure 5.34 Slope decrease S/S_0 with S_0 = initial ramp slope during experiments A5 and A10 under steady conditions and B2 and B4 under quasi-steady conditions for q = 27 l/(sm). The time refers to model dimensions.

5.3.3 Effect of increased erosion

The effect of increased erosion downstream of the block ramp was investigated by lowering the fix point at the flume end (Chap. 4.3.3, Figure 4.9 and Figure 4.11). The induced erosion was specifically applied for high discharges, to test the ramp under particularly unfavourable conditions. In Figure 5.35 the stability diagrams of B2 and B4 (without increased erosion) are compared with those of B3 and B5 (with increased erosion). At the discharge steps where the erosion was induced, the resulting slopes of B3 and B5 are higher than of B2 and B4. In this case the analysis of the stability diagram is misleading: the steeper slopes resulted from the higher level difference between ramp head and ramp toe, due to the removal of the plate. Presumably, the duration of a discharge step was not sufficient to balance this effect and so the slope resulted steeper.

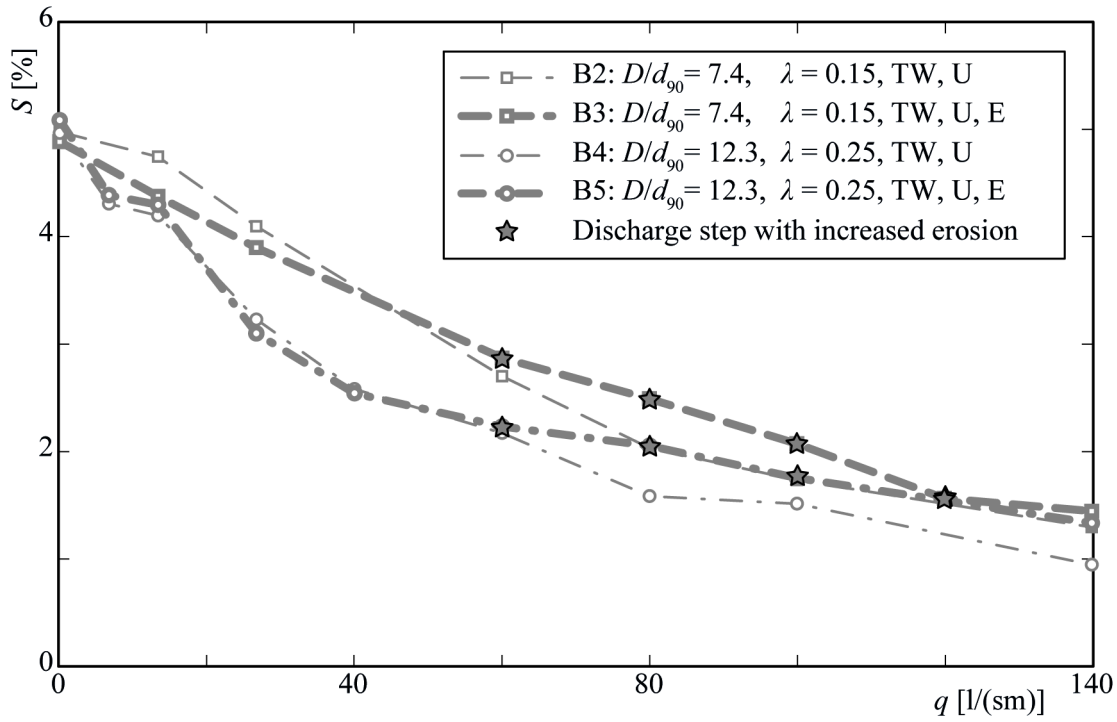

Figure 5.35 Stability diagram of B2 and B4 without and of B3 and B5 with increased erosion (E) downstream of the block ramp, respectively, and carried out under quasi-steady conditions (U) and with erodible tail water (TW). Discharge steps where the fixed-point was lowered are indicated by a star.

The longitudinal profiles of the ramp after three discharge steps with increased erosion are illustrated in Figure 5.36. For both parameter configurations, the effect of the increased erosion for q = 60 l/(sm) was limited to the erodible tail water (from 7000 to 9000 mm in Figure 5.36) where the bed elevation difference Δz was approximately 10-15 mm. For $q \geq 80$ l/(sm) the lowering of the bed increased and concerned also the ramp. For the more stable parameter combination (B2 and B3 with $D/d_{90} = 7.4$ and $\lambda = 0.15$, Figure 5.36 top) the ramp erosion was slightly less pronounced than for the other (B4 and B5 with $D/d_{90} = 12.3$ and $\lambda = 0.25$, Figure 5.36 bottom).

The increased erosion downstream of the ramp toe aggravates the effect on the ramp head and on the ramp toe. As described above for the erodible TW (Chap. 5.3.1), the lowering of the ramp head, of the ramp toe as well as of the entire ramp is undesired. Firstly, the fixed-point function of UBR would not be achieved, because the elevation of the ramp toe and ramp head would change. The ramp adjusts itself to the discharge condition by flattening and without undergoing a failure, but the fixed-point function vanishes. Secondly, the lowering could potentially damage or destroy constructions

connected to the UBR, as e.g. a drop upstream of the UBR or bank protection measures at the UBR banks.

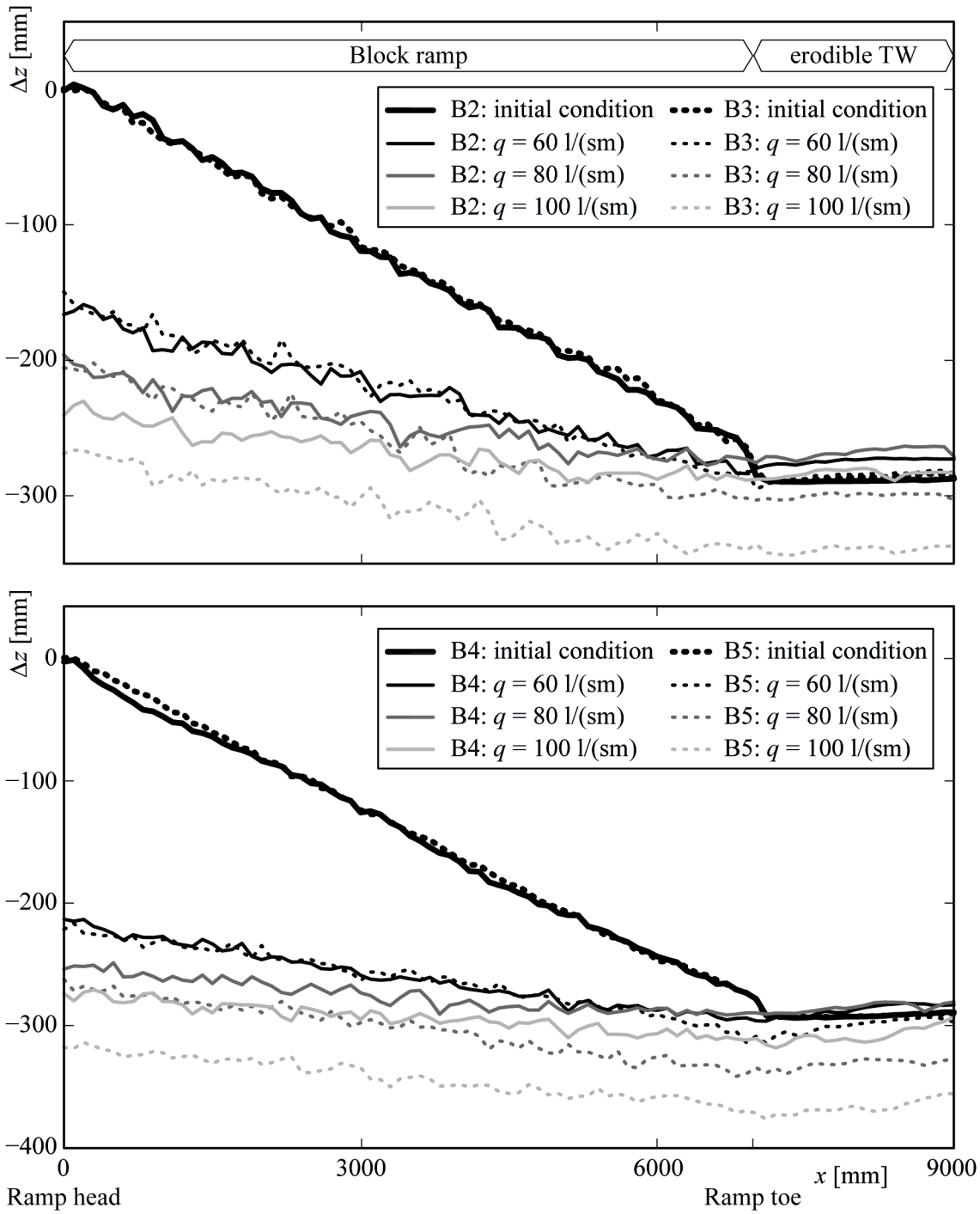

Figure 5.36 Longitudinal sections for $q = 0$ (initial condition), 60, 80 and 100 l/(sm) of B2 without and of B3 with increased erosion downstream of the ramp (top), and similarly of B4 and B5 (bottom). The zero elevation refers to the initial condition.

The most significant effect of the increased erosion was the block loss, corresponding to the transport of the blocks downstream of the ramp and to the decrease of the block placement density. During B3, 4 blocks were transported downstream of the ramp during q = 100 l/(sm), 1 during q = 120 l/(sm) and 58 during q = 140 l/(sm), leading to a total block loss of 63 blocks corresponding to 33% of the total number of blocks. Concerning B5, 35 blocks were transported downstream of the ramp during q = 140 l/(sm), corresponding to 5% of the total number of blocks. In particular the block loss has a negative impact on the next flood event, for which the total resistance of the block ramp is reduced, increasing the risk of ramp erosion. Neither during B2 nor during B4 (with constant fix point) was any block transported. The plan view of the ramps after experiments B2, B3, B4 and B5 are illustrated in Figure 5.37, where the block loss is visible for the experiment with increased erosion (B3 and B5). Therefore, the erosion at the ramp toe and downstream of it increases the block loss on the ramp, leading to a decreased block placement density and to reduced ramp stability, which can cause even stronger erosion during the next flood event.

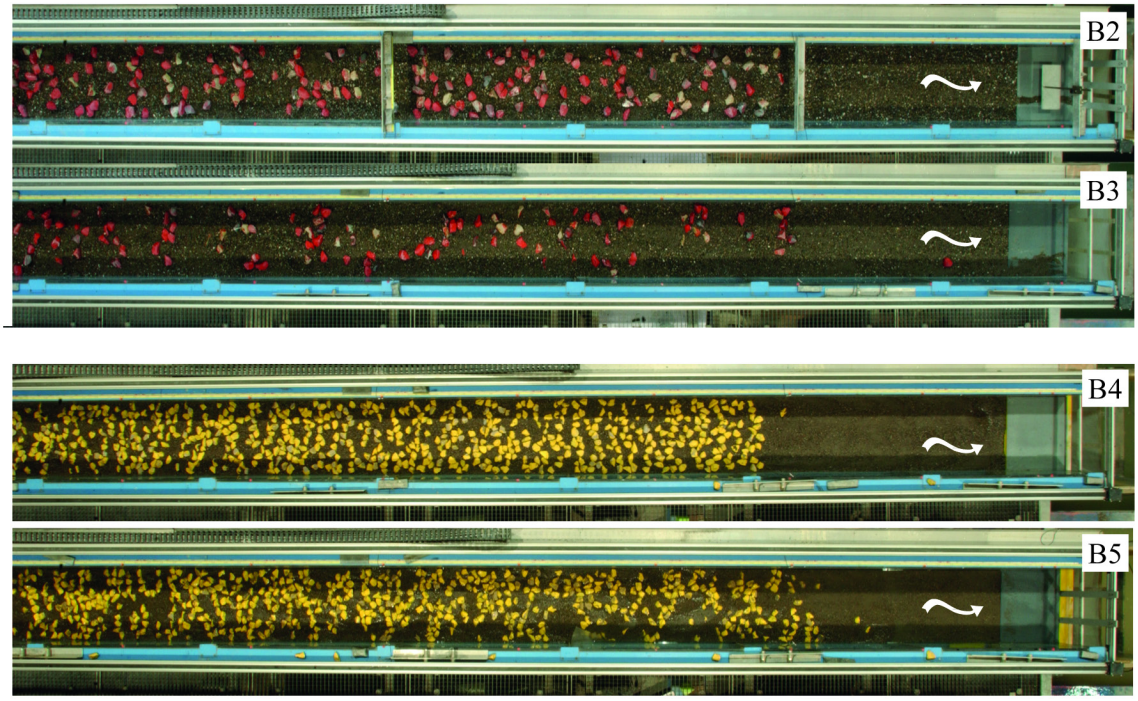

Figure 5.37 Plan view of ramp after q = 140 l/(sm) at the end of experiment B2, B3, B4 and B5.

5.3.4 Implications for the prototype

The general ramp behaviour resulting from phase B is related to typical Swiss river conditions, in order to show an example on how the results of the tests of phase B can be interpreted. The selected Swiss rivers correspond to those considered for the two sediment mixtures (Chap. 4.2.3). The geometrical scale factor Ω for the different rivers was derived by upscaling the given model sediment material to the actual sediment mixtures of the rivers according to Zarn (1992, Chap. 4.5). Table 5.1 summarizes characteristic flood events HQ_1, HQ_2, HQ_{10}, HQ_{30}, HQ_{100} and EHQ for the selected rivers in prototype dimensions (subscript P) with Q_P = prototype discharge [m^3/s] and q_P = prototype specific discharge [$m^3/(sm)$], as well as in model dimension (subscript M) with q_M = model specific discharge [l/(sm)]. Table 5.1 gives an example of the order of magnitude of typical flood events HQ_i in Swiss rivers so that the results of the model tests can be better interpreted. Note that the decisive quantity for the ramp stability and for the comparison between model results and prototype conditions is the specific discharge q. The experimental setup represents a longitudinal slice taken from the middle part of a river. For this reason the model width W_M does not represent the decisive parameter for the determination of the scale factor. As described above, the geometrical scale factor Ω is derived from the sediment material of the considered river reach.

The discharges of the characteristic flood events HQ_i were taken from the statistic data of the Swiss Federal Office for the Environment FOEN (*http://www.hydrodaten.admin.ch/en*, status: April 2013) for all the considered rivers, except for the Emme River which was taken from Hunziker, Zarn & Partner (2012). EHQ was assumed to be 1.5 HQ_{100}. The corresponding specific discharges q_P were determined with regard to the river width W_P as

$$q_P = Q_P/W_P \; . \tag{5.9}$$

The specific model discharges q_M were then downscaled according to Froude similitude and the correspondent geometrical scale factor Ω (Chap. 4.5) as

$$q_M = q_P/(\Omega^{1.5}) \; . \tag{5.10}$$

Table 5.1 Characteristic flood events for some Swiss rivers in prototype (subscript P) and in model (subscript M) dimensions, with Ω = geometrical scale factor derived from the sediment material, W_P = river width at the considered reach, and A_{catch} = catchment area. The gauging station considered is indicated in brackets.

River		HQ_1	HQ_2	HQ_{10}	HQ_{30}	HQ_{100}	EHQ
Engelberger Aa (Buochs, Flugplatz) $\Omega = 25$ $W_P = 20$ m $A_{catch} = 227$ km^2	Q_P [m^3/s]	35	72	111	139	172	258
	q_P [m^3/(sm)]	2	4	6	7	9	13
	q_M [l/(sm)]	14	29	44	56	69	103
Emme (Emme Wiler) $\Omega = 40$ $W_P = 25$ m $A_{catch} \approx 940$ km^2	Q_P [m^3/s]	-	-	450	560	650	975
	q_P [m^3/(sm)]	-	-	18	22	26	39
	q_M [l/(sm)]	-	-	71	89	103	154
Kleine Emme (Werthenstein, Chappelboden) $\Omega = 20$ $W_P = 25$ m $A_{catch} = 311$ km^2	Q_P [m^3/s]	107	196	320	417	544	816
	q_P [m^3/(sm)]	4	8	13	17	22	33
	q_M [l/(sm)]	48	88	143	187	243	365
Landquart (Felsenbach) $\Omega = 30$ $W_P = 27$ m $A_{catch} = 616$ km^2	Q_P [m^3/s]	52	176	284	352	430	645
	q_P [m^3/(sm)]	2	7	11	13	16	24
	q_M [l/(sm)]	12	40	64	79	97	145
Moesa (Lumino, Sassello) $\Omega = 30$ $W_P = 65$ m $A_{catch} = 471$ km^2	Q_P [m^3/s]	50	303	479	571	663	995
	q_P [m^3/(sm)]	1	5	7	9	10	15
	q_M [l/(sm)]	5	28	45	54	62	93

River		HQ_1	HQ_2	HQ_{10}	HQ_{30}	HQ_{100}	EHQ
Muota (Ingenbohl) $\Omega = 35$ $W_P = 30$ m $A_{catch} = 316$ km^2	Q_P [m^3/s]	90	165	243	298	365	548
	q_P [m^3/(sm)]	3	5.5	8.1	9.9	12.2	18
	q_M [l/(sm)]	15	27	39	48	59	88
Rhone (Sion) $\Omega = 25$ $W_P = 45$ m $A_{catch} = 3373$ km^2	Q_P [m^3/s]	275	457	630	743	874	1311
	q_P [m^3/(sm)]	6	10	14	17	19	29
	q_M [l/(sm)]	49	81	112	132	155	233
Thur (Andelfingen) $\Omega = 50$ $W_P = 50$ m $A_{catch} = 1696$ km^2	Q_P [m^3/s]	160	572	820	945	1067	1601
	q_P [m^3/(sm)]	3	11	16	19	21	32
	q_M [l/(sm)]	9	32	46	54	60	91

Figure 5.38 indicates the expected ramp slopes after a HQ_{100} flood event according to Table 5.1. Depending on the characteristics of the sediment material of the considered river (fine or coarse mixture), the expected ramp slope is derived from the results of B2 with coarse sediment mixture or of B4 with fine sediment mixture, assuming λ and D/d_{90} as for the tested ramps. Since the tested hydrograph was derived considering typical duration and peak of floods for the same rivers considered here (Chap. 4.3.2), the resulting stability diagram is assumed to be representative for these rivers. According to Figure 5.38, an UBR built with the same parameter combination (λ and D/d_{90}) as for B2 and B4 in the Engelberger Aa, Moesa, Muota, Rhone or Thur River maintain a slope higher than 2% after a HQ_{100}. In the case of the Emme and of the Landquart River, the resulting ramp slope is 1.5% and 1.7%, respectively. In the case of the Kleine Emme River, the HQ_{100} discharge is higher than the tested discharges, meaning that the resulting ramp slopes would be < 1%. Whether the resulting ramp slopes are acceptable or not has to be analysed separately for each case.

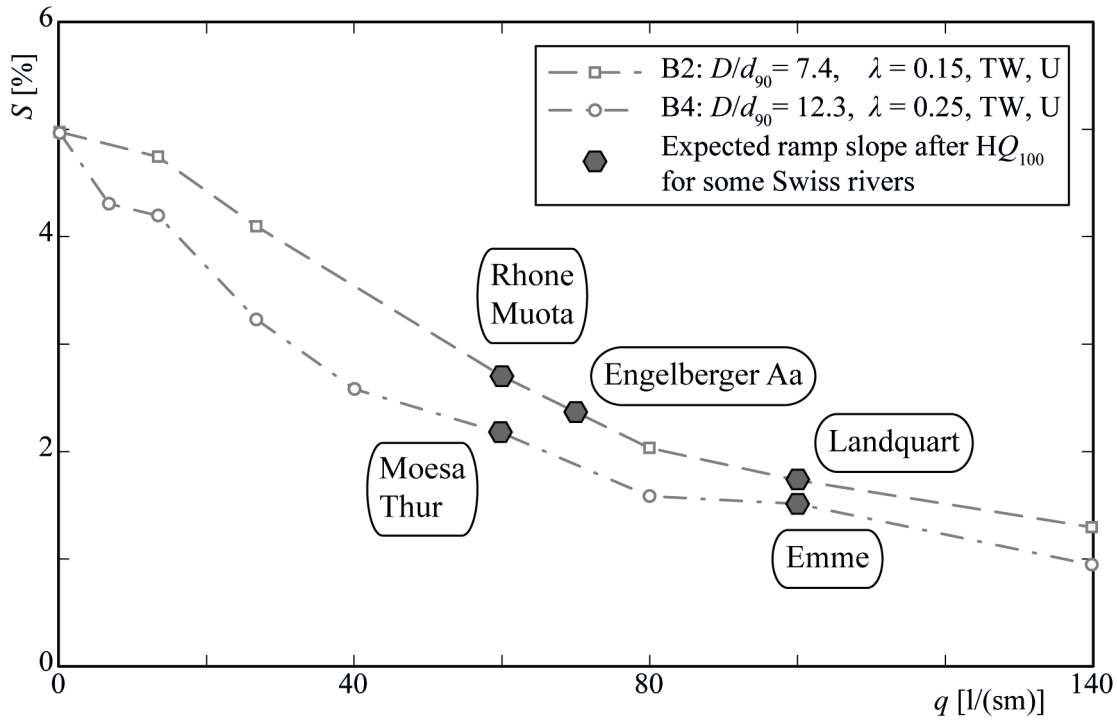

Figure 5.38 Stability diagram of B2 and B4, both carried out with erodible tail water (TW) and under quasi-steady conditions (U). The grey dots indicate the expected ramp slopes after HQ_{100} of some Swiss rivers, assuming for UBR the same parameter combination (λ and D/d_{90}) as for the tested ramps.

Appendix A summarizes the ramp behaviour of five different block ramps during a high flood event that occurred in Switzerland in 2005. The goal is to show some aspects of the ramp design which responded well or less well to the high hydraulic load.

5.4 Turbulence tests – Phase C

The results of the turbulence tests with 2D LDA velocity measurements are presented in the following sections. The parameter combination tested corresponds to the experiment A10 (see Table 4.5) with the most stable ratio $D/d_{90} = 7.4$ resulting from the stability tests (see Chap. 5.2) and the lower block placement density $\lambda = 0.15$. The experimental details can be found in Chap. 4.4. Firstly, the subdivision into characteristic flow layers according to Nikora *et al.* (2001, see Chap. 2.4.3) was adapted for the present case and the interfacial sublayer was subdivided into a macro-roughness and a sedimentary sublayer. Secondly, the local flow conditions were described by analyzing the resulting time-averaged velocities and turbulence intensities, allowing also consideration about the ecological effectiveness in terms of fish migration. Finally, considering the spatially-averaged (in time and in space) quantities, the general flow conditions were also analysed. Velocity and turbulence intensity vertical profiles are presented. A quadrant analysis was carried out to investigate correlation between velocity fluctuations and spatial disturbances, and the bed shear stress was determined with two different methods.

5.4.1 Flow subdivision and characteristic heights

The flow layers suggested by Nikora *et al.* (2001) described in Chap. 2.4.3 were considered and adapted for UBR. The subsurface layer (Figure 2.9) does not exist, since the bed topography was fixed with a cement layer and therefore impermeable. This is also valid in case of sediment mixtures with low permeability, as for the experiments of phase A (Chap. 4.2.4). The outer layer and the logarithmic layer are not present due to the small relative submergence $h_m/P < 1.5$ (h_m = mean water depth, P = block protrusion, Table 4.8) precluding the formation of an overlap region above the roughness layer. Just the so-called interfacial and the form-induced sublayer remain. In the following a suggestion for the flow subdivision for UBR – namely for flows over heterogeneous bed with macro-roughness elements – is presented. This suggestion reflects flow properties and geometrical features of the bed topography measured with the laser distance sensor (Chap. 4.4.3) with a measuring grid of 1×1 cm^2 (see Figure 4.7). The flow in the interfacial sublayer of UBR is dominated by two geometrical aspects: (1) in the lower part close to the bed the flow is affected by the sedimentary topography (e.g. Figure 4.12), referred to as the sedimentary sublayer; and (2) in the upper part the flow

is affected by the presence of the large blocks, referred to as the macro-roughness sublayer (Figure 5.39). In general the interfacial sublayer includes drag. In the lower part, the sedimentary sublayer, it is assumed that pressure drag and visous drag play a role as indicated in Eq. (2.50). In the upper part, the macro-roughness sublayer, only the pressure drag is active and the viscous drag is negligible, the fifth term of Eq. (2.50) vanishes. For large h_m/P, as e.g. during floods, the form-induced sublayer can develop well.

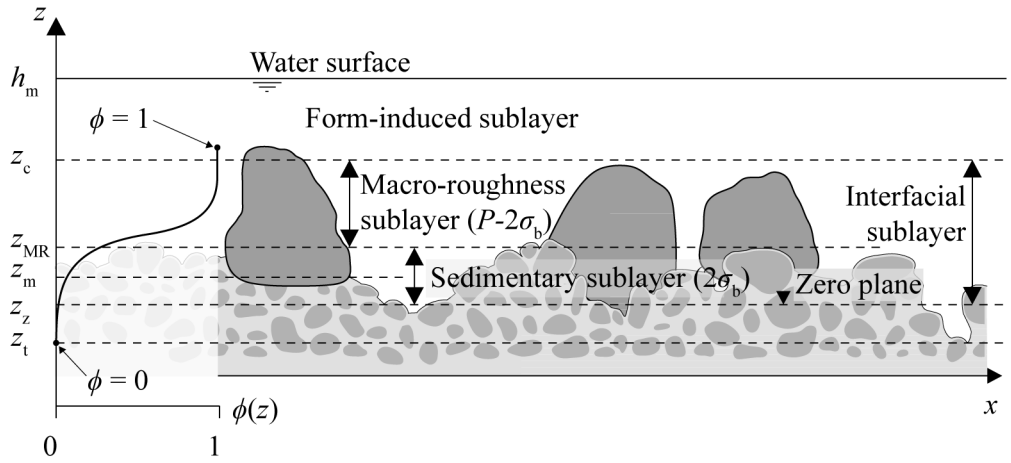

Figure 5.39 Proposed flow subdivision for the present study with fixed impermeable bed material with macro-roughness elements.

To define the thickness of the two lower layers, geometrical parameters are used, as explained in the following; the relevance of these layers with respect to the flow conditions is given in Chap. 5.4.3. Aberle (2000) and Aberle and Smart (2003) used the standard deviation of the bed levels (including large boulders) to characterize the bed roughness, a concept similarly used herein. In the present study two roughness height measures are considered, one for the original sedimentary bed, and one for the protruding blocks. The mean bed level z_m (Figure 5.39) is determined by averaging measured bed level elevations without accounting for regions covered by blocks. The thickness of the sedimentary sublayer is defined as $2\sigma_b$ (Figure 5.39), where σ_b is the standard deviation of the measured bed levels, again without taking into account regions with blocks. In absolute values the thickness of the sedimentary sublayer is herein 20 mm. The zero plane as the origin of the vertical coordinate is defined as $z_z = z_m - \sigma_b$, whereas the boundary between the sedimentary and the macro-roughness sublayers is $z_{MR} = z_m + \sigma_b$, respectively. The thickness of the macro-roughness sublayer is given by the upper edge z_c defined as an average value of all measured block crest heights as $z_c = P = 48$ mm, and the lower edge z_{MR}. In absolute values the thickness of the macro-roughness sublay-

er is 28 mm (Figure 5.39). The height z_t defines the level of the lowest trough and in absolute values is approximately 24 mm below the zero plane z_z.

The right-handed coordinate system is employed herein, with the x-axis parallel to the average bed elevation (with velocity component u), the y-axis has the origin at the right bank and represents the spanwise direction (with velocity component v, not measured herein), and the z-axis is directed toward the water surface (with velocity component w, Figure 4.13). Figure 5.39 also shows a general roughness geometry function $\phi(z)$ indicating the normalized fraction of the cross-sectional area filled with fluid in relation to the overall cross-sectional area (Chap. 2.4).

The flow in each layer is strongly influenced by the roughness geometry function $\phi(z)$. Its value varies between $\phi(z) = 0$ (= cross-sectional area is completely filled with bed material) and 1 (= cross-sectional area is filled with fluid only), which is reached in the considered case at the highest block crest. Figure 5.40 shows $\phi(Z)$ for the present study derived from the bed topography of the entire ramp of phase C with $Z = z/z_c$ as the vertical coordinate z normalized with the representative block crest height z_c. The function $\phi(Z)$ shown in Figure 5.40 is similar to that of Nikora *et al.* (2001). Its gradients in the macro-roughness sublayer above z_{MR} vary with the block placement density and are smaller compared to a regular rough bed. With the given definition of z_z, $\phi(Z)$ becomes zero at the lowest trough below z_z. Similarly $\phi(Z)$ is equal to one at the maximum crest height, above the averaged block crest height z_c. At the characteristic heigths z_z, z_m and z_c the roughness geometry function is $\phi(z = z_z) = \phi(Z = 0) \approx 0.08$, $\phi(z = z_m) = \phi(Z \approx 0.21) \approx 0.35$, and $\phi(z = z_c) = \phi(Z = 1) \approx 0.96$.

In the present study the time-averaged flow variable are spatially-averaged in planes at different heights z parallel to the zero-plane defined above with an average longitudinal slope of S = 2.86%. The different terms in Eq. (2.50) (see Chap. 2.4) have different importance in each layer. In the form-induced sublayer the form-induced stresses $\langle\tilde{u}\tilde{w}\rangle$ generally are non-zero due to the effect of the individual blocks. In the newly defined macro-roughness sublayer the part of the form drag $(1/\rho)\langle\partial\tilde{p}/\partial x\rangle$ becomes significant in the momentum balance. In the newly defined sedimentary sublayer it is assumed that form drag is joined by viscous drag $\nu\langle\partial\tilde{u}/\partial z\rangle$ to become significant in the momentum balance. The viscous stress is assumed to be negligible as indicated in Chap. 2.4 and proved in Chap. 5.4.3

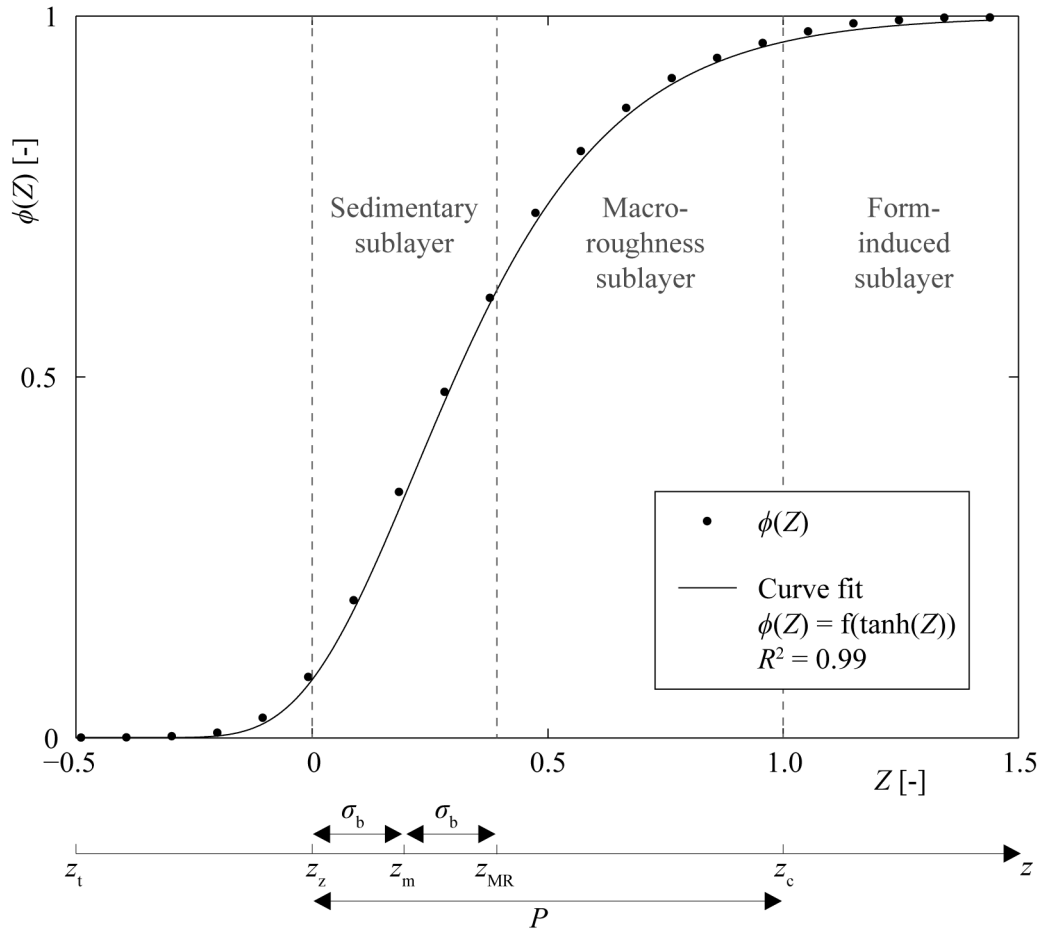

Figure 5.40 Roughness geometry function $\phi(Z)$ resulting from the measured bed topography and fitted with a hyperbolic tangent in relation to the normalized height $Z = z/z_c$.

5.4.2 Flow characteristics and ecological effectiveness

The flow characteristics on the tested UBR are presented using time-averaged velocities and turbulence intensities at representative sections (Figure 5.41). Figure 5.42 shows the contour map of the time-averaged velocity component $\bar{u}$ normalized with the bulk flowvelocity $u_{b,i}$ for the three different tested submergences $h_{m,i}/P$ at y = 84 mm through two blocks (Figure 5.41). The velocities vary between negative values and nearly the double of $u_{b,i}$. Negative velocities were measured downstream of a block, where a recirculation zone occurs. The highest velocities were measured above the blocks, where the flow is locally supercritical for sufficient high $h_{m,i}/P$. For $h_{m,1}/P = 0.63$, the velocity range is smaller, because the flow does not overflow each block so that no strongly accelerating overflow exists. For $h_{m,1}/P = 0.63$ the flow around the blocks is presumably decisive for the hydraulic characteristics: since the transverse velocity component v was

not be measured (Chap. 4.4.2 and 4.4.4), the present results do not fully describe and quantify these characteristics. The selected longitudinal section in Figure 5.42 illustrates the flow heterogeneity along the ramp, affecting positively the ecological effectiveness in terms of fish migration: the higher the range of local velocities, the better are the possibilities for a certain fish to find suitable conditions with respect to swimming capacity and, therefore, the higher are the migration options for that fish considered. A general definition of sufficient heterogeneity can be hardly formulated, since its sufficiency depends on the fish species and their age living in the considered river. Note that a high flow variety could also impact negatively on the migration possibilities, leading to restricted areas with suitable flow velocities. Heterogeneity is therefore favourable within a certain range of flow velocities, corresponding to these of the fish living in the considered river.

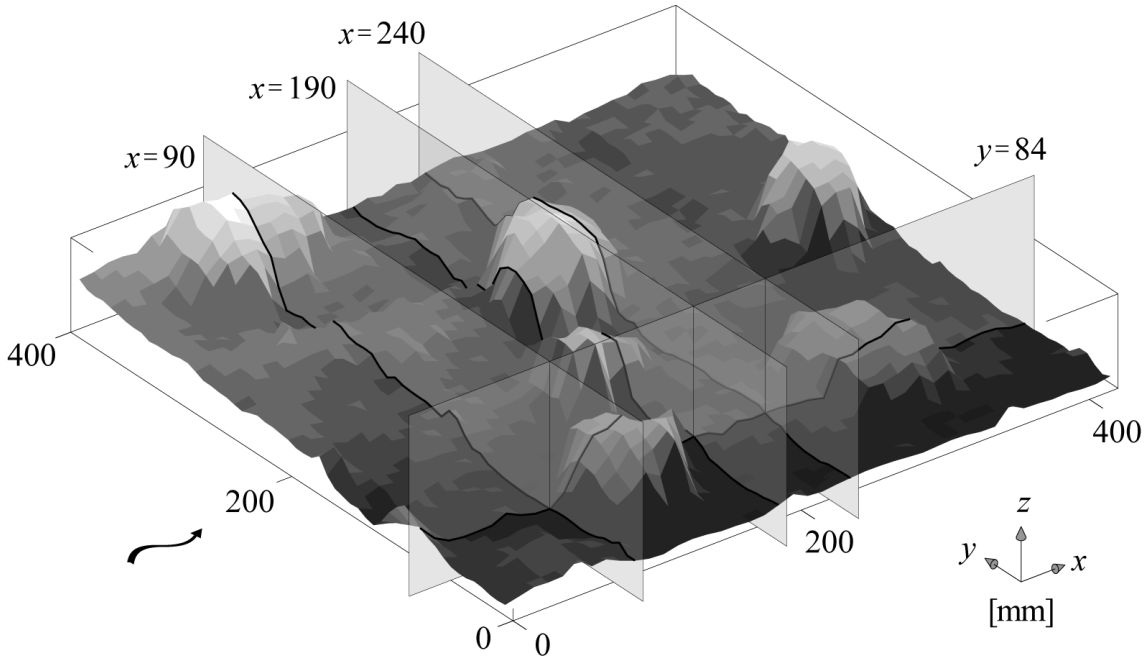

Figure 5.41 Topography of the measurement area (Figure 4.13) with slices indicating cross-sections at $x = 90$ (just upstream of a block), 190 (just downstream of a block) and 240 mm (between two blocks) as well as longitudinal section at $y = 84$ mm (through two blocks). Values in this diagram and in the following refer to model dimensions.

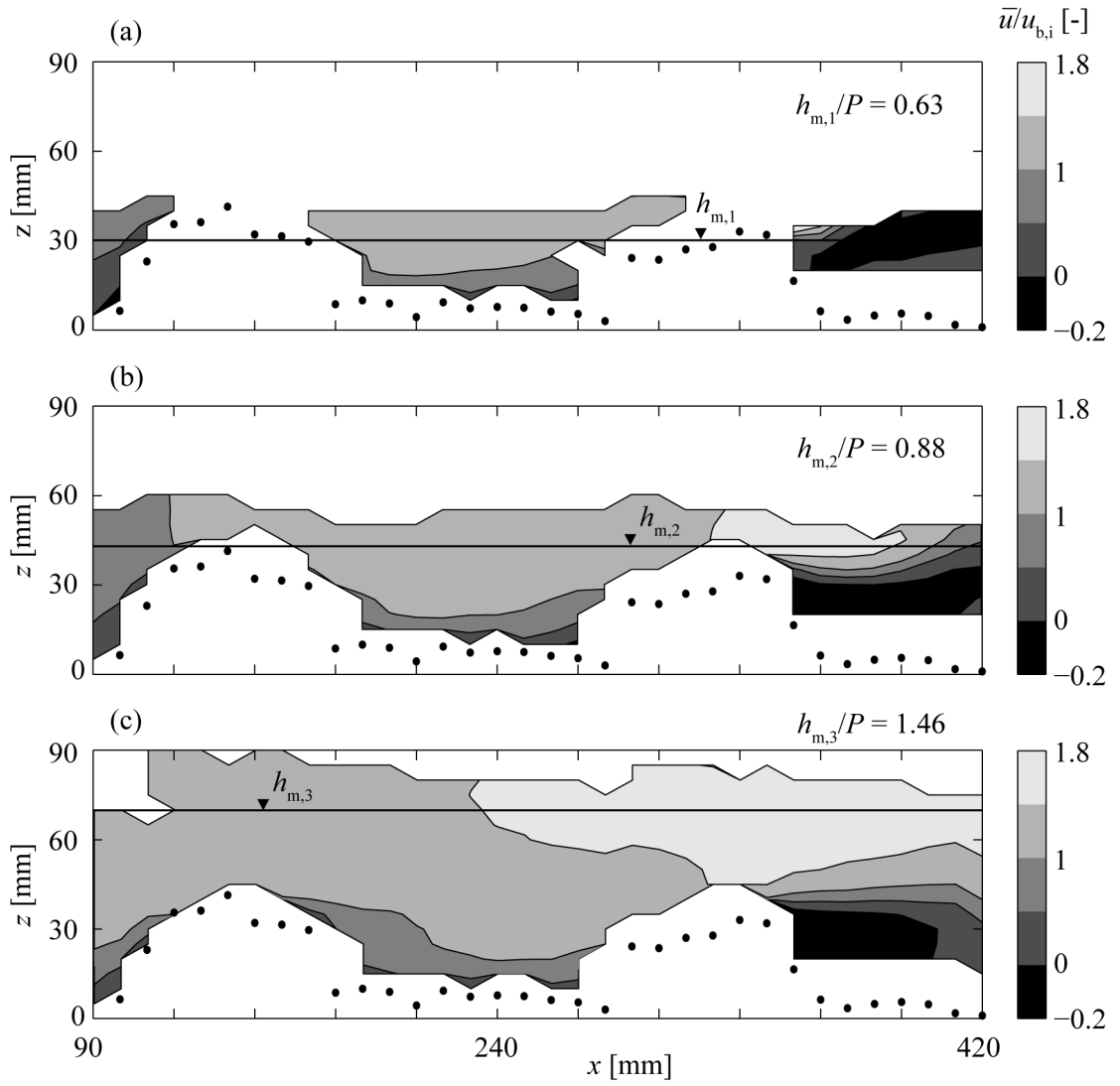

Figure 5.42 Representative longitudinal contour map of local time-averaged velocities $\bar{u}$ normalized with bulk velocity $u_{b,i}$ at $y = 84$ mm for 90 mm $< x <$ 420 mm for $h_{m,i}/P =$ (a) 0.63, (b) 0.88, and (c) 1.46. Dots correspond to measured bed topography; an identical notation is also applied for following contour maps.

To analyze the cross-sectional heterogeneity the velocity ratio $\bar{u}/u_{b,2}$ was plotted as contour map at $x = 90$, 190 and 240 mm (Figure 5.41) for $h_{m,2}/P = 0.88$. Figure 5.43a represents a cross-section without blocks just upstream of a block at 30 mm $< y <$ 80 mm (Figure 5.41). The velocity range does not include neither the minimum nor the maximum values, as for the other two cross-secions (Figure 5.43a and b). However the velocities are not homogeneous, showing a variation range, providing versatility for the fish. At $x = 190$ mm (Figure 5.43b) the block effect is evident: in the area downstream of the block (at 30 mm $< y <$ 80 mm) the time-averaged local velocities are negative due to recirculation zone typically occurring in the lee of a protruding

roughness element. Outside this area but directly affected by the block, the velocities are higher than $u_{b,2}$ due to the flow around the block. Figure 5.43c represents a cross-section between two blocks (Figure 5.41). The influence of the upstream placed block is recognized, whereas the local time-averaged velocities are positive again. The area with the highest velocities at $y \cong 200$ mm corresponds to a corridor between two blocks in this cross-section and the block placed just downstream of it: velocities are accelerated due to the restriction resulting from the block presence. Note also here a heterogeneity of velocity varying within a broad velocity range, providing versatility and allowing different fish to find their optimal migration corridor.

One of the aims of this research is to provide detailed velocity distributions on UBR in order to be used by fish biologists to rate the efficiency of these structures with respect to fish migration. For this reason, additional cross-sections with $\overline{u}/u_{b,i}$, $\overline{w}/u_{b,i}$ and $-\overline{u'w'}/u_{*,b,i}^2$ with $u_{*,b,i} = (gh_{m,i}S)^{0.5}$ are presented in Appendix B.

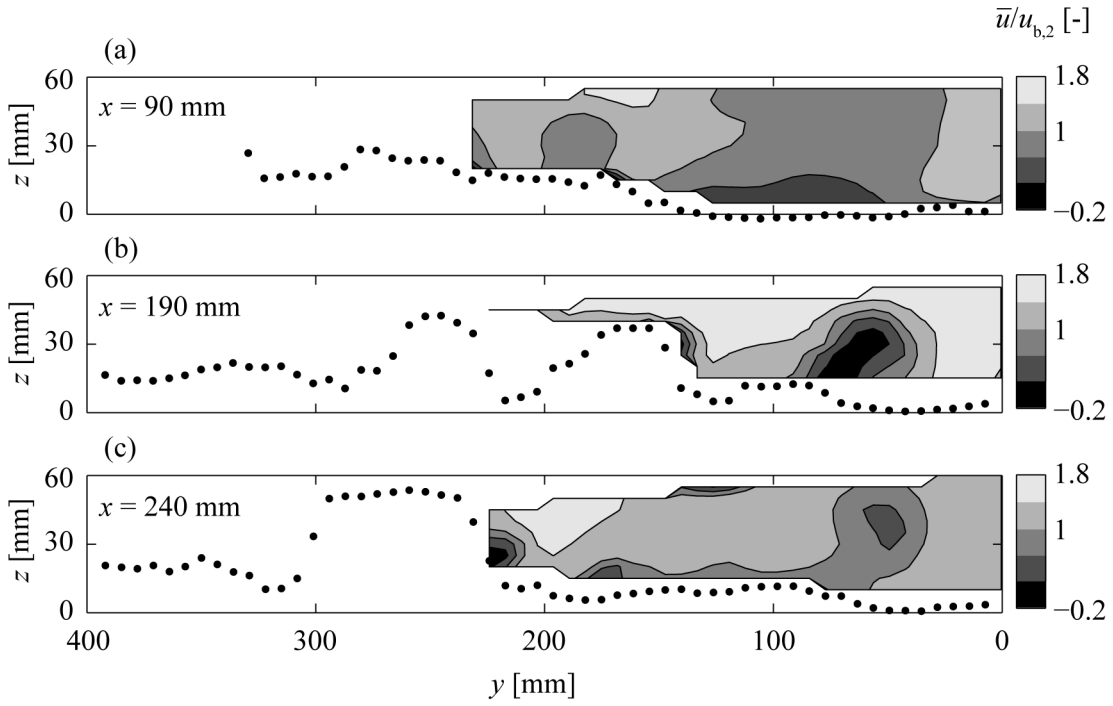

Figure 5.43 Cross-sectional downstream view showing the local time-averaged velocities $\overline{u}$ normalized with the bulk velocity $u_{b,2}$ at x = (a) 90, (b) 190 and (c) 240 mm for q_2 = 13.8 l/(sm) with $h_{m,2}/P$ = 0.88.

The bulk (subscript b) turbulence intensity TI_b, defined as ratio between the standard deviation of the instantaneous velocities $\sqrt{\overline{u'^2}}$ and the bulk velocity u_b, quantifies the variation of the velocity magnitude relative to the bulk velocity. Figure 5.44 shows the contour maps of TI_b at the same cross-sections and for the same relative submergence considered in Figure 5.43. The areas with high TI_b correspond basically to two kind of regions: 1) these with high velocity variation, which are directly influenced by a block and where recirculation occurs (at x = 190 and 240 mm at y = 30-80 mm, Figure 5.43b, c and Figure 5.44b, c), and 2) those adjacent to the flow corridor with accelerated velocity, e.g. at x = 240, and y = 150 and 210 mm (Figure 5.43c and Figure 5.44c). UBR therefore offer a variability of the occurring turbulence intensity, which is positive in terms of hydraulic heterogeneity and ecological aspects, similarly to the velocity variability.

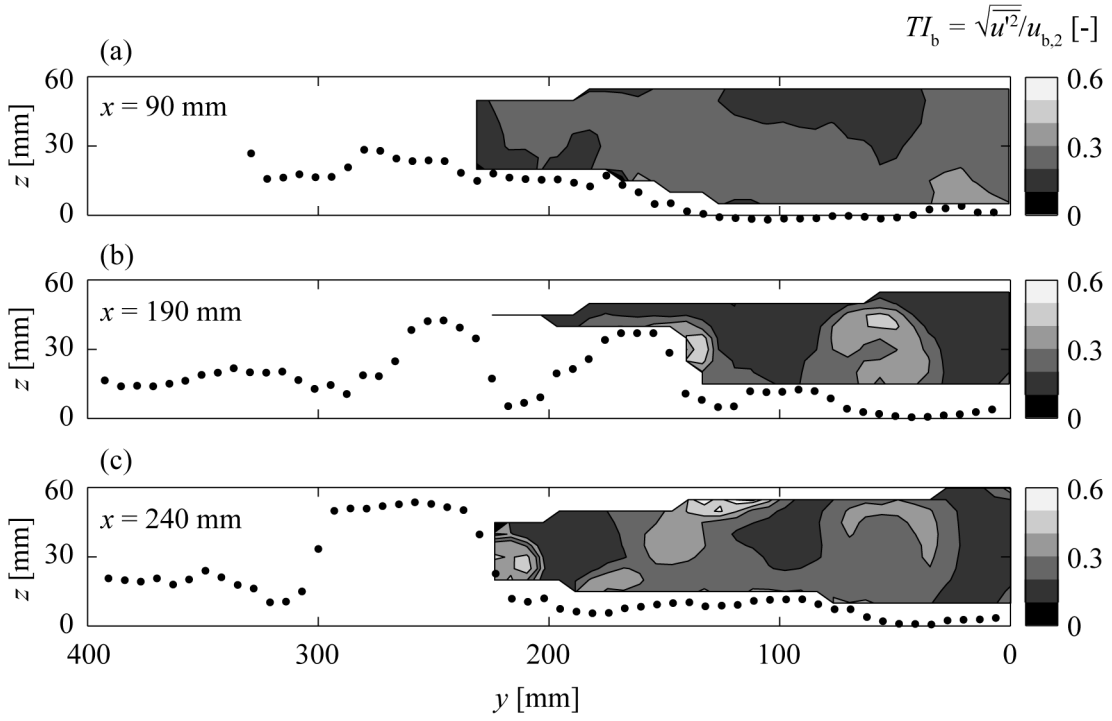

Figure 5.44 Cross-sectional downstream view of the bulk turbulence intensity TI_b at x = (a) 90, (b) 190 and (c) 240 mm for q_2 = 13.8 l/(sm) with $h_{m,2}/P$ = 0.88.

From ecological considerations the local flow characteristics on UBR are decisive for various fish species to pass a ramp. An important parameter affecting the fish behaviour is the local (subscript l) turbulence intensity TI_l (Cotel *et al.* 2006), defined as the ratio between the standard deviation of the instantaneous velocities $\sqrt{\overline{u'^2}}$ and the abso-

lute value of the *local* time-averaged velocity $|\bar{u}|$, which is "felt" by the fish. Thus, TI_l quantifies the variation in velocity magnitude relative to the *local* time-averaged velocity. Unfortunately, it is difficult to find quantitative information on limiting values of TI_l for the swimming capacity of a certain fish (Adam and Lehmann 2011), as well as statements on the effect of turbulence on the swimming capacity (Chap. 2.6.4). Figure 5.45 shows TI_l at the same cross-sections and for the same relative submergence as in Figure 5.44. Compared to TI_b, Figure 5.45 shows almost binary conditions, consisting of quite homogeneous areas with low TI_l, where $\bar{u}$ is high but not the fluctuations, and of regions where $\bar{u}$ is low leading to high TI_l.

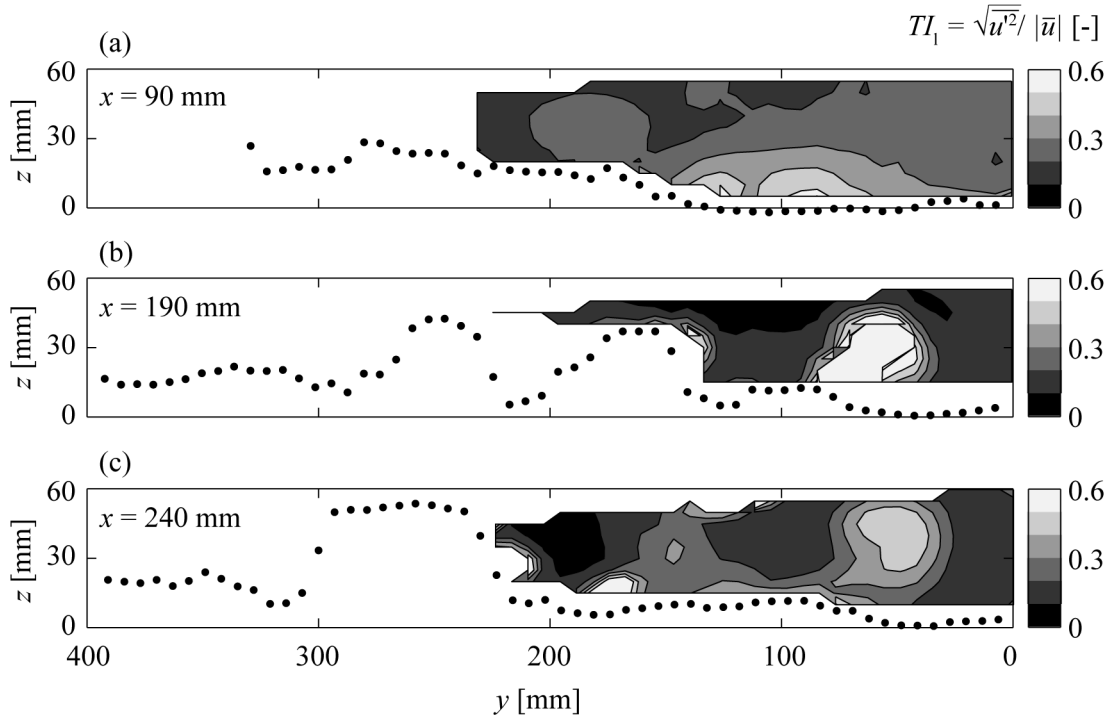

Figure 5.45 Cross-sectional downstream view of the local turbulence intensity TI_l at x = (a) 90, (b) 190 and (c) 240 mm for q_2 = 13.8 l/(sm) with $h_{m,2}/P$ = 0.88.

In the following, velocity measurements are used to create ethohydraulic plots (Adam and Lehmann 2011) indicating specific areas with appropriate flow conditions for a target fish (Figure 5.46). In these plots the velocities are represented as tolerable (light grey) or as intolerable (dark grey) for the target fish selected with a certain critical swimming velocity U_{crit}. Ethohydraulic plots are used to theoretically prove the migration efficiency of e.g. a UBR. If in each cross-section regions with tolerable velocities were identified, it can be assumed that at least the criterion of the maximum velocity for

the considered fish is satisfied, suggesting upstream migration possibilities. The smaller these regions, the more difficult is the link between them in each cross-section and the smaller is the chance to find a passable corridor.

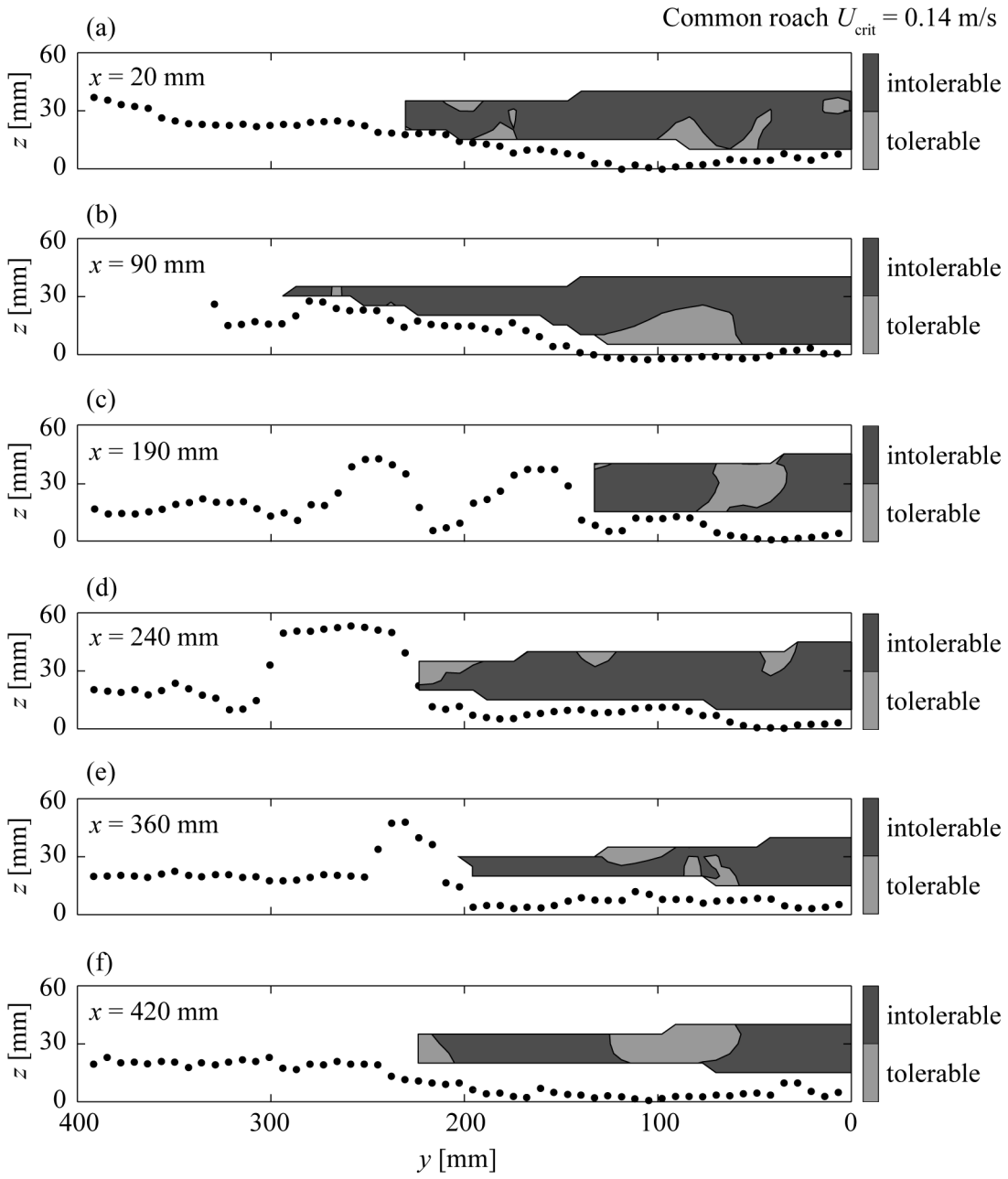

Figure 5.46 Cross-sectional downstream view with velocities U below (light grey) and above (dark grey) the tolerable velocity for common roach with U_{crit} = 0.14 m/s at x = (a) 20, (b) 90, (c) 190, (d) 240, (e) 360, and (f) 420 mm for q_1 = 6.8 l/(sm) with $h_{m,1}/P$ = 0.63 representing approximately Q_{330} to HQ_1.

For example, considering a fish with average swimming capacity living in Swiss rivers as a common roach (*Rutilus rutilus*) with a body length of 30 cm, the critical velocity is $U_{crit} = 0.69$ m/s (Geitner and Drewes 1990, Table 3.2), corresponding to 0.14 m/s in model dimensions assuming Froude similarity and a geometrical scale of 1:25.

As described above, only the longitudinal and the vertical velocity components were measured. To determine the absolute local time-averaged velocity it was assumed that the spanwise component was equal to the vertical, leading to $U = (u^2+2w^2)^{0.5}$. Figure 5.46 shows the distribution of the absolute velocities above and below the critical value $U_{crit} = 0.14$ m/s at the six selected cross-sections (Figure 5.41) for $q_1 = 6.8$ l/(sm), corresponding to relevant hydraulic conditions for fish migration (for many Swiss rivers 6.8 l/(sm) < HQ_1, depending on the scale factor). In each cross-section, regions with tolerable velocities are identified. However, the present measurements did not cover regions close to the bed and in the shadow of a block (Chap. 4.4.4). It is assumed that an extrapolation of the measured data towards the regions that could not be covered leads to a realistic estimate of fish migratability. It can be stated that if the velocities in the measured part allow fish migration, then at least one corridor on the ramp is available, even if the velocities in the part not measured were much higher. For higher discharges it was observed that the regions with tolerable velocities reduce and are close to the bed. The smaller these regions, the more difficult the links between them in each cross-section and the smaller is the chance to find a passable corridor.

Figure 5.47 illustrates tolerable and intolerable velocities for a common roach for $q_1 = 6.8$ l/(sm) and $q_2 = 13.8$ l/(sm) at $x = 90$ and 420 mm. By doubling the specific discharge the regions with tolerable velocity diminish considerably (Figure 5.47, b and d) compared to the case with lower q (Figure 5.47, a and c), leading to reduced migration possibilities for the selected fish. However, $q_2 = 13.8$ l/(sm) is equal or even higher than HQ_1 for many Swiss rivers (depending on the scale factor). These results suggest that UBR can represent a barrier for fish migration already for discharges in the range of Q_{330} – HQ_1, corresponding to the highest discharge for which the ramp should be passable (Chap. 3.3).

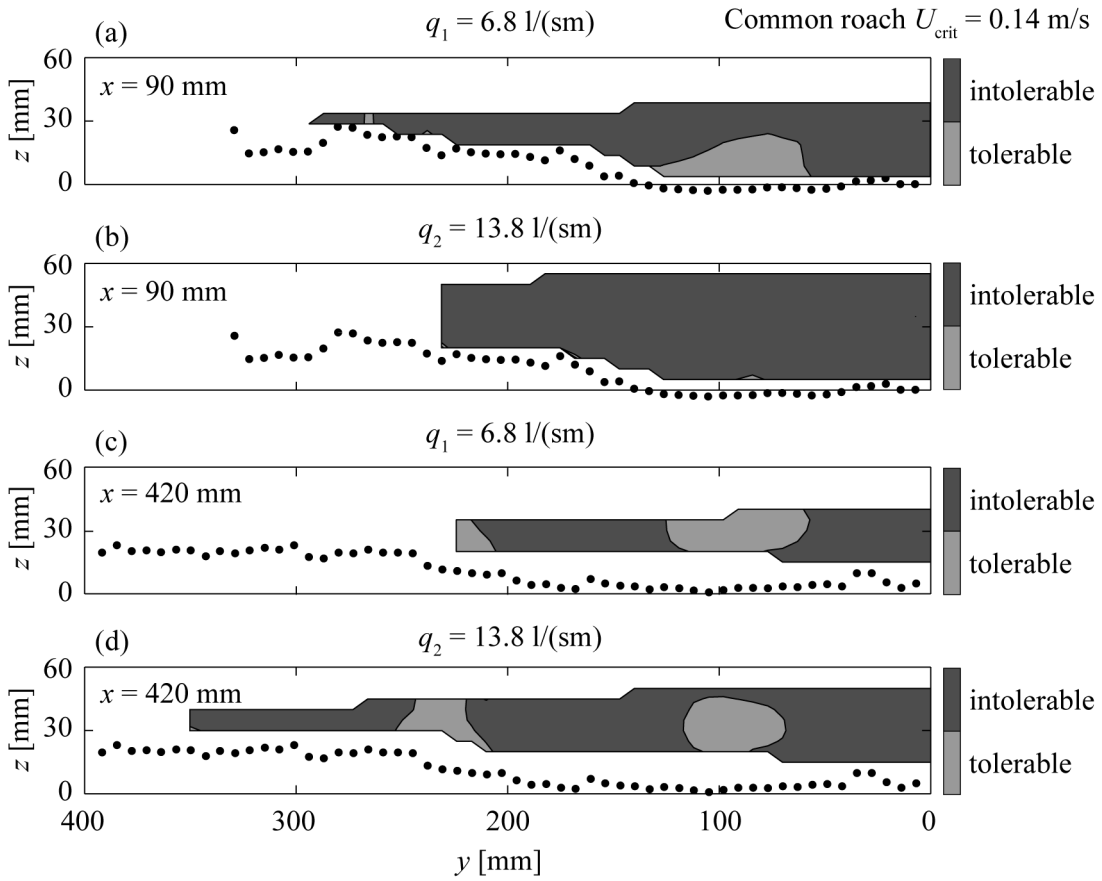

Figure 5.47 Comparison between velocities U below (light grey) and above (dark grey) the tolerable velocity for common roach with U_{crit} = 0.14 m/s at sections x = (a,b) 90, and (c,d) 420 mm for (a,c) q_1 = 6.8 l/(sm) and (b,d) q_2 = 13.8 l/(sm) with $h_{m,1}/P$ = 0.63 and $h_{m,2}/P$ = 0.88.

Figure 5.48 shows tolerable and intolerable velocities for three different fish species at x = 90 mm for q_1 = 6.8 l/(sm). The three considered fish species are the common roach (*Rutilus rutilus*, average swimming capacity) with U_{crit} = 0.14 m/s, the bullhead (*Cottus gobio*, poor swimming capacity) with U_{crit} = 0.07 m/s, and the brown trout (Salmo trutta fario, good swimming capacity) with U_{crit} = 0.18 m/s. The critical velocities were taken from Table 3.2 and downscaled to model dimensions assuming Froude similarity and with a geometrical scale factor of 25 as shown above. As expected, the migration possibilities are more pronounced for stronger rather than for weaker fish. Generally, regions with tolerable velocity diminish with the decrease of swimming capacity of the considered fish. Note that the preferable swim region for the different fish species should also be considered. For instance, the bullhead swims preferably close to the bed. Therefore, the theoretical migration corridor is given in the case of Figure 5.48 (a), even if the region is small and limited. If the common roach would only

swim in the upper part of the flow depth, then the theoretical migration corridor is not given according to Figure 5.48 (b), where the region with tolerable flow velocity is bigger but limited to an area close to the bed. Note that all these considerations about the ecological efficiency of UBR from the LDA measurements are theoretical and do not give any advice about the fish behaviour within such ramps.

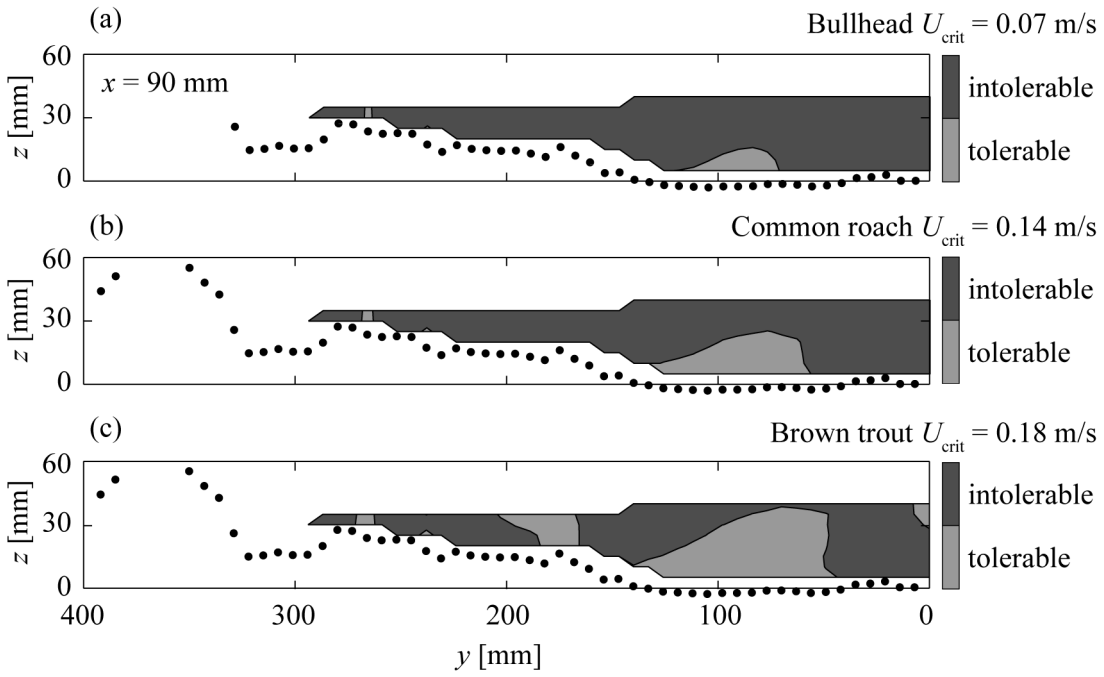

Figure 5.48 Comparison between velocities U below (light grey) and above (dark grey) the tolerable velocity for (a) bullhead $U_{crit} = 0.07$ m/s, (b) common roach $U_{crit} = 0.14$ m/s, and (c) brown trout $U_{crit} = 0.18$ m/s at $x = 90$ mm for $q_1 = 6.8$ l/(sm) with $h_{m,1}/P = 0.63$.

5.4.3 Spatially-averaged variables

Despite the strong heterogeneity of the measured local time-averaged velocities (Figure 5.42 and Figure 5.43), the double-averaged profiles of $\langle\bar{u}\rangle$ (defined in Chap. 2.4) for $h_{m,1}/P = 0.63$ and $h_{m,2}/P = 0.88$ show an almost uniform distribution (Figure 5.49 a). On average $\langle\bar{u}\rangle/u_b$ exceeds the value of 1 throughout the profile. Measurements could not be taken close to the bed and near the walls, leading to a slight bias towards higher velocities. This effect is more pronounced for the cases with lower relative submergence. However, due to the convergence of the statistical moments the results are considered significant for the general description of the flow conditions. For the lower relative submergences the flow occurs mainly below the block crests, i.e. within the interfacial sublayer, where the flow is dominated by form drag of the blocks in the upper part (macro-roughness sublayer) and by form and viscous drag close to the bed (sedimentary sublayer). The entire water column is influenced by the total roughness of the bed material and the blocks and therefore, the double-averaged velocity profile is nearly uniform over the whole flow depth. In contrast, the vertical profile $\langle\bar{u}\rangle$ for the highest relative submergence $h_{m,3}/P = 1.46$ strongly varies over the flow depth, having an S-shape, similar to Bathurst (1985) and Ferro and Baiamonte (1994), amongst others. They showed that flows with ratios of flow depth and the characteristic grain size between 2 and 7.5 have an S-shaped velocity profile, due to the existence of two zones: a lower zone, in which the velocity is reduced by drag effects of the boulders, and an upper zone located above the boulders, in which a quasi-smooth flow with high velocities occurs. In the present case the maximum velocity $\langle\bar{u}\rangle$ is at $Z \approx 1.56$ corresponding to $z = 75$ mm, i.e. at the central elevation of the form-induced layer above the block crests. The highest velocity gradient occurs just below z_c in the macro-roughness layer, where $\phi(z)$ has also its maximum gradient (Figure 5.40), indicating that the strongest flow velocity variation occurs in correspondence with the largest roughness density variation. At this height the S-shaped profile has an inflection-point, which separates the lower and the upper zone described above; the velocity profile is similar to a mixing-layer type profile (Ghisalberti and Nepf 2002, Okamoto and Nezu 2013).

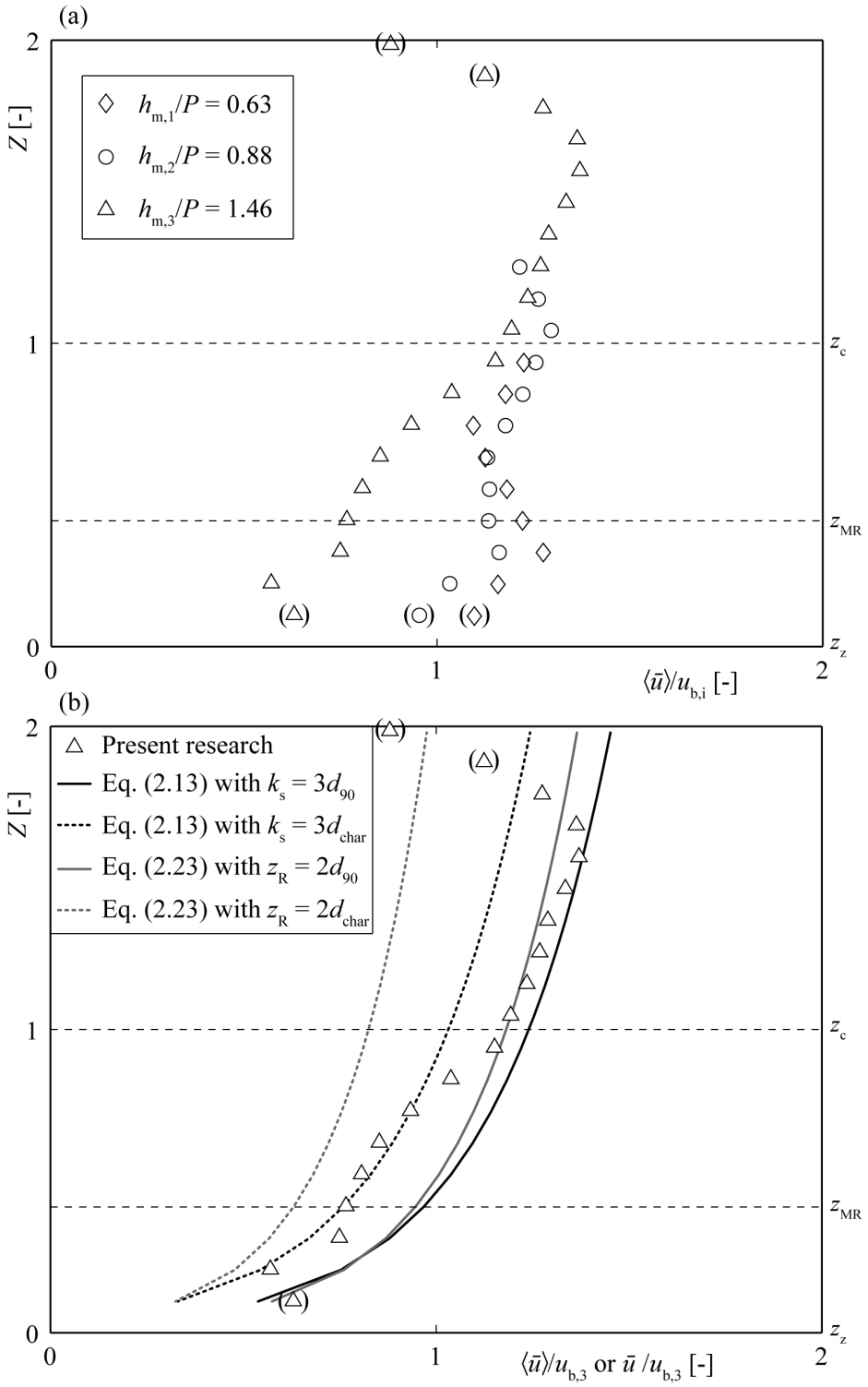

Figure 5.49 (a) Vertical distribution of $\langle\bar{u}\rangle/u_{b,i}$ for three relative submergences $h_{m,i}/P$ versus dimensionless height $Z = z/P$, and (b) Comparison between $\langle\bar{u}\rangle$ resulting from the measurements with $h_{m,3}/P = 1.46$ and velocity profiles determined accordingly to logarithmic law (Eq. 2.13) and to Bezzola 2002 (Eq. 2.23), both with two different assumptions for the bed roughness. Dashed lines: boundary of sedimentary sublayer z_{MR} (lower line) and macro-roughness sublayer z_c (upper line). Data in round brackets: statistically less significant; the same notation is also applied for the following diagrams.

The data with $h_{m,3}/P = 1.46$ were compared with two different relationships describing the flow resistance for open channel flows: the logarithmic law according to Eq. (2.13) and the relationship suggested by Bezzola (2002) with Eq. (2.16), considering the reduction of the momentum flux in the roughness layer (see Chap. 2.2). For the determination of the velocity profiles, different assumptions were considered. (1) For Eq. (2.13): $\kappa = 0.41$ (e.g. Nezu and Rodi 1986), $k_s = 3\,d_{90}$ (Bezzola 2010) and $u_* = u_{*,II} = \left(-\langle\overline{u'w'}\rangle_{max}\right)^{0.5}$ (Biron *et al.* 2004, see also below), (2) for Eq. (2.16): $z_R = 2\,d_{90}$ and $u_* = u_{*,II}$. Since the bed of a UBR is made of sediment material characterized by d_{90} and of blocks characterized by D, d_{90} and D were considered together with respect to the block placement density λ in a kind of weighted average as $d_{char} = d_{90}\,(1-\lambda) + D\,\lambda \approx 17.2$ mm. Figure 5.49 (b) shows the comparison between the double-averaged profile of $\langle\bar{u}\rangle$ for $h_{m,3}/P = 1.46$ and the velocity profiles determined according to Eq. (2.13) and Eq. (2.16), assuming d_{90} and d_{char} as two different representative bed roughness. The velocity decrease toward the water surface above the maximum value at $Z \approx 1.56$ is not described with any of the relationships considered. Also by extending the logarithmic law with the wake function (i.e. the velocity decrease close to the water surface typical for 2D flows, see e.g. Nezu and Rodi 1986), this aspect is not better described. The velocity decrease in the upper half of the form-induced sublayer and the maximum flow velocity below the water surface result from the secondary currents in narrow open-channels with $W/h < 5$ and is called "velocity dip-phenomenon" (e.g. Nezu *et al.* 1985, Guo and Julien 2005).

The velocity profiles resulting from Eq. (2.13) and Eq. (2.16) and assuming d_{90} better describe the measured profile of $\langle\bar{u}\rangle$, in particular in the lower half of the form-induced sublayer for approximately $1 < Z < 1.5$. At $Z > 1.5$ the velocity dip-phenomenon occurs and is not described by any equations illustrated in Figure 5.49 (b). For $Z < 1$ in the macro-roughness and in the sedimentary sublayers, where the blocks and the heterogeneous bed have their maximum influence on flow conditions, Eq. (2.13) assuming d_{char} returns similar velocities as the measured ones, whereas it does not describe the velocity profile of $\langle\bar{u}\rangle$. Despite these differences, note that the resulting double-averaged velocity profile of $\langle\bar{u}\rangle$ for $h_{m,3}/P = 1.46$ varies in the range given by the logarithmic law (Eq. 2.13) determined assuming d_{90} and d_{char}, respectively, as representative bed roughness.

The present results are compared with those of Ghisalberti and Nepf (2006), who investigated the structure of the shear layer in flows over submerged rigid and flexible canopies measuring the velocity components u and w. Figure 5.50 shows their experimental setup. The data on submerged rigid canopies for experiment R9 (s. Table 1 in Ghisalberti and Nepf 2006) are considered, where the canopy height is 0.138 m, and the canopy placement density determined with the definition of λ used herein (see Eq. 3.5) is $\lambda \approx 0.03$. The mean flow velocity is 0.0275 m/s and the flow depth 0.467 m, leading to submerged conditions.

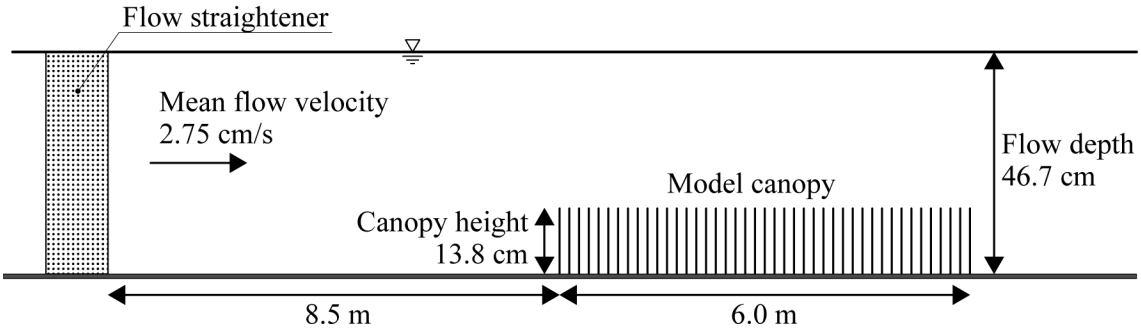

Figure 5.50 Longitudinal section of the experimental setup of the investigation of Ghisalberti and Nepf (2006) with submerged rigid canopies (Ghisalberti and Nepf 2006, adapted).

Figure 5.51 compares the vertical profiles of $\langle\bar{u}\rangle/u_b$ from the $h_{m,3}/P = 1.46$ case herein with the R9 case of Ghisalberti and Nepf (2006). The normalized height Z corresponds to the ratio between the vertical coordinate z and the representative block crest height z_c (or the block protrusion P), and the protrusion of the roughness element, namely the canopy height, respectively. The shape of the two velocity profiles is similar. The difference consists in the occurring velocity range, which is wider for the data from Ghisalberti and Nepf (2006). The normalized velocities below the canopy height ($Z < 1$, Figure 5.51) are significantly smaller compared to the present research, basically due the following reason: the canopies are placed homogeneously with a much lower placement density than in the present study and velocities are presumably similar over the entire canopy layer, whereas the heterogeneity of the blocks leads to areas, especially between two blocks, where the flow is strongly accelerated and contributes to a higher mean velocity for $Z < 1$. The measurements of Ghisalberti and Nepf (2006) were conducted for a relative submergence of approximately 3.4 and the velocity measured

up to $Z \approx 2.9$. This relative submergence allows the development of the outer layer, where the flow is no more directly affected by the canopy and the velocity increases. On the contrary, for the relative submergence tested in the present study with submerged blocks the flow layer above the block crests is affected by the roughness and the velocity increase is limited. Despite these differences in magnitude, both normalized velocity profiles are similar in shape with an inflection point slightly below z_c.

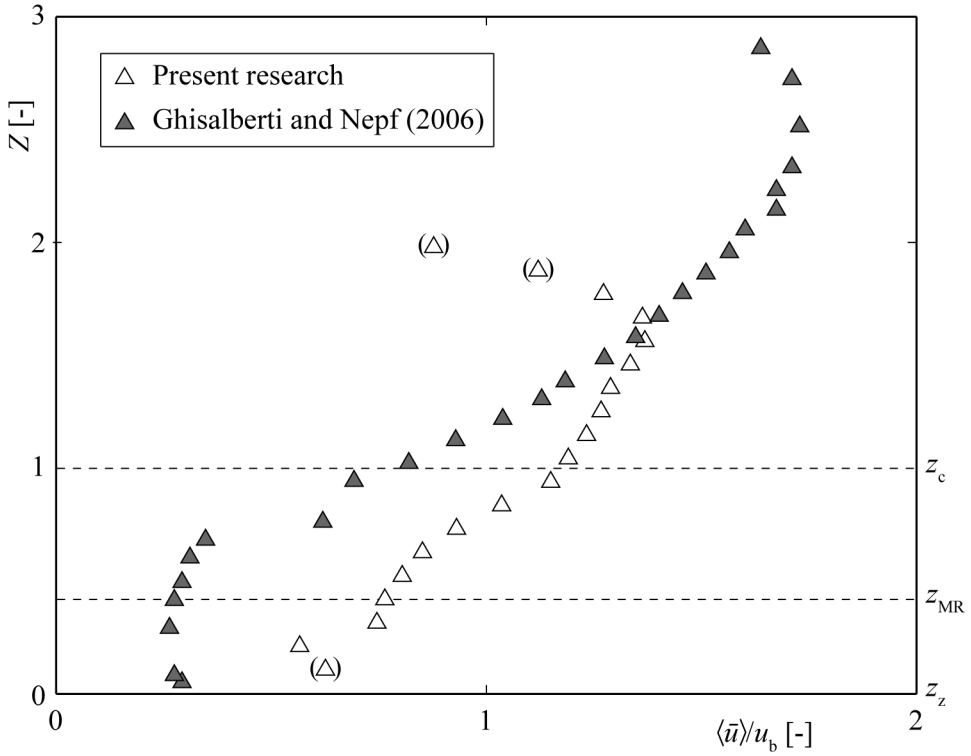

Figure 5.51 Vertical distribution of normalized velocities $\langle\bar{u}\rangle/u_{b,i}$ from present research for $h_{m,3}/P = 1.46$ and Ghisalberti and Nepf (2006). The vertical coordinate z is normalized for the present research with the block protrusion P (equal to the representative block crest height z_c) and for the data from Ghisalberti and Nepf (2006) with the canopy height.

The bulk velocities u_b together with the RMS (Root Mean Square)-values of the time-averaged velocities $\bar{u}$ resulting from phase C are compared with u_b of phase A in Figure 5.52. Note that u_b was measured with the salt dilution method in both phases A and C, whereas RMS($\bar{u}$) resulted from the LDA measurements of phase C. Note also that RMS($\bar{u}$) represents the spatially-averaged RMS and not the time fluctuation. The u_b values resulting from phase A (Figure 5.52) vary more than the range given by RMS($\bar{u}$)

from phase C (grey area, Figure 5.52). The reason lies in the different slopes for a given discharge: the ramp slope in phase C was constant at 2.9%, whereas it varies in phase A depending on the parameter combination and resulted in an equilibrium slope S_e. The different S_e corresponding to the different u_b in Figure 5.52 are indicated in brackets for some experiments as an example, to highlight that the ramp slope varied during phase A, whereas it remained constant during phase C. It can also be suggested that the block placement density affects RMS by increasing it. In the majority of cases u_b measured during phase A varied within the range resulting from $u_b \pm \mathrm{RMS}(\bar{u})$ measured during phase C.

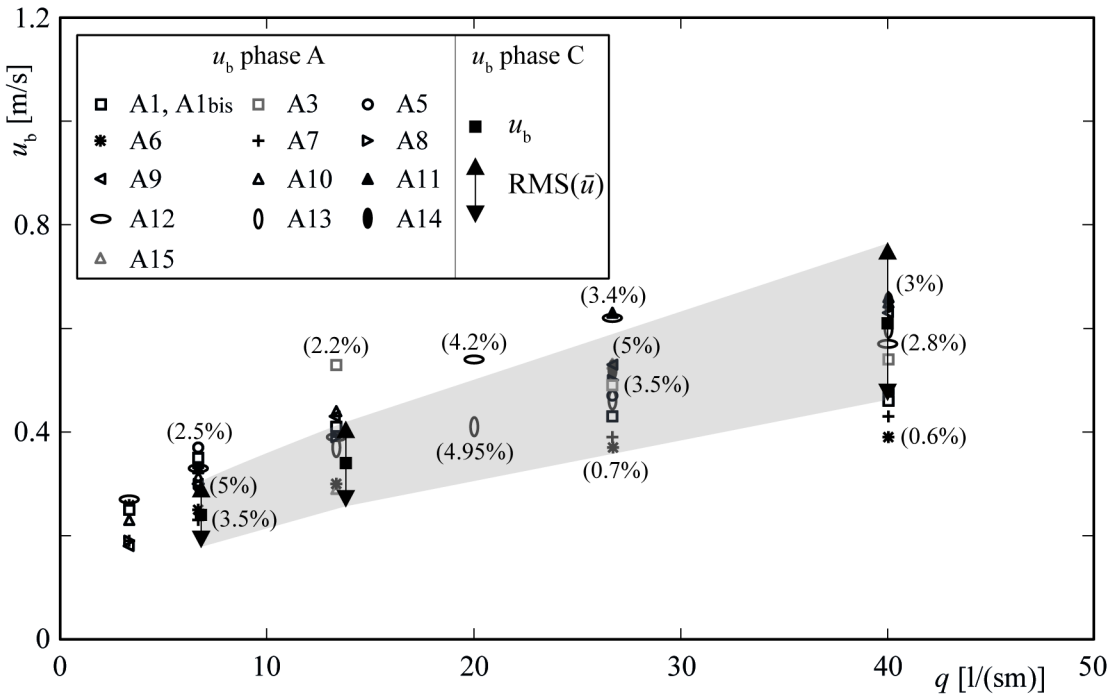

Figure 5.52 Bulk velocities u_b measured with salt dilution method both in phase A and C for $q < 50$ l/(sm). Arrows: RMS-values resulting from LDA measurements corresponding to RMS($\bar{u}$) = spatially-averaged RMS ≈ ±25%. Resulting equilibrium slopes S_e of some experiments are indicated in brackets.

The double-averaged vertical profiles of $\langle \bar{w} \rangle$ are similar for all three different relative submergences without any distinct profile (Figure 5.53). Due to the low relative submergences investigated, the flow always occurs within the layers affected by the influence of the blocks. Thus, the flow is relatively heterogeneous over the entire flow depth (see also Figure 5.42), leading to $\langle \bar{w} \rangle$ with a magnitude of about 5-10% of the

bulk velocity $u_{b,i}$. Figure 5.53 suggests that the flow is on average directed to the water surface ($\langle \overline{w} \rangle_{mean} > 0$), whereas the vertical component of the flow should be zero on average. The reason may lie in the difference between the local bed slope within the measurement area and the average bed slope of the 4 m long block ramp. The local bed slope strongly varied influencing in particular the vertical component of the flow velocity. This influence is more pronounced for small relative submergences h/P, because high water levels compensate this local effect. For this reason $\langle \overline{w} \rangle$ is less representative for the entire ramp. The data sufficiency for the main velocity component $\langle \overline{u} \rangle$ was proven with the convergence of statistical moments (see Chap. 4.4.2). Regarding the fluctuation component w' and the resulting time- and spatially-averaged Reynolds shear stresses it is assumed to be representative, because w' is derived from the local time-averaged velocities which are representative (Chap. 4.4.2).

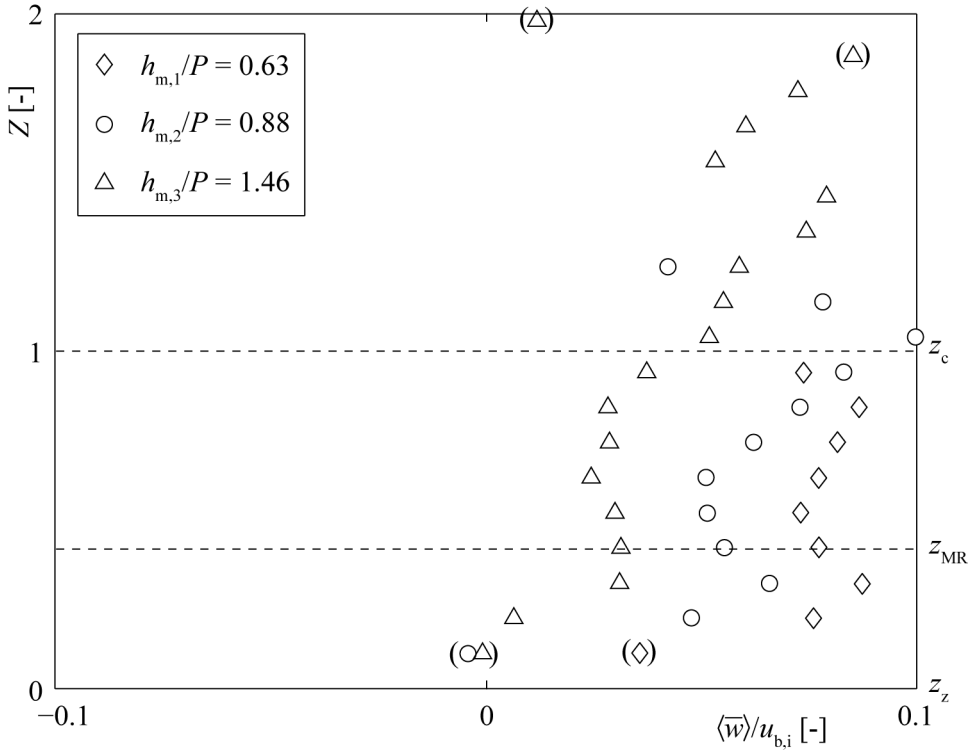

Figure 5.53 Vertical distribution of $\langle \overline{w} \rangle / u_{b,i}$ for three relative submergences $h_{m,i}/P$ versus dimensionless height $Z = z/P$.

The spatially-averaged Reynolds stresses for the three tested relative submergences are shown in Figure 5.54. The vertical profile for $h_{m,3}/P = 1.46$ has a triangular shape with its maximum at $Z \approx 0.83$, or $z = 40$ mm (Figure 5.54), respectively, i.e. just below z_c, corresponding to the point with the maximum momentum exchange due to the maximum interaction between the form-induced and the macro-roughness sublayers. In absolute model values the Reynolds stress varies from -0.0018 m^2/s^2 at $Z \approx 1.77$ (lower representative data in Figure 5.54) to 0.0057 m^2/s^2 at $Z \approx 0.83$. The maximum of $-\langle\overline{u'w'}\rangle$ corresponds to the height of the inflection point in the velocity profile $\langle\bar{u}\rangle$ (Figure 5.49 a) as in the case of e.g. Okamoto and Nezu (2013). Below this height the values of $-\langle\overline{u'w'}\rangle$ decrease almost linearly to the bottom of the macro-roughness sublayer at z_{MR}; in the sedimentary sublayer for $z < z_{MR}$ the decrease is less pronounced and the distribution is nearly uniform. The Reynolds stress varies in a range which is about twice the magnitude of the maximum value, with a minimum at the highest measured height. Negative Reynolds stresses occur in the upper half of the form-induced sublayer, in correspondence with decreasing $\langle\bar{u}\rangle$ (Figure 5.49 a). This phenomenon can be explained by considering the momentum exchange between the flow layers: the upper half of the form-induced sublayer is the only region of the vertical profile where a water particle is accelerated if it moves to a lower flow level, because the mean velocity increases with decreasing z (Figure 5.49 a). Below the height of the maximum velocity, the velocity reduces and thus a water particle is on average decelerated by moving downward. Therefore, the momentum transfer has an opposite sign above and below the maximum double-averaged mean velocity, respectively. For the same reason the Reynolds shear stresses have opposite signs above and below that point. In general this indicates that momentum is absorbed in the upper half of the form-induced sublayer. It is assumed that this phenomenon can be explained by the presence of local water level changes. The bulk Froude number is around 0.74; locally above the blocks we have much higher values leading to local undulating waves that absorb momentum. This phenomenon occurs only in the upper part of the flow when h_m is larger than the block height.

The vertical profile determined for the two lower relative submergences do not show the characteristic shape (Figure 5.54) and it appears difficult to generally describe the flow processes. The highly irregular bed and the randomly placed roughness elements render the flow chaotic. The gradient of the Reynolds shear stress profiles are smaller in general, corresponding to the velocity profiles (Figure 5.49 a). Furthermore,

because the blocks are not fully submerged, the spanwise velocity component (not measured herein) becomes important for the description of the hydraulic and turbulence structures. For this reason, mainly the results of the higher relative submergence $h_{m,3}/P$ are considered here, which are decisive in terms of bed stability.

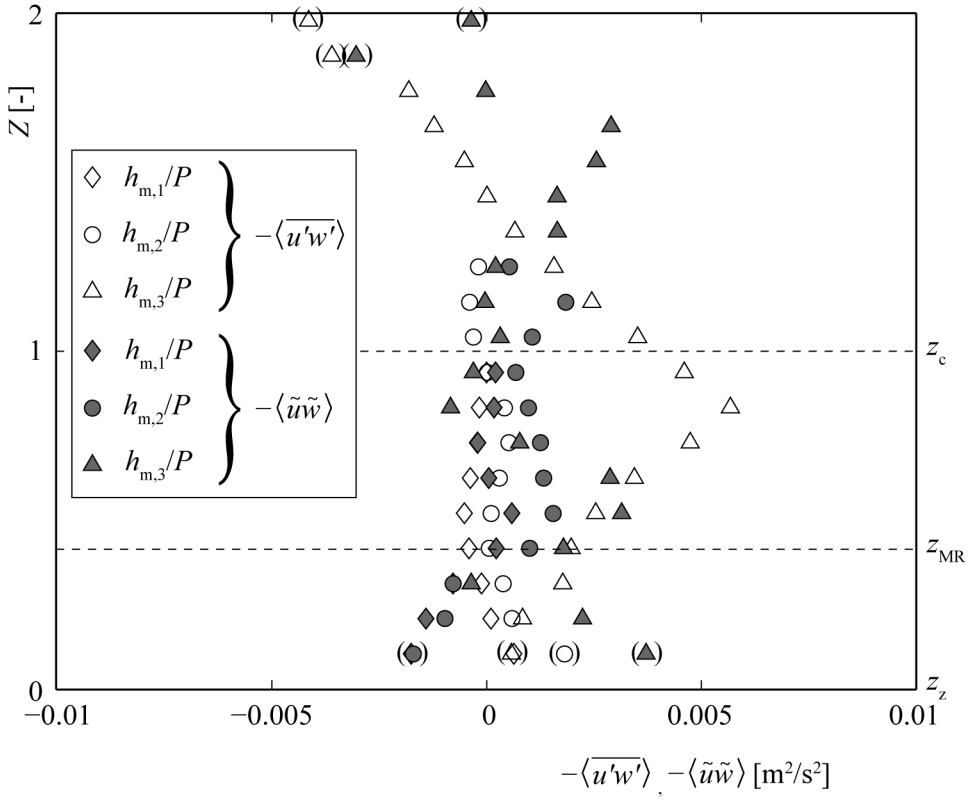

Figure 5.54 Vertical distribution of spatially-averaged Reynolds stresses $-\langle\overline{u'w'}\rangle$ and form-induced stresses $-\langle\tilde{u}\tilde{w}\rangle$ for three relative submergences $h_{m,i}/P$ versus dimensionless height $Z = z/P$.

The vertical profiles of the form-induced stresses $-\langle\tilde{u}\tilde{w}\rangle$ are plotted in Figure 5.54. For $h_{m,1}/P = 0.63$ and $h_{m,2}/P = 0.88$ the distributions are almost uniform and the values of $-\langle\tilde{u}\tilde{w}\rangle$ are in the same order of magnitude as those of $-\langle\overline{u'w'}\rangle$. The distribution of the form-induced stresses for $h_{m,3}/P = 1.46$ has two maxima: (1) just above the lower edge of the macro-roughness sublayer z_{MR}, where the heterogeneity of the bed topography has its maximum effect on the flow conditions; and (2) in the upper half of the form-induced sublayer, in correspondence with negative Reynolds stresses (see above), suggesting that the spatial variability given by the blocks effects the flow up to this height and confirming the presence of the form-induced sublayer. The values of

$-\langle\overline{u'w'}\rangle$ and $-\langle\tilde{u}\tilde{w}\rangle$ (Figure 5.54) are much higher (1 or 2 orders of magnitude) compared to the viscous stress which can be determined from the vertical profile $\langle\bar{u}\rangle$ (Figure 5.49 a) as $\nu\ \partial\langle\bar{u}\rangle/\partial z$, confirming that the viscous stress can be assumed as negligible (Chap. 5.4.1). The influence of viscous drag in the sedimentary sublayer could not be verified with the present measurements.

Figure 5.55 compares the vertical profiles of $-\langle\overline{u'w'}\rangle$ of the present research for $h_{m,3}/P = 1.46$ and of the experiment R9 of Ghisalberti and Nepf (2006). The spatially-averaged Reynolds shear stress $-\langle\overline{u'w'}\rangle$ is scaled with the shear velocity defined as $u_{*,II} = (-\langle\overline{u'w'}\rangle_{max})^{0.5}$, characterizing the momentum flux and thus being an appropriate scale for turbulence parameters (e.g. Stephan and Gutknecht 2002, Biron *et al.* 2004, Järvelä 2005, Ghisalberti and Nepf 2006, Manes *et al.* 2007). The shape of both profiles is similar. The maximum Reynolds shear stresses are reached just below the roughness crest; above and below this maximum the Reynolds shear stresses decrease almost linearly. As described above, negative Reynolds stresses occur in correspondence with negative gradient (Figure 5.51). For $Z < 1$ $-\langle\overline{u'w'}\rangle$ decreases stronger below the roughness crests in the case of Ghisalberti and Nepf (2006) than for the present research, presumably due to the regular roughness spacing. On the contrary, for $Z > 1$ $-\langle\overline{u'w'}\rangle$ decreases stronger in the present research, due to more heterogeneous flow field dominated by accelerating flows over and between the blocks and by regions of low turbulence and low velocities. Under such heterogeneous hydraulic conditions, the momentum exchange is higher than over a regularly rough bed as in the case of Ghisalberti and Nepf (2006). It should be noted that the experiments by Ghisaberti and Nepf (2006) are performed under low Froude number conditions ($F \approx 0.013$ for the experiment R9) whereas in the present case the flow at the block crest and above is close to critical and sometimes becomes locally supercritical. In the Ghisalberti and Nepf (2006) case a mixing layer develops, where coherent flow structures can evolve and travel with the mean flow velocity. In the present study the flow at and above the block crests has more a jet-like behaviour with changing water depth due to surface waves.

The vertical profiles of the spatially-averaged RMS-values of both velocity components u_{RMS} and w_{RMS}, respectively, normalized with $u_{b,3}$ for $h_{m,3}/P = 1.46$ have a double-curved shape (Figure 5.56). The shape is similar for the *u* and *w* component with u_{RMS} approximately 1.2-1.5 times larger than w_{RMS}. In the macro-roughness sublayer the RMS-values reaches its maximum below the representative block crest height z_c, at the

point where the Reynolds stresses are maximum (Figure 5.55). From this point upwards, u_{RMS} and w_{RMS} decrease until elevation $Z = 1.46$, and increase again towards to the water surface, because of the surface waves This increase towards the water surface should be interpreted with care. Only a few points were measured near the water surface, because surface waves result in higher velocity fluctuations (see considerations about the statistical significance made in Chap. 4.4.2).

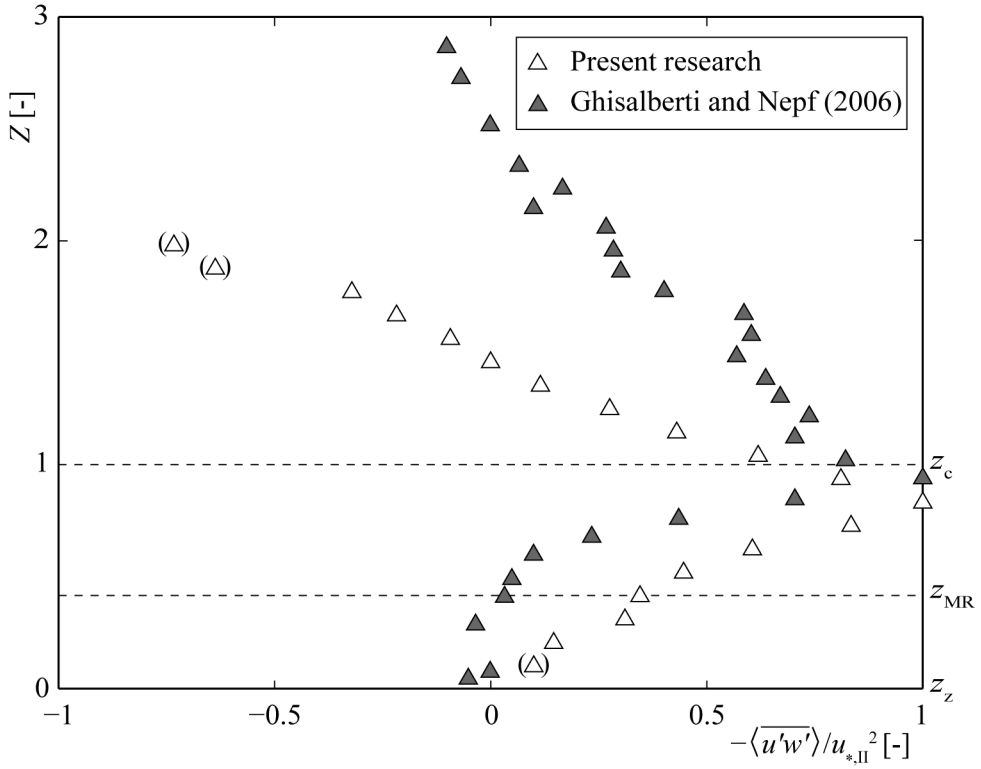

Figure 5.55 Vertical distribution of normalized spatially-averaged Reynolds shear stress $-\langle\overline{u'w'}\rangle/u_{*,II}{}^2$ with $u_{*,II}{}^2 = -\langle\overline{u'w'}\rangle_{max}$ versus Z from present research for $h_{m,3}/P = 1.46$ and Ghisalberti and Nepf (2006).

The spatially-averaged RMS-values derived from the same data set of Ghisalberti and Nepf (2006) considered in Figure 5.51 and Figure 5.55 are also plotted in Figure 5.56. Except for the sedimentary sublayer, the shape of both profiles is nearly triangular with the maximum at approximately the roughness crests. The velocity fluctuations u_{RMS} of the data Ghisalberti and Nepf (2006) are approximately 1.5 times than w_{RMS}. The difference is slightly higher than for the present data, where the irregular placed blocks strongly affect also w, leading to higher turbulence intensities compared with the more regular rough beds of Ghisalberti and Nepf (2006). Looking at the x-z-plane the

flow is more isotropic in the present study due to the stronger vertical momentum exchange.

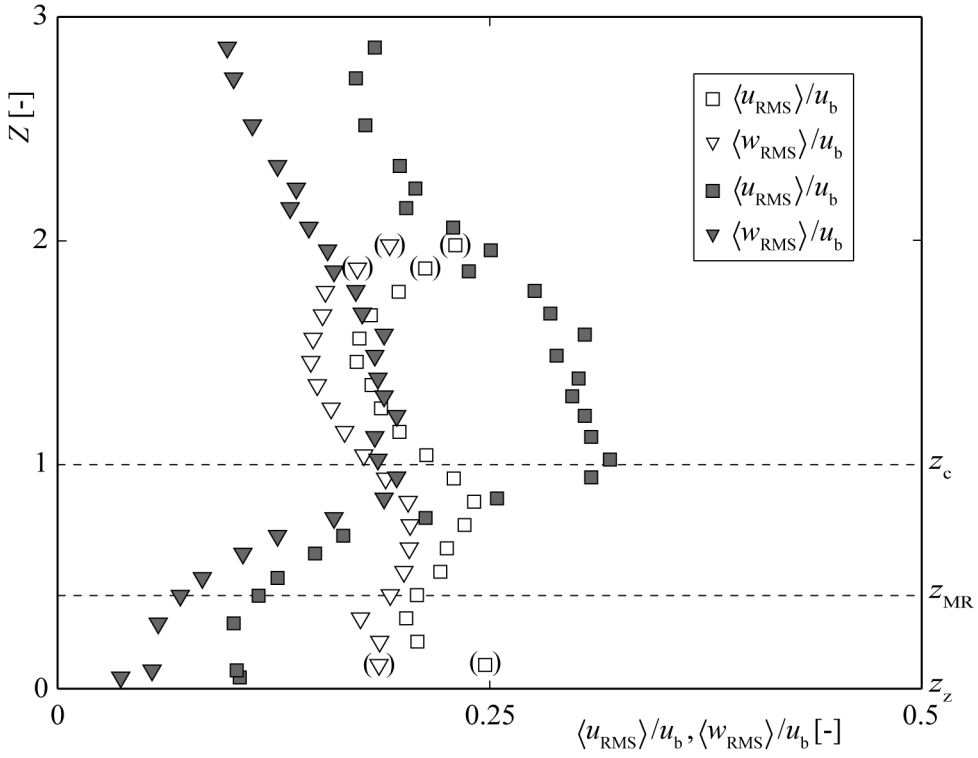

Figure 5.56 Vertical distribution of the standard deviation of the velocities u_{RMS} and w_{RMS}, respectively, normalized with the bulk velocity u_b from present research for $h_{m,3}/P = 1.46$ (empty symbols) and Ghisalberti and Nepf (2006, filled symbols).

5.4.4 Quadrant analysis

The conventional quadrant method of the fluctuations terms of the velocity (herein u' and w') is often used to analyze the structure of turbulent stresses. Through the analysis of the correlation between u' and w', dominant turbulent events as outward interactions (Q1), ejections (Q2), inward interactions (Q3) or sweeps (Q4) can be identified (see Chap. 2.5). Poor correlation indicates absence of coherent turbulent structures. Here the conventional quadrant analysis is applied for two selected locations in the measurement area (Figure 4.13). Figure 5.57 shows the quadrant analysis at x = 190 mm, y = 63 mm at different heights z = (a) 25 mm, (b) 40 mm, (c) 50 mm, and (d) 75 mm (indicated also as normalized height $Z = z/P$) for the specific discharge q_3 = 40 l/(sm) corresponding to a relative submergence $h_{m,3}/P$ = 1.46. This location corresponds to the region just upstream of a block on the right side (see Figure 5.41).

At height z = 40 mm (Figure 5.57 b) just below the representative block crest height z_c = 48 mm the points in the quadrants Q2 and Q4 (Chap. 2.5) preponderate. This would suggest ejection and sweep events, whereas the considered height z = 40 mm is not close to the bed where these events usually occur. This correlation could suggest flow separation, whereas other points analysed where flow separation occurs (not shown here) do not show a correlation between u' and w'. There is no correlation between u' and w' at the height between the sedimentary and the macro-roughness sublayer (z = 25 mm, Figure 5.57 a), indicating the absence of coherent structures. The same applies at the height just above the block (z = 50 mm, Figure 5.57 c) in the lower part of the form-induced sublayer as well as in the middle of it at z = 75 mm (Figure 5.57 d).

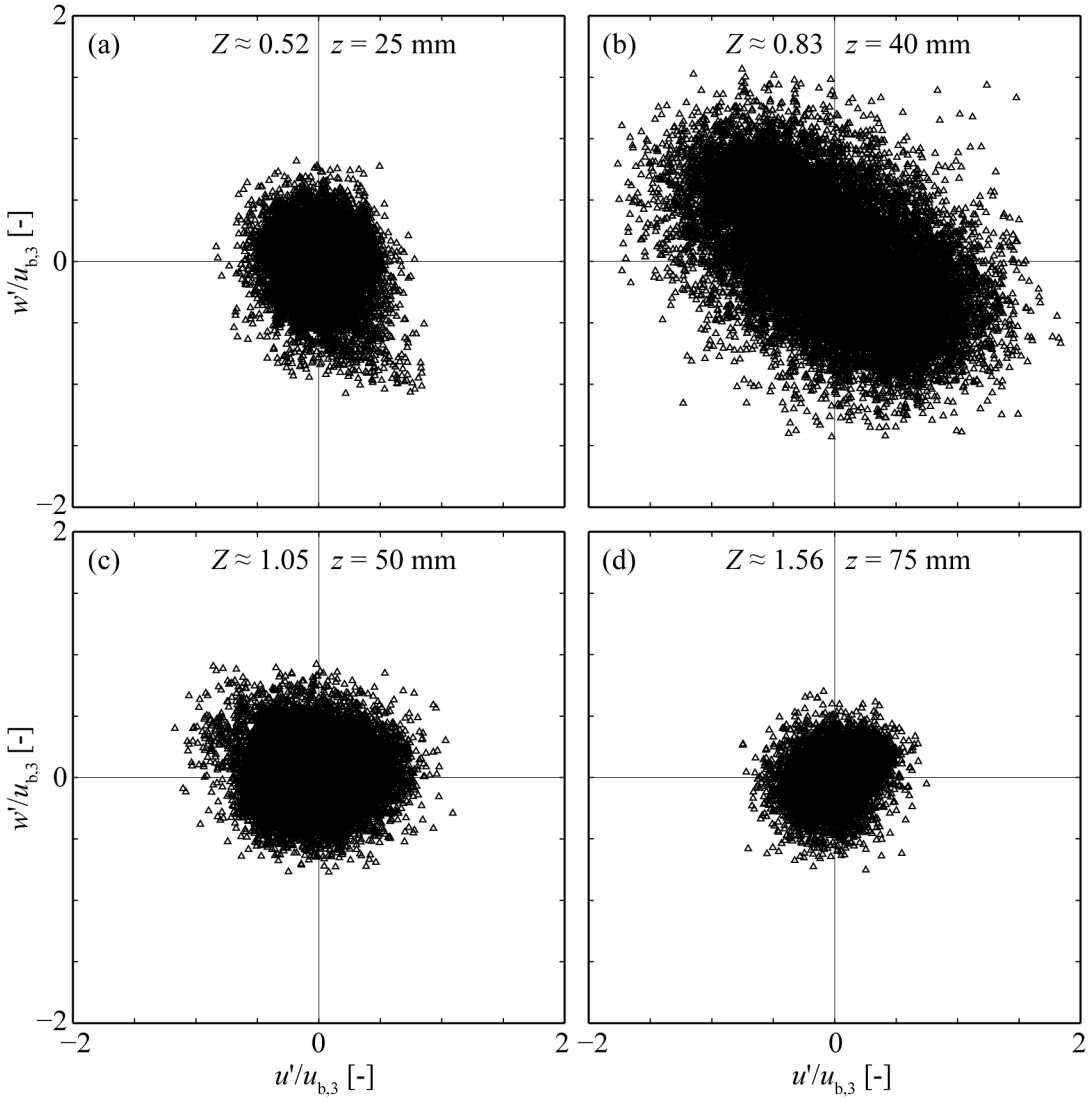

Figure 5.57 Quadrant analysis for the fluctuation terms *u*' and *w*' normalized with the bulk velocity $u_{b,3}$ for $h_{m,3}/P = 1.46$ at $x = 190$ mm and $y = 63$ mm at four different heights *z*.

Figure 5.58 illustrates the results at $x = 90$ mm, $y = 84$ mm at heights $z =$ (a) 15 mm, and (b) 60 mm, corresponding to the centre of the region upstream of the blocks (see Figure 5.41). Both diagrams do not indicate any correlation between *u*' and *w*'. At $z = 60$ mm the shape of the distribution in the quadrants is smaller than at $z = 15$ mm, indicating lower fluctuation terms *u*' and *w*'and more regular flow velocity in both directions over time. At $z = 60$ mm the flow just upstream of the block and above it was similar to a directed jet overflowing the block. At $z = 15$ mm the flow shows a very different behaviour, leading to higher *u*' and *w*' and to wider shape of the distribution in the quadrant analysis (Figure 5.58 a). The general absence of correlation indicates that

the in considered case the quadrant analysis does not provide additional information about the flow and turbulence characteristics. It shows the magnitude of the velocity fluctuations at a certain point. This information is also given by the RMS-values RMS(u) and RMS(w).

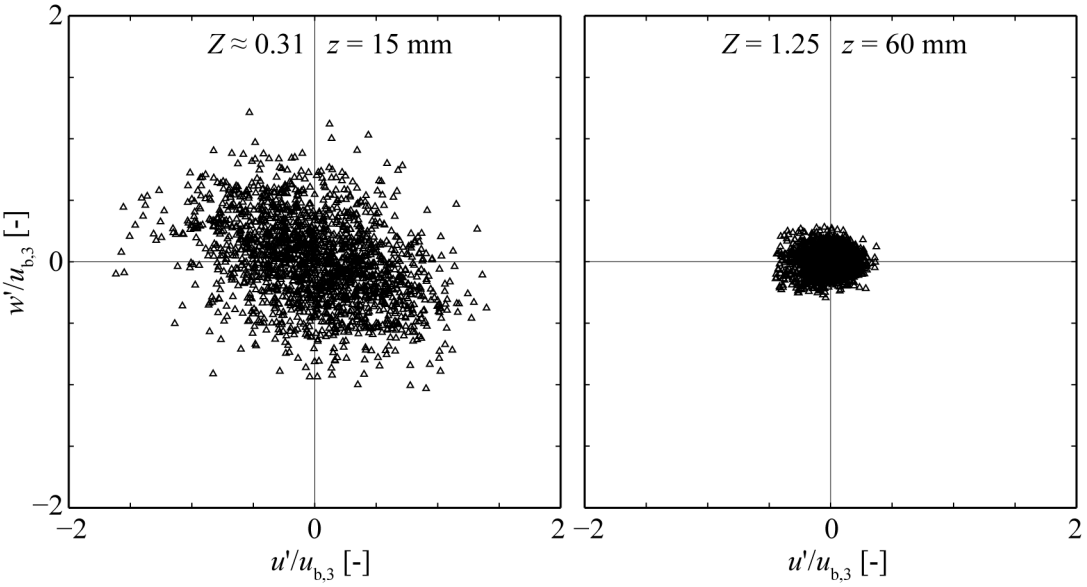

Figure 5.58 Quadrant analysis for u' and w' normalized with $u_{b,3}$ for $h_{m,3}/P = 1.46$ at x= 90 mm and y = 84 mm at two different heights z.

A similar analysis can be applied to the spatial disturbances $\tilde{u}$ and $\tilde{w}$ of time-averaged velocity components. In this case the quadrant analysis is made for all data measured in a plane at a certain height z. Analysing the correlation between $\tilde{u}$ and $\tilde{w}$, the momentum exchange produced by the form-induced stresses $\langle\tilde{u}\tilde{w}\rangle$ can be investigated. Figure 5.59 shows the quadrant analysis for $\tilde{u}$ and $\tilde{w}$ at height z = 35 mm for (a) q_1 = 6.8 l/(sm), (b) q_2 = 13.8 l/(sm), and (c) q_3 = 40 l/(sm). For all three cases $\tilde{u}$ varies more than $\tilde{w}$, indicating higher spatial variation of the mean flow component than of the vertical one. The height z = 35 mm corresponds approximately to the height in the center of the macro-roughness sublayer, where the presence of the blocks strongly affects the flow. In this region, the flow changes continuously its mean direction due to the blocks. For this reason, $\tilde{u}$ resulted generally higher than $\tilde{w}$ considering all measured data points at z = 35 mm.

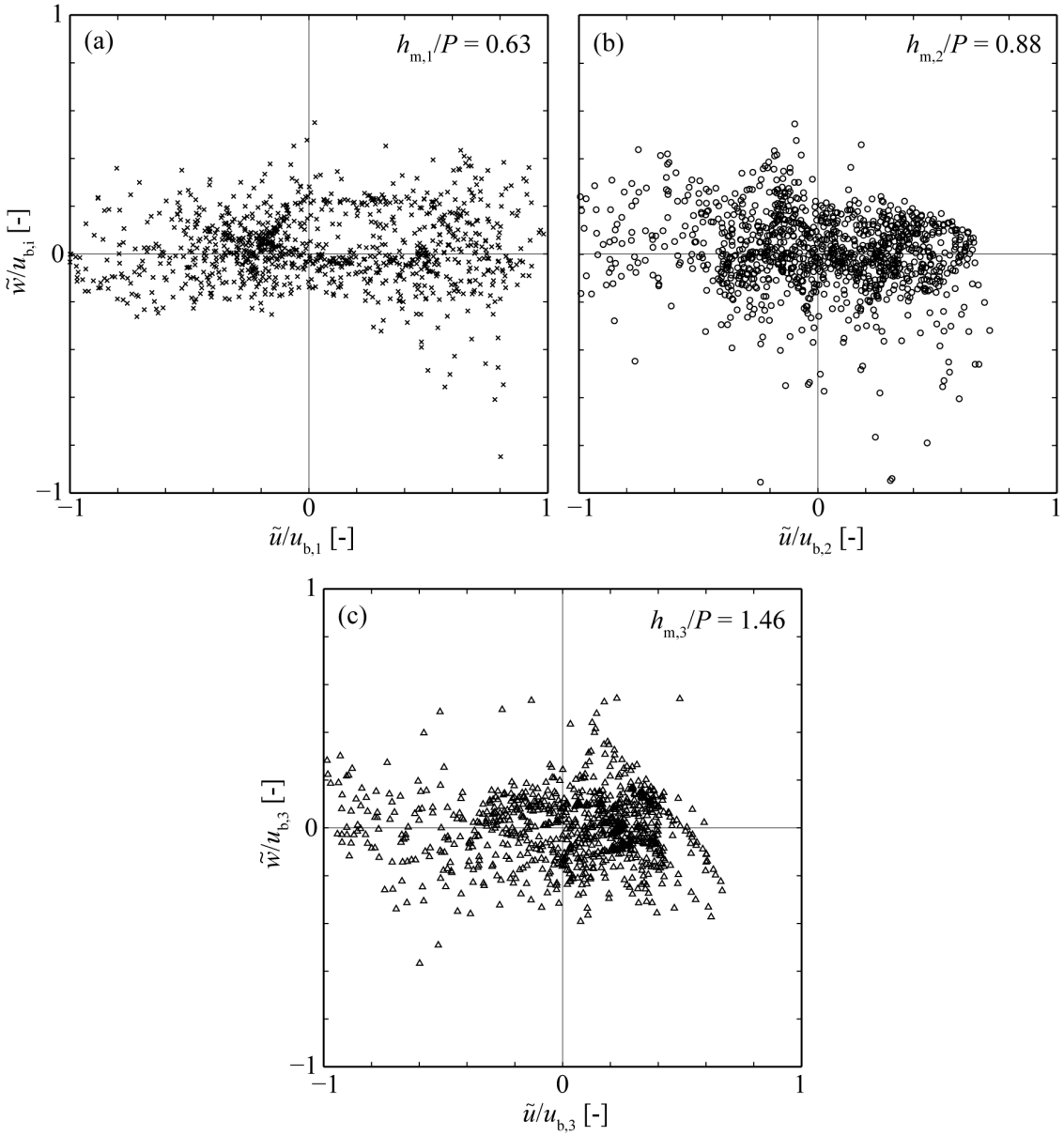

Figure 5.59 Quadrant analysis for the spatial disturbances $\tilde{u}$ and $\tilde{w}$ normalized with the bulk velocity $u_{b,i}$ for three relative submergences $h_{m,i}/P$ at height $z = 0.35$ or $Z = z/P = 0.73$, i.e. in the middle of the macro-roughness layer.

Figure 5.60 shows the quadrant analysis at height $z = 50$ mm for (a) $h_{m,2}/P = 0.88$, and (b) $h_{m,3}/P = 1.46$. No results are available for $h_{m,1}/P = 0.63$ because the flow depth was smaller than $z = 50$ mm, corresponding to the height just above the representative block crest z_c in the lower region of the macro-roughness sublayer. Also in this case, the majority of the points indicates higher $\tilde{u}$ than $\tilde{w}$. For $h_{m,2}/P = 0.90$ spatial disturbances $|\tilde{w}|$ are high for positive $\tilde{u}$ (Q1 and Q4), corresponding to local time-averaged velocity $\bar{u} > \langle\bar{u}\rangle$ (i.e. $\bar{u} = \langle\bar{u}\rangle + \tilde{u}$). This suggests that the accelerated flow above the blocks had

also a high variation in the vertical component, due to the water surface at the same height as the mean block crest height ($h_{m,2}/P = 0.88$) and to the undulating flow. In contrast, for $h_{m,3}/P = 1.46$ spatial disturbances $|\tilde{w}|$ are high for negative $\tilde{u}$ (Q2 and Q3), corresponding to $\bar{u} < \langle\bar{u}\rangle$. For positive $\tilde{u}$ by accelerating flow the low $\tilde{w}$ indicate an almost directed jet at $z = 50$ mm, overflowing the blocks and not being affected by the water surface due to the present overlapping flow region (50 mm < z < $z_{max,3}$ ≈ 95 mm).

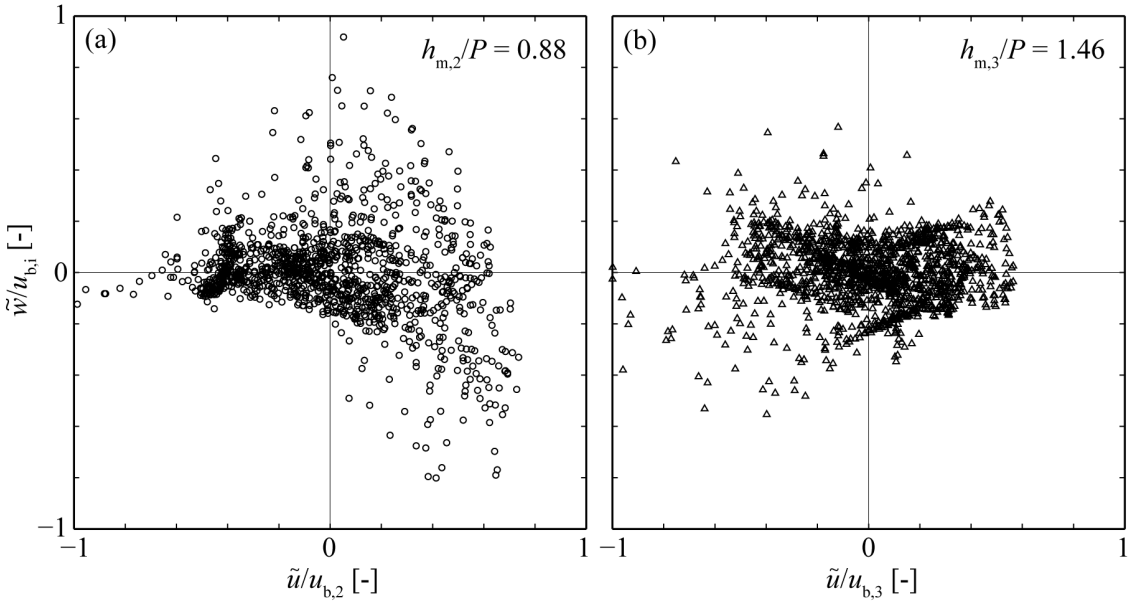

Figure 5.60 Quadrant analysis for $\tilde{u}$ and $\tilde{w}$ normalized with $u_{b,i}$ for two $h_{m,i}/P$ at $z = 0.50$ or $Z = z/P = 1.05$, i.e. just above the representative block crest z_c.

Figure 5.61 shows the quadrant analysis at height $z = 75$ mm for $h_{m,3}/P = 1.46$. The shape of the distribution is almost round and regular, indicating no particular correlation between $\tilde{u}$ and $\tilde{w}$ and no predominant spatial disturbance in one direction. For $h_{m,3}/P = 1.46$ the water surface was regular and not undulated as for $h_{m,1}/P = 0.63$ and $h_{m,2}/P = 0.88$. The flow in the upper part of the form-induced layer was homogeneous over the measurement area at $z = 75$ mm, resulting in an almost round and compact shape of the distribution in the quadrant analysis.

Also in the case of the spatial quadrant analysis, the present data show a general absence of correlation between $\tilde{u}$ and $\tilde{w}$. They show the magnitude of the spatial disturbance at a certain elevation, which can be obtained also by the RMS-values RMS($\bar{u}$)

and RMS($\overline{w}$). However, without the quadrant analysis both the correlations between u' and w'and $\tilde{u}$ and $\tilde{w}$ cannot be estimated a priori.

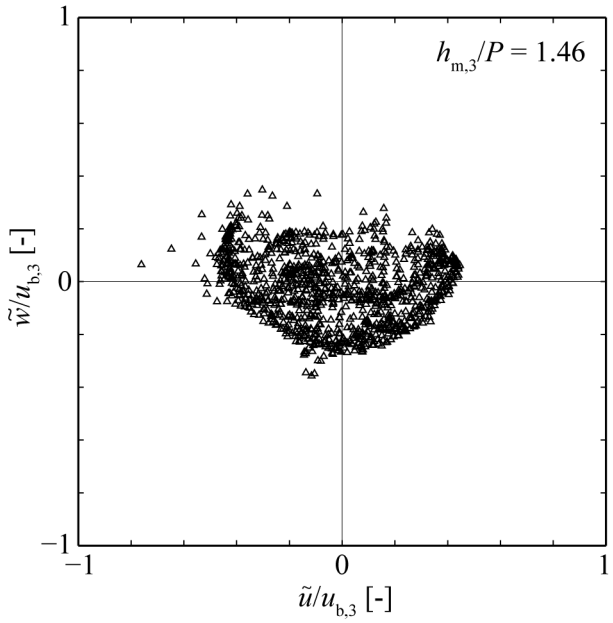

Figure 5.61 Quadrant analysis for $\tilde{u}$ and $\tilde{w}$ normalized with $u_{b,3}$ for $h_{m,3}/P = 1.46$ at $z = 0.50$ or $Z = z/P = 1.05$, i.e. just above the representative block crest z_c.

5.4.5 Bed shear stress

The bed shear stress τ_0 and the corresponding shear velocity $u_{*,\mathrm{I}} = \sqrt{\tau_0/\rho}$ characterize the flow and determine the flow resistance and sediment entrainment. By integrating Eq. (2.49) (Chap. 2.4.1) along the vertical coordinate τ_0 follows for two cases: 1) water level $h_\mathrm{m} > z_\mathrm{c}$, where a form-induced sublayer develops; 2) water level $h_\mathrm{m} < z_\mathrm{c}$, where no form-induced sublayer exists. For case (1) and with $h_\mathrm{w} = \int_{z_\mathrm{t}}^{z_\mathrm{c}} \phi(z)\mathrm{d}z$ (Nikora *et al.* 2007a and 2007b) as the characteristic flow depth it follows

$$\frac{\tau_0}{\rho} = gS[h_\mathrm{m} - z_\mathrm{c} + h_\mathrm{w}] = [-\phi\langle\overline{u'w'}\rangle(z_\mathrm{t}) - \phi\langle\tilde{u}\tilde{w}\rangle(z_\mathrm{t})] + \int_{z_\mathrm{t}}^{z_\mathrm{c}} \frac{\phi(z)}{\rho}\langle\frac{\partial\tilde{p}}{\partial x}\rangle\,\mathrm{d}z \quad (5.11)$$

This means that in general the overall bed shear $gS[h_\mathrm{m} - z_\mathrm{c} + h_\mathrm{w}]$ is given by the Reynolds shear stress, by the form-induced stress, and by the form drag.

In the present case, at the height of the roughness crest z_c the Reynolds stress are maximum (Figure 5.54) and the form-induced stress also gives a contribution to the total fluid shear stress. However, moving downwards to the lowest bed level z_t, the fluid shear stress decreases because momentum is absorbed by drag (Manes *et al.* 2007). Therefore, at z_t both Reynolds and form-induced stress are negligible and the bed shear stress τ_0 corresponds to the sum of the gravity term above the blocks and the drag acting on the impermeable base as

$$\tau_0 = \rho gS[h_\mathrm{m} - z_\mathrm{c} + h_\mathrm{w}] = \rho gS[h_\mathrm{m} - z_\mathrm{c}] + \int_{z_\mathrm{t}}^{z_\mathrm{c}} \phi(z)\rho gS\,\mathrm{d}z, \quad (5.12)$$

where the gravity term $\rho gS(h_\mathrm{m} - z_\mathrm{c})$ exists only for $h_\mathrm{m} > z_\mathrm{c}$ and represents the part of the shear above the blocks ($z > z_\mathrm{c}$), and the drag term represents the part of the shear below the blocks ($z < z_\mathrm{c}$).

Table 5.2 shows the resulting bed shear stresses from Eq. (5.12), the shear velocities $u_{*,\mathrm{I}} = \sqrt{\tau_0/\rho}$, and the values of the determined integrals of the roughness geometry function $\phi(z)$. The highest bed shear stress is determined for $h_{\mathrm{m},3}/P = 1.46$, i.e. when the blocks are fully submerged. In this case, the gravity term plays a role and is added to the term dependent on the roughness geometry function, which also reaches the maximum level (because $\phi(z) = 1$ for $z > z_{\mathrm{c,max}}$).

The last row of Table 5.2 shows the total bed shear stress for $h_{\mathrm{m},3}/P = 1.46$ including the Reynolds stress at the free surface, which are usually negligible. In the present experiment non-negligible negative Reynolds stresses were measured at the free-surface

(see Figure 5.54). Taking these values $\langle\overline{u'w'}\rangle_{\mathrm{surface}}$ into account the total bed shear stress is reduced by approximately 25%. One hypothesis about the absorbed momentum above the block crests leading to negative Reynolds stresses can be given by the presence of local hydraulic undulations. The bulk Froude number is around 0.74; locally above the blocks they can be higher values leading to local hydraulic jumps that absorb momentum. This phenomenon occurs of course only in the upper part of the flow when h_m is larger than the block height z_c.

Table 5.2 Integrals of roughness geometry function, total bed shear stresses, and resulting shear velocities derived from Eq. (5.12) for three relative submergences $h_{m,i}/P$: z_{max} = maximal elevation up to which integral of $\phi(z)$ was determined (for $h_{m,1}/P$ and $h_{m,2}/P$, $z_{max} = h_{m,1}$ and $h_{m,2}$, respectively, because $h_{m,1}, h_{m,2} < z_c$). In Eq. (5.12) the term $(h_m - z_c)$ exists only for $h_{m,i} > z_c$. The accuracy in the measuremen of S was ±0.1%, resulting in an error of the shear velocities $u_{*,I}$ of ±2%. *) Values determined considering the negative Reynold shear stresses at the surface (see Figure 5.54).

$h_{m,i}/P$	z_{max}	$\int_{z_t}^{z_{max}} \phi(z)\mathrm{d}z$	τ_0	$u_{*,I}$
[-]	[m]	[m]	[N/m^2]	[m/s]
0.63	0.030	0.0148	4.15	0.064
0.88	0.042	0.0256	7.18	0.085
1.46	0.048	0.0313	14.95	0.122
1.46	0.048	0.0313	10.80*)	0.104*)

6 Field tests

6.1 Overview

The hydraulic parameters decisive for the ecological effectiveness of UBR in terms of migration possibilities were measured and determined during the physical model tests (Chap. 4 and 0). However, the description of the hydraulic conditions allows for theoretical considerations only: the measured quantities can be compared with limiting values (e.g. maximal tolerable flow velocity or minimum required water depth) given for a certain fish species. These limiting values are generally derived from other experiments, where the swimming capacity was investigated depending on a certain parameter variation. Therefore, these values are always limited to the tested conditions and cannot be easily generalized. Furthermore, the variability between and within the different fish species (e.g. juvenile and adult individuals) makes the comparison difficult. For this reason, to investigate the effective migration possibilities at least for two existent UBR, field tests were carried out in collaboration with Dr. Armin Peter and his research group of the Swiss Federal Institute of Aquatic Science and Technology (Eawag). In Chap. 6.2 the technique used for the field tests is presented; then in Chap. 6.3 and 6.4 the field sites at the Landquart River and at the Wyna River are described; finally, the results are shown in Chap. 6.5. Data about the test technique, the specifications about fish species and the test results at the Wyna River were taken from the Eawag internal report on these field tests (Peter and Herz 2013).

6.2 Test technique

The field tests are based on the concept of homing behaviour (e.g. Armstrong and Herbert 1997), namely the tendency of fish to swim back to its home site after translocation. It is assumed that a fish captured upstream of the block ramps, and released downstream, will have a tendency to swim back. The detected fish upstream of the block ramp are an appropriate indicator of the migration efficiency of the considered block ramp (Weibel and Peter 2013).

Electrofishing and Passive Integrated Transponders (PIT) tags were used at both sites of the investigated UBR at the Landquart River and at the Wyna River (Chap. 6.3 and 6.4, respectively). Electrofishing (e.g. Cowx and Lamarque 1990, Nielsen 1998) is a

common method used to sample fish populations. The fish responds to the electric field created in water with a form of forced swimming (galvanotaxis) toward the anode and then stunning when it is sufficiently near to the anode. So the fish can be easily captured. Assuming correctly performed electrofishing, this method does not permanently harm fish. The fish recovers a few minutes after being stunned.

To detect the fish passage, PIT tags (e.g. Prentice *et al.* 1990, Castro-Santos *et al.* 1996, Roussel *et al.* 2000) were used in combination with an antenna installed upstream of the ramp. PIT tags are microchips transmitting its unique number whenever the tag is excited by a magnetic field created e.g. by an antenna. The unique code permits the identification of previously sampled individuals. The PIT tags used in the present research were purchased from Oregon RFID and were 23 mm long (Half Duplex PIT tags) for fish with body length larger than 150 mm and 12 mm long for smaller fish (Figure 6.1).

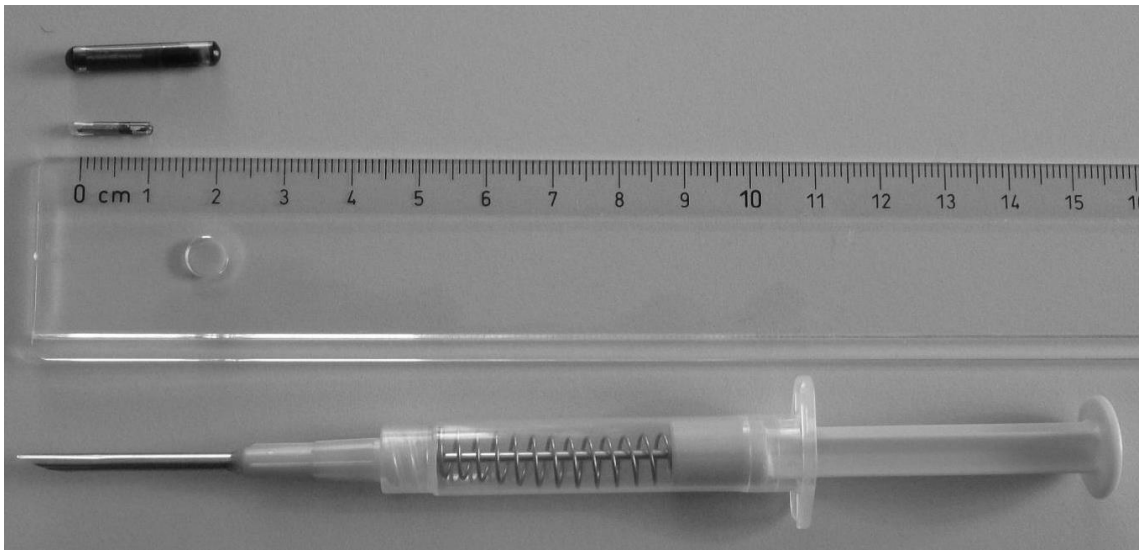

Figure 6.1 PIT tag equipment with large (23 mm) and small (12 mm) PIT tags and needle.

In the present field tests the procedure was always the same (see also Weibel and Peter 2013). Fish were captured by electrofishing (electroshocker Grassl 12kW, 150-300/3000-600 V) primarily upstream of the UBR and collected in oxygenated water tanks. Fish were then anaesthetized with clove oil (Hänseler AG, Herisau, Switzerland; 0.5 ml diluted in 9.5 ml alcohol added to 30 l water), in order to determine the fish species and body length, as well as to allow the injection of PIT tags into the body

cavity with a needle. Afterwards, they were released downstream of the UBR. The upstream migration was monitored with a stationary antenna placed at the ramp head and stretched over the river width and with a backpack antenna (Chap. 6.4).

6.3 Field test at the Landquart River

In 2007 and 2008 VAW performed physical model tests on UBR projected at different reaches at the Landquart River (Canton Graubünden, Switzerland, VAW 2008a). The goal of the model tests was to optimize the parameter combination (block diameter D and block placement density λ) in terms of stability. According to the VAW results, six similar UBR were built from 2008 to 2012 in the area of "Malans/Igis" along a river reach of approximately 1.3 km length. The ramps with lengths between 70 and 250 m were built with a slope of 2%. The river is approximately 18– 22 m wide. The blocks have an equivalent spherical diameter of $D \approx$ 1.2-1.5 m and a mass of 4-5 t. The block placement density is $\lambda = 0.20$ (Figure 1.1). Because of the good data available of these ramps, they were selected for the first field test.

Electrofishing was conducted on the 8th of March 2011 (Figure 6.2 top) within and upstream of a ramp within the ramp series. The test procedure is described in Chap. 6.2. Due to the high turbidity, only about 20 individuals were captured and tagged. Merely two different species were found in the Landquart River, namely the bullhead (*Cottus gobio*, Figure 6.2 bottom) and the brown trout (*Salmo trutta fario*), precluding an analysis of a broader variety of fish species and their different swimming capacities.

The bullhead is not a suitable target fish to indicate migration activity, due to its particularly poor swimming capacity and its limited homing behaviour. On the contrary, the brown trout is one of the strongest fish in terms of swimming capacity living in the Swiss Rivers and has no problem overcoming the ramp. Therefore, a second field site was selected (Chap. 6.4).

Figure 6.2 Field test were conducted at the Lanquart River on the 8th March 2011. Top: Electrofishing upstream of UBR with Eawag team (view in flow direction). Bottom: captured bullhead (*Cottus gobio*) with body length of about 14 cm.

6.4 Field tests at the Wyna River

In 2009 VAW wrote an expertise about the project of an UBR at the Wyna River (Canton Aargau, Switzerland, VAW 2009), so that the boundary conditions (geometry, characteristic dimensions, etc.) of the ramp were well documented. Different fish species live in the Wyna River, offering interesting conditions for the field tests. The ramp is approximately 95 m long. Its width as well as the river width varies from 12 m (at the upstream part of the ramp) to 20 m (at the downstream part). The ramp is located on a river bend. The blocks have an equivalent spherical diameter of $D \approx 1.15 – 1.25$ m and a mass of 2.5 – 3.2 t. The block placement density $\lambda = 0.20 – 0.24$. The ramp was built in 2009 with an initial slope of 2.9% (Figure 6.3). The bigger blocks with the higher placement density were used in the outer bend, where the hydraulic load is assumed to be higher.

Figure 6.3 UBR at the Wyna River with a specific discharge of $q \approx 0.03$ m^3/(sm) corresponding to one of the smallest discharges measured in 2012, approximately corresponding to Q_{30} (view in flow direction).

Electrofishing and PIT tagging were performed during the following days:

- on 29th of August 2012: approximately 75 m downstream of the UBR in the direction of the Suhr River (which merges with the Wyna River just downstream of the UBR) as well as for 20 m upstream of it;
- on 26th of September 2012: upstream of the UBR along a reach of approximately 360 m;
- on 30th of October 2012: upstream of the UBR along a reach of approximately 360 m;
- on 15th of November 2012: upstream of the UBR along a reach of approximately 360 m and also upstream of the next migration barrier for about 200 m.

Each fish captured with a body length greater than 55 mm was tagged with a PIT tag (Chap. 6.2). 375 individuals were caught and released approximately 15 m downstream of UBR; the time of release was recorded to determine the migration duration.

For the detection of the fish passage, a stationary antenna was mounted at the ramp head over the ramp width (Figure 6.4 top) and was connected to a tuner box (Figure 6.4 bottom). The antenna detected and read the PIT tags implanted in the fish when the fish swam by or near of it (within about 30 cm). The antenna was functioning between 29th of August and 15th of December 2012, unfortunately not without interruptions. Several high discharge events interrupted the connection between the antenna and the tuner box. For this reason, there were periods of missing data corresponding mostly to high discharge conditions, where the probability of fish migration was ower , however.

To complete the measurements and the data from the stationary antenna, a backpack antenna was used to search for fish upstream of the ramp head and on the ramp itself. The backpack antenna was used on the following days, when low discharge conditions allowed walking within the river:

- on 14th of September 2012: along the UBR;
- on 1st of October 2012: along the UBR;
- on 23rd of October 2012: along the UBR and downstream of it;
- on 30th of October 2012: upstream of the UBR up to the next migration barrier (approximately 360 m);
- on 19th of November 2012: upstream of the UBR;

- on 20th of November 2012: upstream, along and downstream of the UBR and along the banks of the Suhr River parallel to the Wyna River
- on 13th of December 2012: upstream, along and downstream of the UBR.

Figure 6.4 Equipment for the field tests. Top: stationary antenna stretched over the river width (water flows from right to left); bottom: tuner box with standard remote tuner board placed besides the river.

6.5 Results of the field tests at the Wyna River (from Peter and Herz 2013)

During the four electrofishing campaigns, 375 fish of 9 different species were captured. Figure 6.5 shows the distribution of each species divided into the four electrofishing campaigns.

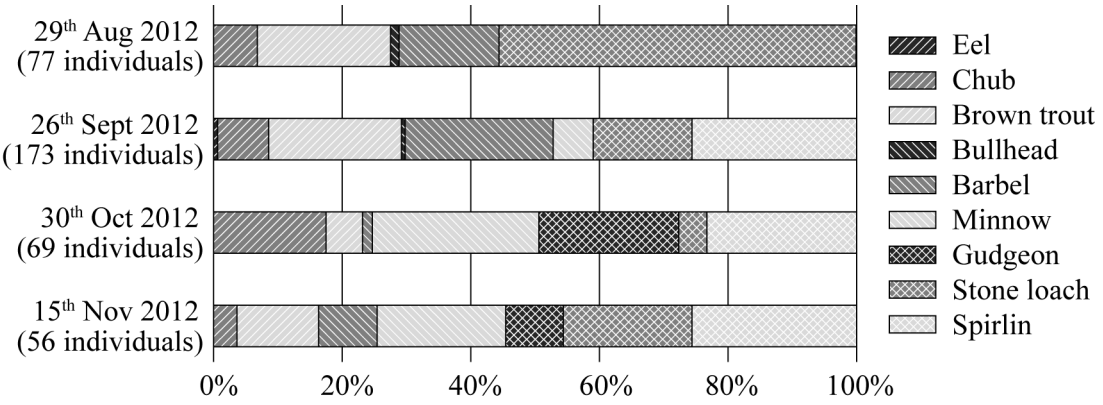

Figure 6.5 Distribution of each species captured and tagged per electrofishing campaign.

The body length of the tagged fish ranged between 58 mm (bullhead) and 843 mm (eel). The average body length was 125.2 mm and, excluding the eel, the biggest captured fish was a brown trout measuring 475 mm. The largest species (excluding eel) tagged on average were brown trout (230 mm), followed by barbel (148 mm) and gudgeon (129 mm); the smallest one were bullhead, of which only two individuals were tagged. The most abundant species captured were stone loach with 84 individuals, then schneider with 75 individuals and brown trout with 63 individuals (Figure 6.5).

The migration efficiency was determined as the overall percentage of tagged fish and the percentage of each species tagged that was successfully detected with the stationary antenna or with the backpack antenna. Table 6.1 summarizes the results from the field tests at the Wyna River for each species.

In general 16% of the tagged fish were able to overcome the UBR and were detected upstream of the ramp head, whereas 12% were detected in the general test area but downstream of the stationary antenna (on the UBR or downstream of it). 72% of the tagged fish were not detected, presumably because (1) the fish have been preyed upon by birds that hunt in this area; or (2) the fish have been drifted downstream during the

high discharge events or have migrated actively downstream. Considering the total number of detected individuals only (i.e. 104), the percentage of successful upstream migration is 59%.

Table 6.1 Results of the field tests for each tagged fish species: no. of captured individuals and % of individuals with successful migration.

Fish species	Number of tagged fish	successful migration
All	375	16%
Barbel	58	33%
Brown trout	63	57%
Bullhead	2	0%
Chub	33	9%
Eel	1	0%
Gudgeon	20	0%
Minnow	40	0%
Schneider	74	3%
Stone loach	84	1%

In the following some general considerations about the field tests are summarized:

- Fish of all sizes prefer to migrate during periods with relatively low discharge ($Q < 5$ m^3/s and $q < 0.3$ m^2/s, respectively, corresponding to roughly a Q_{30}).
- In general, smaller fish were not detected within the study area and larger fish were most often able to migrate.
- Most small fish that were relocated did not manage to overcome the UBR, but remained within the habitat on the UBR or downstream of it.
- Individuals that were captured upstream of the UBR and released downstream of it had a higher tendency of migrating compared to individuals captured downstream of the UBR.
- Five over nine species were able to overcome the ramp: barbel, brown trout, chub, spirlin and stone loach.
- Four over nine species were unable to overcome the ramp: bullhead, eel, gudgeon, and minnow (i.e typically smaller individuals compared to the other five

species). Note that the eel, which was not redetected, is a strong swimmer surely able to overcome the ramp.

- The most successful species were barbel and brown trout: almost all sizes were able to migrate upstream.

6.6 Conclusions on the field tests

Field tests are challenging to perform and expensive. An adequate study area has to be located, where suitable hydrological conditions (low discharge variations at least within the test period) should occur, good water quality in terms of turbidity is given, and the target fish are present. The field tests have to be carried out by a specialized team with appropriate knowledge about test procedure and fish. Discharge variation can interrupt the measurements (e.g. by disturbing the electronics) or impede electrofishing or detection campaigns.

Two different rivers – Landquart and Wyna River – were selected for the field tests, whereas only at the Wyna River tests could be carried out successfully. Considering the total number of tagged fish (375 individuals), only 28% could be detected within the test area: 16% upstream of the UBR (successful migration) and 12% on the UBR or downstream of it (Table 6.1).

Considering the individuals that were detected within the test area only (104 fish), the percentage of a successful upstream migration was 59%. Especially brown trout and barbel showed satisfactory migration efficiency (57% and 33%, respectively).

In order to generalize the results of this single test data set, further field campaigns are needed. However, the present results show that a typical UBR (regarding geometrical and discharge conditions) can be overcome by a certain variety of fish species and sizes, and does not represent a migration barrier like drops or sills.

7 Conclusions and outlook

7.1 Conclusions

Physical model tests were carried out to investigate the hydraulic stability and the ecological efficiency of unstructured block ramps (UBR). The model investigation was divided into three different phases A, B, and C. For all three sets of tests the experimental setup represented a longitudinal slice, taken from the middle part of a river within an UBR (2D investigation). Compared to typical prototype conditions in the Swiss Alps, the geometrical model scale, based on the grain size distribution, varies between 20 and 30.

The goal of the experiments of **phase A** was to investigate the effect of different parameters on the ramp stability. Varying the parameter combination (ratio between the equivalent spherical block diameter and the characteristic grain of the sediment material $4.9 < D/d_{90} < 18.6$, block placement density $\lambda = 0.15$ and 0.25) different ramps were tested under steady conditions. Additionally, the effect of sediment supply and of uniformity of the grain size distribution was investigated.

The main findings of **phase A** are:

- The best ratio D/d_{90} in terms of ramp stability and no abrupt failure was in the range of $6.5 < D/d_{90} < 7.4$. Within this range a block placement density $\lambda = 0.25$ has a significant stabilizing effect on the ramp, resulting in an equilibrium slope S_e 30% – 50% steeper than for $\lambda = 0.15$.
- The sediment supply has a stabilizing effect on UBR leading to at least 10% steeper equilibrium slope S_e for high discharges.
- An empirical approach to determine the equilibrium slope and another one for the mean flow depth have been presented. These approaches consist in a parameterisation, allowing a generalization of the experimental results and their application for other data set and especially for design purposes. The suggested equations are

  $S_e = \frac{11}{q_d{}^* + 200}$ for $q_d{}^* < 1700$,

  describing the equilibrium slope and the stability of UBR with $q_d{}^* = q/\sqrt{g(s-1)D^3}\ \lambda^{-1}(D/d_{90})^2$; and

$h_m/D = 0.69\ {q_d}^{**0.64}$ for ${q_d}^{**} < 10$
describing the mean flow depth of UBR with ${q_d}^{**} = q/\sqrt{g(s-1)D^3}\ \lambda^{-0.2}(D/d_{90})^{0.5}$.

- The equation suggested by Pagliara and Chiavaccini (2006a) for the determination of the flow resistance was modified according to the experimental results as
$\frac{U}{u_*} = \frac{u_b}{u_{*,b}} = 1.9\ (1+\lambda)^{-0.5}\ S^{-0.21}\left(\frac{h}{P}\right)^{0.29}$ for $h/P < 3.5$, $0.15 < \lambda < 0.25$.
This equation is suggested for the determination of the flow resistance of UBR with natural erodible bed and protruding blocks.

The goal of the experiments of **phase B** was to investigate the overall behaviour by varying the boundary conditions and by testing the effect of quasi-steady discharge conditions. The considered river reach was extended with an erodible tail water reach downstream of the ramp toe. Additionally, the erosion downstream of the UBR was simulated by lowering the fix point at the flume end. The experiments were conducted under steady as well as quasi-steady conditions to test the effect of a selected characteristic flood event (≈ HQ_{100}).

The main findings of **phase B** are:

- An erodible river reach downstream of the ramp results in a lowering of the ramp toe and of the ramp head. The ramp adjust itself to the load by flattening without structural failure, but the fixed-point function of the UBR is then lost. This can negatively affect other existent constructions, as e.g. the bank protection, or create a high elevation difference between the drop upstream of the ramp and the ramp itself, precluding the fish migration. Therefore, the river reach downstream of the ramp has to be stabilized against erosion; upstream of the UBR a buffer area should be integrated to minimize the effect of the ramp erosion on the bed elevation upstream of it.
- To reach equilibrium conditions the run duration was very high compared to typical prototype conditions. The highest slope decrease during the experiments happened during the first 42-84 hours (prototype dimensions). Afterwards, the slope decrease reduces. In general, high discharges in the prototype do not occur for so long. So the quasi-steady tests showed that the stability diagrams resulting

from the tests under steady conditions (phase A) characterize the absolute lower stability limit for the tested ramp, representing a conservative assumption for the design. This applies for one flood event; the effect of different floods was not investigated.

- The increased erosion downstream of the erodible tail water reach caused a block loss along the ramp, leading to reduced block placement density and to reduced flow resistance, which affects the ramp stability particularly during the next occurring high discharge conditions.

Phase C had two main objectives: (1) understand the hydraulic and turbulence conditions in strong heterogeneous bed topography with macro-roughness elements, and (2) describe the ecological conditions of UBR, in particular related to migration corridors. To measure velocities, shear stress and turbulence intensity profiles, two dimensional (2D) Laser Doppler Anemometry (LDA) measurements were performed with fixed bed topography using the optimal parameter combination in terms of stability derived from phase A. The measurements were conducted under steady conditions for three different specific discharges with relative submergence of $h/P = 0.63$, 0.88 and 1.46. The data were analysed both with local time-averaged and double-averaged (in time and in space) quantities.

The main findings of **phase C** are:

- Local flow conditions were described on the basis of some exemplary cross- and longitudinal sections. A generalization of the occurring local flow conditions on UBR is difficult, because only one bed topography with a mean slope of 2.9% was tested. However, it is assumed that due to the presence of the blocks, similar flow variability as presented herein can be generally found on UBR.
- Additional velocity and Reynolds shear stress cross-sections are collected in Appendix B for numerical modelling purposes and for comparison with critical values of different fish species.
- Some ethohydraulic plots indicating specific areas with appropriate flow conditions have been shown for three different typical fish living in Swiss rivers. For $q_1 = 6.8$ l/(sm), corresponding to relevant hydraulic conditions for fish migration (for many Swiss rivers 6.8 l/(sm) < HQ_1, depending on the scale factor), regions

with tolerable velocities in each cross-section were identified. This suggests that at least the criterion of the maximum velocity for the considered fish is satisfied and that a theoretical migratability is given. These results are valid for the three fish species considered and for the assumed geometrical scale factor $\Omega = 25$. For different cases new ethohydraulic plots should be created and analysed.

- Overall flow conditions were analysed with spatially-averaged quantities. The vertical profiles of the velocity components $\langle\bar{u}\rangle$ and $\langle\bar{w}\rangle$, of the Reynolds shear stress $-\langle\overline{u'w'}\rangle$, and of form-induced stresses $-\langle\tilde{u}\tilde{w}\rangle$ were described for the three relative submergences investigated. The data were compared with other approaches and studies, to better understand the effect of the presence of randomly placed macro-roughness elements. The vertical profiles indicate a different division of flow layers compared to those suggested by Nikora *et al.* (2001), which was adapted for the present case by subdividing the interfacial sublayer into a macro-roughness and a sedimentary sublayer.
- The correlation between the fluctuation terms of the velocity *u*' and *w*' and of the spatial disturbances $\tilde{u}$ and $\tilde{w}$ of time-averaged velocity components were investigated with the quadrant method. The analysis indicated general absence of correlation in both cases. This means that in the considered case the quadrant method does not provide additional information about the flow and turbulence characteristic. It only shows the magnitude of the fluctuations at a certain point (for *u*' and *w*') or at a certain elevation (for $\tilde{u}$ and $\tilde{w}$), which is also given by the RMS-values.
- The mean bed shear stress was determined considering the form drag and the negative Reynolds shear stress at the surface. The maximum bed shear stress is found when the blocks are fully submerged, namely for $h_m \approx 1.5\,P$, corresponding to the most problematic case in terms of bed erosion for UBR.

EAWAG (group Dr. A. Peter) carried out **field test** in collaboration with VAW to investigate the effective migration possibilities within an UBR under field conditions. One set of experiments was conducted for an UBR at the Wyna River (Canton Aargau, Switzerland) featuring different fish species. To detect the fish passage, Passive Integrated Transponders (PIT) tags were used in combination with an antenna installed upstream of the ramp. 375 individuals of 9 different fish species were captured. Consid-

ering the total number of tagged fish, only 28% could be detected within the test area: 16% upstream of the UBR (successful migration) and 12% on the UBR or downstream of it. Considering the individuals that were detected within the test area only (104 fish), the percentage of a successful upstream migration was 59%. Especially brown trout and barbel showed satisfactory migration efficiency (57% and 33%, respectively). The second test site at the Landquart River did not lead to any useful data.

In addition to the main results presented above, the behaviour of some UBR during the flood event in August 2005 in Switzerland as well as the results of a survey on existing Swiss UBR are shown in the appendix. Some constructive details that can be decisive for the ramp stability in case of overload are shown, giving an overview on some characteristic parameters of existing UBR.

7.2 Outlook

It would be worthwhile from both a scientific and an engineering point of view to extend the present results by investigating the following topics:

- Investigate the ramp behaviour in case of local discharge concentration, as e.g. in a river bend, and deduce necessary countermeasures.
- Study the effect of different ratios D/d_{90} (from $D/d_{90} = 7.4$ to 12.3 and from $D/d_{90} = 12.3$ to 18.6) on the ramp stability, so that the transition between stable and unstable parameter combinations would be more distinct.
- Test the ramp stability for block placement densities $0.15 < \lambda < 0.25$ and $\lambda < 0.15$ to understand if the ramp stability depends linearly on λ and to find an optimum λ also in terms of cost effectiveness.
- Optimization of practical design features such as the transition zone between the UBR and bank protection and between an existing drop and the UBR, or protection against erosion downstream of the ramp.
- Measure the spanwise velocity component to extend the hydraulic and turbulence characterization of the flow.
- Test the effective migration possibilities with field tests on UBR with other parameter combinations (block diameter, block placement density, ramp slope) and with different fish species of different life stages.
- Perform numerical simulations to reproduce the overall flow and turbulence conditions on UBR to rate their ecological efficiency and to determine the hydraulic parameter (as the flow velocity and the flow depth) necessary for the design.

8 Notation

Symbols

a = acceleration [m/s^2];

A = area [m^2];

A_B = block flow area [m^2];

A_{catch} = catchment area [km^2];

A_{CS} = area of the critical cross-section by the permeability tests [m^2];

A_D = projected area of the grain against the flow [m^2];

A_{eff} = effective flow cross-sectional area [m^2];

A_L = base area [m^2];

B = buoyancy [N];

c = Chézy coefficient [−];

c' = Chézy coefficient for skin friction [−];

c'' = Chézy coefficient for form resistance [−];

C_D = drag or resistance coefficient [−];

C_L = lift coefficient [−];

$d_{b,i}$ = clearance between block in x and y direction [m];

d_i = grain diameter at which i% of the sediment sample is finer than [m];

D = equivalent spherical block diameter [m];

D_i = block diameter at which i% of the sediment sample is finer than [m];

e_i = relative error of a certain quantity i;

EHQ = extreme flood, often EHQ = (1.3 – 2) · HQ_{100} [m^3/s];

F = Froude number [−];

f = Darcy-Weisbach friction factor [−];

f_i = error of a certain quantity i [−];

F = force [N];

F_B = resistance force of a single block [N];

F_D = drag force [N];

F_L = lift force [N];

g = gravity acceleration [m/s^2]; g = 9.81 m/s^2

G = force due to the gravity [N];

h = flow depth [m];

h_c = critical flow depth [m]; $h_c = (q^2/g)^{1/3}$

h_{eff} = effective flow depth [m];

h/P, h/D = relative submergence [−];

h_S = scour depth [m];

h_{th} = theoretical mean depth occupied by blocks [m];

h_{TW} = tail water depth [m];

H = ramp height [m];

H_0 = energy head upstream of the block ramp [m];

H_1 = energy head at the ramp toe [m];

H_{fish} = fish body height [m];

HQ_i = flood with a return period of i-years [m^3/s];

k_B = equivalent sand roughness for blocks [m] or [mm];

k_f = permeability coefficient [m/s];

k_s = equivalent sand roughness [m] or [mm];

k_{Str} = Strickler coefficient [m$^{1/3}$/s];

$k_{Str,b}$ = Strickler coefficient for bed material [m$^{1/3}$/s];

$k_{Str,g}$ = Strickler coefficient for grain friction [m$^{1/3}$/s];

i = hydraulic gradient [−];

L = length [m];

L_{fish} = fish body length [m];

L_M = characteristic length in the model [m];

L_P = characteristic length in the prototype [m];

M = mass [kg];

n = Manning coefficient [−];

N = number of blocks along the entire ramp [−];

N_A = number of blocks per unit area [−];

p = pressure [N/m^2];

P = block protrusion [m];

P_D = dissipated specific power density [W/m^3];

P_w = wetted perimeter [m];

q = specific discharge [m^2/s] or [l/(sm)];

q^* = dimensionless bed-load transport rate [−];

q_b = volumetric bed-load rate [g/s];

q_d^*, q_d^{**} = dimensionless specific discharge [−];

Q = discharge [m^3/s] or [l/s];

Q_{GW} = groundwater flow [m^3/s] or [l/s];

Q_s = sediment supply discharge [g/s];

Q_{30} = discharge, which is not exceeded 30 days per year [m^3/s];

Q_{330} = discharge, which is not exceeded 330 days per year [m^3/s];

R = hydraulic radius [m];

R = Reynolds number [−]; for open-channel flows: $\mathsf{R} = uR/\nu$;

R^* = grain Reynolds number [−]; $\mathsf{R}^* = u_* k_s/\nu$;

s = ratio between sediment and water density [−];

S = slope [−] or [%];

S' = slope of grain friction [−] or [%];

S'' = slope of form friction [−] or [%];

S_e = equilibrium ramp slope [−] or [%];

S_0 = initial ramp slope [−] or [%];

t = time [s];

TI = turbulence intensity [−];

TI_b = bulk turbulence intensity [−];

TI_l = local turbulene intensity [−];

u = instantaneous velocity in the flow direction [m/s];

u' = fluctuation component of the instantaneous velocity u [m/s];

$u' = u - \overline{u}$, similarly: v', w'

$\overline{u}$ = time-averaged velocity of the instantaneous velocity u [m/s];

similarly: $\overline{v}$, $\overline{w}$

$\tilde{u}$ = spatial disturbance of the time-averaged velocity $\overline{u}$ [m/s];

$\tilde{u} = \overline{u} - \langle\overline{u}\rangle$, similarly: $\tilde{v}$, $\tilde{w}$

$\langle\overline{u}\rangle$ = double-averaged velocity [m/s]; similarly: $\langle\overline{v}\rangle$, $\langle\overline{w}\rangle$

$-\langle\overline{u'w'}\rangle$= Reynolds shear stress [m^2/s^2];

$\langle\tilde{u}\tilde{w}\rangle$ = form-induced stress [m^2/s^2];

u_* = shear velocity [m/s]; $u_{*,I} = (\tau_0/\rho)^{0.5} = (gSR)^{0.5}$, $u_{*,II} = (-\langle\overline{u'w'}\rangle_{max})^{0.5}$, $u_{*,b} = (gh_mR)^{0.5}$

u_b = bulk velocity determined with the salt dilution method [m/s];

u_f = ground water flow velocity [m/s];

U = depth-averaged flow velocity [m/s];

U_{burst} = burst velocity of a fish [m/s];

U_{coeff} = uniformity coefficient $U_{coeff} = d_{60}/d_{10}$ [−];

U_E = flow velocity at the ramp toe [m/s];

U_{prol} = prolonged velocity of a fish [m/s];

U_{ref} = reference flow velocity acting on grain particles [m/s];

U_{sust} = sustained velocity of a fish [m/s];

v = instantaneous velocity in the spanwise direction [m/s];

V = volume [m^3];

w = instantaneous velocity in the vertical direction [m/s];

W = Weber number [−];

W = width [m];

x = axis parallel to the average bed [m] or [mm];

y = axis representing the spanwise direction [m] or [mm];

z = vertical axis [m] or [mm];

Z = normalized vertical coordinate [m] or [mm]; $Z = z/z_c$

z_c = block crest height [m];

z_R = thickness of the roughness layer [m];

z_t = height at the upper boundary of the sedimentary sublayer [m];

z_z = zero plane [m];

Greek symbols

α = angle against the horizontal [°] or [rad];

β = block placement density expressed in [t/m^2];

ΔH = energy dissipation [−]; = $H_0 - H_1$

θ_c = critical shear stress [−];

$\theta_{c,a}$ = critical shear stress of armour layer [−];

θ^* = dimensionless shear stress [−];

κ = Von Karman constant [m/s]; usually $\kappa = 0.41$

λ = block placement density [−]; $\lambda = N \pi D^2/(4 L_R W_R) = N_A \pi D^2/4$

ν = kinematic fluid viscosity [m^2/s]; here: $\nu = 10^{-6}$ m^2/s

ρ = water density [kg/m^3];

ρ_s = sediment density [kg/m^3];

σ = standard deviation of the grain-size distribution $\sigma = (d_{84}/d_{16})^{0.5}$ [−];

σ_a = air content parameter [−];

σ_b = standard deviation of the bed elevations (without blocks) [−];

σ_i = standard deviation of a certain quantity i;

τ_0 = total bed shear stress [N/m^2];

τ_0' = shear stress generated by grains [N/m^2];

τ_0'' = shear stress generated by bed irregularities [N/m^2];

ϕ = roughness geometry function [−];

Φ = packing factor [−];

Ω = scale factor [−];

Subscripts

crit = critical;

d = design;

m = mean;

min = minimum;

max = maximum;

Abbreviations

CM = coarse sediment mixture;

DANS = Double-Averaged Navier-Stokes equations;

FM = fine sediment mixture;

LDA = Laser Doppler Anemometry;

NS = Navier-Stokes equations;

PIV = Particle Image Velocimetry;

RANS = Reynolds time-Averaged Navier-Stokes equations;

UBR = unstructured block ramp(s);

UM = uniform material;

9 References

Aberle, J. (2000). Untersuchung der Rauheitsstruktur zur Bestimmung des Fliesswiderstandes in Gebirgsbächen unter Klarwasserabfluss (Study of roughness structure to determine flow resistance in mountain rivers under clear water conditions). *Mitteilung des Instituts für Wasserwirtschaft und Kulturtechnik* 207, Universität Karlsruhe, D [in German].

Aberle, J. (2007). Measurements of armour layer roughness geometry function and porosity. *Acta Geophysica* 55(1), 23-32.

Aberle, J., Smart, G.M. (2003). The influence of roughness structure on flow resistance on steep slopes. *Journal of Hydraulic Research* 41(3), 259-269.

Abt, S.R., Wittler, R.J., Ruff, J.F., Khattak, M.S. (1988). Resistance to flow over riprap in steep channels. *Water Resources Bulletin* 24(6), 1193-1200.

Adam, B., Lehmann, B. (2011). *Ethohydraulik: Grundlagen, Methoden und Erkentnisse* (Ethohydraulics: Bases, methods and findings). Springer Verlag, Berlin Heidelberg, D [in German].

Alp, M., Karpati, T., Werth, S., Gostner, W., Scheidegger, C., Peter, A. (2011). Erhaltung und Förderung der Biodiversität von Fliessgewässern (Perservation and valorizaton of the biodiversity in rivers). *Wasser Energie Luft* 103(3), 216-223 [in German].

Armstrong, J.D., Herbert, N.A. (1997). Homing movements of displaced stream-dwelling brown trout. *Journal of Fish Biology* 50(2), 445-449.

Baiamonte, G., Ferro, V. (1997). The influence of roughness geometry and Shields parameter on flow resistance in gravel-bed channels. *Earth Surface Processes and Landforms* 22(8), 759-772.

Bainbridge, R. (1958). The speed of swimming of fish as related to size and to the frequency and amplitude of the tail beat. *Journal of Experimental Biology* 35(1), 109-133.

Bainbridge, R. (1960). Speed and stamina in three fish. *Journal of Experimental Biology* 37(1), 129-153.

Bathurst, J.C. (1985). Flow resistance estimation in mountain rivers. *Journal of Hydraulic Engineering* 111(4), 625-643.

Beamish, F.W.H. (1978). Swimming capacity. In *Fish physiology Vol. VII*, Hoar, W.S., Randall, D.J. eds. Academic Press, New York, USA, 101-187.

Bernhardt, E.S., Palmer, M.A., Allan, J.D., Alexander, G., Barnas, K., Brooks, S., Carr, J., Clayton, S., Dahm, C., Follstad.Shah, J., Galat, D., Gloss, S., Goodwin, P., Hart, D., Hassett, B., Jenkinson, R., Katz, S., Kondolf, G.M., Lake, P.S., Lave, R., Meyer, J.L., O'Donnell, T.K., Pagano, L., Powell, B., Sudduth, E. (2005). Synthesizing U.S. river restoration efforts. *Science* 308(5722), 636-637.

Beyer, W. (1964). Zur Bestimmung der Wasserdurchlässigkeit von Kiesen und Sanden aus der Kornverteilungskurve (About the determination of the water permeability of gravel and sand from the grain size distribution curve). *Wasserwirtschaft – Wassertechnik (WWT)* 14(6), 165–168 [in German].

Bezzola, G.R. (2002). Fliesswiderstand und Sohlenstabilität natürlicher Gerinne unter besonderer Berücksichtigung des Einflusses der relativen Überdeckung (Flow resistance and bed stability of natural open-channels particularly accounting for the effect of relative submergence). *VAW-Mitteilung* 173, Minor, H.-E., ed., ETH Zürich, CH [in German].

Bezzola, G.R., Hegg, C. (2008). Ereignisanalyse Hochwasser 2005, Teil 2 – Analyse von Prozessen, Massnahmen und Gefahrengrundlagen (Analysis of flood event 2005, Part 2 – Analysis of processes, measures and foundamentals of risks). *Umwelt-Wissen Nr.* 0825. Bundesamt für Umwelt BAFU, Eidgenössische Forschungsanstalt WLS, CH, 243-247 [in German].

Bezzola, G.R. (2010). Flussbau (River engineering). *Vorlesungsmanuskript* der Vorlesung Flussbau an der ETH Zürich, Fassung Frühjahrsemester 2010, CH [in German].

Biron, P.M., Robson, C., Lapointe, M.F., Gaskin, S.J. (2004). Comparing different methods of bed shear stress estimates in simple and complex flow fields. *Earth Surface Processes and Landforms* 29(11), 1403-1415.

Blakely, T.J., Harding, J.S., McIntosh, A.R., Winterbourn, M.J. (2006). Barriers to the recovery of aquatic insect communities in urban streams. *Freshwater Biology* 51(9), 1634-1645.

Brumley, B.H., Jirka, G.H. (1987). Near-surface turbulence in a grid-stirred tank. *Journal of Fluid Mechanics* 183, 235-263.

Blaxter, J.H.S., Dickson, W. (1959). Observations on the swimming speed of fish. *Journal Conseil Permanent International pour l'Exploration de la Mer* 24, 472-479.

Buffington, J.M., Montgomery, D.R. (1997). A systematic analysis of eight decades of incipient motion studies, with special reference to gravel-bedded rivers. *Water Resources Research* 33(8), 1993-2029.

Castro-Santos, T., Haro, A., Walk, S. (1996). A passive integrated transponder (PIT) tag system for monitoring fishways. *Fisheries Research* 28(3), 253-261.

Coleman, S.E., Nikora, V.I., McLean, S.R., Clunie, T.M., Melville, B.W. (2007). Sub-element form-drag parameterization in rough-bed flows. *Journal of Hydraulic Engineering* 133(2), 121-129.

Cotel, A.J., Webb, P.W., Tritico, H. (2006). Do brown trout choose locations with reduced turbulence? *Transactions of the American Fisheries Society* 135(3), 610-619.

Cowx, I.G., Lamarque, P. (1990). *Fishing with electricity: applications in freshwater fisheries management*. Fishing News Books, Oxford, UK.

Denil, G. (1937). La mécanique du poisson de rivière. Chapitre X : Les capacités mecaniques de la truite et du saumon (The mechanics of river fish. Chapter X: The mechanical abilities of trout and salmon). *Annales des Travaux Publics de Belgique* 38, 412-433.

Detert, M., Nikora, V., Jirka, G.H. (2010). Synoptic velocity and pressure fields at the water-sediment interface of streambeds. *Journal of Fluid Mechanics* 660, 55-86.

Dittrich, A., Hammann de Salazar, K. (1993). Bed instability caused by clear water and hyperconcentrated flow. *Bericht des Instituts für Wasserbau und Kulturtechnik*, Universität Karlsruhe, D.

Dittrich, A., Koll, K. (1997). Velocity field and resistance of flow over rough surface with large and small submergence. *International Journal of Sediment Research* 12(3), 21-33.

Durst, F., Melling, A., Whitelaw, J.H. (1981). *Principles and practice of Laser-Doppler anemometry*. Academic Press, New York, USA.

DWA Deutsche Vereinigung für Wasserwirtschaft, Abwasser und Abfall e.V. (2005). Fischschutz- und Fischabstiegsanlagen – Bemessung, Gestaltung, Funktionskontrolle. 2. Korrigierte Auflage (Fish protection and fish passage facilities – Design, configuration, performance check. 2nd edition). *DWA-Themen* WW-8.1, DWA, Hennef, D [in German].

DWA Deutsche Vereinigung für Wasserwirtschaft, Abwasser und Abfall e.V. (2009). Naturnahe Sohlengleiten (Natural block ramps). *DWA-Themen* WW-1.2-9, DWA, Hennef, D [in German].

DWA Deutsche Vereinigung für Wasserwirtschaft, Abwasser und Abfall e.V. (2010). Fischaufstiegsanlagen und fischpassierbare Bauwerke – Gestaltung, Bemessung, Qualitätssicherung. Entwurf. (Fish passage facilities and fish passable constructions – Configuration, design, quality check. Draft). *Merkblatt DWA* M 509, DWA, Hennef, D [in German].

Einstein, H.A., Banks, R. (1950). Fluid resistance of composite roughness. *Transactions American Geophysical Union* 31(4), 603-610.

Einstein, H.A., Barbarossa, N.L. (1952). River channel roughness. *Transactions of the American Society of Civil Engineers* 117, 1121-1132.

Everts, C.H. (1973). Particle overpassing on flat granular boundaries. *Journal of the Waterways, Harbors and Coastal Engineering Division ASCE* 99(4), 425-438.

Fehr, R. (1987). Geschiebeanalysen in Gebirgsbächen (Grain size analysis in mountain rivers). *VAW-Mitteilung* 92, Vischer, D., ed. ETH Zürich, CH [in German].

Fenton, J.D., Abbott, J.E. (1977). Initial movement of grains on a stream bed: the effect of relative protrusion. *Proceedings of the Royal Society of London* A 352, 523-537.

Fenzl, R.N., Davis, J.R. (1964). *Discussion of* Natural roughness effects in rigid open channels. *Proc. ASCE* 90(HY3), 351-359.

Ferro, V. (1999). Friction factor for gravel-bed channel with high boulder concentration. *Journal of Hydraulic Engineering* 125(7), 771-778.

Ferro, V., Baiamonte, G. (1994). Flow velocity profiles in gravel-bed rivers. *Journal of Hydraulic Engineering* 120(1), 60-80.

Finnigan, J.J. (2004). A re-evaluation of long-term flux measurement techniques. Part II: coordinate systems. *Boundary-Layer Meteorology* 113(1), 1-41.

Flammer, G.H., Tullis, J.P., Mason, E.S. (1970). Free surface, velocity gradient flow past hemisphere. *Journal of the Hydraulic Division, Proc. of ASCE* 96(HY7), 1485-1502.

Garcia, M.H. (2008). Sediment transport and morphodynamics. In *Sedimentation engineering – Processes, measurements, modeling, and practice*, M.H. Garcia ed. ASCE Report no. 110, Virginia, USA, 21-164.

Gaudio, R., Miglio, A., Dey, S. (2010). Non-universality of von Karman's k in fluvial streams. *Journal of Hydraulic Research* 48(5), 658-663.

Gebler, R.J (2007). Hydraulische und konstruktive Anforderungen an Blockrampen zur Herstellung der biologischen Durchgängigkeit (Hydraulic and structural requirements for block ramps to establish biological connectivity). In *VAW-Mitteilung* 201, H.-E. Minor ed. Laboratory of Hydraulics, Hydrology and Glaciology (VAW), ETH Zürich, CH, 37-46 [in German].

Geitner, V., Drewes, U. (1990). Entwicklung eines neuartigen Pfahlfischpasses (Development of a novel pale fish passage). *Wasser & Boden* 42, 604-607 [in German].

Gessler, J. (1970). Self-stabilizing tendencies of alluvial channels. *Journal of the Waterways, Harbors and Coastal Engineering Division* 96(2), 235-249.

Ghisalberti, M., Nepf, H. (2002). Mixing layers and coherent structures in vegetated aquatic flows. *Journal of Geophysical Research* 107(C2), 3-1-3-11.

Ghisalberti, M., Nepf, H. (2006). The structure of the shear layer in flows over rigid and flexible canopies. *Environmental Fluid Mechanics* 6(3), 277-301.

Giménez-Curto, L.A., Corniero Lera, M.A. (1996). Oscillating turbulent flow over very rough surface. *Journal of Geophysical Research* 101(C9), 20745-20758.

Gray, J. (1953). The locomotion of fishes. In *Essays in marine biology*, Marshall, S.M., Orr, A.P. eds. Oliver & Boyd, Edinburgh, UK, 1-16.

Günter, A. (1971). Die kritische mittlere Sohlenschubspannung bei Geschiebemischungen unter Berücksichtigung der Deckschichtbildung und der turbulenzbedingten Sohlenschubspannungen (The critical mean bed shear stress for sediment mixture by considering the formation of the armour layer and the bed shear stress caused by turbulence). *VAW-Mitteilung* 3, Vischer, D., ed., ETH Zürich, CH [in German].

Guo, J., Julien, P.Y. (2005). Shear stress in smooth rectangular open-channel flows. *Journal of Hydraulic Engineering* 131(1), 30-37.

Hammer, C. (1995). Fatigue and exercise tests with fish. *Comparative Biochemistry and Physiology* 112(A), 1-20.

Hartung, F., Scheuerlein, H. (1970). Design of overflow rockfill dams. *Dixieme Congrès des Grands Barrages*, Montreal, CDN.

Hassinger, R. (1991). Beitrag zur Hydraulik und Bemessung von Blocksteinrampen in flexibler Bauweise (Contribution to hydraulic and design of block ramps in a flexible construction method). *Mitteilungen des Instituts für Wasserbau und Kulturtechnik* Nr. 74, Universität Stuttgart, D [in German].

Hazen, A. (1892). Some physical properties of sands and gravels, with special reference to their use in filtration. *24th Annual Rep., Massachusetts State Board of Health* Pub. Doc. No 34, 539-556.

Heller, V. (2011). Scale effects in physical hydraulic engineering models. *Journal of Hydraulic Research* 49(3), 293-306.

Huet, M. (1949). Aperçu des relations entre la pente et les populations piscicoles des eaux courantes (Summary of the relationships between slope and fish populations in watercourses). *Revue Suisse d'Hydrologie* 11(3/4), 332-351 [in French].

Hunziker, Zarn & Partner (2008). Blockrampen Normalien: Manual zur Sanierung von Abstürzen (Block ramp guidelines: Manual to improve drops). *Projekt Nr.* A-300. HZP: Aarau, CH [in German].

Hunziker, Zarn & Partner (2012). Hochwasserschutz und Revitalisierung Emme – Wehr Biberist bis Aare. Vorstudie (Flood protection and revitalisation of the Emme River – Dam in Biberist to Aare River. Preliminary Studies). *Projekt Nr.* A-596. HZP: Aarau, CH [in German].

Janisch, T. (2007). Aufgelöste Blockrampen im Modellversuch – Untersuchungen an der VAW (Model tests on unstructured block ramp – Investigation at the VAW). In *VAW-Mitteilung* 201, Minor, H.-E., ed. ETH Zürich, CH, 63-79 [in German].

Janisch, T., Weichert, R., Bezzola, G.R. (2007). Verhalten von aufgelöster unstrukturierter Blockrampen (Behaviour of unstructured block ramps). *Wasser Energie Luft* 99(2), 146-152 [in German].

Järvelä, J. (2005). Effect of submerged flexible vegetation on flow structure and resistance. *Journal of Hydrology* 307(1-4), 233-241.

Jähnig, S.C., Lorenz, A.W., Hering, D. (2009). Restoration effort, habitat mosaics, and macroinvertebrates – does channel form determine community composition? *Aquatic Conservation* 19(2), 157-169.

Jens, G., Born, O., Hohlstein, R., Kämmerheit, M., Klupp, R., Labatzki, P., Mau, G., Seifert, K., Wondrak, P. (1997). Fischwanderhilfen: Notwendigkeit, Gestaltung, Rechtsgrundlagen (Fish migration facilities: Exigency, configuration, legal basis).

Schriftenreihe des Verbands Deutscher Fischereiverwaltungsbeamter und Fischereiwissenschaftler, Heft 11 [in German].

Jirka, G.H., Lang, C. (2004). Gerinnehydraulik (Open channel hydraulics). *Vorlesungsmanuskript* der Vorlesung Gerinnehydraulik an der Universität Karlsruhe, Fassung April 2004, D [in German].

Keulegan, G.H. (1938). Laws of turbulent flow in open channels. *Journal of Research of the National Bureau of Standards* 21(6), 707-741.

Lange, D. (2007). Blockrampen - ökologische Bauwerke zur Sohlstabilisierung (Block ramps – Ecological structures to stabilize the river bed). In *VAW-Mitteilung* 201, Minor, H.-E., ed. ETH Zürich, CH, 5-21 [in German].

Lawrence, D.S.L. (1997). Macroscale surface roughness and frictional resistance in overland flow. *Earth Surface Processes and Landforms* 22(4), 365-382.

Lee, A. (1998). The hydraulics of steep streams. *PhD-Thesis*, Sheffield University, Sheffield, UK.

Li, Z., Komar, P.D. (1986). Laboratory measurements of pivoting angles for applications to selective entrainment of gravel in a current. *Sedimentology* 33(3), 413-423.

Liao, J.C. (2007). A review of fish swimming mechanics and behaviour in altered flows. *Philosophical Transactions of the Royal Society B* 362, 1973-1993.

Liao, J.C., Beal, D.N., Lauder, G.V., Triantafyllou, M.S. (2003). The Kármán gait: novel body kinematics of rainbow trout swimming in a vortex street. *Journal of Experimental Biology* 206(6), 1059-1073.

Little, W.C., Mayer, P.G. (1972). The role of sediment gradation on channel armouring. *Report* ERC-0672, Environmental Resources Center, Georgia Inst. of Technology. Atlanta, USA.

Lu, S.S., Willmarth, W.W. (1973). Measurements of the structure of the Reynolds stress in a turbulent boundary layer. *Journal of Fluid Mechanics* 60, 481-511.

Lupandin, A.I. (2005). Effect of flow turbulence on swimming speed of fish. *Biology Bulletin* 32(5), 461-466.

LUBW Landesanstalt für Umwelt, Messungen und Naturschutz Baden-Württemberg (2006). *Durchgängigkeit für Tiere in Fliessgewässern 2: Umgehungsgewässer und fischpassierbare Querwerke* (Passage for animals in rivers 2: By-passes and passages for fish). LUBW: Karlsruhe, D [in German].

Manes, C., Pokrajac, D., McEwan, I. (2007). Double-averaged open-channel flows with small relative submergence. *Journal of Hydraulic Engineering* 133(8), 896-904.

Manes, C., Pokrajac, D., McEwan, I., Nikora, V. (2009). Turbulence structure of open channel flows over permeable and impermeable beds: a comparative study. *Physics of Fluids* 21(12), 125109-1-125109-12.

Marti, C. (2006). Morphologie von verzweigten Gerinnen (Morphology of braided open-channels). *VAW-Mitteilung* 199, Minor, H.-E., ed., ETH Zürich, CH [in German].

Martin, H., Pohl, R. (2009). *Technische Hydromechanik 4* (Technical hydromechanics 4). Verlag Bauwesen, Berlin, D [in German].

Maynord, S.T. (1991). Flow resistance of riprap. *Journal of Hydraulic Engineering* 117(6), 687-696.

McLean, S.R., Wolfe, S.R., Nelson, J.M. (1999). Spatially averaged flow over a wavy boundary revisited. *Journal of Geophysical Research* 104(C7), 15743-15753.

McLean, S.R., Nikora, V.I., Coleman, S.E. (2008). Double-averaged velocity profiles over fixed dune shapes. *Acta Geophysica* 56(3), 669-697.

Mc Keown, B.A. (1984). *Fish migration*. Timber Press, Beaverton, USA.

Meyer-Peter, E., Müller, R (1948). Formulas for bed-load transport. *2nd Meeting IAHSR,* Appendix 2, Stockholm, S, 1-26.

Mignot, E., Barthelemy, E., Hurther, D. (2009). Double-averaging analysis and local flow characterization of near-bed turbulence in gravel-bed channel flows. *Journal of Fluid Mechanics* 618, 279-303.

Morris, H.M. (1959). Design methods for flow in rough conduits. *Journal of the Hydraulic Division ASCE* 85(HY7), 43-61.

Müller, K. (1950). Fische und Fischregionen der Fulda (Fish and fish regions in the Fulda River). *Jahresbericht der limnologischen Flussstation Freudenthal* 1, 18-23 [in German].

Myers, G.S. (1949). Usage of Anadromous, Catadromous and allied terms for migratory fishes. *Copeia* 1949, 89-97.

Nepf, H.M. (2012a). Flow and transport in regions with aquatic vegetation. *Annual Review of Fluid Mechanics* 44, 123-142.

Nepf, H.M. (2012b). Hydrodynamics of vegetated channels. *Journal of Hydraulic Research* 50(3), 262-279.

Nezu, I., Nakagawa, H., and Tominaga, A. (1985). Secondary currents in a straight channel flow and the relation to its aspect ratio. *Turbulent shear flows* 4, Springer, Berlin, Germany, 246–260.

Nezu, I, Rodi, W. (1986). Open-channel flow measurements with a laser Doppler anemometer. *Journal of Hydraulic Engineering* 112(5), 335-355.

Nezu, I, Nakagawa, H. (1993). *Turbulence in open-channel flows*, Balkema, Rotterdam, NL.

Nielsen, J.L. (1998). Scientific sampling effects: electrofishing California's endangered fish populations. *Fisheries* 23(12), 6-12.

Nikora, V., Goring, D., McEwan, I., Griffiths, G. (2001). Spatially averaged open-channel flow over rough bed. *Journal of Hydraulic Engineering* 127(2), 123-133.

Nikora, V.I., Aberle, J., Biggs, B.J.F., Jowett, I.G., Sykes, J.R.E. (2003). Effects of fish size, time-to-fatigue and turbulence on swimming performance: a case study of *Galaxias maculatus*. *Journal of Fish Biology* 63(6), 1365-1382.

Nikora, V., McEwan, I., McLean, S., Coleman, S., Pokrajac, D., Walters, R. (2007a). Double-averaging concept for rough-bed open-channel and overland flows: Theoretical Background. *Journal of Hydraulic Engineering* 133(8), 873-883.

Nikora, V., McLean, S., Coleman, S., Pokrajac, D., McEwan, I., Campbell, L., Aberle, J., Clunie, D., Koll, K. (2007b). Double-averaging concept for rough-bed open-

channel and overland flows: Applications. *Journal of Hydraulic Engineering* 133(8), 884-895.

Nikuradse, J. (1933). Strömungsgesetze in rauhen Rohren (Flow laws in rough pipes). *Forschungsheft* 361, VDI-Verlag GmbH (Beilage zu „Forschung auf dem Gebiet des Ingenieurwesens“, Ausgabe B Band 4) [in German].

Northcote, T.G. (1998). Migratory behaviour of fish and its significance to movement through riverine fish passage facilities. In *Fish migration and fish bypasses*, Jungwirth, M., Schmutz, S., Weiss, S. eds. Fishing New Books, Oxford, UK, 3-18.

Odeh, M., Noreika, J.F., Haro, A., Maynard, A., Castro-Santos, T., Cada, G.F. (2002). Evaluation of the effects of turbulence on the behavior of migratory fish. *Final Report 2002, Report to Bonneville Power Administration*, Contract No. 00000022, Oak Ridge National Laboratory, USA.

Oertel, M., Schlenkhoff, A. (2012). Crossbar block ramps: flow regimes, energy dissipation, friction factors, and drag forces. *Journal of Hydraulic Engineering* 138(5), 440-448.

Okamoto, T.-a., Nezu, I. (2013). Spatial evolution of coherent motions in finite-length vegetation patch flow. *Environmetal Fluid Mechanics* 13(5), 417-434.

O’Loughlin, E.M., MacDonald, E.C. (1964). Some roughness concentration effects on boundary resistance. *La Houille Blanche* 7, 773-783.

Pagliara, S., Chiavaccini, P. (2006a). Flow resistance of rock chutes with protruding boulders. *Journal of Hydraulic Engineering* 132(6), 545-552.

Pagliara, S., Chiavaccini, P. (2006b). Energy dissipation on reinforced block ramps. *Journal of Irrigation and Drainage Engineering* 132(3), 293-297.

Pagliara, S., Chiavaccini, P. (2007). Failure mechanisms of base and reinforced block ramps. *Journal of Hydraulic Research* 45(3), 407-420.

Pagliara, S., Palermo, M. (2011). Block ramp failure mechanisms: critical discharge estimation. *ICE Proceeding Water Management* 164(WM6), 303-309.

Palt, S., Dittrich, A. (2002). Stabilität von Gebirgsflüssen und rauen Rampen (Stability of mountain rivers and rough ramps). *Österreichische Wasser- und Abfallwirtschaft* 54(5/6), 75-86 [in German].

Papanicolaou, A.N., Diplas, P., Dancey, C.L., Balakrishnan, M. (2001). Surface roughness effects in near-bed turbulence: implications to sediment entrainment. *Journal of Engineering Mechanics* 127(3), 211-218.

Parker, G. (1979). Hydraulic geometry of active gravel rivers. *Journal of the Hydraulic Division ASCE* 105(HY9), 1185-1201.

Pavlov, D.S. (1989). Structures assisting the migrations of non-salmonid fish:USSR. Food and Agriculture Organization of the United Nations (FAO) *Fisheries Technical Paper* 308, Rome, I.

Pavlov, D.S., Lupandin, A.I., Skorobogatov, M.A. (2000). The effects of flow turbulence on the behavior and distribution of fish. *Journal of Ichthyology* 40(Suppl. 2), 232-261.

Peckarsky, B.L., Taylor, B.W., Caudill, C.C. (2000). Hydrologic and behavioral constraints on oviposition of stream implications for adult dispersal. *Oecologia* 125(2), 186-200.

Peter, A. (1998). Interruption of the river continuum by barriers and the consequences for migratory fish. In *Fish migration and fish bypasses*, Jungwirth, M., Schmutz, S., Weiss, S. eds. Fishing New Books, Oxford, UK, 99-112.

Peter, A. Herz, C. (2013). Review of the Wyna block ramp fish assessment 2012. *Internal report*, Swiss Federal Institute of Aquatic Science and Technology (Eawag), Kastanienbaum, CH [unpublished].

Pokrajac, D., Campbell, L.J., Nikora, V., Manes, C., McEwan, I. (2007). Quadrant analysis of persistent spatial velocity perturbations over square-bar roughness. *Experiments in Fluids* 42(3), 413-423.

Prandtl, L. (1933). Neuere Ergebnisse der Turbulenzforschung (New results of the turbulence research). *Zeitschrift des Vereins deutscher Ingenieure*, Band 77(5), 105-113 [in German].

Prentice, E.F., Flagg, T.A., McCutcheon, C.S. (1990). Feasibility of using implantable passive integrated transponder (PIT) tags in salmonids. In *Fish-marking techniques*, Parker, N.C., Giorgi, A.E., Heidinger, R.C., Jester, D. eds. American Fisheries Society, Symposium 7, Bethesda, USA, 317-322.

Raudkivi, A.J., Ettema, R. (1982). Stability of armour layers in rivers. *Journal of the Hydraulics Division ASCE* 108(HY9), 1047-1057.

Raupach, M.R., Shaw, R.H. (1982). Averaging procedures for flow within vegetation canopies. *Boundary Layer Meteorology* 22(1), 79-90.

Requena, P. (2008). Seitenerosion in kiesführenden Flüssen – Prozessverständnis und quantitative Beschreibung (Side erosion in gravel rivers – Process understanding and quantitative description). *VAW-Mitteilung* 210, Minor, H.-E., ed. ETH Zürich, CH [in German].

Rice, C.E., Kadavy, K.C., Robinson, K.M. (1998). Roughness of loose rock riprap on steep slopes. *Journal of Hydraulic Engineering* 124(2), 179-185.

Rickenmann, D. (1990). Bedload transport capacity of slurry flows at steep slopes. *VAW-Mitteilung* 103, Vischer, D., ed. ETH Zürich, CH.

Roni, P., Hanson, K., Beechie, T. (2008). Global review of the physical and biological effectiveness of stream habitat rehabilitation techniques. *North American Journal of Fisheries Management* 28(3), 856-890.

Rouse, H. (1965). Critical analysis of open-channel resistance. *Journal of the Hydraulic Division ASCE* 91(HY4), 1-25.

Roussel, J.M., Haro, A., Cunjak, R.A. (2000). Field test of a new method for tracking small fishes in shallow rivers using passive integrated transponder (PIT) technology. *Canadian Journal of Fisheries and Aquatic Sciences* 57(7), 1326-1329.

Ruck, B. (1987). *Laser-Doppler-Anemometrie*. AT Verlag, Stuttgart, D [in German].

Rüedlinger, D. (2012). Aufgelöste unstrukturierte Blockrampen als Teil des übergeordneten Systems „Fluss“: Experimentelle Untersuchung (Unstructured block ramps as

part of the river system: an experimental study). *Master Thesis*, ETH Zürich, CH [in German, unpublished].

Schager, E., Peter, A. (2004). Methoden zur Untersuchung und Beurteilung der Fliessgewässer. Fische Stufe F (flächendeckend) (Methods to study and evaluate a watercourse, fish level "area-wide"). *Mitteilungen zum Gewässerschutz Nr.* 44. Bundesamt für Umwelt, Wald und Landschaft BUWAL, Bern, CH [in German].

Scheuerlein, H. (1968). Der Rauhgerinneabfluss (The flow in rough open-channels). *Bericht der Versuchsanstalt für Wasserbau* Nr. 14, Technische Universität München, D [in German].

Schlichting, H. (1936). Experimentelle Untersuchungen zum Rauhigkeitsproblem (Experimental study on roughness). *Ingenieur Archiv* 7(1), 1-34.

Schlichting, H. (1960). *Boundary layer theory*. McGraw-Hill Book Company, New York, USA.

Schneider, K.-J. (2004). *Bautabellen für Ingenieure mit Berechnungshinweisen und Beispielen* (Construction tables for engineers with calculation information and examples). 16. Auflage, Werner Verlag, Stuttgart, D [in German].

Shields, A. (1936). Anwendung der Ähnlichkeitsmechanik und Turbulenzforschung auf die Geschiebebewegung. *Mitteilung der Preussischen Versuchsanstalt für Wasserbau und Schiffbau* Nr. 26, Versuchsanstalt für Wasser- und Schiffbau, Berlin, D [in German].
or translated by W.P. Ott and J.C. van Uchelen
Shields, A. (1936). Application of similarity principles and turbulence research to bed-load movement. *California Institute of Technology*, Pasadena, USA.

Smart, G.M., Jäggi, M.N.R. (1983). Sedimenttransport in steilen Gerinnen (Sediment transport in steep channels). *VAW-Mitteilung* 64, Vischer, D., ed. ETH Zürich, CH [in German].

Smith, J.D., McLean, S.R. (1977). Spatially averaged flow over a wavy surface. *Journal of Geophysical Reserach* 82(12), 1735-1746.

Sörensen, I. (1951). An investigation of some factors affecting the upstream migration of the eel. *Reports of the Institute of Freshwater Research of Drottningholm* 32, Drottningholm, S, 126-172.

Stahlberg, S., Peckmann, P. (1986). Bestimmung der kritischen Strömungsgeschwindigkeit für einheimische Kleinfischarten (Determination of the critical flow velocity for indigenous small fish species). *Wasserwirtschaft* 76(7/8), 340-342 [in German].

Stephan, U., Gutknecht, D. (2002). Hydraulic resistance of submerged flexible vegetation. *Journal of Hydrology* 269(1-2), 27-43.

Strickler, A. (1923). Beiträge zur Frage der Geschwindigkeitsformel und der Rauhigkeitszahlen für Ströme, Kanäle und geschlossene Leitungen (Contributions to the question about the velocity equation and roughness data for rivers, channels and pipes). *Amt für Wasserwirtschaft, Eidgenössisches Departement des Innern*, Bern, CH [in German].

Studer, M.J., Schleiss, A.J. (2009). Velocity and water depth analysis on different types of block ramps. *33rd IAHR Congress: Water engineering for a sustainable environment*, IAHR, Vancouver, CDN, 710-717.

Tamagni, S. (2006). Aufgelöste unstrukturierte Blockrampen: Experimentelle Untersuchung (Unstructured block ramps: an experimental study). *Master Thesis*, ETH Zürich, CH [in German, unpublished].

Tritico, H.M., Cotel, A.J. (2010). The effects of turbulent eddies on the stability and critical swimming speed of creek chub (*Semotilus atromaculatus*). *The Journal of Experimental Biology* 213(13), 2284-2293.

Tschopp, J., Bisaz, E. (1972). Profundidad de erosion al pie de un vertedero para la aplication de correction de arroyos en quebradas empinados (Erosion depth at weir toe for the application of river corrections at steep canyons). *5. Congresso Latinoamericano de Hidraulica*, IAHR, Lima, PE [in Spanish].

Van Zyll de Jong, M.C., Cowx, I.G, Scruton, D.A. (1997). An evaluation of instream habitat restoration techniques on salmonid populations in a Newfoundland stream. *Regulated Rivers Research and Management* 13(6), 603-614.

VAW (2007) Blockrampen: Anforderungen und Bauweisen (Block ramps: requirements and construction methods). *VAW-Mitteilung* 201, Minor, H.-E., ed. ETH Zürich, CH [in German].

VAW (2008a) Blockrampen Landquart – Hydraulische Modellversuche zu klassischen und aufgelösten unstrukturierten Blockrampen (Block ramps at the Landquart River – Model tests on ramp of block carpet type and on unstructured block ramps). *Technical Report Nr.* 4236, VAW, ETH Zürich, CH [in German, unpublished].

VAW (2008b) Ereignisanalyse Hochwasser 2005 – Teilprojekt Wirksamkeit von Massnahmen: Sammler und Rechen, Blockrampen (Analysis of flood event 2005 - Subprojekt on effectiveness of measures: retention basins and racks, block ramps). *Technical Report Nr.* 4242, VAW, ETH Zürich, CH [in German, unpublished].

VAW (2009) Aufgelöste Blockrampe an der Wyna – Begutachtung (Unstructured block ramp at the Wyna River – Expertise). *Technical Report Nr.* 4282, VAW, ETH Zürich, CH [in German, unpublished].

Videler, J.J. (1993). *Fish Swimming*. Fish and Fisheries Series 10, Chapman & Hall, London, UK.

Vogel, S. (2003). Ansätze zur Bemessung rauer Rampen in aufgelöster Bauweise. *Mitteilung des Instituts für Wasserwesen* 88, Universität der Bundeswehr, Munich, D [in German].

Wallace J.M., Eckelmann, H., Brodkey, R.S. (1972). The wall region in turbulent shear flow. *Journal of Fluid Mechanics* 54, 39-48.

Webb, P.W., Cotel, A.J. (2011). Assessing possible effects of fish-culture systems on fish swimming: the role of stability in turbulent flows. *Fish Physiology and Biochemistry* 37(2), 297-305.

Weibel, D., Peter, A. (2013). Effectiveness of different types of block ramps for fish upstream movement. *Aquatic Sciences* 75(2), 251-260.

Weichert, R. (2006). Bed morphology and stability of steep open channels. *VAW-Mitteilung* 192, Minor, H.-E., ed. ETH Zürich, CH.

Weichert, R. (2007). Die Gutmütigkeit von Blockrampen im Überlastfall (The good-natured behaviour of block ramps in case of overload). In *VAW-Mitteilung* 201, Minor, H.-E., ed. ETH Zürich, CH, 111-123 [in German].

Weichert, R., Bezzola, G.R., Minor, H.-E. (2009). Bed erosion in steep open channel. *Journal of Hydraulic Research* 47(3), 360-371.

Werth, S., Weibel, D., Alp, M., Junker, J., Karpati, T., Peter, A., Scheidegger, C., (2011). Lebensraumverbund Fliessgewässer: Die Bedeutung der Vernetzung (Habitat interconnection in rivers: the importance of connectivity). *Wasser Energie Luft* 103(3), 224–234 [in German].

Whittaker, J., Jäggi, M. (1986). Blockschwellen (Block ramps). *VAW-Mitteilung* 91, D. Vischer ed. ETH Zürich, CH [in German].

Whittaker, J.G., Hickman, W.E., Corad, R.N. (1988). River-bed stabilization with placed blocks. *Report* 3-88/3, Hydraulics Section, Central Laboratories Works Corporation, Lower Hutt, NZ.

Wilson, N.R., Shaw, R.H. (1977). A higher order closure model for canopy flow. *Journal of Applied Meteorology* 16(11), 1197-1205.

Yalin, M.S. (1963). An expression for bed-load transportation. *Journal of the Hydraulic Division ASCE* 89(HY3), 221-250.

Zarn, B. (1992). Lokale Gerinneaufweitungen: Eine Massnahme zur Sohlenstabilitisierung der Emme bei Utzendorf (Local river widenings: A measure to stabilize the river bed at the Emme River in Utzendorf). *VAW-Mitteilung* 118, Vischer, D., ed. ETH Zürich, CH [in German].

Zeh Weissmann, H., Könitzer, C., Bertiller, A. (2009). Strukturen der Fliessgewässer in der Schweiz. Zustand von Sohle, Ufer und Umland (Ökomorphologie); Ergebnisse der ökomorphologischen Kartierung; Stand: April 2009 (Structures in Swiss rivers. Situation of river bed, band and environs (ecomorphology); results of the ecomorphological mapping; status: April 2009). *Umwelt-Zustand Nr.* 0926. Swiss Federal Office for the Environment (FOEN), Bern, CH [in German].

Appendix – Supplementary material

Appendix A: Experience in Switzerland with unstructured block ramps

In August 2005 extreme rainfalls over vast areas of Switzerland caused devastating floods, leading to high damages. In many places the flood was in the magnitude of the design discharge (often HQ_{100}), or even exceeded it (sometimes EHQ). The Swiss Federal Office for the Environment (FOEN) commissioned the analysis of this event and published the results of this analysis in Bezzola and Hegg (2008). The processes and the structures affected by the flood were both analysed to understand what reacted positively and what did not. Each type of block ramp and their behaviour during the flood were analysed. The results are presented in the technical report VAW (2008b). The reasons which caused the damage of UBR are summarized below. Additionally, the results of a survey on UBR are illustrated: each Swiss canton was questioned about existing UBR and their parameter combination, in order to collect the acquired experience on building UBR.

Block ramp failure events in Switzerland

Eight block ramps were considered in VAW (2008b): five ramps of block carpet type and three UBR. All of them incurred in damages during the flood in 2005, two ramps completely failed, both of block carpet type. Two UBR and their reaction to the flood are described hereafter to highlight the problems that occurred.

UBR at the Simme River in St. Stephan (Canton of Bern)

In 2002 and 2003 two UBR were constructed at the Simme River in St. Stephan with a slope of 3% (Figure A.1). The ramps were built subsequently to existing drops for a specific design discharge $q_d = 10.0$ m^2/s VAW (2008b). During the flood in 2005 the peak in this region was $q_{2005} = 7.1$ m^2/s, i.e. $q_{2005} < q_d$. During the flood some blocks upstream of the drop embedded in the finer sediment material, leading to a height difference of approximately 1 m. Apart from that, the ramp maintained its stabilizing function after the flood.

The scour upstream of the drop could cause increased erosion in the area of the ramp head during the next high discharge, leading eventually to a ramp failure. The

transition between fixed (drop) and flexible structure (UBR) is problematic and the scouring risk is high. In order to avoid this, a buffer area with the same slope as the river should be introduced between the existing drops and the UBR with higher slope, decreasing the scouring risk and giving more flexibility to the system of structures (drop + UBR).

Figure A.1 UBR at the Simme River in St. Stephan in June 2005, before the flood event.

UBR at the Kander River in Augand (Canton of Bern)

An UBR was built in 2005 at the Kander River with a slope of 2.5% and with a buffer area (Figure A.2). The specific design discharge was set at $q_d = 11.4$ m^2/s, which was exceeded during the flood event 2005 by $q_{2005} = 15.1$ m^2/s for more than 18 hours. This high discharge caused the embedding of blocks in the finer sediment material, particularly in the upstream right part of the ramp. This induced the ramp to deform and to flatten, reducing the ramp slope.

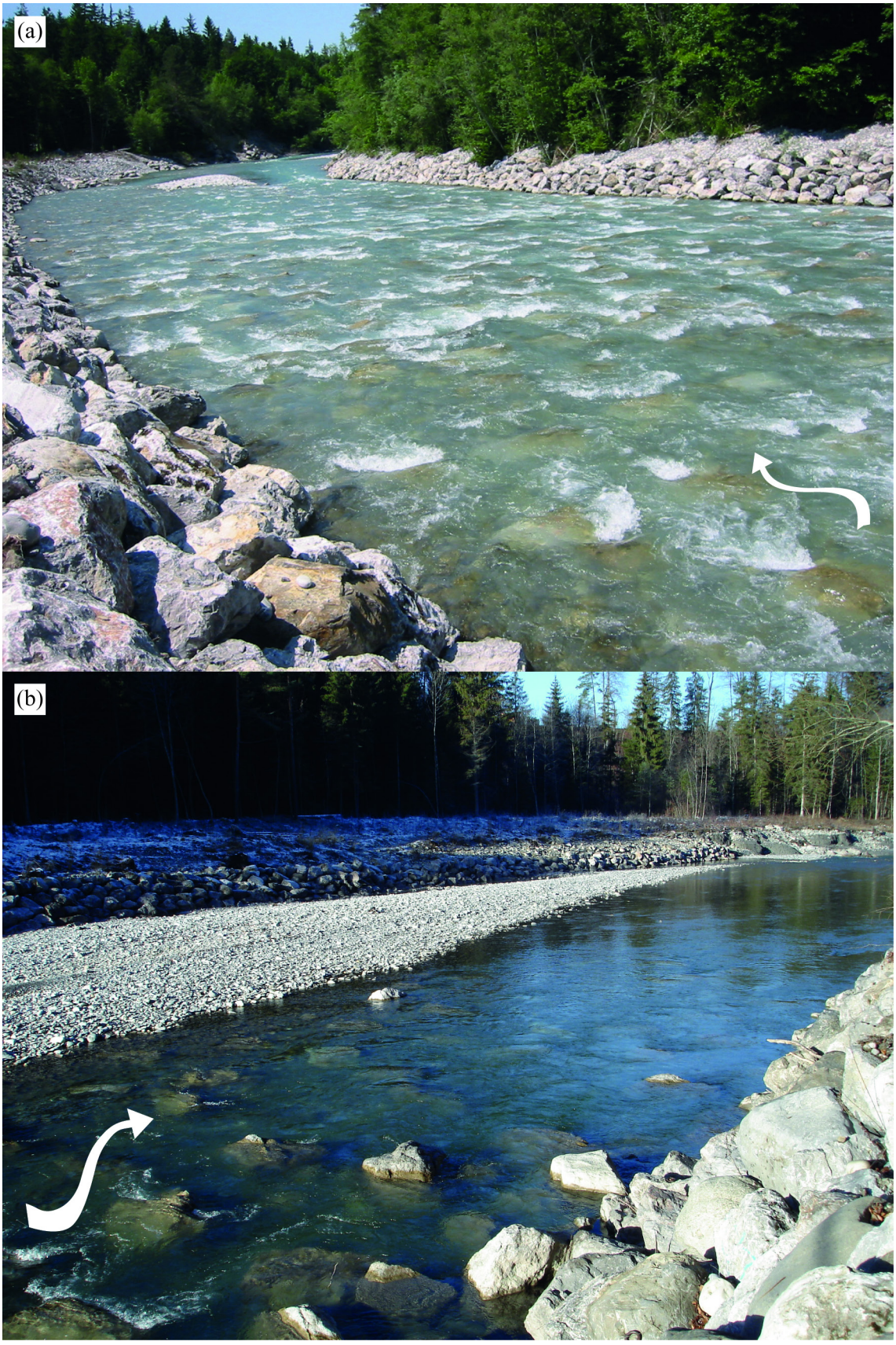

Figure A.2 UBR at the Kander River in Augand (a) in June 2005, and (b) in December 2006. After the flood event in August 2005 the left side of UBR was covered with gravel deposit.

Upstream of the ramp, the river changed locally its course, causing flow concentration at one river side. Presumably for this reason, the blocks embedded locally at the right ramp side. Note that the ramp did not fail even with a higher local specific discharge.

The flood event in 2005 (VAW 2008b) confirmed two aspects regarding block ramp behaviour for high discharges or in case of overload: (1) failure mechanism of ramps of block carpet type is binary and for discharges higher than q_d the ramp may fail abruptly (Chap. 3.2.2); (2) the construction and execution details (as the connection between existing drop and the ramp as well as between the ramp and the bank protection, or the construction method) are decisive and if not considered properly, they can lead to the ramp failure also for discharges lower than the design discharge. The goal of this short review on the flood event analysis was to highlight that not only the parameter combination (D, D/d_{90} and λ) and the selected slope are decisive for the ramp stability and its behaviour in case of overload, but also that construction details play an important role.

Today's block ramps in Switzerland

During this PhD research, a survey about existing UBR in Switzerland was conducted and each Swiss Canton was questioned. Table A.1 shows the collected data on UBR, subdivided into the different Cantons (AG = Aargau, BE = Bern, GR = Graubünden, NW = Nidwalden, SH = Schaffhausen, SO = Solothurn, SZ = Schwyz, UR = Uri). As the data could not be controlled, their reliability is not assured. Unfortunately, the collected data are not comprehensive and cannot be directly compared with the experimental results. For this reason, the goal of this chapter is exclusively to give an overview on the existing UBR in Switzerland and on their characteristic parameters.

Table A.1 Existing UBR in Switzerland according to the survey conducted in 2013. Empty boxes: no data obtained with survey. *) Values determined with collected data.

Canton	Location	River	Year of construction	Slope	Width	Length	Block mass	Block diameter	Block placement density		Design discharge	Specific design discharge
				S_R [%]	W_R [m]	L_R [m]	M_B [t]	D [m]	[block/m^2]	λ [-]	Q [m^3/s]	q [m^2/s]
AG	Seengen	Aabach	2007	1.7	7.7	64	0.8-1.2	0.7-0.8			13.6 *)	1.77
	Vordemwald	Pfaffneren	2007	8	5.6	13.4	0.67	0.74				
	Eiken	Sissle	2006	2	8.5	64	1-2	0.82			151.3 *)	17.8
	Eiken	Sissle	2006	3	11	38	1-2	0.80			151.8 *)	13.8
	Eiken	Sissle	2006	3	10	30	0.8	0.79			151.0 *)	15.1
	Reinach	Wyna	2005	3	8	22	0.7-1	0.64				
	Gränichen	Wyna	2004	6	8.3		0.7-1	0.7				
	Gränichen	Wyna	2006	6	9.2	8	0.7-1	0.7				
	Gränichen	Wyna	2006	3	7.2	22	0.52	0.7				
	Suhr	Wyna	2005	3	7.5	32	0.7-1	0.7				
BE	Opplingen	Rotache	2010	2-7	10	65	1.0-2.5	0.7-1.2				
	Schwarzenburg	Dorfbach	2009	7	8	25.5	0.5-1.5	0.6-0.9			9	1.1*)
	Wolfey	Simme	2002	1.8-2	12	70	2.5-3		0.06		120	10.0*)
	Riedsagi	Simme	2002	3.3	12	70	2.8-3.5	1.3	0.1	0.13*)	120	10.0*)
	Latterbach	Simme	2006	1.4	20	110	2.5-3.0		0.19		348	17.4*)
	Wimmis, Reutigen	Simme	2011	2.5	30	200	2.5-4.0	1.0	0.2	0.16*)	340	11.3*)

Canton	Location	River	Year of construction	Slope	Width	Length	Block mass	Block diameter	Block placement density		Design discharge	Specific design discharge
				S_R [%]	W_R [m]	L_R [m]	M_B [t]	D [m]	[block/m^2]	λ [-]	Q [m^3/s]	q [m^2/s]
BE	Wimmis, Reutigen	Simme	2012	2.5	30-35	150	2.5-3.5	1.0	0.2	0.16*)	340	11.3-9.7*)
	Wimmis	Simme	2008	2	30	135	2.3-3.5	1.0	0.2	0.16*)	340	11.3*)
	St. Stephan	Simme	2003	3	15	60	2.8-3.5	1.3	0.1	0.13*)	120	8.0*)
	Spiez, Reutigen	Kander	2005	3.5	30-50	105	1.7	1.0	0.5	0.39*)		
	Spiez, Wimmis	Kander	2005	5	20-25	84	1.7	1.0	0.5	0.39*)	250	12.5-10.0*)
	Spiez, Wimmis	Kander		2.5	30	100	2.5	1.0	0.35	0.27*)	250	8.3*)
	Kandersteg	Kander	2011	2.3	10	105	1.5-3.0	0.6-1.0	0.25	0.07-0.20*)	70	7.0*)
	Unterseen	Lombach	2000	5	13-17	66	4.0-5.0	1.5			153	11.8-9.0*)
GR	Chur	Alpenrhein		0.55	80	220	2	1.07	0.2	0.18*)		
	Haldenstein	Alpenrhein		1.1	50	60	4.5	1.48	0.27	0.46*)	2250	45.0*)
	Untervaz	Alpenrhein		0.9	55	150	4.5	1.48	0.26	0.45*)		
	Malans/Igis (ramp series)	Landquart		2	22	70-250	4.0-5.0	1.5	0.11	0.19*)	445*)	20.2*)
	Grüsch (ramp series)	Landquart		2	15-20	110-170	5.0-6.0		0.10-0.13			

Canton	Location	River	Year of construction	Slope	Width	Length	Block mass	Block diameter	Block placement density		Design discharge	Specific design discharge
				S_R [%]	W_R [m]	L_R [m]	M_B [t]	D [m]	[block/m^2]	λ [-]	Q [m^3/s]	q [m^2/s]
NW	Buochs	Engelberger Aa		2	20	7	3.2	1.3	0.2	0.27*)	240	12.0*)
SH	Thayngen, Hofen	Biber	201	2	5	47	2.4	1.0	0.18*)	0.14*)	30	6.0*)
SO	Boningen	Aare	1998					0.6-0.8			5-8	
SZ	Sand	Muota	2007	2.5	22	80	5.0-6.0	1.6	0.075	0.15*)	340	15.5*)
	Tristel	Muota	2009	1.4	10	150	3.0-5.0	1.4	0.06-0.1	0.09-0.15*)	260	26.0*)
	Muotatal	Muota	1990/2006	1.2	25	1350	2.0-4.0				240	16.0*)
	Biberbrugg	Alp	2008	2.5	12-14	5 × 80 2 × 40	5.0-6.0	1.6	0.085	0.17*)	200	16.7-14.3*)
	Steinbach	Wellchessibach	2012	12	8-10	350	0.7-3.0	0.7-1.3	0.43-0.23	0.17-0.31*)	34	4.3-3.4*)
UR	Amsteg	Reuss	2009	1.15	40	430	4.0-5.0	1.6-1.7	0.05-0.06	0.10-0.14*)	520	13.0*)
	Andermatt	Unteralpreuss	2013	1.5	11	750	4	1.4	0.18	0.28*)	130	11.8*)

Appendix B: Local velocities and Reynolds stresses

One of the goals of the 2D LDA measurements of phase C was to provide detailed velocity and turbulence distributions on UBR to be used by fish biologists to rate the efficiency of these structures with respect to the swimming capacity of fish. Additionally, the data can be used for numerical modelling purposes. For this reason, in this appendix cross-sections with the experimental data of $\overline{u}/u_{b,i}$ (Figure B.2 to B.7), $\overline{w}/u_{b,i}$ (Figure B.8 to B.13) and $-\overline{u'w'}/u_{*,b,i}^2$ (Figure B.14 to B.19), where $u_{*,b,i} = (gh_{m,i}S)^{0.5}$, are presented. The area considered in this appendix is 200 mm < x < 300 mm (Figure B.1) and was selected due to its different regions of interest as e.g.: 1) area downstream of a block at approximately 30 mm < y < 80 mm; 2) region between two blocks at approximately 0 mm < y < 100 mm, 3) area above, around and downstream of a block at approximately 200 mm < y < 320 mm.

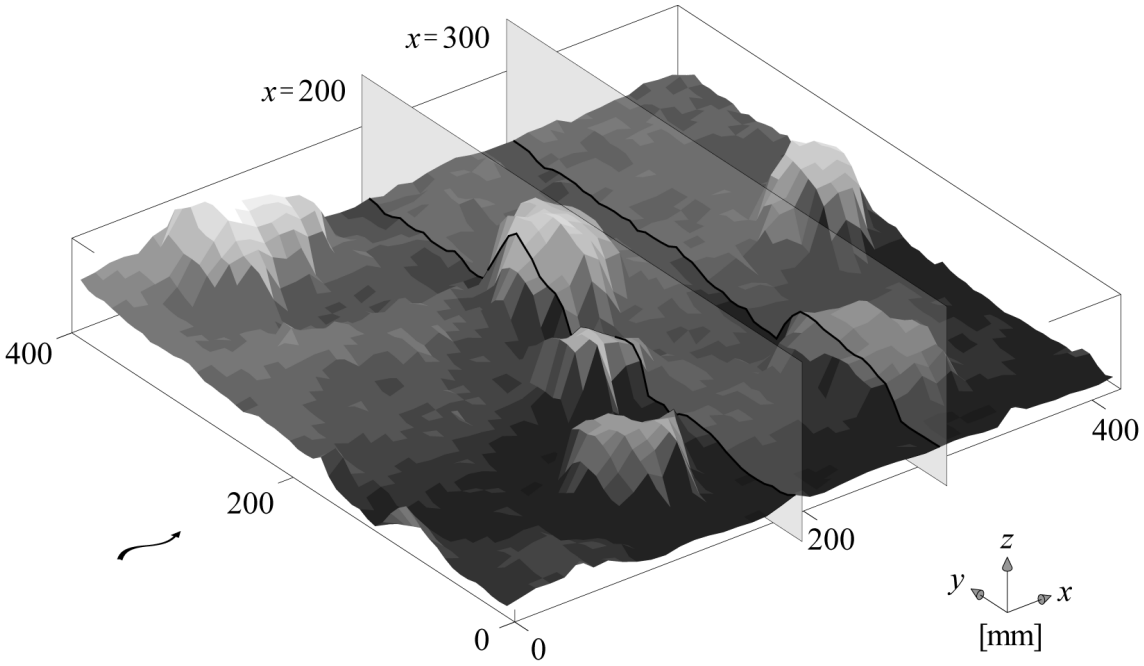

Figure B.1 Topography of the measurement area of phase C with slices at x = 200 mm and x = 300 mm indicating the area considered for the following contour maps. Values in this diagram and in the following refer to model dimensions

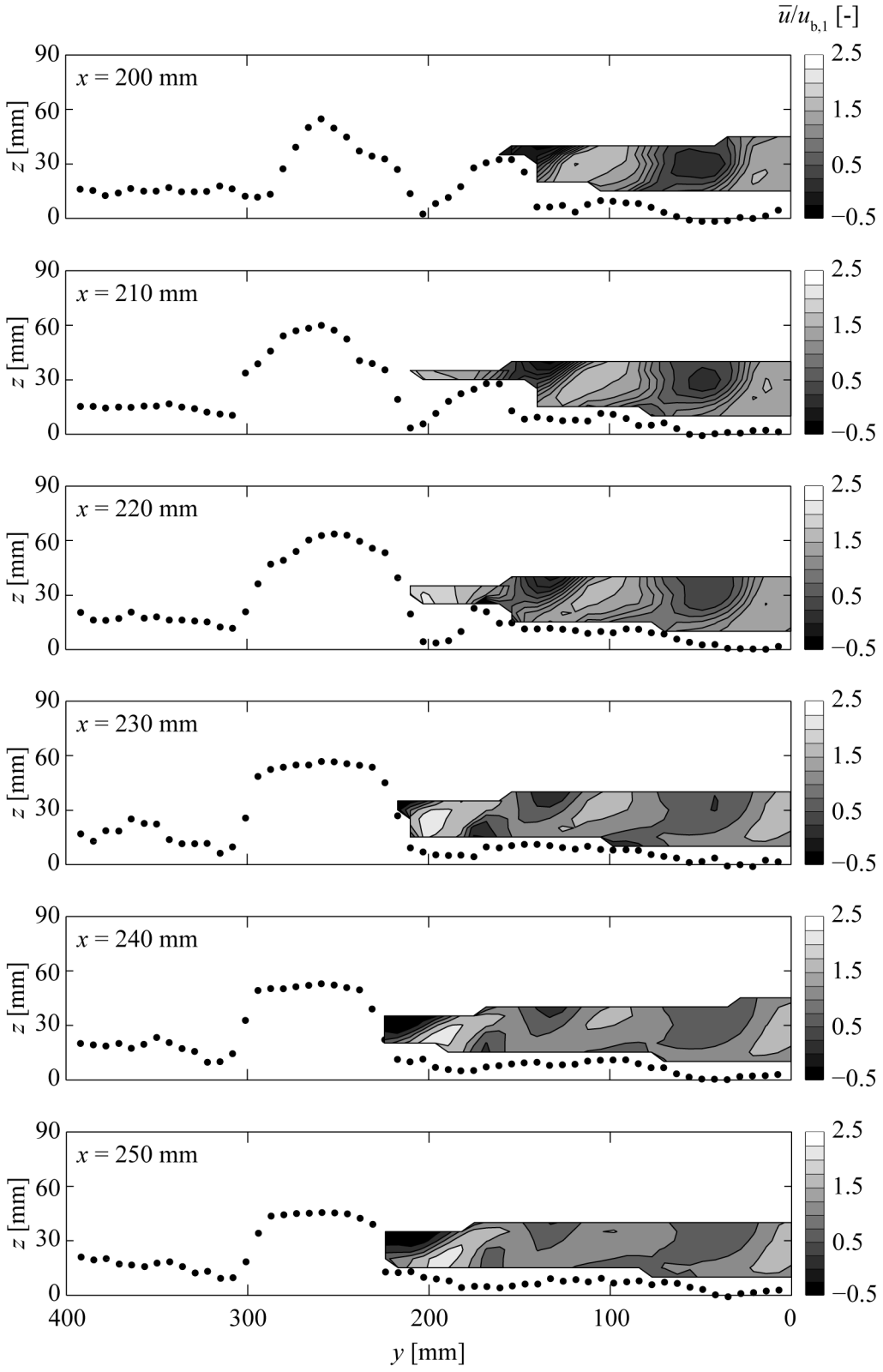

Figure B.2 Cross-sectional downstream view of time-averaged velocities $\overline{u}$ normalized with bulk velocity $u_{b,1} = 0.24$ m/s for specific discharge $q_1 = 6.8$ l/(sm) and relative submergence level $h_{m,1}/P = 0.63$.

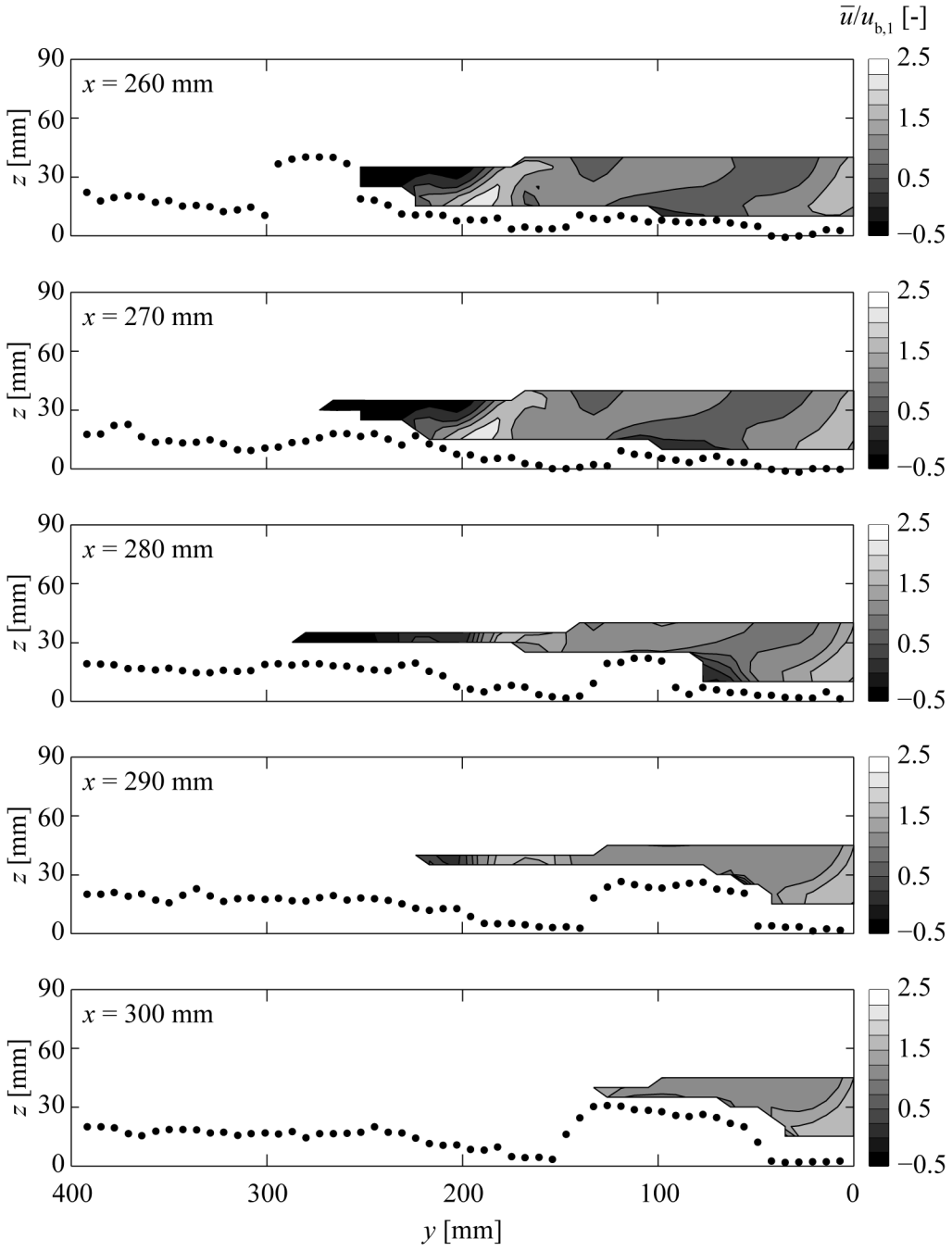

Figure B.3 Cross-sectional downstream view of time-averaged velocities $\overline{u}$ normalized with bulk velocity $u_{b,1}$ = 0.24 m/s for specific discharge q_1 = 6.8 l/(sm) and relative submergence level $h_{m,1}/P$ = 0.63.

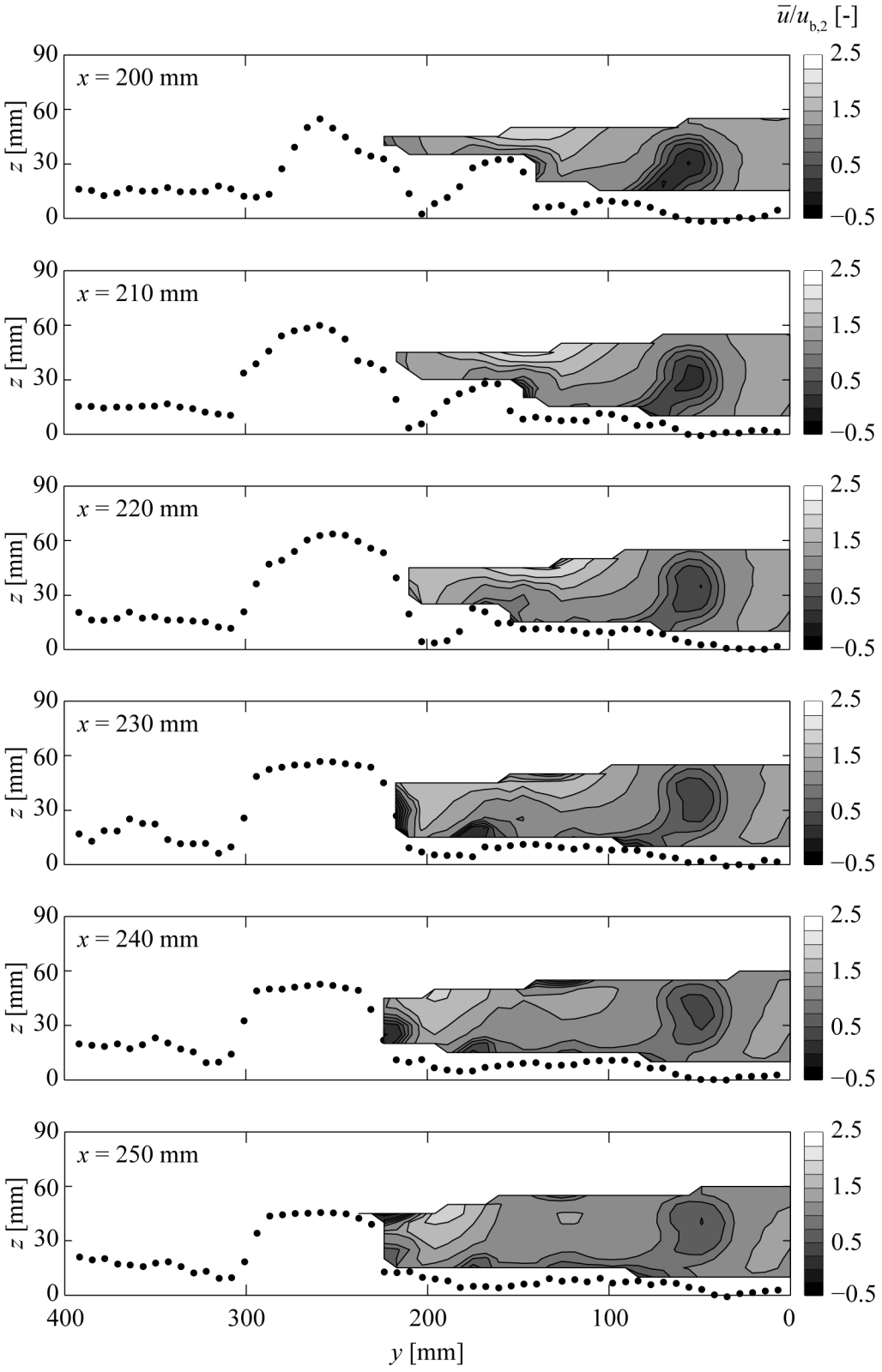

Figure B.4 Cross-sectional downstream view of time-averaged velocities $\overline{u}$ normalized with bulk velocity $u_{b,2} = 0.34$ m/s for specific discharge $q_2 = 13.8$ l/(sm) and relative submergence level $h_{m,2}/P = 0.88$.

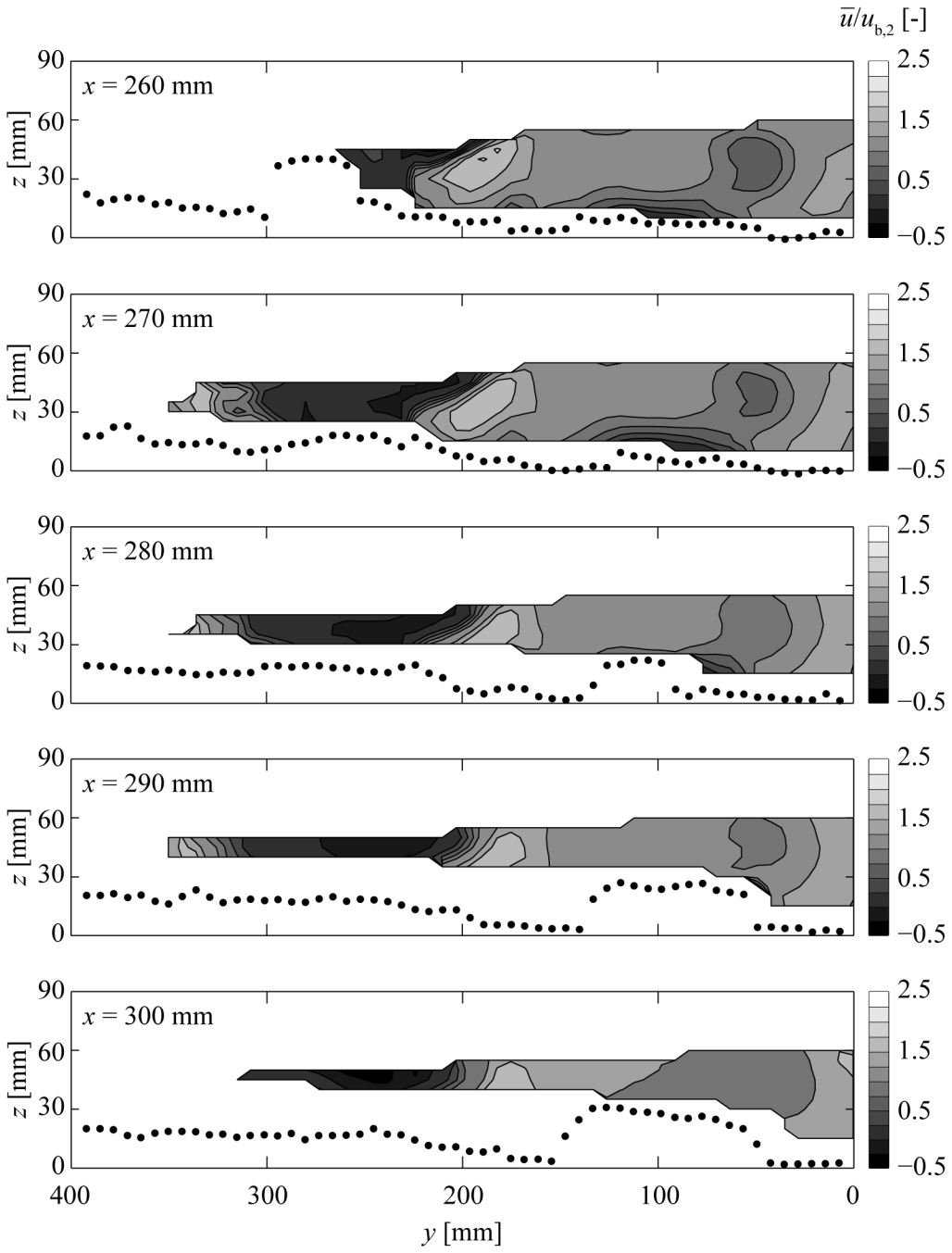

Figure B.5 Cross-sectional downstream view of time-averaged velocities $\overline{u}$ normalized with bulk velocity $u_{b,2} = 0.34$ m/s for specific discharge $q_2 = 13.8$ l/(sm) and relative submergence level $h_{m,2}/P = 0.88$.

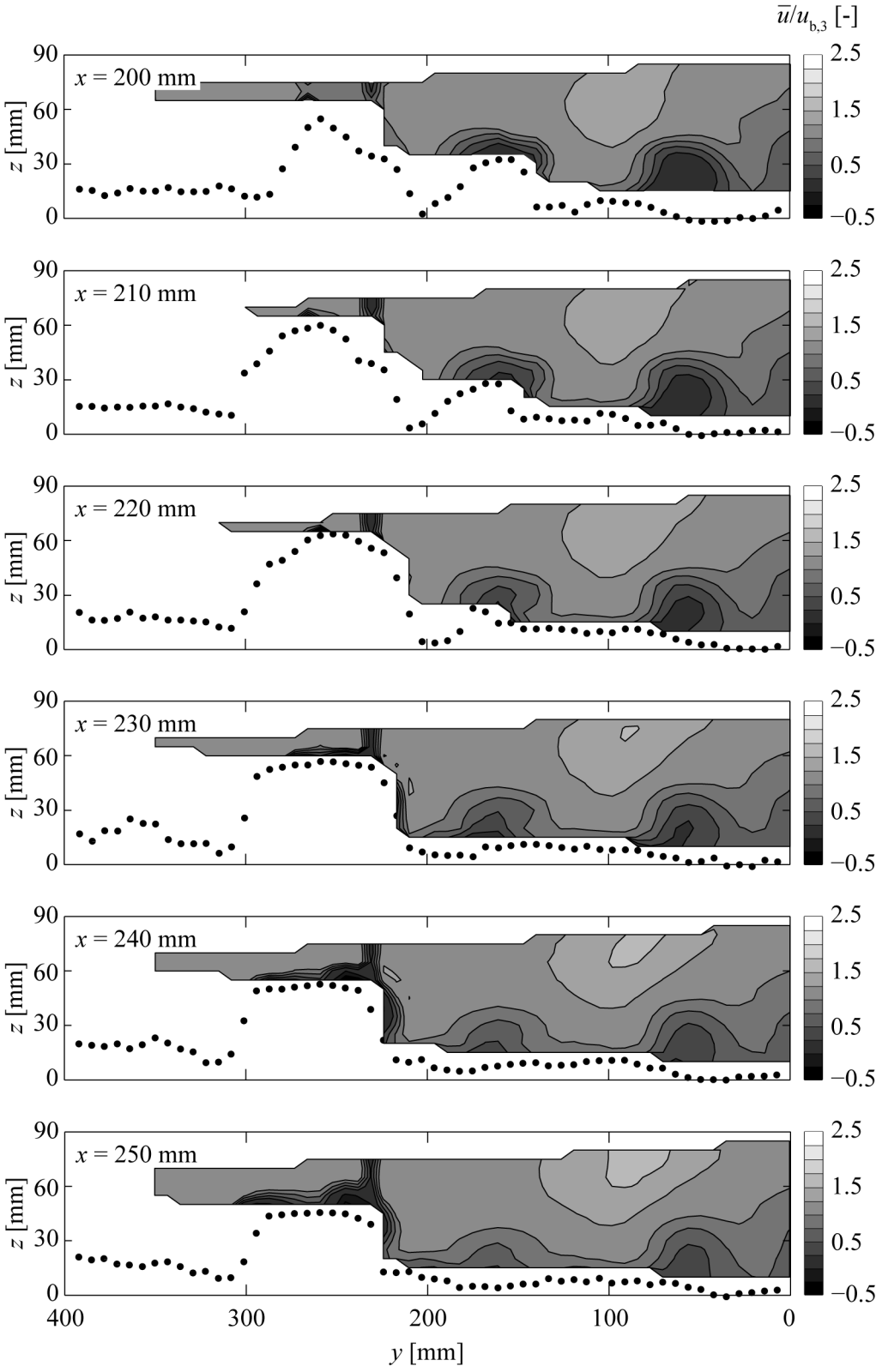

Figure B.6 Cross-sectional downstream view of time-averaged velocities $\overline{u}$ normalized with bulk velocity $u_{b,3} = 0.61$ m/s for specific discharge $q_3 = 40$ l/(sm) and relative submergence level $h_{m,3}/P = 1.46$.

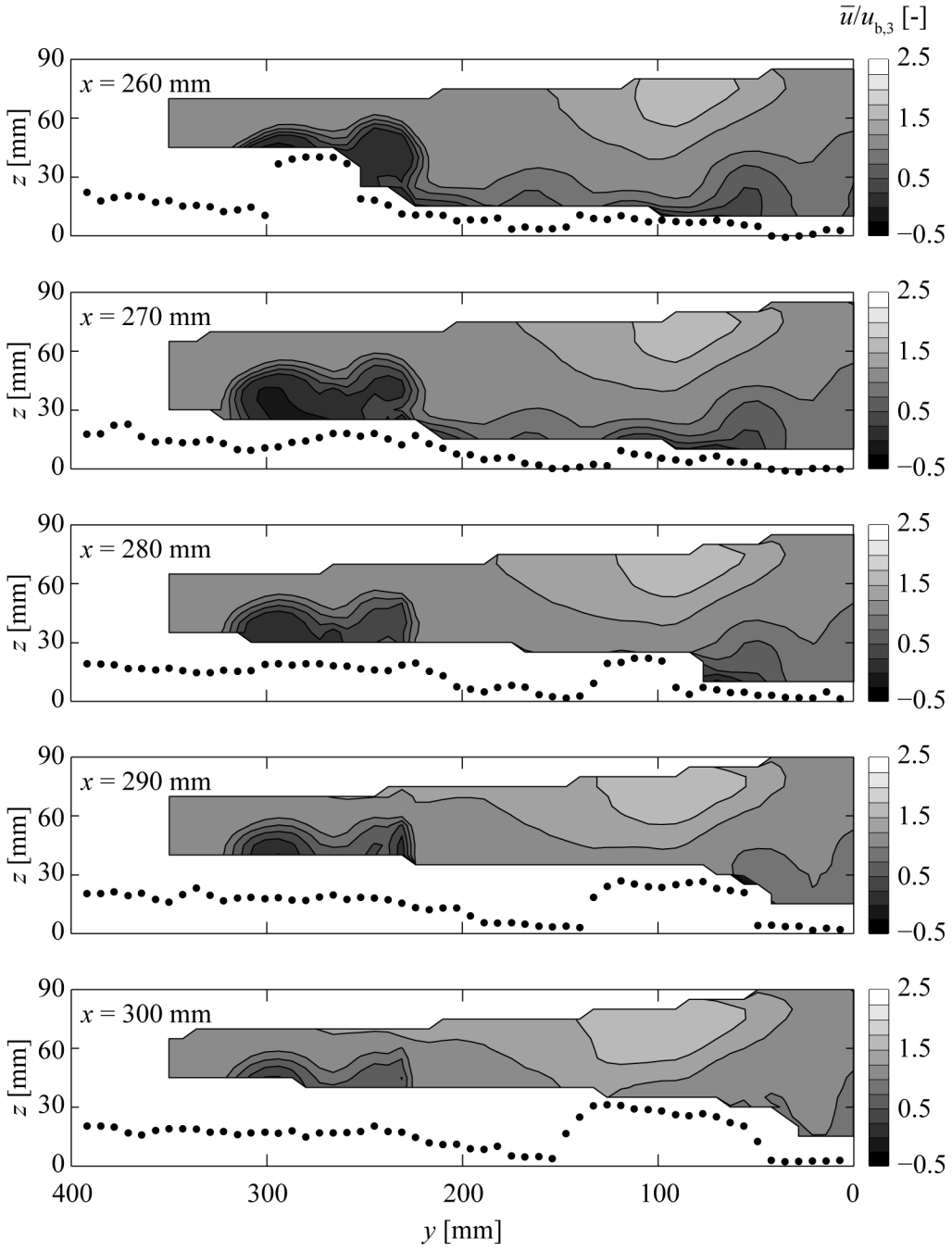

Figure B.7 Cross-sectional downstream view of time-averaged velocities $\overline{u}$ normalized with bulk velocity $u_{b,3} = 0.61$ m/s for specific discharge $q_3 = 40$ l/(sm) and relative submergence level $h_{m,3}/P = 1.46$.

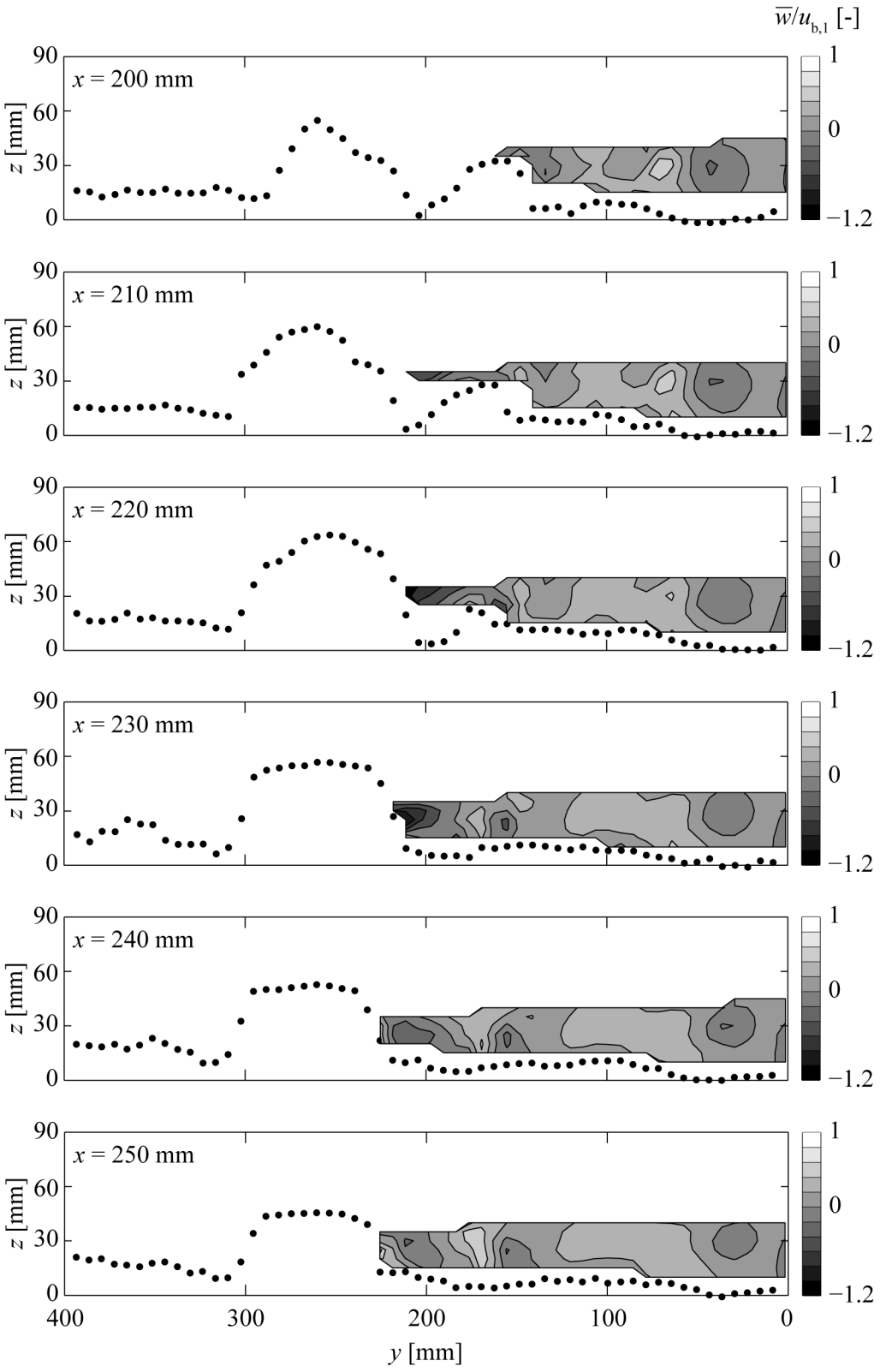

Figure B.8 Cross-sectional downstream view of time-averaged velocities $\overline{w}$ normalized with bulk velocity $u_{b,1} = 0.24$ m/s for specific discharge $q_1 = 6.8$ l/(sm) and relative submergence level $h_{m,1}/P = 0.63$.

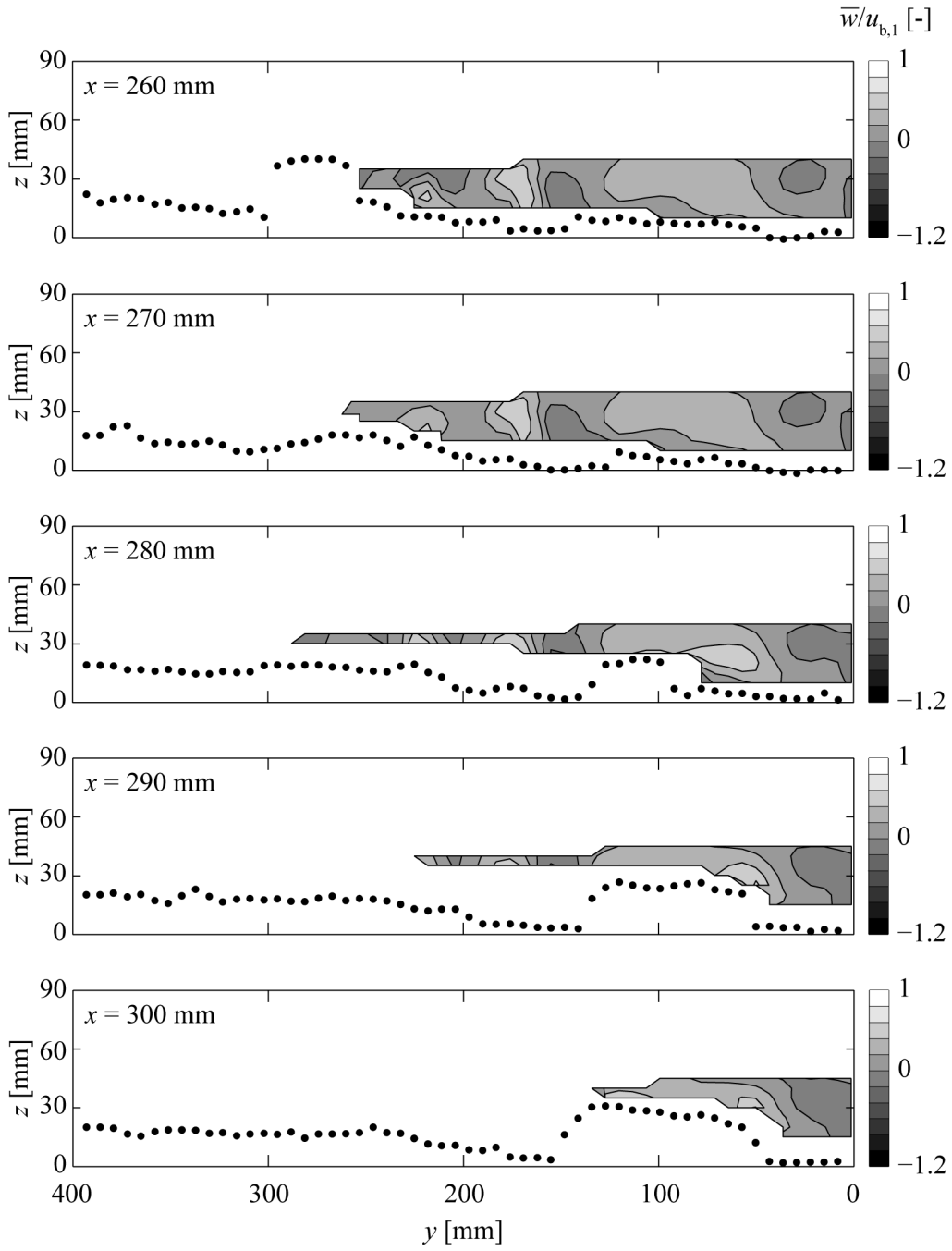

Figure B.9 Cross-sectional downstream view of time-averaged velocities $\overline{w}$ normalized with bulk velocity $u_{b,1}$ = 0.24 m/s for specific discharge q_1 = 6.8 l/(sm) and relative submergence level $h_{m,1}/P$ = 0.63.

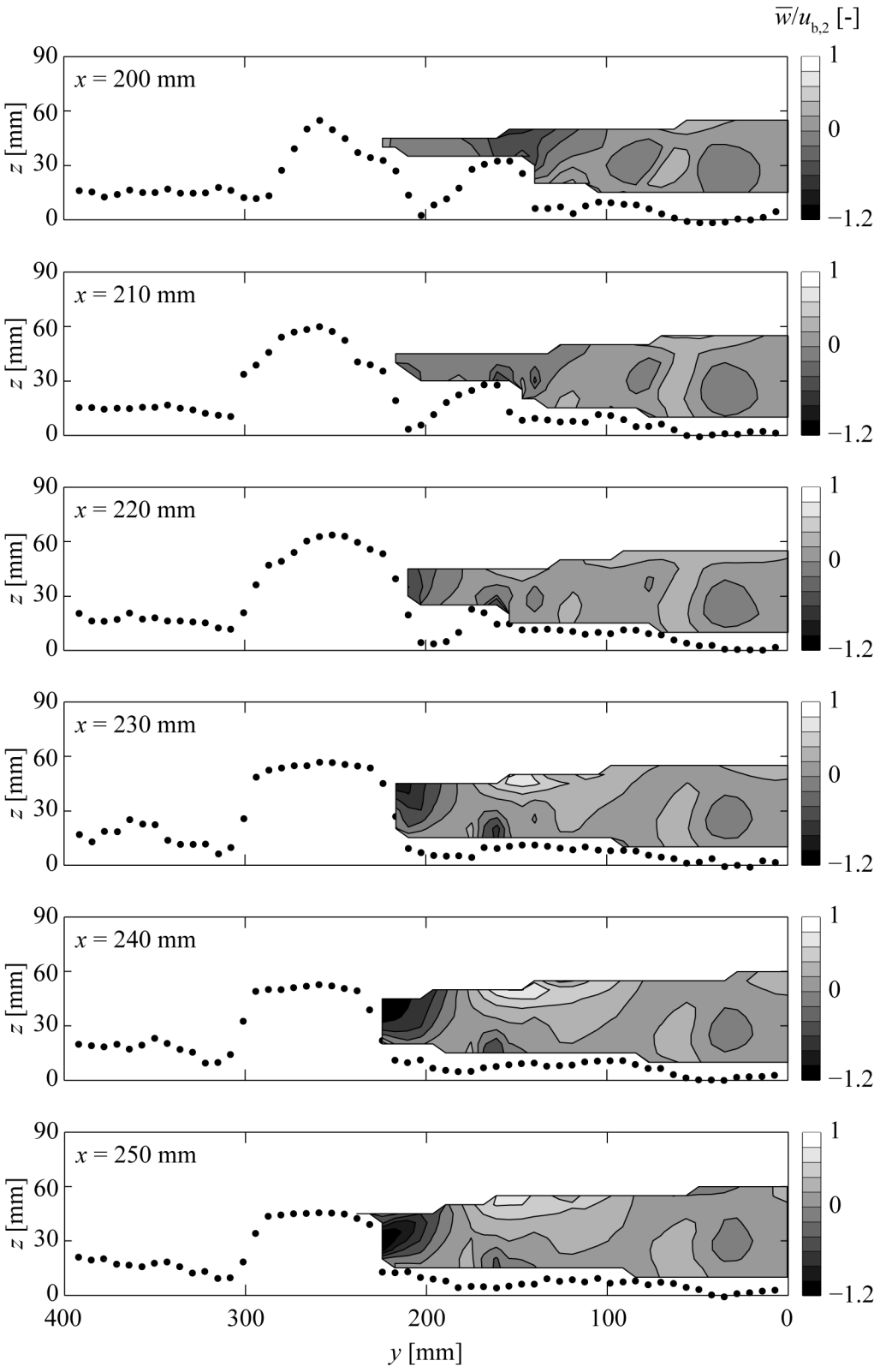

Figure B.10 Cross-sectional downstream view of time-averaged velocities $\overline{w}$ normalized with bulk velocity $u_{b,2} = 0.34$ m/s for specific discharge $q_2 = 13.8$ l/(sm) and relative submergence level $h_{m,2}/P = 0.88$.

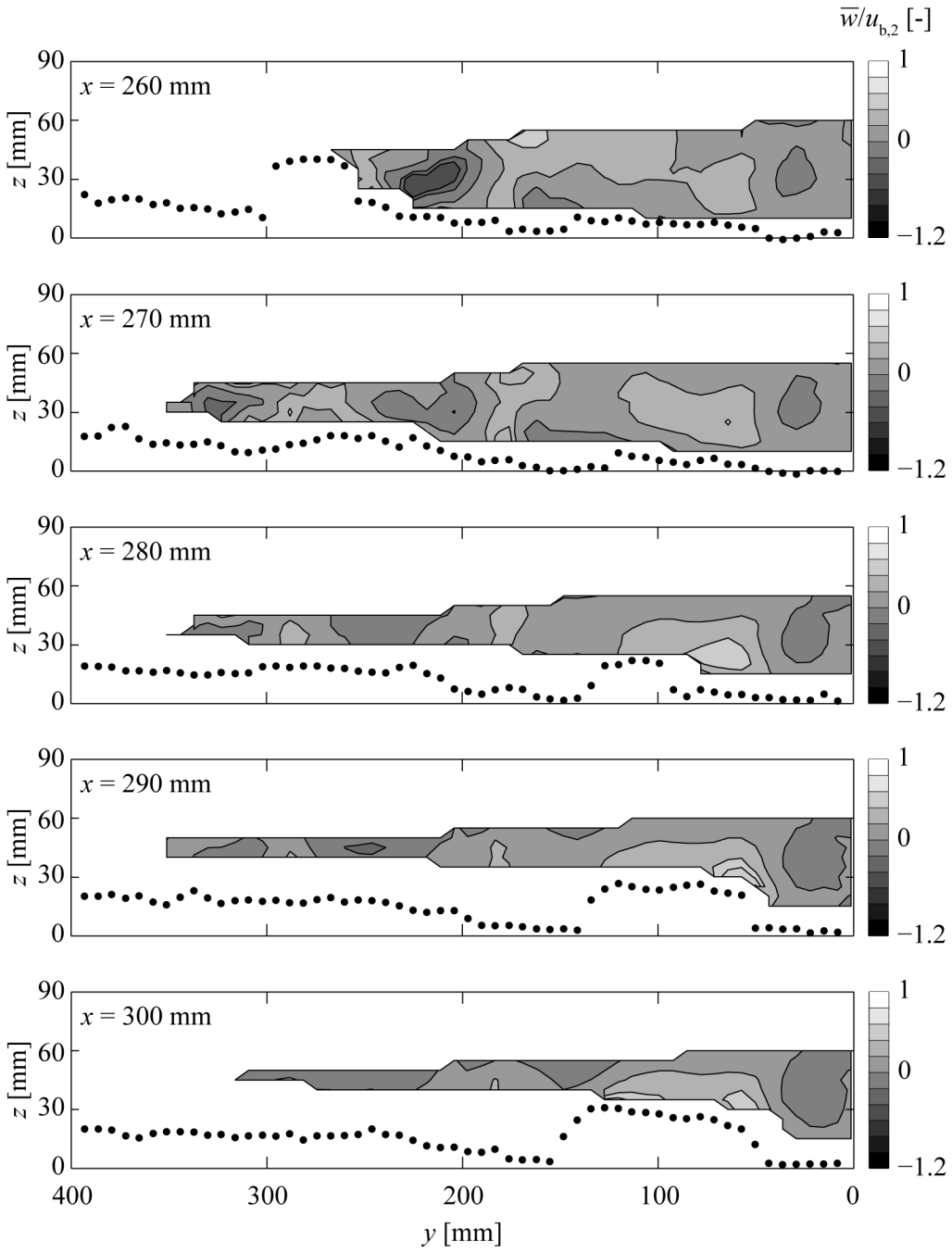

Figure B.11 Cross-sectional downstream view of time-averaged velocities $\overline{w}$ normalized with bulk velocity $u_{b,2} = 0.34$ m/s for specific discharge $q_2 = 13.8$ l/(sm) and relative submergence level $h_{m,2}/P = 0.88$.

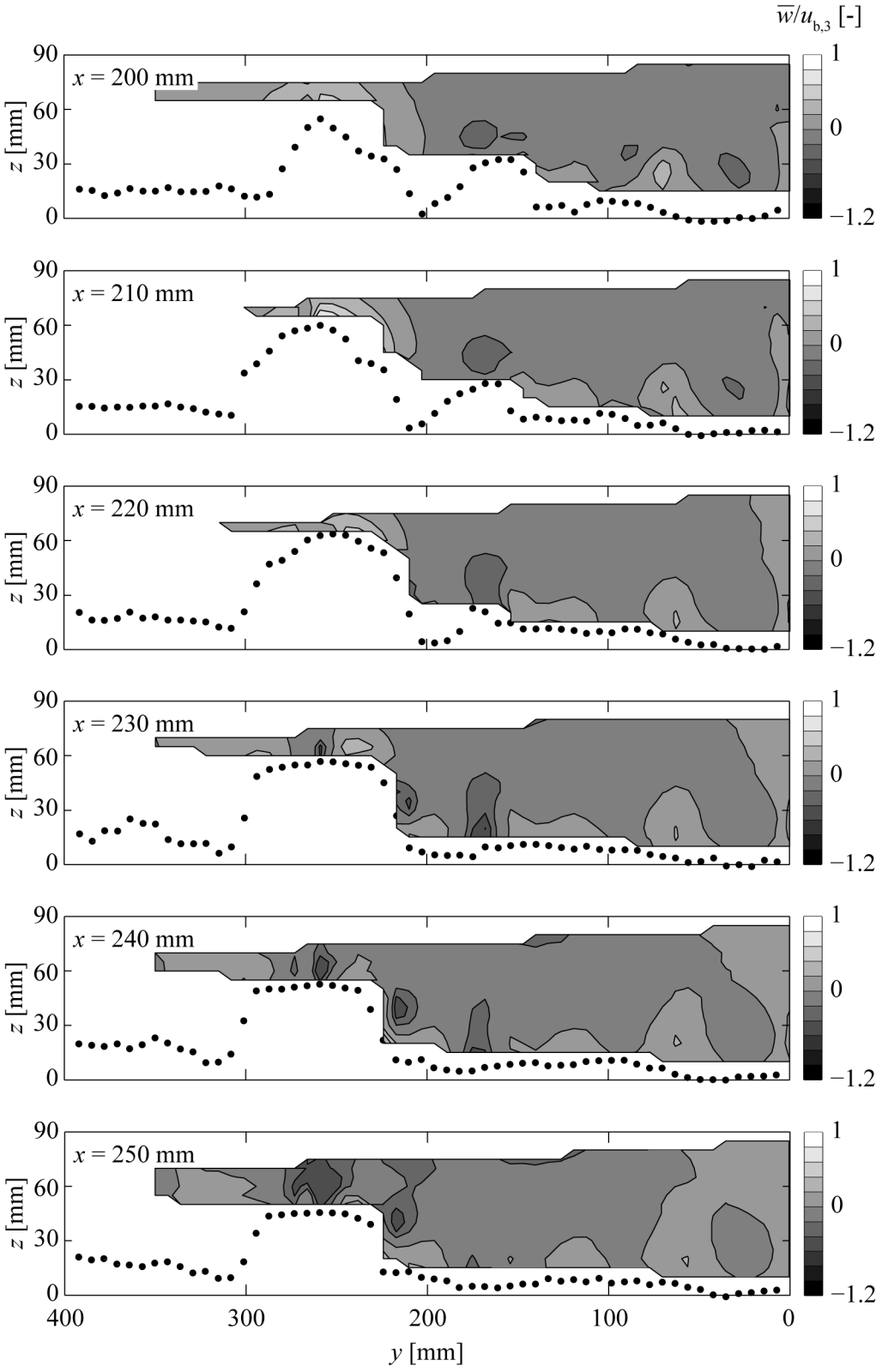

Figure B.12 Cross-sectional downstream view of time-averaged velocities $\overline{w}$ normalized with bulk velocity $u_{b,3} = 0.61$ m/s for specific discharge $q_3 = 40$ l/(sm) and relative submergence level $h_{m,3}/P = 1.46$.

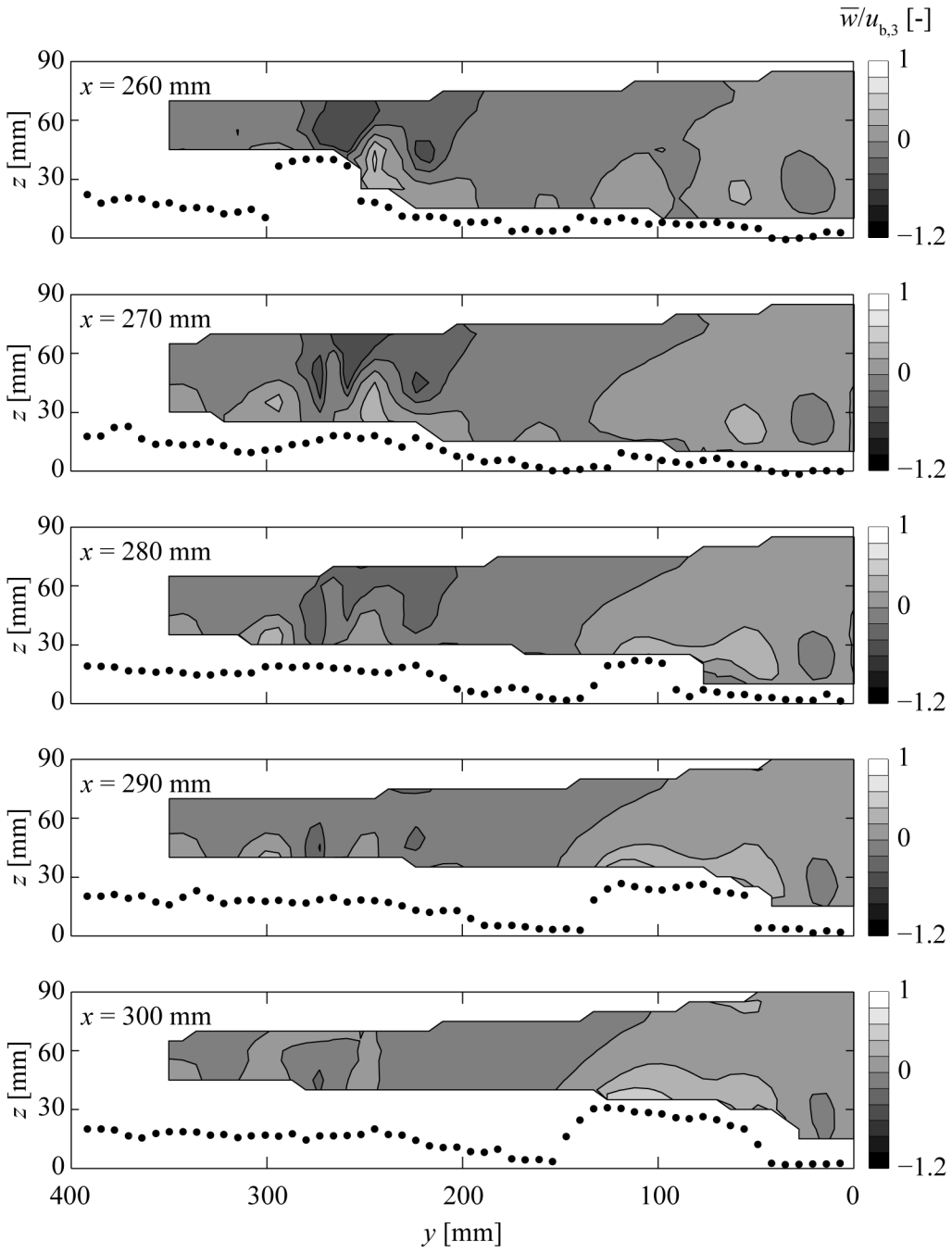

Figure B.13 Cross-sectional downstream view of time-averaged velocities $\overline{w}$ normalized with bulk velocity $u_{b,3} = 0.61$ m/s for specific discharge $q_3 = 40$ l/(sm) and relative submergence level $h_{m,3}/P = 1.46$.

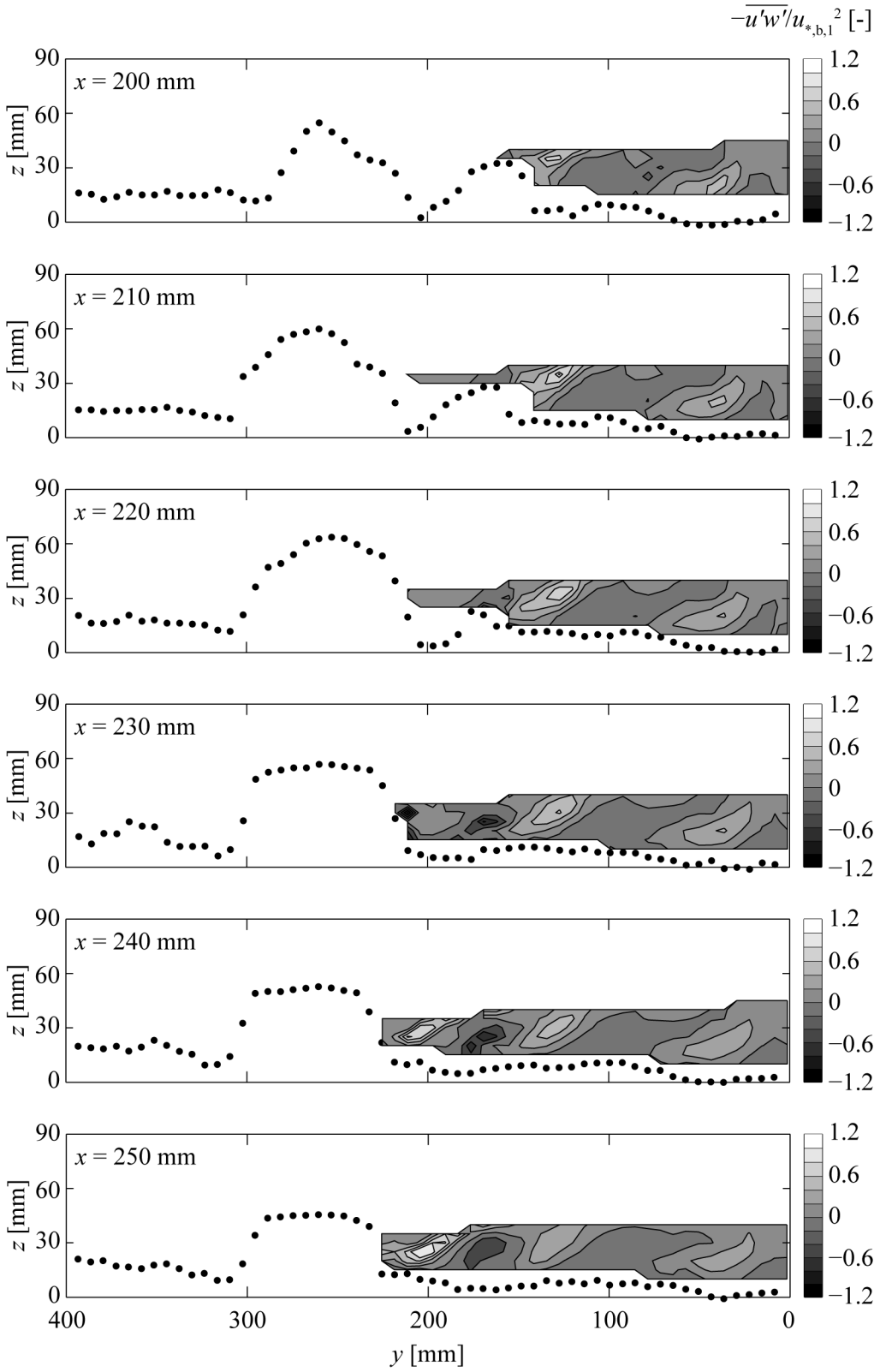

Figure B.14 Cross-sectional downstream view of Reynolds shear stresses $-\overline{u'w'}$ normalized with bulk shear velocity $u_{*,b,1}{}^2 = (0.09 \text{ m/s})^2 = 0.008 \text{ m}^2/\text{s}^2$ for specific discharge $q_1 = 6.8$ l/(sm) and relative submergence level $h_{m,1}/P = 0.63$.

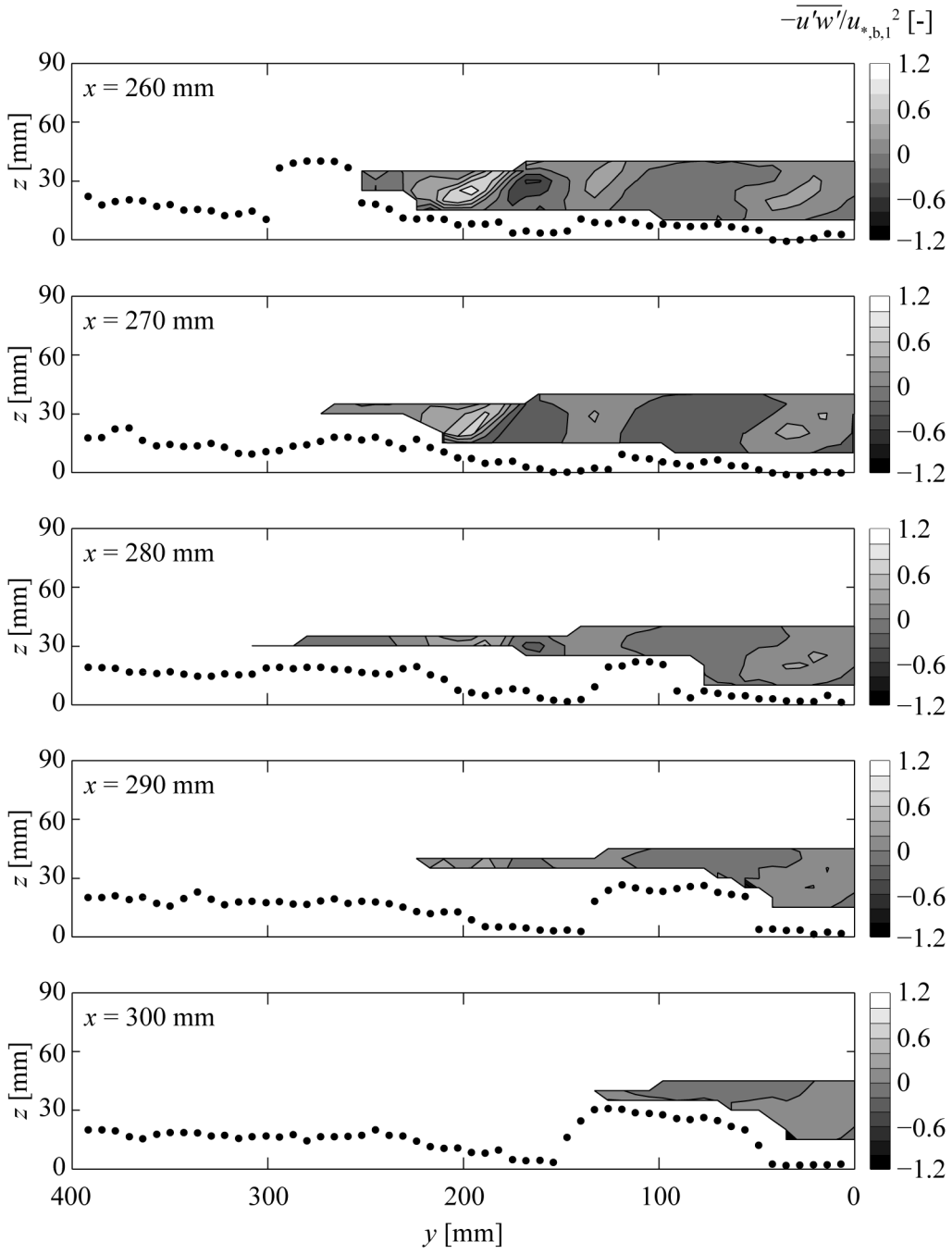

Figure B.15 Cross-sectional downstream view of Reynolds shear stresses $-\overline{u'w'}$ normalized with bulk shear velocity $u_{*,b,1}{}^2 = (0.09\ \text{m/s})^2 = 0.008\ \text{m}^2/\text{s}^2$ for specific discharge $q_1 = 6.8$ l/(sm) and relative submergence level $h_{m,1}/P = 0.63$.

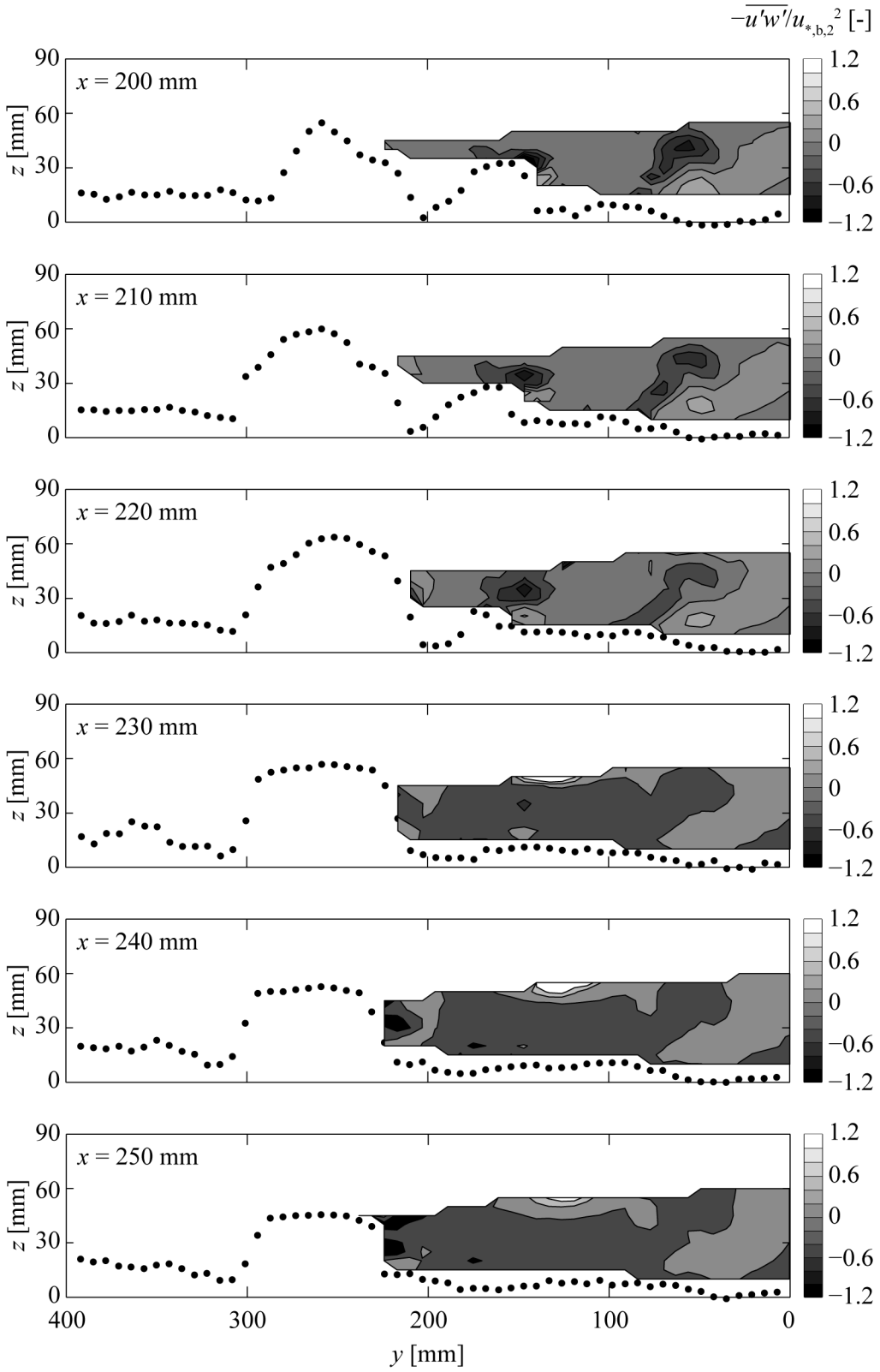

Figure B.16 Cross-sectional downstream view of Reynolds shear stresses $-\overline{u'w'}$ normalized with bulk shear velocity $u_{*,b,2}{}^2 = (0.11 \text{ m/s})^2 = 0.012 \text{ m}^2/\text{s}^2$ for specific discharge $q_2 = 13.8$ l/(sm) and relative submergence level $h_{m,2}/P = 0.88$.

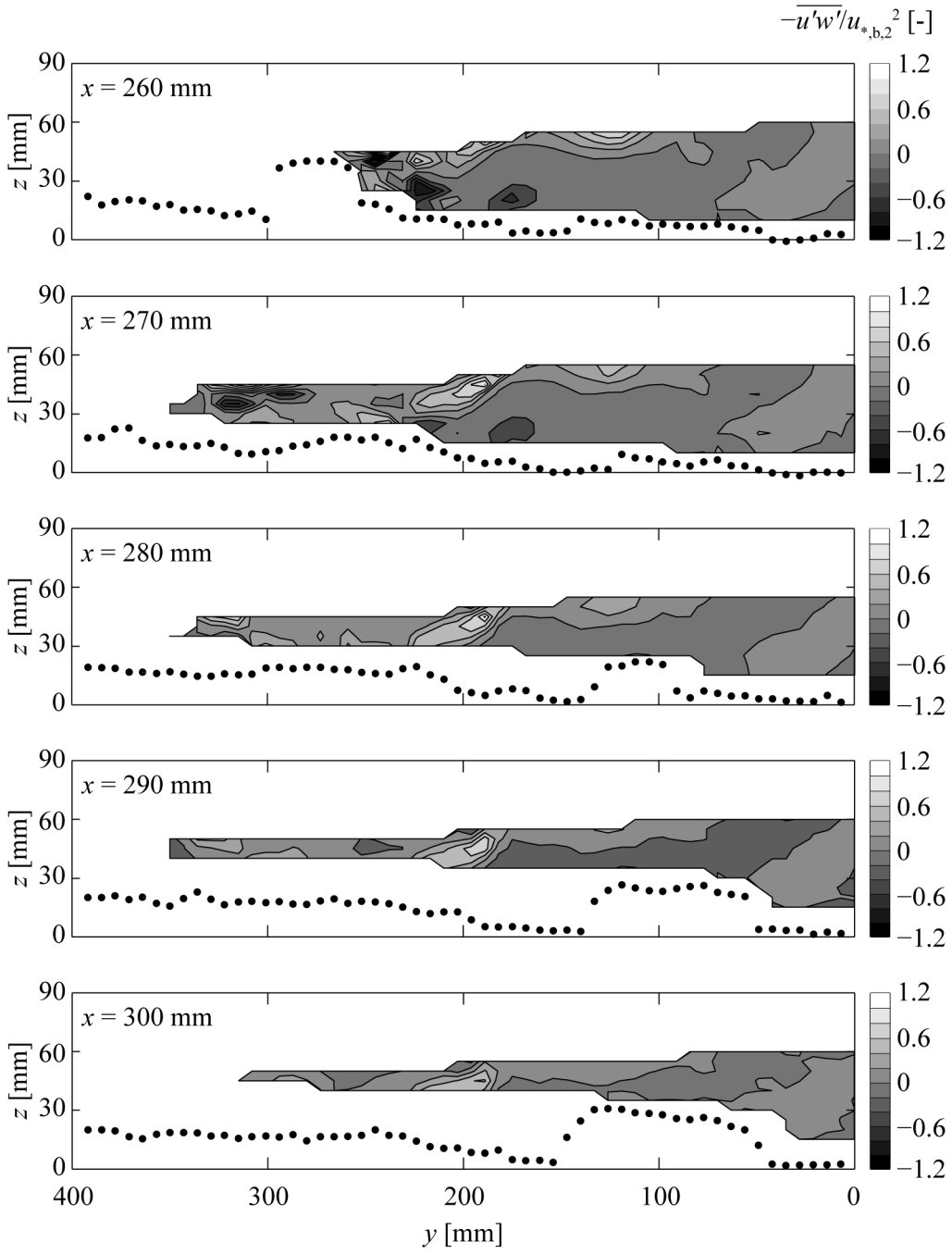

Figure B.17 Cross-sectional downstream view of Reynolds shear stresses $-\overline{u'w'}$ normalized with bulk shear velocity $u_{*,b,2}{}^2 = (0.11 \text{ m/s})^2 = 0.012 \text{ m}^2/\text{s}^2$ for specific discharge $q_2 = 13.8$ l/(sm) and relative submergence level $h_{m,2}/P = 0.88$.

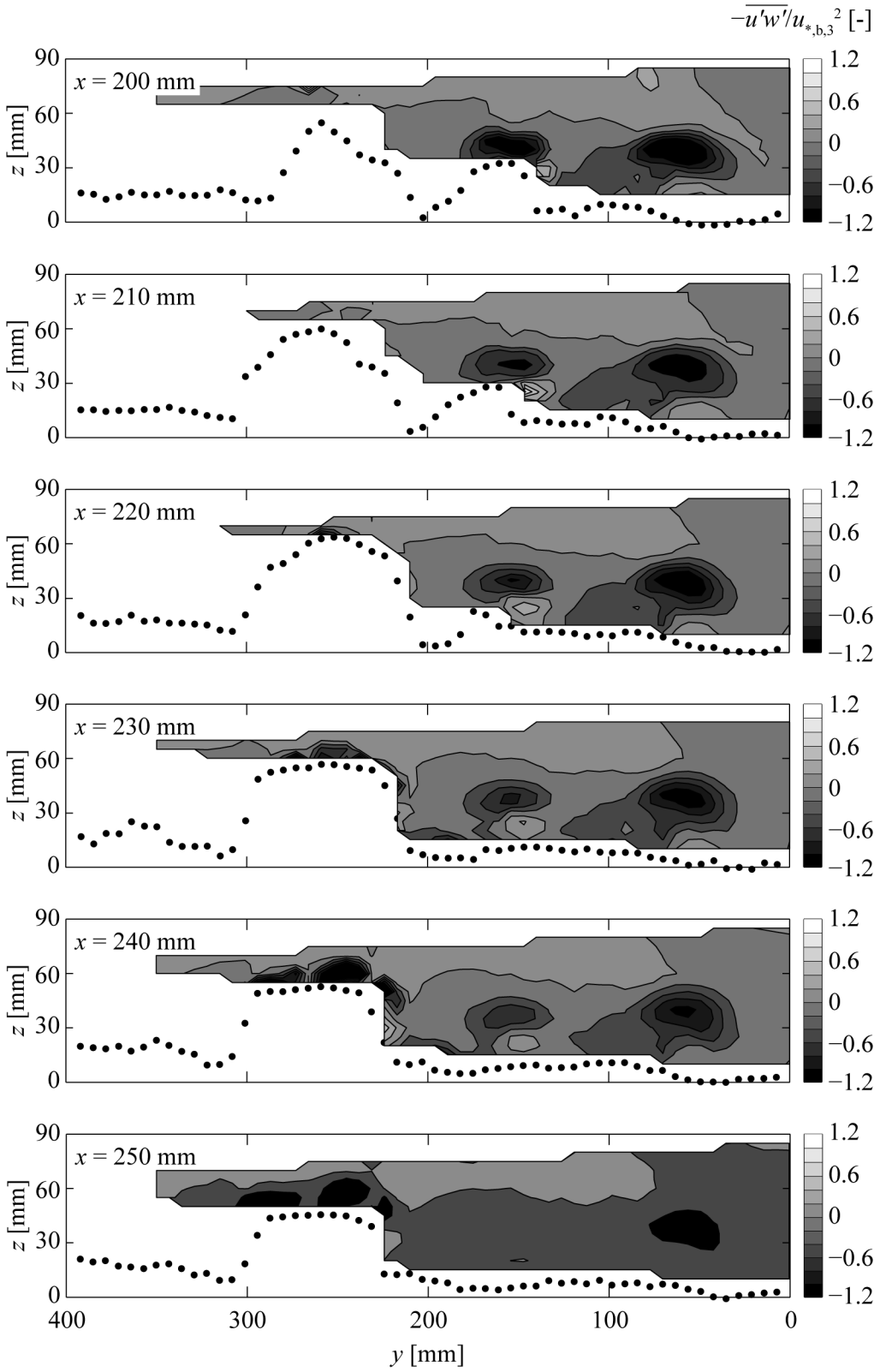

Figure B.18 Cross-sectional downstream view of Reynolds shear stresses $-\overline{u'w'}$ normalized with bulk shear velocity $u_{*,b,3}{}^2 = (0.14 \text{ m/s})^2 = 0.020 \text{ m}^2/\text{s}^2$ for specific discharge $q_3 = 40$ l/(sm) and relative submergence level $h_{m,3}/P = 1.46$.

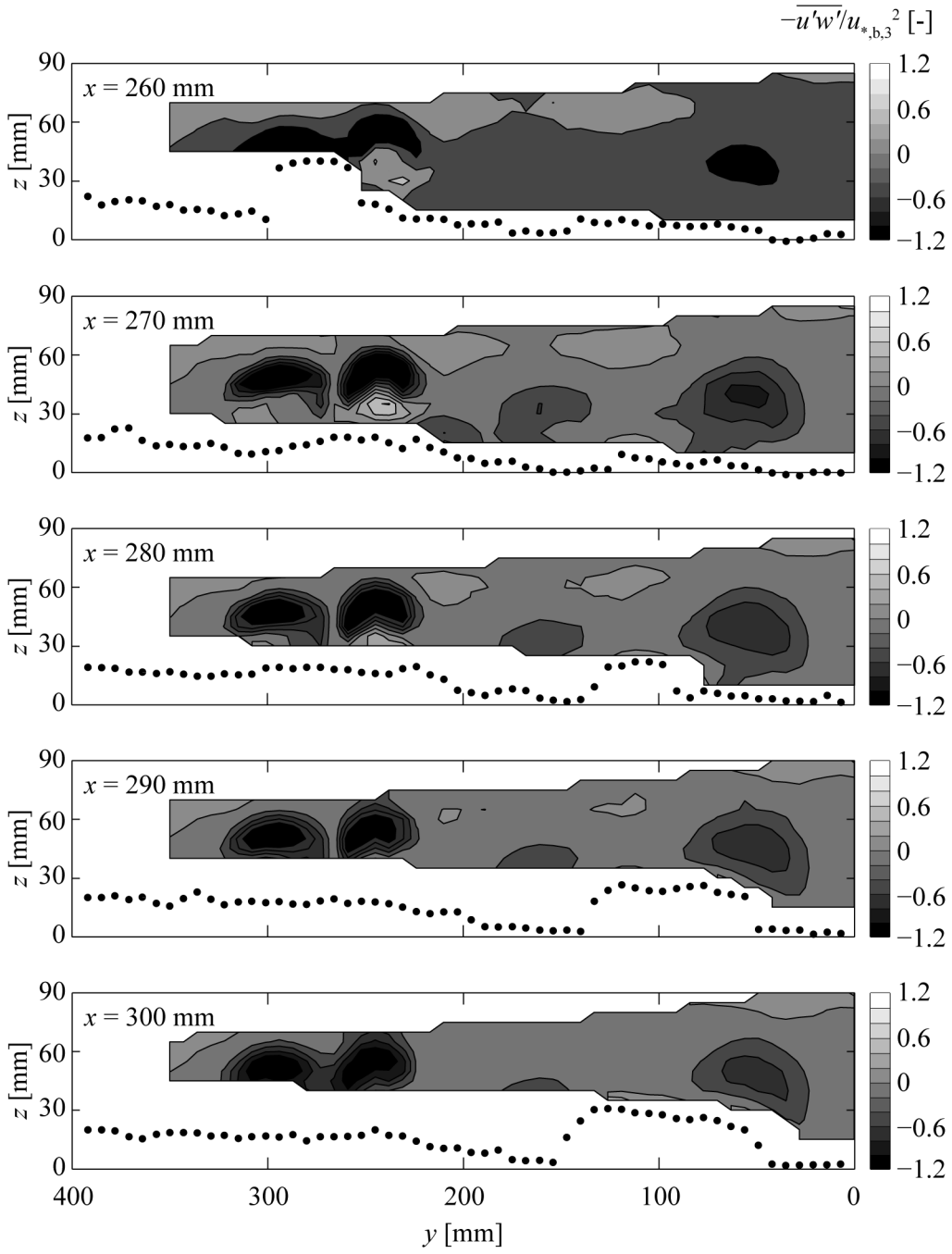

Figure B.19 Cross-sectional downstream view of Reynolds shear stresses $-\overline{u'w'}$ normalized with bulk shear velocity $u_{*,b,3}{}^2 = (0.14\ \text{m/s})^2 = 0.020\ \text{m}^2/\text{s}^2$ for specific discharge $q_3 = 40$ l/(sm) and relative submergence level $h_{m,3}/P = 1.46$.